DEGRADATION MODELS FOR THE COLLAPSE ANALYSIS OF COMPOSITE AEROSPACE STRUCTURES

by

Adrian Cirino Orifici

B. Eng (Aero) (Hon I) (RMIT)

A thesis submitted in fulfilment of the requirements for the degree of Doctor of Philosophy

School of Aerospace, Mechanical & Manufacturing Engineering
Science, Engineering and Technology Portfolio
RMIT University

July 2007

The work described in this thesis was conducted as part of a research program of the Cooperative Research Centre for Advanced Composite Structures (CRC-ACS) Ltd

DECLARATION

I certify that except where due acknowledgement has been made, the work is that of the author alone; the work has not been submitted previously, in whole or in part, to qualify for any other academic award; the content of the thesis is the result of work which has been carried out since the official commencement date of the approved research program; any editorial work, paid or unpaid, carried out by a third party is acknowledged; and, ethics procedures and guidelines have been followed.

_____

Adrian Cirino Orifici

ACKNOWLEDGEMENTS

Firstly, I sincerely thank my supervisors Dr Rodney Thomson of the Cooperative Research Centre for Advanced Composite Structures (CRC-ACS) as Second Supervisor and Dr Javid Bayandor of Royal Melbourne Institute of Technology (RMIT) as First Supervisor, for the wonderful level of guidance I received throughout this PhD. They have always provided tireless support and advice across all aspects of the project, and have been an invaluable source of knowledge and inspiration both professionally and personally.

I would like to express my gratitude for the continued support of my Consultants, Prof. Chiara Bisagni at Politecnico di Milano (Polimi), Italy, and Dr Richard Degenhardt of the German Aerospace Center (DLR). Their expertise and guidance have been critical to the success and timeliness of this project. In particular, their dedicated support during my 5-month placement in the Institute of Composite Structures and Adaptive Systems at DLR and 6-month stay in the Department of Aerospace Engineering at Polimi ensured that this time was both highly productive and personally enriching, and I thank them both for such a rewarding opportunity.

I would like to thank Prof. Murray Scott (CRC-ACS), Prof. Chiara Bisagni (Polimi) and Prof. Adrian Mouritz (RMIT), who supported my involvement in the European Commission project COCOMAT, and were responsible for such a challenging and rewarding opportunity for my research. I would also like to thank my original RMIT First Supervisor Dr Minh Nguyen for his initial support in the early stages of the project.

This work was funded by the Australian Postgraduate Award and the CRC-ACS, whose support I acknowledge as fundamental to this thesis. Additional financial support was provided by the German Academic Exchange Service, the Italian Ministry of Foreign Affairs and RMIT University. The contributions of the European Commission, Priority Aeronautics and Space, Contract AST3-CT-2003-502723, and the Australian Government under the "Innovation Access Programme – International Science and Technology" are also duly acknowledged.

I would like to thank all those that have contributed to the work in this project. I am particularly indebted to colleagues at the CRC-ACS, including Drs Israel Herszberg and Andrew Gunnion and Dr Stefanie Feih of RMIT, who have provided a wealth of expertise and

advice throughout my PhD that has been invaluable to the development of both this work and of myself as a research engineer. I would like to thank the technical support provided by MSC.Software throughout the project, including Dr Andrew Currie who provided initial assistance, and in particular I am sincerely grateful for the assistance of Dr Michael Giess, whose support was critical in the development stages of this work. I would also like to acknowledge Mr Howard Moreton and Mr Greg Cunningham of the Defence Science and Technology Organisation (DSTO) and Mr Caleb White of RMIT for their insight and assistance with scanning and inspection of several test specimens, and the resources provided by the Victorian Partnership of Advanced Computing.

I would like to thank the members of the COCOMAT consortium, led by Dr Degenhardt, for their continued support within the project. The high level of technical discussion and advice provided by the COCOMAT members was greatly beneficial to this thesis, and in particular I would like to acknowledge the valued contributions of Prof. Haim Abramovich and Prof. Tanchum Weller at Israel Institute of Technology (Technion), Mr Alexander Kling at DLR, and Mr Iñigo Ortiz de Zarate Alberdi of Aernnova Engineering Solutions (Aernnova). I would also like to express my gratitude to the experimental test teams at DLR, Technion, Aernnova and RWTH Aachen University for the generous consent to use results from their laboratories, which has been fundamental to the success of the work in this thesis.

I wish to thank my fellow students, in particular Shannon Ryan, Dr Henry Li and Asimenia Kousourakis of RMIT, Zoltan Mikulik at the University of New South Wales, Axel Reinsch and Andrea Winzen at DLR, and Potito Cordisco and Igor Gaudioso at Polimi. Their enthusiasm, inventiveness and dedication have been both instructive and inspirational, and their friendships have been a continual source of motivation and support.

To my family and friends, I thank them for the wonderful support I have had not only during this thesis but over my entire academic career. This work would not have been possible without the thoughtfulness and understanding of the people close to me, and I consider myself fortunate to have had such care and support throughout every stage of my life.

Finally, to my Adriana, who I am indebted to beyond measure, and to whom I dedicate this and every achievement of our lives.

CONTENTS

DECLARATION ii

ACKNOWLEDGEMENTS iii

SUMMARY 1

1 INTRODUCTION 4

1.1 Context 5

1.2 Outline 8

1.3 Outcomes 9

List of Publications 12

2 POSTBUCKLING AND DAMAGE MODELLING 16

2.1 Introduction 16

2.2 Literature Review 16

2.2.1 Structural Analysis 16

2.2.1.1 Plate Theory 17

2.2.1.2 Analytical Versus Numerical 18

2.2.1.3 Explicit Versus Implicit 19

2.2.1.4 Postbuckling Analysis 20

2.2.2 Failure Mechanisms 24

2.2.2.1 Fibre Failure 25

2.2.2.2 Buckling 25

2.2.2.3 Delamination 26

2.2.2.4 Skin-Stiffener Debonding 26

2.2.2.5 Matrix Cracking 27

2.2.2.6 Conclusion 28

2.2.3 Damage Characterisation 28

2.2.3.1 Strength 28

2.2.3.2 Fracture Mechanics 29

2.2.3.3 Experimental Identification 33

2.2.4 Damage Modelling 34

2.2.4.1 Damage Mechanics 35

2.2.4.2 Progressive Damage 35

2.2.4.3 Interface Elements 37

2.2.4.4 Cohesive Elements 39

2.2.4.5 Fracture Mechanics 40
2.3 Benchmarking Study 41
2.3.1 Experimental Data 41
2.3.2 Numerical Analysis 43
2.4 Discussion 48
2.4.1 Structural Analysis 48
2.4.2 Damage Modelling 49
2.4.3 Analysis Tool 50
2.5 Conclusion 51
3 INTERLAMINAR DAMAGE INITIATION 53
3.1 Introduction 53
3.2 Experimental Investigation 55
3.3 Numerical Analysis 59
3.4 Discussion 66
3.5 Conclusion 68
4 INTERLAMINAR DAMAGE PROPAGATION 69
4.1 Introduction 69
4.2 Model Development 71
4.2.1 Modelling Approach 71
4.2.2 Strain Energy Release Rates 74
4.2.3 Propagation Modelling 79
4.2.4 Automatic Cut-Backs 83
4.3 Experimental Comparison 84
4.3.1 Experimental Results 85
4.3.2 Numerical Analysis 89
4.3.3 Discussion 99
4.4 Numerical Investigations 100
4.4.1 Mode III: Edge Crack Torsion 100
4.4.1.1 Introduction 100
4.4.1.2 Numerical Analysis 101
4.4.2 Abaqus Comparison 104
4.4.3 Asymmetric Laminates 105
4.5 Conclusion 107
5 ANALYSIS METHODOLOGY 109
5.1 Analysis Methodology 109

5.1.1 Ply Degradation 109
5.1.2 Global-Local Analysis 112
5.1.3 Interface Location 114
5.1.4 Impact Analysis 116
5.1.5 Subroutines and External Files 116
5.1.6 Overview 119
5.2 Validation 120
5.2.1 Intact Specimens 121
5.2.1.1 Experimental Results 121
5.2.1.2 Numerical Analysis 122
5.2.2 Debond Specimens 127
5.2.2.1 Experimental Results 127
5.2.2.2 Numerical Analysis 132
5.2.3 Discussion 140
5.3 Conclusion 142
6 ANALYSIS TOOL 143
6.1 Introduction 143
6.2 Analysis Tool Functionality 143
6.2.1 Main Menu 144
6.2.2 Define Damage Sub-Menu 145
6.2.3 Define Properties Sub-Menu 145
6.2.4 Run Analysis Sub-Menu 149
6.2.5 Post-Processing Sub-Menu 151
6.3 Conclusion 153
7 APPLICATION TO DESIGN AND ANALYSIS 154
7.1 Introduction 154
7.2 Design 156
7.2.1 Intact 156
7.2.2 Pre-Damaged 162
7.3 Analysis 166
7.3.1 Intact 166
7.3.2 Pre-Damaged 170
7.4 Discussion 175
7.5 Conclusion 177
8 CONCLUSION 178

8.1 Summary of Findings 178
8.2 Further Work 180
8.3 Final Remarks 183
REFERENCES 184
Appendix A – Modification Factor Investigation 197

LIST OF FIGURES

Figure 1.1: COCOMAT (a) current and (b) future design scenarios for typical stringer stiffened composite panels 6
Figure 2.1: Homogenisation of ply properties in Classical Laminated Plate Theory 17
Figure 2.2: Crack growth modes: a) I. Peeling b) II. Shearing c) III. Tearing 30
Figure 2.3: Fracture mechanics characterisation tests: a) Mode I b) Mode II c) Mixed-Mode I-II 34
Figure 2.4: Cohesive zone bilinear material model 39
Figure 2.5: B1 panel: (a) Experimental panel in test rig (courtesy of Technion) (b) Schematic of panel restraints with boundary condition (BC) definition 42
Figure 2.6: B2 load-displacement graph, with photogrammetry mode shapes superimposed 43
Figure 2.7: B3 panel: (a) FE model (MPCs not shown) (b) Boundary conditions (c) Experimental impact sites (d) FE model impact delamination modelling 44
Figure 2.8: B1 and B3 load versus displacement, experiment and Nastran FE results 46
Figure 2.9: B2 mode shape progression, all FE models (stroke values in mm) 47
Figure 2.10: B2 load versus displacement, all FE solvers 48
Figure 3.1: Deformation patterns in postbuckling skin-stiffener interfaces: (a) Local buckling (antisymmetric) (b) Global buckling (symmetric) (Abramovich & Weller 2006) 54
Figure 3.2: T-section geometry, all dimensions in mm (Abramovich & Weller 2006) 55
Figure 3.3: Antisymmetric test rig at Technion Aerospace Structures Laboratory (Herszberg et al. 2007) 56
Figure 3.4: Failure types: (a) 1. Skin-stiffener bend (b) 2. Stiffener (c) 3. Flange edge (Herszberg et al. 2007) 57
Figure 3.5: Symmetric tests, data range and failure energies, with outliers 58
Figure 3.6: Antisymmetric tests, data range and failure energies, failure types 1 and 2, outliers removed 59
Figure 3.7: 2D FE models: (a) Antisymmetric (b) Symmetric tests 60
Figure 3.8: Skin-stiffener junction modelling showing element orientations 60
Figure 3.9: Symmetric specimen: (a) Normalised applied energy versus loading displacement (b) delamination failure index at first failure 63

Figure 3.10: Antisymmetric specimen: (a) Normalised applied energy versus loading angle (b) delamination failure index at first failure 63
Figure 3.11: Lateral displacement of specimen under loading: (a) Unloaded (b) Loaded (c) Schematic taken from (a) and (b) showing y displacement of piston and x displacement measured at left and right stiffener edges 63
Figure 3.12: (a) Antisymmetric model through-thickness tensile and shear stress (b) Effect of Z_t / S_{yz} on the failure index at first failure 65
Figure 3.13: Antisymmetric specimen with 2 mm (updated) and 3 mm inner bend radius (a) Normalised applied energy versus loading angle (b) Failure index at first failure 65
Figure 4.1: DCB modelling with user-defined MPCs 71
Figure 4.2: Laminate definition with dummy layers shown 72
Figure 4.3: Error in interlaminar shear stress distribution due to zero-stiffness layers 72
Figure 4.4: Nonlinear analysis flow with user subroutines for degradation modelling 73
Figure 4.5: Crack closure method: (a) Step 1. Crack closed (b) Step 2. Crack extended 75
Figure 4.6: VCCT model with arbitrary rectangular shell elements 75
Figure 4.7: Determining the local crack front coordinate system for an arbitrary crack front, after Krueger (2002) 76
Figure 4.8: Crack front pattern, VCCT MPCs and crack growth area for each crack type 78
Figure 4.9: Analysis flow and example growth for propagation methods 1, 2 and 3 79
Figure 4.10: Analysis flow and several example growths for propagation method 4 80
Figure 4.11: PM 4 f_m values, for each crack front type and growth type 83
Figure 4.12: Example output written to .out file for increment size cut-back using the automatic cut-back functionality 84
Figure 4.13: (a) DCB, (b) ENF and (c) MMB experimental test setups 88
Figure 4.14: Applied load versus displacement (a) DCB tests (b) ENF tests 88
Figure 4.15: (a) Applied load versus displacement, MMB tests (b) Woven fabric 950-GF3-5H-1000, curve-fitting fracture toughness values for mixed-mode failure criteria 88
Figure 4.16: DCB, ENF and MMB modelling, ENF 2.5 mm model shown in top figure 90
Figure 4.17: Applied load versus displacement, DCB Test #7 and 2.5 mm model with PMs 1-4 91
Figure 4.18: Applied load versus displacement, DCB Test #7 and PM 1, all FE models 91
Figure 4.19: DCB strain energy release rate at 1.3 mm applied displacement, all FE models 92

Figure 4.20: DCB model, crack growth progression with applied displacement for: left – PM 1 with all models; right – 2.5 mm model with all propagation methods. 93
Figure 4.21: ENF models, applied load versus displacement: (a) PM 1, Power law, varying mesh density (b) Varying propagation method 94
Figure 4.22: MMB models (varying G_{II} / G_T), applied load versus displacement: (a) Varying failure criterion (b) Varying propagation method....94
Figure 4.23: G distribution along crack front: (a) ENF, all models (b) MMB 50% 5 mm 94
Figure 4.24: MMB 25% 5 mm model, deformed shape and crack growth, 3 mm displacement....95
Figure 4.25: Crack growth initiation for PMs 1 and 4, showing the difference between assumed and actual strain energy release rates for both methods 98
Figure 4.26: Mode III ECT configuration 101
Figure 4.27: Geometry and support conditions for ECT tests, dimensions in mm....101
Figure 4.28: ECT model: (a) Applied load versus displacement, 2.5 mm model (b) Strain energy release rates across the crack front at crack growth onset....103
Figure 4.29: Final deformed shape and crack growth region, ECT 103
Figure 4.30: Marc VCCT, Abaqus VCCT and Abaqus cohesive comparison: (a) Applied load versus displacement (b) Strain energy release rate at 1.3 mm displacement, 2.5 mm mesh, ...104
Figure 4.31: Strain energy release rate across crack front, all models: (a) 0-90 (b) D1....106
Figure 4.32: Strain energy release rate (a) across crack front, D2 (b) at the crack front mid-point versus the number of elements per mm 106
Figure 5.1: Example skin-stiffener interface: (a) Global model (b) Local model with global-local boundary conditions shown 114
Figure 5.2: Developed methodology analysis procedure for intact and pre-damaged models 119
Figure 5.3: Single-stiffener specimen geometry 121
Figure 5.4: Single-stiffener intact specimens, load-displacement: (a) D1 (b) D2....121
Figure 5.5: Single-stiffener intact specimens: (a) D1 antisymmetric buckling pattern (b) D2 antisymmetric buckling pattern (c) example damage at failure (D2 test #1) showing fibre fracture, matrix cracking and skin-stiffener debonding (courtesy of Aernnova) 122

Figure 5.6: Single-stiffener specimen: (a) Global model, load and boundary conditions (b) Local model skin-stiffener interface with material definition (D1 model shown) 123
Figure 5.7: Single-stiffener intact specimens, applied load versus displacement, experiment and FE predictions: (a) D1 (b) D2 124
Figure 5.8: Single-stiffener intact specimens, local delamination prediction at applied displacement: (a) D1 (b) D2 124
Figure 5.9: Single-stiffener intact specimens, out-of-plane fringe plot and ply damage failure index at various applied displacement levels: (a) D1 (b) D2 125
Figure 5.10: Single-stiffener debond specimens, load-displacement: (a) D1 (b) D2 128
Figure 5.11: Single-stiffener debond specimens: (a) Deformation before failure (D2 Test #6) (b) D2 asymmetric buckling (D2 Test #8) (c) Damage at failure: skin-stiffener debonding, stiffener delamination and fracture (D1 Test #3) (courtesy of Aernnova) 129
Figure 5.12: Debond specimens, ultrasonic scans after collapse, lengths in mm (a) D1 (b) D2 129
Figure 5.13: Debond specimens segments: (a)-(b) D1 stiffener L-R, (c)-(d) D1 skin L-R, (e)-(f) D2 stiffener L-R, (g)-(h) D2 skin L-R, (i) D1 stiffener (j) D2 stiffener 130
Figure 5.14: Single-stiffener specimen global FE model: (a) Skin-stiffener interface (dummy plies not shown) (b) User-defined MPC definition (D1 model shown) 133
Figure 5.15: Single-stiffener debond specimens, load-displacement: (a) D1 (b) D2 134
Figure 5.16: Single-stiffener debond specimens, buckling deformation pattern at applied displacement: (a) D1 (b) D2 134
Figure 5.17: Single-stiffener debond specimens, debond growth at applied displacement, with PM 4: (a) D1 (b) D2 with G_{Ic} = 1.25 kJ/m^2, G_{IIc} = 2.5 kJ/m^2, (all values in mm) 135
Figure 5.18: Single-stiffener debond specimens, strain energy release rate distribution at onset of crack growth: (a) D1 PM 4 (b) D2 PM 4 135
Figure 5.19: Single-stiffener debond specimens, strain energy release rate at different element sizes (in mm) at the crack front: (a) D1 lower debond edge (b) D2 upper debond edge 136
Figure 5.20: Single-stiffener debond specimens, ply damage at collapse (D2 model shown) 136

Figure 6.1: Analysis tool menu system in Patran with help text box displayed 144
Figure 6.2: The Define Damage sub-menu with the form for element softening shown.....146
Figure 6.3: Example model (single-stiffener specimen) showing damage definition.....146
Figure 6.4: The Define Properties sub-menu with form for reading property data 147
Figure 6.5: Forms from the Define Properties sub-menu for material and control properties.....148
Figure 6.6: The Run Analysis sub-menu 149
Figure 6.7: The Create job form from the Run Analysis sub-menu.....150
Figure 6.8: The Post-Processing sub-menu 151
Figure 6.9: The Query ply failure results form from the Post-Processing sub-menu 152
Figure 7.1: Panel geometry: (a) D1 (b) D2.....155
Figure 7.2: Load-shortening and debond predictions, D1 proposals 158
Figure 7.3: Load-shortening and debond predictions, D2 proposals 159
Figure 7.4: D2 proposal V21r, out-of-plane displacement at applied axial compression 159
Figure 7.5: D2 global model, out-of-plane displacement at applied axial compression 161
Figure 7.6: D2 local model, debond initiation prediction.....161
Figure 7.7: Load-shortening and debond predictions, D2 Nastran and Marc models.....161
Figure 7.8: D1 proposed damage configurations: 100 mm and 200 mm damage region.....162
Figure 7.9: Damage configuration proposals using the 100 mm Teflon debond and modifying the location and stiffener used.....163
Figure 7.10: DLR 100 mm and 200 mm damaged configurations: (a) Load and debond length versus end shortening (b) Radial displacement and debond at 3.0 mm applied compression 164
Figure 7.11: Off-centre location 2 design, out-of-plane displacement and debond size at applied compression values.....165
Figure 7.12: D2 panel (a) imperfection data (b) thermography scan after collapse (scans taken from the panel skin side) (courtesy of DLR) 167
Figure 7.13: D2 experimental load-shortening, with radial displacement contours (stiffener side) (courtesy of DLR) 167
Figure 7.14: D2 panel, load-shortening and debond prediction, experiment and FE models 168
Figure 7.15: D2 panel, (a) global model with local location shown (b) local model.....169
Figure 7.16: D1 panel: (a) imperfection data (b) thermography scan after 3700 cycles (c) ultrasonic scan after collapse (scans taken from the panel skin side) (courtesy of DLR).....171

Figure 7.17: D1 test images with radial displacement contour overlays, showing debond progression (courtesy of DLR) 171
Figure 7.18: D1 experimental load-shortening, with radial displacement contours (stiffener side) (courtesy of DLR) 172
Figure 7.19: D1 cyclic test pre-damage: (a) Schematic representation, (b) Mesh-based approximation, distances given in mm to inside of potting on non-loading side 172
Figure 7.20: D1 panel, experiment and FE load-displacement results, and FE debond length predictions 173
Figure 7.21: D1 panel, out-of-plane deformation (stiffener side) 173
Figure 7.22: D1 panel, debonded area at applied displacement (skin side) 174
Figure 7.23: D1 panel at 2.98 mm applied displacement (collapse): (a) Ply failure index showing stiffener fibre failure (FF) sequence (b) Out-of-plane deformation . 174

LIST OF TABLES

Table 1.1: COCOMAT participant list 5
Table 2.1: Strength criteria for failure initiation 31
Table 2.2: Summary of delamination fracture mechanics approaches 33
Table 2.3: Progressive damage summary 36
Table 2.4: Interface elements summary 38
Table 2.5: Benchmark panel specifications 42
Table 3.1: FE model nominal parameters, symmetric and antisymmetric models 59
Table 3.2: FE model parametric investigation 64
Table 4.1: Geometry and material details for DCB, ENF and MMB tests, dimensions in mm 87
Table 4.2: DCB, ENF and MMB model details 89
Table 4.3: FE analysis summary, for all FE models and all propagation methods 92
Table 4.4: FE analysis time summary, for all FE models and all propagation methods 92
Table 4.5: Material specifications for ECT tests, from Lee (1993) 102
Table 4.6: Non-default analysis parameters, Abaqus VCCT and Abaqus cohesive models 104
Table 4.7: Lay-up definition for asymmetric laminate investigation. 106
Table 5.1: In-plane failure criteria and property reduction 111
Table 5.2: User-defined output variable for in-plane ply failure 112
Table 5.3: D1 and D2 single-stiffener specimen details, all dimensions in mm 120
Table 5.4: Material properties for carbon unidirectional tape IM7/8552 123
Table 5.5: Single-stiffener specimen FE model details 123
Table 5.6: Fracture properties for carbon unidirectional tape IM7/8552 133
Table 5.7: Single-stiffener specimen PM 4 f_m factors from first 25 instances of crack growth 133
Table 7.1: D1 and D2 panel details, all dimensions in mm 155
Table 7.2: D1 panel parameters, all design proposals, all distances in mm 156
Table 7.3: IM7/8552 fracture toughness values for design, taken from literature 157
Table 7.4: D2 panel, FE model details 160
Table 7.5: Material and fracture properties for carbon unidirectional tape IM7/8552 168

ABBREVIATIONS AND ACRONYMS

Term	Definition
2D, 3D	Two-dimensional, Three-dimensional
Aernnova	Aernnova Engineering Solutions
B1, B2, etc.	COCOMAT Benchmarking panel 1, 2, etc.
BC (123 etc.)	Boundary condition (numbers indicate DOF restrained)
CLPT	Classical Laminated Plate Theory
COCOMAT	Improved **MAT**erial Exploitation at Safe Design of **CO**mposite Airframe Structures Through More Accurate Predictions of **CO**llapse
CRC-ACS	Cooperative Research Centre for Advanced Composite Structures
D1, D2	COCOMAT Design 1, COCOMAT Design 2
DCB	Double Cantilever Beam
DLR	German Aerospace Center (Deutsches Zentrum Für Luft und Raumfahrt)
DOF	Degree of freedom
DSTO	Defence Science and Technology Organisation
ECT	Edge crack torsion
ENF	End notched flexure
FE	Finite element
LVDT	Linear-Variable Differential Transducer
MMB	Mixed-mode bending
MPC (123 etc.)	Multi-point constraint (numbers indicted DOF tied)
PM 1, 2, etc.	Propagation Method 1, 2, etc.
Polimi	Politecnico di Milano
POSICOSS	Improved **PO**st-buckling **SI**mulation for Design of Fibre **CO**mposite **S**tiffened Fuselage **S**tructures
RMIT	Royal Melbourne Institute of Technology
RWTH	RWTH Aachen University (Rheinisch Westfälische Technische Hochschule Aachen)
SERR	Strain energy release rate
Technion	Israel Institute of Technology
(V)CCT	(Virtual) Crack Closure Technique
WP	Workpackage

NOMENCLATURE

Term	Unit	Definition
ΔA	mm^2	New crack surface area formed in VCCT
a	mm	Distance from the crack front in VCCT
a_0	mm	Pre-crack length, in fracture mechanics characterisation tests
b	mm	Stiffener pitch, measured in arc length between stiffener centrelines
c	mm	Mixed-mode bending lever arm length
E	MPa	Young's Modulus
F	N	Crack tip force in VCCT
f	-	Failure index, used with crack growth criterion and delamination onset criteria, 0 = no failure, ≥ 1 = failure
f, m, s	-	In-plane failure indices for fibre, matrix and fibre-matrix shear failure
f_m	-	Modification factor, used with PM 4 of interlaminar damage model
G	MPa	Shear modulus (with subscripts x, y, z or 1, 2, 3)
G	kJ/m^2	Strain energy release rate (with subscripts I, II, III)
h	mm	Stiffener height
L, L_f	mm	Total length and Free length, used with large panels
R	mm	Radius of large curved panels
S	MPa	Shear strength
t	mm	Ply thickness
W	mm	Arc length (circumferential distance) of large curved panels
w	mm	Stiffener width
X, Y, Z	MPa	Normal strengths
α	-	Curve-fit parameter for Power law mixed-mode delamination criterion
δ	mm	Displacement from nodes in VCCT
η	-	Curve-fit parameter for B-K mixed-mode delamination criterion
	θ	Location around skin-stiffener junction in bend coordinate system
	σ	Normal stress
	τ	Shear stress

SUBSCRIPTS

Term	Definition
0, 1, 2	In VCCT, values taken from MPCs of states 0, 1 or 2
1, 2, 3	In ply coordinate system, fibre, matrix and through-thickness directions
I, II, III	Crack opening modes: I. Peeling; II. Shearing; III. Tearing
c	Critical, used with strain energy release rate G to indicate toughness
c, C	Compression, used with material strength data
f, m	Fibre, matrix directions, when used with material properties
T	Total, used with strain energy release rate G
t, T	Tensile, used with material strength data
u, l	Upper and lower, used with displacement in VCCT
x, z, yz	In local models of skin-stiffener cross-sections, longitudinal, through-thickness tensile and through-thickness shear directions

SUMMARY

The ever-present need in the aerospace industry for reductions in weight and development costs means that aircraft designers are always looking for more efficient solutions. Advanced fibre-reinforced polymer composites offer numerous advantages over metals due to their high specific strength and stiffness, and have seen a rapid increase in use in recent years. Another approach for design efficiency is to use so-called "postbuckling" structures, which can withstand substantial loads after they have buckled. As a result, designers of the next generation of aircraft are looking to postbuckling composite structures to achieve substantial improvements in aircraft efficiency.

Though the concept of postbuckling has successfully been used to design more efficient metallic aircraft structures for decades, to date its weight-saving potential for composite structures remains largely unexploited. This is because today's analysis tools are not capable of representing the damage mechanisms that lead to structural collapse of composites in compression. In response, the major objective of this work was the development of an analysis methodology and complementary software tool for the design of composite postbuckling structures, which included the degrading effects of the critical damage mechanisms. This work was conducted with the Cooperative Research Centre for Advanced Composite Structures (CRC-ACS) as part of the COCOMAT project, a European Commission Sixth Framework Programme Research Project.

A comprehensive literature review and an extensive benchmark study were conducted to assess the state of the art of postbuckling analysis and damage modelling of stiffened structures. The results of these showed that current analysis tools were capable of handling the structural analysis of postbuckling designs, though confirmed the conclusion that damage prediction and modelling techniques were still largely unreliable for accurate predictions of collapse. From this, a framework for an analysis methodology was proposed, which included the critical effects of interlaminar damage and in-plane ply degradation, and recommended failure theories and modelling approaches suitable for application to postbuckling design of large fuselage-representative composite structures.

As a first step in the analysis methodology, an approach was developed to predict the initiation of interlaminar damage in intact structures. Interlaminar damage, which in stiffened

composite structures is manifested as delaminations and skin-stiffener debonding, is a critical damage type for intact structures as its initiation typically leads to catastrophic failure. An approach was implemented with user subroutines in the finite element (FE) code MSC.Marc (Marc), which monitored a damage failure criterion at every element. This was applied to models of skin-stiffener cross-sections to predict the initiation of damage. The approach was then validated using experimental results on T-section specimens, which were thin sections of fuselage-representative skin-stiffener interfaces that were manufactured and tested at Israel Institute of Technology as part of the COCOMAT project.

A degradation model was developed to represent interlaminar damage growth, which is necessary in the collapse analysis of structures containing a pre-existing damage region. In the degradation model, user-defined multi-point constraints (MPCs) were modelled between composite shell layers, and fracture mechanics calculations using the Virtual Crack Closure Technique (VCCT) were used to control the connection of these MPCs to model damage growth. A novel approach was developed to adapt the VCCT analysis to crack propagation, and was shown to be more accurate than a simple fail-release crack growth method. Gap elements were also introduced across the damaged interface, and all aspects were implemented with user subroutines in Marc. The degradation model was validated using experimental results from COCOMAT for mode I and mode II fracture mechanics tests performed at the German Aerospace Center (DLR), and mixed-mode I-II tests conducted at RWTH Aachen University. The application of the approach was then further studied in numerical investigations, including the analysis of other test specimens and studies into the accuracy of the VCCT calculation.

Following this, a complete methodology was developed for the collapse analysis of composite postbuckling structures including the critical damage types. The methodology included the approach for predicting interlaminar damage, the degradation model for interlaminar crack growth, and a separate degradation model developed for capturing in-plane ply damage mechanisms such as matrix cracking and fibre fracture. Increased functionality was added to make the methodology suitable for large postbuckling structures, including modelling interlaminar damage at only the skin-stiffener interface and using a coarse global model to input deformations on a fine local model. The complete methodology was validated using experimental results for single-stiffener specimens manufactured and tested at Aernnova Engineering Solutions within COCOMAT from fuselage-representative designs. This

demonstrated the application of the methodology for intact and pre-damaged composite postbuckling structures in both design and analysis scenarios.

The analysis methodology was incorporated into a user-friendly software tool, to provide an industry-ready analysis tool for composite postbuckling structures including damage. The tool was implemented as a menu system within MSC.Patran, to provide a series of pre- and post-processing functions for analysing models using the damage and degradation subroutines. The validity and applicability of the analysis methodology and software tool was then demonstrated in both design and analysis scenarios. This was done using several examples for intact and pre-damaged structures taken from the COCOMAT project, including experimental results for fuselage-representative panels tested at the DLR.

Significant research outcomes have been produced as a result of this work. The major outcome has been the development of a comprehensive, validated analysis methodology and accompanying software tool for the collapse analysis of composite postbuckling structures taking degradation into account. This methodology and the separate approaches for damage modelling were extensively validated using experimental results for a wide range of intact and pre-damaged structures. Other key outcomes include the literature review and benchmark study, the novel approach for modelling propagation of interlaminar damage, and design and analysis studies in support of experimental investigations of composite airframe structures.

CHAPTER 1

INTRODUCTION

In the aerospace industry, weight is paramount, and aircraft designers are always striving for more efficient solutions. One of the most successful approaches in recent years has been to use advanced fibre-reinforced polymer composites, which offer considerable advantages over metals due to their high specific strength and stiffness, amongst other properties. Another approach is to design so-called "postbuckling" structures that can withstand high loads even after they have buckled. As a result, the design of postbuckling structures using composite materials remains a key focus for the next generation of aircraft.

The concept of postbuckling design has the potential to produce significant improvements in structural efficiency, particularly in combination with the high performance behaviour of advanced composite materials. By allowing a structure to be operated safely past its buckling point, lighter and more efficient designs can be realised, which leads to a reduction in weight and an increase in the strain energy and ultimate load of a structure. Composite materials also have a range of high performance properties that are particularly advantageous for lightweight, postbuckling structures, such as improved fatigue performance, better performance at high strain rates, the ability to tailor material properties, and the application of low-cost and rapid manufacturing processes.

Though postbuckling has successfully been used to design more efficient metallic aircraft structures for decades, its application to composite structures to date has been limited. This is due to concerns related to both the durability of composite structures and the accuracy of design tools. Composites, unlike metals, do not yield locally due to high local stresses that can be experienced during postbuckling. This, coupled with concerns related to high through-thickness stresses and the development and growth of defects, has restricted the acceptance and application of postbuckling in composite structures.

In compression, composite postbuckling structures develop a range of damage mechanisms, which under further loading combine and lead to the eventual collapse of the structure. Today's analysis tools are not capable of capturing the development and interaction of these damage mechanisms, and the onset of damage in composite postbuckling structures is

currently not allowed. Therefore these types of structures are not currently used in aircraft designs and their weight-saving potential, and the related environmental benefits from more efficient aircraft, remain largely unexploited.

1.1 Context

The European aircraft industry has set requirements for reducing development and operating costs by 20% and 50% in the short and long terms, respectively. The currently running European Commission project COCOMAT contributes to this aim by focusing on applying postbuckling design with improved damage modelling to composite structures (Degenhardt et al. 2006; www.cocomat.de). COCOMAT, or "Improved **MAT**erial Exploitation at Safe Design of **CO**mposite Airframe Structures by Accurate Simulation of **CO**llapse", is a four-year Specific Targeted Research Project under the European Commission Sixth Framework Programme, and is scheduled for completion by the end of 2007. The COCOMAT consortium consists of 15 international partners, consisting of aircraft manufactures, research institutions and software developers, listed in Table 1.1. The project benefits from a high degree of synergy with a recently completed European Commission project POSICOSS (www.posicoss.de), or "Improved **PO**st-buckling **SI**mulation for Design of Fibre **CO**mposite **S**tiffened Fuselage **S**tructures", which similarly investigated the behaviour of stiffened composite panels in compression, but did not include the effects of material degradation.

Table 1.1: COCOMAT participant list

Partner	Country	Type
German Aerospace Center (DLR)	Germany	Research institution
Cooperative Research Centre for Advanced Composite Structures	Australia	Research institution
Swedish Defence Research Agency (FOI)	Sweden	Research institution
Aernnova Engineering Solutions (Aernnova)	Spain	Industrial partner
Agusta S.p.A	Italy	Industrial partner
Hellenic Aerospace Industries	Greece	Industrial partner
Israel Aircraft Industries	Israel	Industrial partner
PZL Swidnik	Poland	Industrial partner
Politecnico di Milano	Italy	University
University of Karlsruhe	Germany	University
Riga Technical University	Latvia	University
RWTH Aachen University	Germany	University
Israel Institute of Technology (Technion)	Israel	University
SMR	Switzerland	Software developer
Samtech	Belgium	Software developer

The main scientific and technological objective of COCOMAT is the increased exploitation of postbuckling composite structures, to such an extent that material degradation is allowed within the operating safety region of aircraft. To do this, degradation models are required that more accurately capture the effects of material degradation, which lead to more accurate predictions of the final structural collapse. This is summarised in Figure 1.1, which gives the current and future industrial design scenarios for composite stiffened structures. These design scenarios are shown as simplified representations of the load response of stiffened structures to an applied compression load.

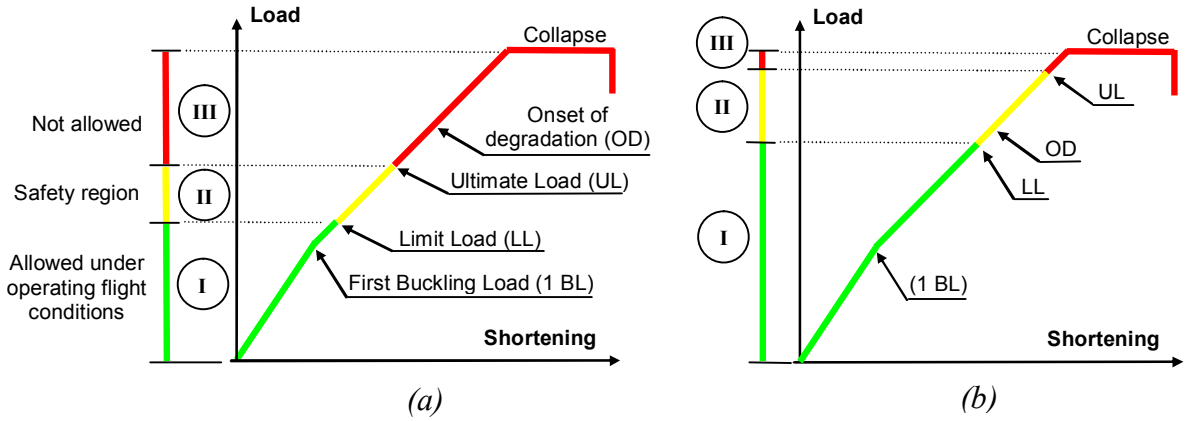

Figure 1.1: COCOMAT (a) current and (b) future design scenarios for typical stringer stiffened composite panels

From Figure 1.1, as a structure is compressed, or the shortening increases, it undergoes buckling, degradation and final collapse. In the current design scenario for composite structures, Figure 1.1(a), degradation is not allowed in any flight condition, so the design limit load and ultimate load (typically 150% of the limit load) need to be set accordingly. This leaves a large strength reserve, in which the onset of degradation has occurred, though the structure is still capable of withstanding further increased load. In the future design scenario of Figure 1.1(b), the onset of degradation is allowed in the safety region of the flight loading, which mirrors the situation currently existing in metallic aircraft design where plasticity is allowed. In order to achieve the future design scenario, accurate and validated degradation models for the composite damage mechanisms are required to allow a more accurate prediction of the final collapse. More accurate predictions of the damage and collapse will allow the strength reserve to be exploited, which will lead to lighter and more efficient composite structures for the next generation of aircraft designs.

This thesis was conducted in conjunction with the CRC-ACS and in contribution to the COCOMAT project. A large part of this was integrated within collaborative work between

CRC-ACS, DLR and Aernnova, which was centred on experimental testing of fuselage-representative composite panels and involved design, testing, analysis and model validation. The work in this thesis was principally focused on developing a validated methodology for the collapse analysis of composite postbuckling structures taking degradation into account. This also included a comprehensive literature review and benchmarking study, and design studies to recommend undamaged and pre-damaged panel configurations. All of the experimental results reported in this work were obtained by other partners and are used with their permission. As a result of these considerations, the thesis objectives were defined as follows:

- Benchmark the current state of the art for analysis of stiffened composite panels in compression, both with and without the inclusion of damage.

- Develop a validated degradation model to simulate the propagation of delaminations or debonds in postbuckling structures.

- Develop a validated methodology to predict the collapse of stiffened structures.

- Validate the analysis methodology by application to experimental results.

- Assist in the design and analysis of test panels for experimental investigation of composite stiffened compression panels.

- Develop an analysis tool by implementing the validated methodology into a commercial FE program.

- Demonstrate the applicability of the developed tool for the analysis of stiffened composite panels.

In terms of the project scope, this work was focused on the development of an "industry-ready" analysis tool, for implementation into current design and analysis practices. As such, the research was focused on practicable, proven and adaptable theories, with an emphasis on analysis approaches suitable for large, postbuckling structures. The structures analysed were principally based on those representative of aircraft fuselage designs, and the damage types investigated were those considered relevant for compression-loaded composite structures.

1.2 Outline

A comprehensive literature review is presented in Chapter 2 that covers all aspects relevant to the analysis of composite stiffened structures in postbuckling and damage modelling up to final collapse. The literature concerning the structural analysis and damage modelling are summarised, with a focus on application to fuselage-representative structures. Following this, results are presented of an extensive benchmark study conducted to investigate the capabilities of current analysis tools and act as a reference point for this research. Finally, the literature review and benchmark study are used to formulate the framework of the analysis methodology developed in this work.

In Chapter 3, an approach is developed to predict the initiation of interlaminar damage in intact structures. This is motivated by the fact that the collapse of structures that do not contain any pre-existing damage usually occurs catastrophically, due to the development of damage between plies of the laminate. An approach is presented that monitors a damage criterion at every element, which is applied to finite element (FE) models of cross-sections to predict the initiation of damage. This approach is then validated using experimental results that were achieved at Technion on T-sections, or thin sections of skin-stiffener interfaces cut from a fuselage-representative panel.

A degradation model to represent the growth of interlaminar damage is given in Chapter 4, which was developed to capture the structural degradation caused by the growth of delaminations and skin-stiffener debonds. The degradation model was based on the application of the Virtual Crack Closure Technique (VCCT), and was implemented into the commercial software program MSC.Marc (Marc). The degradation model was validated using experimental results for fracture mechanics characterisations tests performed at DLR and RWTH Aachen University. The application of the approach was then further studied in numerical investigations, including the analysis of other test specimens and studies into the accuracy of the VCCT calculation.

In Chapter 5, a complete methodology is presented for the collapse analysis of composite postbuckling structures taking degradation into account. The methodology incorporated the analysis approach and degradation model for interlaminar damage developed in previous chapters. Further functionality was added for the complete methodology, including a degradation model to represent ply-based damage mechanisms, and the ability to take deformations from a coarse global model and predict damage in fine local models. The

complete methodology was validated using experimental results produced at Aernnova for single-stiffener specimens based on fuselage representative designs. The application of the analysis methodology for both the design and analysis of composite postbuckling structures was demonstrated.

Chapter 6 presents the user-friendly software tool that was developed to incorporate the developed analysis methodology. The software tool was implemented as a menu system within MSC.Patran (Patran), to provide a series of pre- and post-processing functions necessary for analysing structures using the damage subroutines. The tool was intended to complement the standard Patran framework and functionality, and allow the user to define the damage regions and properties, run the analysis, and assist in the post-processing of results.

In Chapter 7 the validity and applicability of the analysis methodology is demonstrated for a range of scenarios. This includes the design process, where typically various configurations are investigated and comparatively evaluated, and the analysis process, which is commonly used for pre- and post-test simulations. Using examples taken from the COCOMAT project, the developed methodology is shown to be applicable for both of these processes, and for both intact and pre-damaged structures. All of the examples given are for the COCOMAT D1 and D2 large multi-stiffener panels, with experimental results for these panels provided by DLR.

Finally, a conclusion to this work is given in Chapter 8. A summary of the key findings are presented, and some thoughts for further work arising from the research are also provided. A list of references follows, where relevant publications by the author are also detailed in the footnotes at the beginning of each chapter. A bibliography containing all references used in this thesis is also provided. A summary of all the numerical investigations used in support of the interlaminar damage propagation degradation model is then presented in Appendix A.

1.3 Outcomes

The major outcome of this research has been the development of a comprehensive, validated analysis methodology and accompanying software tool for the collapse analysis of composite postbuckling structures taking degradation into account. In support of this outcome, a number of significant achievements have been made.

A comprehensive literature review was produced covering the state of the art in postbuckling analysis and damage modelling of stiffened composite structures. In conjunction with this, a benchmarking exercise was conducted to assess the capabilities of current analysis software for intact and damaged postbuckling composite stiffened structures. The benchmarking exercise included comparisons across different modelling techniques and analysis codes, including between implicit and explicit analysis solvers. Both outcomes were used to act as a reference and to formulate the framework for the development work in this thesis.

A range of approaches were developed to represent the critical damage mechanisms for composite stiffened structures in compression. An approach was developed for predicting the initiation of interlaminar damage in cross-section models of skin-stiffener interfaces. A degradation model was developed for modelling the growth of interlaminar damage during finite element analysis that was based on an application of VCCT. Another degradation model was developed to capture the in-plane ply damage mechanisms such as matrix cracking and fibre failure. The implementation of all these approaches into the FE code Marc demonstrated that relatively simple models and current failure theories could be used to give accurate representations of damage, and results showed very good comparison with experimental data.

As part of the interlaminar damage degradation model, a significant amount of work was performed to investigate the relationship between the VCCT calculation and the method of propagating crack growth in the FE model. Though the VCCT approach has been in use for almost thirty years, the author believes that this is the first time that the adaptation of VCCT to crack propagation analysis has been studied to such an extent. In fact, it was repeatedly shown both numerically and in comparison with experiment that VCCT as commonly applied to propagation studies leads to overly conservative results. A novel approach was proposed that applied a modification to the strain energy release rates based on the local crack front, and this was shown to give more accurate and realistic results in comparison with experiment.

A methodology was developed for the analysis of composite stiffened structures in compression, which incorporated all the critical damage mechanisms leading to collapse. This included predicting the initiation of interlaminar damage, modelling the growth of an existing interlaminar damage area and capturing the ply-based degradation mechanisms. Various techniques were applied to make the methodology suitable for analysing large postbuckling composite structures, which included applying simple and practical theories that were efficiently implemented into FE analysis, using a coarse global model and a fine local model

in a two-step approach and modelling skin-stiffener debonding at only the skin-stiffener interface. Importantly, the incorporation of all the critical damage mechanisms meant that their combination and interaction within a structure could be studied. The developed methodology also represented a significant achievement in terms of the synthesis of nine separate Marc user subroutines running throughout the analysis and combining to represent and provide post-processing output for the various damage types.

All aspects of the analysis methodology were extensively validated using experimental results. This included: validation of the interlaminar damage prediction using T-section tests; validating the interlaminar damage growth modelling fracture mechanics tests for mode I, II and mixed mode I-II loading; and using both single-stiffener specimens and large multi-stiffener panels representative of composite fuselage designs to validate the use of the methodology for the design and analysis of intact and pre-damaged structures.

A user-friendly software tool was developed, which incorporated all aspects of the developed analysis methodology. The tool was implemented as a menu system in Patran, which was used to provide a range of functions including defining the damage regions and properties, running the analysis, and assisting in the post-processing of results. The tool was developed to be "industry-ready", or suitable for immediate application within current design practices for postbuckling composite structures including the critical damage mechanisms.

This thesis work has also produced significant outcomes as CRC-ACS contributions for the COCOMAT project. This included the literature review, benchmarking analysis, and analysis methodology development as described, which all represented the CRC-ACS contribution to key COCOMAT deliverables. In addition to this, there was considerable work produced for the design and analysis of postbuckling structures in support of the experimental test program, particularly in collaboration with DLR and Aernnova for the D1 and D2 designs.

It is believed that the work in this thesis has made significant contributions to the fields of structural analysis and damage modelling. Although the research was specifically focused on fuselage structures in compression, the analysis techniques and damage modelling approaches are easily transferable to other composite structures and loading types. This work has resulted in significant publication, which has included six international journal papers, nine international conference papers, six CRC-ACS internal technical memorandums and twelve COCOMAT internal technical reports.

List of Publications

Key to publication type:

{jr}	refereed journal	{cp}	refereed conference proceedings
{cr}	COCOMAT technical report	{tm}	CRC-ACS technical memorandum

1. {jr} Orifici, AC, Thomson, RS, Degenhardt, R, Bisagni, C & Bayandor, J 2007, 'Development of a finite element methodology for the propagation of delaminations in composite structures', *Mechanics of Composite Materials*, vol. 43, no. 1, pp. 9-28.
2. {jr} Orifici, AC, Thomson, R, Degenhardt, R, Kling, A, Rohwer, K & Bayandor, J 2008, 'Degradation investigation in a postbuckling composite stiffened panel', *Composite Structures*, vol. 82, no. 2, pp. 217-224.
3. {jr} Degenhardt, R, Kling, A, Rohwer, K, Orifici, AC & Thomson, RS 2008, 'Design and analysis of stiffened composite panels including post-buckling and collapse', *Computers and Structures*, vol. 86, pp. 919-929.
4. {jr} Orifici, AC, Thomson, RS, Herszberg, I, Weller, T, Degenhardt, R & Bayandor, J 2008, 'An analysis methodology for failure in postbuckling skin-stiffener interfaces', *Composite Structures*, doi:10.1016/j.compstruct.2008.03.023
5. {jr} Orifici, AC, Ortiz de Zarate Alberdi, I, Thomson, RS & Bayandor, J 2007, 'Damage growth and collapse analysis of composite blade-stiffened structures', (to appear in *Composites Science and Technology*).
6. {jr} Orifici, AC, Thomson, RS, Degenhardt, R, Bisagni, C & Bayandor, J, 'Development of a degradation model for the propagation of delaminations in composite structures', *Computers, Materials & Continua* (paper submitted).

7. {cp} Orifici, AC, Thomson, RS, Gunnion, AJ, Degenhardt, R, Abramovich, H & Bayandor, J 2005, 'Benchmark finite element simulations of postbuckling composite stiffened panels', in *Eleventh Australian International Aerospace Congress*, Melbourne, Australia, 13-17 March.
8. {cp} Orifici, AC, Thomson, RS, Degenhardt, R, Bisagni, C & Bayandor, J 2006, 'Development of a degradation model for the collapse analysis of composite aerospace structures', in *XIV International Conference on Mechanics of Composite Materials*, Riga, Latvia, May 29-June 2.

9. {cp} Orifici, AC, Thomson, RS, Degenhardt, R, Bisagni, C & Bayandor, J 2006, 'Development of a degradation model for the collapse analysis of composite aerospace structures', in *III European Conference on Computational Mechanics: Solids, Structures and Coupled Problems in Engineering*, Mota Soares, CA, et al. (eds), Lisbon, Portugal, 5-9 June.
10. {cp} Orifici, AC, Herszberg, I, Thomson, RS, Weller, T, Kotler, A & Bayandor, J 2007, 'Failure in stringer interfaces in postbuckled composite stiffened panels', in *12th Australian International Aerospace Congress*, Melbourne, Australia, 19-22 March.
11. {cp} Herszberg, I, Kotler, A, Orifici, AC, Abramovich, H & Weller, T 2007, 'Failure modes in loaded carbon/epoxy composite T-sections', in *12th Australian International Aerospace Congress*, Melbourne, Australia, 19-22 March.
12. {cp} Orifici, AC, Thomson, RS, Degenhardt, R, Büsing, S & Bayandor, J 2007, 'Development of a finite element methodology for modelling mixed-mode delamination growth in composite structures', in *12th Australian International Aerospace Congress*, Melbourne, Australia, 19-22 March.
13. {cp} Scott, ML, Thomson, RS, Gunnion, AJ & Orifici, AC 2007, 'Simulation of defects and damage: Towards a virtual testing laboratory for composite aerospace structures', *1st CFK Valley Stade Convention*, Stade, Germany 13-14 June.
14. {cp} Lee, M, Kelly, D, Orifici, AC & Thomson, RS 2007, 'Postbuckling mode shapes of composite stiffened fuselage panels incorporating stochastic variables', *1st CEAS European Air and Space Conference*, Berlin, Germany, 10-13 September.
15. {cp} Orifici, AC, Thomson, RS, Degenhardt, R & Bayandor, J 2007, 'Development of a finite element methodology for the collapse analysis of composite aerospace structures', *ECCOMAS Thematic Conference on Mechanical Response of Composites*, Porto, Portugal, 12-14 September.

16. {tm} Orifici, AC, Feih, S & Thomson, RS 2005, *Literature Review on Postbuckling and Damage Modelling*, CRC-ACS TM 05107.
17. {tm} Orifici, AC, Thomson, RS & Feih, S 2005, *Undamaged Test Panel Design for COCOMAT*, CRC-ACS TM 05108.
18. {tm} Orifici, AC, Thomson, RS & Gunnion, AJ 2005, *COCOMAT Benchmarking Study*, CRC-ACS TM 05109.
19. {tm} Orifici, AC & Thomson, RS 2007, *Degradation Model Development for Collapse Analysis of Composite Structures*, CRC-ACS TM 07010.

20. {tm} Orifici, AC & Thomson, RS 2007, *Damaged Test Panel Design for COCOMAT*, CRC-ACS TM 07073.
21. {tm} Orifici, AC & Thomson, RS 2007, *Analysis Tool Validation and Application for COCOMAT*, CRC-ACS TM 07074.

22. {cr} Thomson, RS & Orifici, AC 2005, *Design and Analysis of Undamaged Panels – DLR Designs*, COCOMAT Technical Report, Cooperative Research Centre for Advanced Composite Structures, Melbourne, Australia.
23. {cr} Orifici, AC & Thomson, RS 2005, *Design and Analysis of Undamaged Panels – Gamesa Designs*, COCOMAT Technical Report, Cooperative Research Centre for Advanced Composite Structures, Melbourne, Australia.
24. {cr} Orifici, AC & Thomson, RS 2005, *Design and Analysis of Undamaged Panels – Gamesa Designs: Additional Analyses*, COCOMAT Technical Report, Cooperative Research Centre for Advanced Composite Structures, Melbourne, Australia.
25. {cr} Orifici, AC & Thomson, RS 2005, *Design and Analysis of Undamaged Panels – Gamesa Designs: Additional Analyses II*, COCOMAT Technical Report, Cooperative Research Centre for Advanced Composite Structures, Melbourne, Australia.
26. {cr} Thomson, RS & Orifici, AC 2005, *Revised Design and Analysis of Undamaged Panels – DLR Designs*, COCOMAT Technical Report, Cooperative Research Centre for Advanced Composite Structures, Melbourne, Australia.
27. {cr} Orifici, AC, Feih, S & Thomson, RS 2005, *Postbuckling and Damage Modelling Methodology Development*, COCOMAT Technical Report, Cooperative Research Centre for Advanced Composite Structures, Melbourne, Australia,.
28. {cr} Orifici, AC, Thomson, RS & Feih, S 2005, *Undamaged Test Panel Design*, COCOMAT Technical Report, Cooperative Research Centre for Advanced Composite Structures, Melbourne, Australia.
29. {cr} Orifici, AC & Thomson, RS 2006, *Extension of Slow Computational Tools for Degradation (Interim)*, COCOMAT Technical Report, Cooperative Research Centre for Advanced Composite Structures, Melbourne, Australia.
30. {cr} Orifici, AC & Thomson, RS 2006, *Extension of Slow Computational Tools for Degradation (Final)*, COCOMAT Technical Report, Cooperative Research Centre for Advanced Composite Structures, Melbourne, Australia.

31. {cr} Orifici, AC & Thomson, RS 2007, *Extension of Slow Computational Tools for Degradation (Final, version 2)*, COCOMAT Technical Report, Cooperative Research Centre for Advanced Composite Structures, Melbourne, Australia.

32. {cr} Orifici, AC & Thomson, RS 2007, *Damaged Panel Analysis – D1 Design*, COCOMAT Technical Report, Cooperative Research Centre for Advanced Composite Structures, Melbourne, Australia.

33. {cr} Orifici, AC & Thomson, RS 2007, *Damaged Panel Analysis – D2 Design*, COCOMAT Technical Report, Cooperative Research Centre for Advanced Composite Structures, Melbourne, Australia.

CHAPTER 2

POSTBUCKLING AND DAMAGE MODELLING

2.1 Introduction

This section summarises the state of the art for composite stiffened structures in postbuckling and damage modelling up to final collapse. A comprehensive review of all relevant literature is given, and covers analysis of both structural response and composite damage mechanisms. As this research was centred on the development of an analysis tool, the scope of the literature review is focused on practicable, proven and adaptable theories. Following this, results are presented of an extensive benchmark study conducted to demonstrate the capabilities of current analysis tools and act as a reference point for this work. Finally, a discussion is given of the literature review and benchmark study in the context of the analysis methodology developed in this work. This includes a summary of the key decisions made to formulate the analysis methodology, and illustrates the way in which the literature review and benchmarking study were critical to the development process. Some aspects of the research work presented in this chapter have been published in a refereed journal[1].

2.2 Literature Review

2.2.1 Structural Analysis

The first aspect critical to capturing the postbuckling behaviour of composite stiffened panels is an accurate description of the structural behaviour. In this section, various aspects relevant to capturing the structural behaviour are summarised, which includes a description of the fundamental theory underlying the analysis, the choice between analytical or numerical solution methods and the difference between explicit and implicit numerical solvers. This is followed by a description of various structural issues that are particularly relevant to postbuckling stiffened structures, which include accurately capturing mode shape changes,

---

[1] Orifici, AC, Thomson, RS, Gunnion, AJ, Degenhardt, R, Abramovich, H & Bayandor, J 2005, 'Benchmark finite element simulations of postbuckling composite stiffened panels', in *Eleventh Australian International Aerospace Congress*, Melbourne, Australia, 13-17 March.

panel imperfections, contact between delaminated layers, the high degree of nonlinearity, and boundary conditions. Rather than a comprehensive description of all structural theories, the aim of this section is to provide a summary of a few of the structural issues most relevant to postbuckling composite stiffened structures.

2.2.1.1 Plate Theory

This section gives a brief overview of the plate theory most commonly used in composite postbuckling analysis, focusing on assumptions and constraints in application. The reader is referred to texts such as Barbero (1998) and Ochoa and Reddy (1992) for a more thorough description of the derivation and theoretical development.

Classical Laminated Plate Theory (CLPT) is the most widely used theory for laminated composites, and describes the assembly of a finite number of elastic orthotropic laminae, or layers, into a total laminate, or plate. The theory uses a homogenisation of each ply layer, so that the individual fibres and matrix are not separately modelled, but are accounted for by "smearing" their properties into an orthotropic lamina. This is done using a ply-level coordinate system, with 0° aligned with the local fibres, as shown in Figure 2.1. In the assembly of the laminate, the constitutive relation of each ply is transformed to the global laminate coordinate system, and assembled into a single stiffness matrix, so that the entire laminate is represented by a single constitutive relation. CLPT is based on the two-dimensional (2D) assumption that the plate is thin enough so that there is no strain in the thickness direction, which remains accurate as long as the thickness of the laminate is at least two orders of magnitude less than the in-plane dimensions (Ochoa & Reddy 1992).

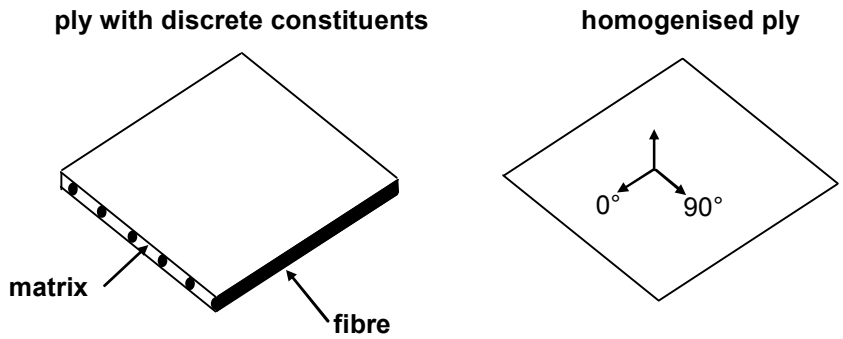

Figure 2.1: Homogenisation of ply properties in Classical Laminated Plate Theory

CLPT has been used extensively by researchers investigating all aspects of laminated composite behaviour, and forms the basis of most implementations of shell elements in

numerical analysis codes. In the World Wide Failure Exercise, a 10-year project aiming to compare and benchmark a wide range of current analysis approaches for composite failure, all 14 approaches presented used CLPT (Kaddour, Hinton & Soden 2004). There have also been numerous investigations into postbuckling stiffened composite structures that have successfully applied CLPT, including experiment and analysis at NASA (Hyer, Loup & Starnes 1990), in Europe (Caputo et al. 2002), and in Australia (Thomson & Scott 2000), amongst many others. Whilst some researchers argue for the use of higher-order plate theories utilising more complex descriptions of the through-thickness shear deformations (Reddy 1990), the advantages in accuracy are yet to overcome the disadvantages of increased complexity, and the use of these higher-order theories is not common.

2.2.1.2 Analytical Versus Numerical

The governing equations describing structural deformation are a set of partial differential equations, so a choice needs to be made regarding the method of solving these equations to obtain the necessary structural information. Though numerical methods, specifically the Finite Element method, are overwhelmingly the most powerful and effective solution methods, it is worthwhile to summarise the reasons for this, in order to understand the application of the solution process. Again, the intention is only to summarise the justification and limitations for applying the FE method to the solution of postbuckling composite structures, and the reader is referred to texts such as Matthews et al. (2000) and Ochoa and Reddy (1992) for a more complete description of the FE technique.

The FE method is the most powerful numerical technique for solving geometrically complicated structural problems (Ochoa & Reddy 1992), and as such is used in the analysis of postbuckling stiffened structures, almost without exception. Exact analytical solutions for the structural equations are available for only the most basic boundary and loading conditions, and likewise the application of analytical approximation techniques such as the Rayleigh-Ritz and Galerkin methods becomes prohibitively difficult for complicated geometries. In contrast, the discretisation applied in the FE method allows for complex, nonlinear and history-dependent definitions of all model parameters, including loads, boundary conditions, geometries, material properties, and structural interactions such as contact. These capabilities are especially necessary for postbuckling composite structures as they involve a high degree of nonlinearity across a number of structural parameters.

For example, both Arnold and Parekh (1987) and Sheinman and Frostig (1988) applied an analytical approach to analyse postbuckling stiffened panels, but in both cases the resulting expressions for structural parameters were complicated, lengthy, and ultimately not specific enough to achieve a high level of accuracy. Similarly, Kim (1997) and separately Ochoa and Reddy (1992) compared analytical with FE solutions for postbuckling composites, and concluded that only FE methods were able to model delaminations, which represent a three-dimensional (3D) nonlinear structural effect. So, the solution of the structural deformation equations in postbuckling composite structures, as with the majority of complex structural problems, is achieved almost exclusively using the FE method.

2.2.1.3 Explicit Versus Implicit

The equations of motion for any structure can be solved using either explicit or implicit numerical solution procedures, with the choice between the two largely problem-dependent. The explicit dynamic procedure uses an explicit central difference time integration rule to obtain displacements at a series of time increments (Crisfield 1991). Each time increment is relatively inexpensive as there is no need to solve a set of simultaneous equations, however, the solution time is dictated by limits to the time increment, so that for some structures necessarily small time increments can negate any computational benefits. In contrast, the implicit solution procedure (Newton's method) requires the solution of a banded set of simultaneous equations at a series of load increments, and needs constant updating of the global stiffness matrix and a series of iterations in order to achieve convergence. In spite of this, for problems involving a smooth nonlinear response, Newton's method has a quadratic rate of convergence response, and in general, implicit solution procedures are more computationally efficient. However, discontinuous processes such as frictional sliding or impact disrupt the implicit solution convergence, and can require a large number of iterations, large cutbacks in increment size, or at worst convergence may not be possible. Furthermore, the implicit run time is proportional to the solution of simultaneous equations, so for problems involving large model sizes the explicit procedure may be more economical (Crisfield 1991). Accordingly, the choice between implicit or explicit solution procedures is problem-dependent, with the deciding factor usually being the amount of smoothness in the solution.

Researchers in postbuckling analysis have used both implicit and explicit procedures, with implicit procedures applied in the majority of cases for postbuckling stiffened composite panels. In most instances, the structural behaviour under static load conditions is of interest, and FE modelling techniques are used to simulate experiments involving an incrementally applied compression load or displacement, as in: Frostig et al. (1991) investigating postbuckling stiffened panels; Whitcomb (1992) analysing postbuckling delamination with contact; Mi et al. (1998) in the development of an interface model for composite degradation; and many others. In these types of cases, explicit procedures would be largely inefficient, with small increments over an extended quasi-static loading period. However, a number of researchers have found the explicit procedure to be more efficient for their analysis, including Bisagni (2000) investigating postbuckling cylinders, Caputo et al. (2002) and separately Falzon and Hitchings (2003) concentrating on the mode-switching of postbuckling stiffened panels, and Borg, Nilsson and Simonsson (2002) investigating impact with a cohesive zone model. So, analysis by previous researchers into postbuckling structures have for the most part used implicit methods, with the use of explicit methods dependent on the degree to which dynamic effects or discontinuities are considered critical and at times the experience and preference of the analyst.

2.2.1.4 Postbuckling Analysis

In this section, a number of issues particularly relevant to postbuckling structures are presented. These include accurately capturing mode shape changes, panel imperfections, contact between delaminated layers, the high degree of nonlinearity, and boundary conditions. The focus here is on assessing both the degree to which each issue is critical, and the ability to handle each issue practically, with reference given to previous work by other researchers in testing and analysis of postbuckling structures.

2.2.1.4.1 Mode Shape Changes

The development of buckling mode shapes is a fundamental feature of compression-loaded structures, and accurate mode shape capturing is critical to successfully representing all aspects of structural deformation. Structures under compression loading adopt specific shapes, or modes, that represent minimum energy states, and these are dependent not only on the structure, but also on the loading. Stiffened structures in compression generally have at least two mode shape regions: a local buckling, or pre-buckling region, where buckles develop in the skin between the stiffeners, with the width of buckling waves of the order of the stiffener

pitch; and, a global buckling, or postbuckling region, where the entire structure buckles, with the width of buckling waves of the order of the panel length or width. Depending on the structure, additional buckling mode shapes may develop, and the tendency for these types of structures to switch, or "snap", to higher-order buckling shapes is common, especially in the deep postbuckling region. This type of behaviour has been found by numerous researchers investigating various compression loaded structures, including: Knight and Starnes (1988), who found that panel curvature affected the postbuckling mode shape changes of curved stiffened panels; Meyer-Piening and Anderegg (1995), who observed a secondary postbuckling mode shape change in a stiffened box structure; and, Bisagni and Cordisco (2003), who investigated the differences in mode shape development of complete cylinders under compression and torsion loadings.

Accurate capturing of the mode shape changes is a challenging mathematical exercise complicated by the multiplicity of equilibrium states at buckling and the nonlinear and dynamic nature of mode shape changes. In FE solution processes, structures are loaded incrementally with either forces or enforced displacements, and this causes difficulties in achieving solutions past buckling points, as mode shape changes require reductions in forces and/or displacements. Additionally, buckling points represent switches between solution paths or "branches", and whilst this switching is based on minimum potential energy, the ability of a solution algorithm to pinpoint these branch-switch points is mathematically sensitive. Most current FE programs have a selection of solution algorithms that employ a range of techniques to mitigate problems in mode switching, which include modulating the loading parameter, "searching" the solution path for the location of a local minimum, and a variety of "predictor-corrector" formulae for estimating and iteratively adjusting solutions, amongst many others (Crisfield 1991).

Numerous researchers have recorded various degrees of success in capturing mode shape changes for postbuckling structures, including: Meyer-Piening and Anderegg (1995) and separately Thomson and Scott (2000), whose analyses predicted global buckling well though both analyses were unable to capture the secondary mode shape changes of the respective structures; Caputo et al. (2002) analysing stiffened plates, who observed differences in mode tracking not only between implicit and explicit codes, but between dynamic and transient solution processes, and also between commercial FE codes; and, Falzon and Hitchings (2003) who employed a modified explicit solution to successfully track two mode snaps for a blade-stiffened composite panel in compression.

2.2.1.4.2 Imperfections

Imperfections are present in all structures to some degree, and whilst in most cases can be ignored, for postbuckling analysis of thin-walled composite structures correct description is often crucial to achieving accurate and meaningful results. Imperfections are geometrical deviations from the intended structural shape, which occur randomly and unavoidably during manufacture, and the effect of these imperfections for postbuckling structures ranges from a slight altering of the deformation pattern, to variations in the progression of mode shape, to the development of entirely different mode shapes.

Researchers have applied a variety of methods to handle the description of imperfections in their models, though all usually involve the basic elements of measuring the imperfections on an actual or representative manufactured panel, and applying this to the "perfect" model, which itself usually requires some means of approximating the imperfection data into a useable form. Examples of this include: Bisagni (2000), who investigated the use of a sinusoidal function to model an axisymmetric deviation pattern for complete cylinders; Spagnoli, Elghazouli and Chryssanthopolous (2001), who measured points on the surface of real panels using a laser scanning system, then used a 2D Fourier analysis to create a mathematical model for the real, imperfect surface, which was applied to their model at the nodal points; and, Tsouvalis et al. (2001), who imported data from LVDT scans of imperfect panels into CAD programs, and applied a bicubic spline fitting technique to generate imperfect model surfaces.

In the absence of real imperfection data, a number of researchers such as Engelstaad, Reddy and Knight (1992), Goldmanis and Riekstinsh (1994), Baranski and Biggers (1999), Yap et al. (2002), and others, used some combination of the lowest eigenvalues of the structure added to the nominal structure to approximate a deviation pattern. Whilst this approach can be necessary for structures such as simple flat plates in which a global buckling solution may be difficult to achieve numerically, the effect for more complex structures is usually not so beneficial, ranging from having no influence or merely causing global buckling to occur slightly earlier, to the development of different or incorrect buckling mode shapes.

2.2.1.4.3 Contact

The inclusion of a contact region, or a defined structural gap, is necessary in the analysis of compression-loaded structures including the effect of delamination and skin-stiffener separations. Delamination, as explained in greater detail in Section 2.2.2.3, is an internal separation between plies, and is typically a critical damage type in compression-loaded structures. Skin-stiffener separation is a similar failure mechanism, and occurs as a result of detachment of the skin and stiffener. To represent these damage types accurately, a contact region is required between the two separating layers to prevent physically impossible penetration of one layer into the other, particularly during buckling.

Numerous researchers have identified the critical nature of incorporating a gap-like description for delamination, most notable of which is Whitcomb (1989), who analysed a postbuckling delamination without a contact description, identified the inaccuracy and physical infeasibility of such a description, and subsequently published an analysis of the same structure using a contact description, which showed an increase in accuracy and feasibility (Whitcomb 1992). All researchers that have implemented a contact zone have used a simple, frictionless definition of contact, as a means of preventing penetration without creating additional friction forces. The inclusion of frictionless contact into an FE model is neither difficult nor computationally expensive, so that a gap or contact region has become almost mandatory for all investigations into buckling failure.

2.2.1.4.4 Nonlinearity

The analysis of postbuckling composite stiffened panels is complicated by the presence of a high degree of nonlinearity, with a combination of interacting nonlinear effects. Primarily, the analysis of postbuckling structures involves large deformations, typically out of the loading plane, so that the common structural analysis assumption of small displacements and strains becomes invalid. Composite properties are non-isotropic, and nonlinear formulations are required to rotate material properties according to the material deformation with the local coordinate system. Mode shape changes are highly nonlinear structural events, and involve large discontinuities in deformation growth that are almost independent of the deformation history. In addition to this, the compression of composite structures results in various damage mechanisms that represent nonlinearities, such as the contact and buckling behaviour of delamination failure, or the reduction in material properties resulting from non-catastrophic degradation. So, whilst nonlinear theories capable of handling these effects are well

developed, almost all researchers to date have clearly recognised the necessity of such descriptions, and the inaccuracies of analyses based on linearising approximations.

2.2.1.4.5 Boundary Conditions

An accurate and representative description of structural boundary conditions is necessary for any type of analysis, though becomes especially important for postbuckling stiffened structures as these can be highly sensitive to boundary condition changes. For buckling structures, the definition of boundary conditions fundamentally defines the structural response, with the degree of restraint imposed on the panel determining the mode shapes and buckling loads.

Numerous researchers have encountered a variety of problems and applied a range of techniques in defining boundary conditions, including: Hyer, Loup and Starnes (1990), who conclude that their correlation with experimental results would be improved by taking the boundary flexibility of their stiffened panels into account; Short, Guild and Pavier (2002), who attempted to approximate an anti-buckling guide for unstiffened panels using edge boundary conditions, and resolved that as the plates were sensitive to boundary conditions a full description of the buckling guide was required; Hilburger and Starnes (2004), who used a separate 2D investigation to study the stiffness properties of a resin encasement "potting" for compression-loaded cylinders; and, Zimmermann, Klein and Kling (2006), who noted that simple boundary conditions overestimated the degree of restraint applied by clamps on the side edges of curved stiffened panels, and investigated the use of springs to match the experimental behaviour. A number of researchers have applied symmetry boundary conditions to reduce model size, such as Skrna-Jakl and Rammerstorfer (1993) and separately Krueger et al. (2002), both analysing stiffened panels, though this approach is generally not applicable, due to the possibility of eliminating global buckling modes (Whitcomb 1989), or asymmetrical buckling modes due to material asymmetry (Stiftinger, Skrna-Jakl & Rammerstorfer 1995).

2.2.2 Failure Mechanisms

In addition to a sufficiently sophisticated structural analysis, capturing the postbuckling behaviour of composite stiffened panels also requires accurate modelling of the various composite failure mechanisms. In this section, the composite failure mechanisms relevant to

postbuckling stiffened structures will be described, with a focus on summarising previous researchers' experimental investigations into fuselage-relevant structures. This will include descriptions of fibre failure, buckling failure, delamination, stiffener debonding and matrix cracking, as evidenced by previous researchers' experimental investigations. The emphasis here is on isolating and distinguishing between the various damage and failure mechanisms, and the way in which they interact to contribute to the degradation and eventual collapse of composite stiffened structures in compression.

2.2.2.1 Fibre Failure

Fibre failure is one of the simplest failure mechanisms to identify and quantify, and occurs when the loads applied to a composite structure cause fracture in the fibres. In fibre-reinforced composites the fibres act as the principal load-bearing constituents, and resist the majority of the applied loads. The failure of any fibres causes a redistribution of loads to the surrounding region that generally promotes further failure, so that the onset of fibre failure typically leads to almost instantaneous structural collapse in the absence of alternative load paths. While some researchers such as Lanzi and Giavotto (2006) have characterised collapse as the onset of ply damage or buckling, the significant loss of load-carrying capacity associated with fibre failure is most commonly taken as the point of final collapse. Numerous investigations into the ultimate strength of postbuckling composite stiffened structures have recorded collapse of the structure due to extensive fibre failure, usually accompanied by a considerable cracking sound, as seen in Frostig et al. (1991), Caputo et al. (2002) and Orifici et al. (2007).

2.2.2.2 Buckling

Buckling, as previously described, involves the structure deforming into a minimum potential energy deformation configuration, which can result in material failure. Buckling itself is a structural deformation and does not necessarily result in failure, as this depends on the buckling deformations inducing stresses, principally bending, that cannot be supported by the material. Failure in buckling typically occurs at locations of maximum bending, with panel mid-span failure most common. Numerous researchers investigating postbuckling stiffened panels have recorded panel failures due to buckling, including: Frostig et al. (1991), where both I- and J-stiffened panels, despite different mode shapes, gave mid-span panel fracture under buckling deformations; Falzon, Stevens and Davies (2000), investigating a range of stiffener cross sections, where only blade-stiffened panels gave failure due to buckling alone; Thomson and Scott (2000), where blade-stiffened panels loaded in shear gave diagonal

buckling waves that led to failure; and, Caputo et al. (2002), where long panels with only two I-stiffeners also displayed mid-span buckling fracture. A number of researchers investigating postbuckling of unstiffened complete cylinders as a fuselage-representative structure have also recorded failure as the structure adopted a postbuckling deformation shape, including Bisagni (2000), Spagnoli, Elghazouli and Chryssanthopoulos (2001) and Bisagni and Cordisco (2003).

2.2.2.3 Delamination

A separation between internal layers of a composite laminate is termed delamination, and this failure mechanism is crucial to the study of postbuckling structures as delamination presence can result in significant structural modification and degradation. Delamination occurs due to high through-thickness stresses overcoming the interlaminar bond strength between plies. This is influenced by residual thermal stresses in the laminate and the presence of any manufacturing defects, and is commonly encountered as a result of impact loading. Whilst delamination occurs during general loading, it is especially critical for compression-loaded structures, as the onset of delamination creates two thin substructures that are more likely to buckle at a lower load than the intact structure.

A large number of researchers experimentally investigating the buckling behaviour of stiffened delaminated structures in compression have found failure due to substructure buckling, including Chang and Kutlu (1990), Wiggenraad et al. (1996), Nilsson et al. (2001) and Greenhalgh et al. (2003). Additionally, a number of researchers have experimentally identified and investigated the phenomenon of substructure buckling inducing further delamination growth, including Gu and Chattopadhyay (1999), Gaudenzi, Perugini and Riccio (2001), Tafreshi (2004) and Wang and Qiao (2004), amongst others. It is important to recognise the separate damage mechanisms occurring in these cases, where delamination is initiated due to interlaminar strength properties, buckles due to structural instability, and can grow in area due to the conditions at the delamination front.

2.2.2.4 Skin-Stiffener Debonding

Skin-stiffener debonds involve detachment of the stiffener from the skin in stiffened panels, which significantly reduces the structural support for both skin and stiffener, and can result in the buckling and failure of both structural elements at lower loads than for an intact structure. Skin-stiffener debonds can occur between the skin and stiffener in co-cured or secondary

bonded structures, either through the initiation and growth of delaminations, or failure in the secondary bonding. Skin-stiffener debonding is a common, and often explosive, form of failure, which has occurred in a large number of experimental investigations into postbuckling stiffened structures.

Examples of the occurrence of skin-stiffener debonding in literature include: Starnes, Knight and Rouse (1985) and Knight and Starnes (1988), where all configurations of flat and curved stiffened panels gave debonding failure; Hachenberg and Kossira (1993) and separately Stevens, Ricci and Davies (1995), who both recorded explosive debond mechanisms causing almost immediate total panel failure; and, Wiggenraad et al. (1996), where compression of stiffened panels caused a delamination in the panel mid-span, which grew under continued loading to the stiffeners causing debonding panel failure; amongst many others. Again, it is important to distinguish between the various mechanisms at work, where delaminations and detachments initiate, grow between the skin and stiffener under continued loading, cause a rapid skin-stiffener debonding action over a significant portion of the panel length, and lead to separate buckling and failure of the skin and stiffener.

2.2.2.5 Matrix Cracking

Matrix cracks are an intralaminar form of damage, and involve cracks or voids between fibres within a single composite layer, or lamina. The initiation and growth of matrix cracks is dependent on the loading, structure and composite lay-up involved, and involves a single matrix crack developing into a series of cracks within a lamina at a characteristic spacing (Masters & Reifsnider 1982). Additionally, buckling sets up significant local tensile strains throughout a structure, which can initiate further matrix cracking. Though the development of matrix cracks is crucial to the damage progression of general composite structures and loading, for compression-loaded structures matrix cracking is rarely critical, and is often undetected or unmonitored. However, the development, and in particular the coalescence, of matrix cracks can lead to delamination in a composite structure. This type of behaviour, where the intralaminar matrix cracks initiate interlaminar delamination, has been identified by a number of researchers, including O'Brien (1985), Ochoa and Reddy (1992) and Yang and Boehler (1992), among others, though is rarely recognised as relevant to the experimental analysis of postbuckling stiffened structures. Additionally, matrix cracking associated with buckling can lead to a reduction in buckling load, which has been observed in cyclic loading

experiments such as those conducted by Thomson (2001), where 3 million fatigue loading cycles caused a reduction of 23% in the buckling load of stiffened composite panels in shear.

2.2.2.6 Conclusion

From a study of past researchers' experimental investigations, it is clear that only a few of the various composite damage and failure mechanisms are relevant for postbuckling stiffened structures. As with all structures failure due to buckling is critical, as compression loading causes buckling shapes and deformations beyond the strength limits of a material. However, composite stiffened structures are particularly sensitive to buckling failure due to the interaction with damage mechanisms that create internal separation, such as delamination and skin-stiffener debonding, which can be related. Additionally, the accumulation of matrix cracks can lead to the initiation of delamination, which would likewise result in buckling failure at lower loads than an undamaged structure. With all experimental analyses, it is crucial to be able to identify the separate damage types interacting, and the actual mechanisms of development and failure for each damage type.

2.2.3 Damage Characterisation

In this section, the various approaches used to characterise the onset and progression of damage in composite structures are summarised. This includes the use of a strength-based approach or applying fracture mechanics theories in order to define parameters that are used to predict and monitor damage development and growth. Following this, a list of several failure criteria are summarised, as a means of demonstrating the way in which previous researchers have applied and combined the two approaches to describe the initiation and accumulation of damage. The intention in this section is to summarise the approaches applied by researchers to characterise damage, as separate from the methods used to include the effects of damage in a numerical model, which are detailed in a later section.

2.2.3.1 Strength

The strength, as defined by the allowable stresses for a material, can be used to characterise the initiation and growth of all types of damage. The application of the strength approach is usually fairly simple, with one or more strength criteria defined, and the material deemed to have been irreversibly damaged once these criteria are satisfied. The criteria themselves can range from single stress parameter limits, combinations of various stress terms, or normalisation of stress terms using structural or material values. Strength criteria can be

applied so that each damage mechanism has a distinct criterion, or a more general damage criterion can be applied. Of these, maximum stress criteria, with strength values taken from experimental tests, are common, as is the quadratic interactive criterion of Tsai, which is most commonly implemented in the Tsai-Wu (1971) variation, and the Hashin (1980) criteria, which have been increasingly used to characterise separate damage types.

Most analyses of postbuckling stiffened structures, and composite structures in general, apply some form of strength-based damage characterisation, including: Engelstaad, Reddy and Knight (1992), who compared maximum stress criteria to the Tsai-Wu criterion in the analysis of damage in postbuckling stiffened structures; Cuntze and Freund (2004), who developed a set of coordinate system-invariant criteria for each damage mechanism based on stress, and applied this to composite pipes under bi-axial loadings; and, Feih and Shercliff (2005) analysing composite T-joints, who used separate criteria to predict matrix cracking and delamination, and applied an area-based maximum stress criteria to predict failure.

Furthermore, numerous researchers have applied criteria using similar parameters to stress, including; Borg, Nilsson and Simonsson (2001), who used the force between two tied nodes to characterise the existence of delaminations; Gosse and Christensen (2001), who developed failure criteria using coordinate system-invariant strain parameters; and, Camanho and Dávila (2002), who developed an element to model delamination that uses the relative displacement between its edge nodes to control damage. It is important to note that strength-based characterisation of damage is most commonly applied to define the damage initiation, and not the progression of an existing damage region, and this is especially relevant for delaminations.

As previously mentioned, numerous researchers have derived a large number of formulae to characterise the initiation of the various composite failure modes using strength criteria. A list of strength-based failure criteria applied in various investigations is given in Table 2.1, where an attempt has been made to reduce instances of similar failure approaches.

2.2.3.2 Fracture Mechanics

Classical fracture mechanics is a theory that studies the growth of existing defects, and whilst not often used for most forms of composite damage, has been successfully applied to the study of delamination and debonding. Classical fracture mechanics were developed and applied for damage analysis of metals, in which a single crack propagates at a mostly uniform rate through the material. In fracture mechanics theory, the growth of a macroscopic defect is

controlled by the rate of strain energy released in propagation, as compared to a threshold maximum strain energy release rate for that material, which as such is a measure of material toughness. The strain energy released in crack propagation is typically split into the separate mechanisms of crack growth: peeling, shearing and tearing, as seen in Figure 2.2.

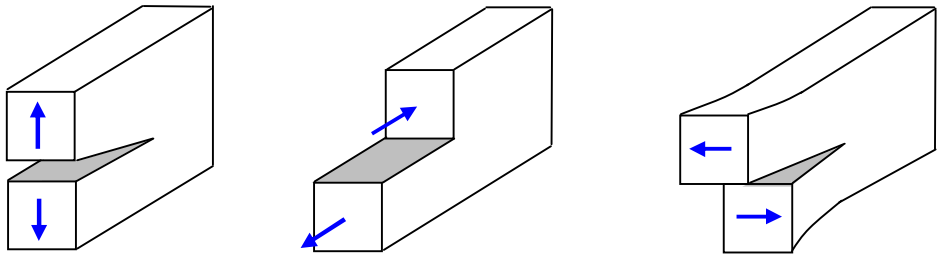

(a) *(b)* *(c)*

Figure 2.2: Crack growth modes: a) I. Peeling b) II. Shearing c) III. Tearing

The study of a single macroscopic crack in metals is analogous to the propagation of delamination, so that composite researchers almost without exception have applied classical fracture mechanics principles in order to study the growth of a pre-existing delamination. Examples of this include: Williams (1988) and separately Davidson (1998) who proposed alternative approaches for decomposing the total strain energy release rate of a delaminated composite into mode I, II and III components; Allix and Ladevèze (1992), who developed a theory for delamination propagation that monitors the dissipative force associated with an introduced damage parameter, as an analogy to strain energy release rate; Yap et al. (2002), who used an adapted form of Williams' criteria in the FE analysis of delamination failure in postbuckling stiffened panels; and, Borg, Nilsson and Simonsson (2002), who modelled delamination by tying nodes together, and used the energy dissipated at each node to define the reduction of the limit force in each node tie; among others. Again, it is important to note that the classical fracture mechanics approach assumes a pre-existing crack, and generally does not characterise the initiation of damage.

The strain energy release rate (SERR) is most commonly used to determine crack growth. Numerous researchers investigating the behaviour of delamination failure have found that the SERR is affected by a wide range of factors, not all of which can be accounted for by the various numerical analysis methods. Obviously, the SERR is dependent on the load, and in particular the degree of crack opening in each mode that the loading performs, as well as the specimen thickness and width (O'Brien 1985). Importantly, the resistance of a material to delamination growth is related to the lay-up direction of the "bounding" plies on either side of

the delamination, with angle changes between plies having less resistance to delamination growth (Davidson, Hu & Hongwei 1996).

Table 2.1: Strength criteria for failure initiation

Reference or Criteria name		Damage type	Description
–	Max Stress (or max strain)	Ply / Material failure	Simple limits for stress (or strain) in the fibre, transverse and interlaminar directions.
Summarised and referenced in Ochoa and Reddy (1992)	Tsai	Ply failure	Interactive criterion, addition of quadratic terms from stress in orthogonal directions with interactive terms.
	Tsai-Wu	Ply failure	Tsai equations, some interaction coefficients modified
	Tsai-Hill	Ply failure	Tsai equation, with different coefficients
	Hoffman	Ply failure	Interactive criterion, addition of terms, though more interaction terms than Tsai.
	Hashin	Fibre failure	2 terms, one purely fibre strength, with tensile and compression separate
		Matrix failure	2 terms, one purely intralaminar strength, tension and compression separate
		Delamination	Similar to fibre failure, with one term for purely interlaminar strength
Summarised and referenced in Ochoa and Reddy (1992)	Tsai	Delamination	3 term quadratic interaction criterion
	Tong-Tsai	Delamination	Tsai criterion, interlaminar term from quadratic to linear
	Degen. Tsai	Delamination	Simplified Tsai criterion, each term dependent on one stress value and strength
	Degen. Tong-Tsai	Delamination	Simplified Tong-Tsai criterion, each term uses one stress value and strength
	Norris	Delamination	Tsai criterion, tensile and compressive strengths used
	Tong-Norris	Delamination	Norris criterion, with interlaminar term changed from quadratic to linear
Summarised and referenced in Eason and Ochoa (1996)	Grezczuk	Fibre failure	Simple, max strength based equation
	Lee	Fibre failure, matrix failure, delamination	Simple equations, separately compare combination of transverse stresses to strengths for fibre failure, matrix tensile and compressive failure and delamination
	Ochoa	Delamination	Quadratic addition of simple terms, interlaminar and intralaminar separate
Chang and Chang (1987)		Fibre failure, matrix failure	Strength based addition of terms, with weighted quadratic stress parameters, tensile and compressive matrix failure
Yang and Boehler (1992)		Delamination	Delamination criterion from micromechanics approach for cross-ply laminates
Skrna-Jakl and Rammerstorfer (1993)		Delamination	Quadratic function, similar to Tsai delamination, uses experimental strengths
		Ply failure	Tsai-Wu, rearranged as damage parameter λ
Puck and Schürmann (1998)		Fibre failure (FF), Inter fibre fracture (IFF)	FF is max stress with stress magnification factor IFF is a fracture plane analysis, based on Mohr
Rotem (1998)		Fibre and matrix failure	Fibre failure is max stress Matrix failure is a quadratic stress criterion
Luciano and Zinno (2000)		Ply failure	Micromechanics basis, introduce 3 damage parameters, use Tsai-Wu, max stress, Hill or Hoffman equations
Gosse and Christensen (2001)		Ply failure	Failure criteria using strain, coordinate system invariant
Cuntze and Freund (2004)		FF and IFF based on Puck	Develop criteria from Puck and Hashin criteria, for coordinate system invariant stress terms. 5 equations given, for 2 FF (tension and compression) and 3 IFF (opening, shear, wedge) damage types

Researchers analysing a pristine structure recommend determining the most likely delamination site by calculating the SERR components at every ply interface to find the set of plies giving the SERR closest to the toughness value in each mode, as in Wang (1984), Sheinman, Kardomateas and Pelegri (1998) and Borg, Nilsson and Simonsson (2004). Additionally, Wang (1984) determined that the resistance to delamination growth depends on the direction of propagation through the interface, which not only affects the maximum strain energy release rate allowable, but the appearance of the delamination fracture surface. A number of researchers have experimentally observed delamination cracks changing ply interfaces, and this is due to another ply interface becoming more energetically favourable, as found by Ochoa and Reddy (1992), and may be influenced the interaction of the delamination with matrix cracks, as observed by Ireman et al. (1996).

One of the key aspects of a fracture mechanics analysis is the determination of the "mode mix", or ratio of mode I, II and III components that exist at the delamination front, where the two most common approaches are the Williams (1988) and Davidson (1998) methods, as alternatives to the classical fracture mechanics approach. The classical approach is inaccurate and inappropriate for a number of reasons: being developed for metals, it can not represent the large damage zone in the vicinity of a delamination for many practical composites; mode mix analysis is computationally expensive, requiring many detailed 2D or 3D analyses; and, mode mix analysis of a delamination between dissimilar materials, occurring frequently in composites where delamination occurs between plies of dissimilar orientations, predicts a numerically oscillatory stress singularity at the delamination front (Davidson 1998). The Williams and Davidson methods both use a non-classical, non-singular decomposition of the total strain energy release rate, which circumvents the problems of the classical approach. Of the two methods, the Williams approach is more computationally efficient, requiring only a single FE analysis, whilst the Davidson approach, which requires the separate analysis of a crack tip element as representative of the delamination front, has been shown to give slightly more accurate results, over a wider range of composite materials (Davidson 1998).

Table 2.2 summarises the fracture mechanics approaches found in the literature to determine either the initiation of delamination from an intact structure, or growth of an existing delamination.

Table 2.2: Summary of delamination fracture mechanics approaches

Reference or Criteria name	Criteria type	Description
O'Brien (1982)	Initiation	Empirical formula for critical strain, using critical strain energy release rate, thickness and stiffness before and after delamination
Wang (1984)	Growth	Classical fracture mechanics approach, delamination onset at critical strain energy release rate, formula given for far field strain at onset
Whitcomb (1989)	Growth	Virtual Crack Closure Technique (VCCT) used to determine SERR in each mode, compared to experimental toughness
Pavier and Clarke (1996)	Growth	Total SERR from a composite plate element developed in the paper, to estimate failure.
Jensen and Sheinman (2002)	Growth	Apply fracture mechanics to derive equations for buckling-driven delamination initiation and steady state growth
Park and Sanker (2002)	Growth	Develop Crack Tip Force Method to determine SERR at crack tip, relative to fracture toughness for delamination, compare to VCCT
Lonetti and Zinno (2003)	Growth	Based on fracture mechanics and empirical results, criteria for growth of double delaminated buckling plate developed
Andersons and König (2004)	Growth	Various empirical based equations given for adjusting fracture toughness values based on ply interface and directional dependence

The use of fracture mechanics in the characterisation of postbuckling composite damage mechanism is, however, mostly limited to the analysis of delaminations. The use of fracture mechanics to analyse ply damage mechanisms such as matrix cracking requires the definition of a pre-existing crack. This is not possible in CLPT as the individual plies are considered "smeared" together (see Section 2.2.1.1). As almost all investigations into postbuckling structures have applied a lamination theory like CLPT, ply damage mechanisms have been characterised using a strength-based approach. Many researchers have however applied fracture mechanics theories to ply damage mechanisms at a micro scale and developed failure criteria for CLPT analysis that have a fracture mechanics basis (see, for example Dávila & Camanho 2003). In recent years there has been considerable development in so-called multi-scale analysis, in which the properties and material definition at different length scales are combined (see, for example Car et al. 2002). However, to date, multi-scale analysis is not implemented in any commercially available FE code, and ply damage models based on micromechanics are difficult to experimentally validate, which limits the application of these techniques for analysing postbuckling composite structures.

2.2.3.3 Experimental Identification

Failure prediction requires accurate determination of material properties from experimental testing, so the various tests for determining the strength and fracture mechanics properties are important to mention, though the reader is referred to texts such as Pendleton and Tuttle (1989) and Vautrin and Sol (1991) for a more complete description. There are a number of

standards organisations, for example the American Society for Testing and Materials (ASTM), or European standards such as the German DIN norms, specifying testing procedures for a large range of material properties. Strength and other mechanical properties are determined with simple, well-established test procedures, such as compression, tensile, shear and three-point bend tests. Fracture mechanics tests are classified according to the mode, or combination of modes, of the loading applied to the specimen, which determines the properties able to be identified. Common fracture mechanics tests (seen in Figure 2.3) include: the Double Cantilever Beam (DCB) test, used for mode I; the End Notched Flexure (ENF) or End Loaded Split (ELS) test, used for mode II; and, Mixed-Mode Bending (MMB) test, developed to determine properties in combined mode I and II loading. These tests however can be relatively problematic for a number of reasons, including: a difficulty in generating pure mode conditions at the crack front; the large amount of scatter in experimental results, especially for mode II tests; and, no reliable or universally accepted tests yet existing to determine the mode III critical strain energy release rate. So, material strength properties are readily available for application to damage characterisations, whilst the range and applicability of fracture mechanics properties are still being established and are limited.

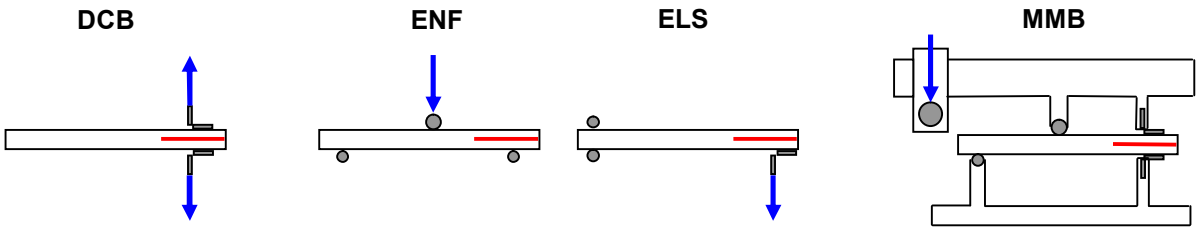

Figure 2.3: Fracture mechanics characterisation tests: a) Mode I b) Mode II c) Mixed-Mode I-II

2.2.4 Damage Modelling

In this section summaries are given on methods for representing composite damage mechanisms in a numerical model that have been applied to both postbuckling stiffened panels and composite structures in general. This involves a description of damage mechanics, where damage parameters are introduced into the material definition, and fracture mechanics for delamination or debond analysis, where a pre-defined crack is incorporated into the FE model and the onset and progression of crack growth can be investigated.

2.2.4.1 Damage Mechanics

Damage mechanics is an approach for modelling material response that attempts to quantify the physical events contributing to the evolving damage state. Though the term has been applied in different ways, the main approach involves reducing the material stiffness to implement the loss in load-carrying capacity due to damage. This is achieved by introducing damage variables into the material constitutive law, and including equations to control the behaviour of these variables, which can include laws for damage initiation and progression. A wide range of damage mechanics theories have been proposed, from a single scalar damage variable (Kachanov 1958) to a fourth-order damage tensor (Cauvin & Testa 1999). However, only a few are summarised here, on the basis of their effectiveness and application to the analysis of postbuckling composite structures. These include: a progressive failure methodology for ply damage where selected structural properties are knocked down according to failure criteria; interface elements, where damage mechanics are applied to a separate layer of elements that is used to model a connection between two substructures; and, cohesive elements, which combine damage mechanics in interface elements with fracture mechanics.

2.2.4.2 Progressive Damage

A progressive damage methodology attempts to represent the accumulation of damage in a composite laminate by reducing selected material properties at the ply level. Typically, the structure is loaded until a failure criterion is satisfied, at which point a corresponding material property or property set is reduced, and the analysis is continued. The degraded material property, most commonly stiffness, is selected so as to simulate the loss of load-carrying capacity in a particular direction, and final failure is assumed when a separate condition is satisfied, typically fibre fracture or delamination. In this application of damage mechanics, the damage variables are usually a single scalar variable for each damage mechanism investigated, which each have a value of either 0 for intact or 1 for damage onset. Though this approach is simple, the trigger-like knockdown of properties is particularly suited to the quasi-brittle nature of fibre-reinforced composites, and numerous researchers have recorded significant success in applying this approach to represent ply damage mechanisms (Kaddour, Hinton & Soden 2004). Almost all researchers applying a progressive damage methodology have applied a unique combination of failure criteria, degrading action – both property selection and knockdown factor − and final failure condition. A number of progressive failure approaches are summarised in Table 2.3, where FPF and FF refer to the criteria used for First Ply Failure and Final Failure respectively, and nomenclature is taken from the references.

Table 2.3: Progressive damage summary

Reference	Damage	Failure criteria	Property selection	Factor	Final Failure
Chang and Chang (1987)	Fibre Matrix Shear	Chang Chang Chang	E_1, E_2, G_{12}, ν_1, ν_2 E_2, G_{12}, ν_1, ν_2 ν_1, ν_2	0	Qualitative, point at which the plates cannot sustain any added load
Hwang and Sun (1989)	Fibre Matrix Delam	Hashin Hashin Lee	Stiffness matrix terms, D_{11}, D_{12}, D_{13}, D_{55}, D_{66} D_{12}, D_{22}, D_{23}, D_{44}, D_{66} Model re-meshed	0 0 –	Qualitative, laminate "experiences gross failure"
Engelstad, Reddy and Knight (1992)	Entire ply	Max stress Tsai-Wu	Stiffness for property associated with failure Use direction groups H_1, H_2, H_3, H_4, H_5 and H_6; calculate largest, then select stiffness according to H_1-E_{11}, H_2-E_{22}, H_4-G_{23}, H_5-G_{13}, H_6-G_{12}.	0	Qualitative, point at which small changes in load give large changes in end shortening
Gamble, Pilling and Wilson (1995)	Fibre Matrix Matrix splitting	Modified Hill	E_{11}, G_{12}, ν_{12}, ν_{13} E_{33}, G_{13}, G_{23}, ν_{31}, ν_{32} E_{22}, G_{12}, ν_{21}, ν_{23}	0	Qualitative, point at which small changes in load give large changes in end shortening
Eason and Ochoa (1996)	Fibre Matrix Delam	Hashin, Greszczuk, max stress or Lee Hashin or max stress Ochoa, max stress or Lee	E_{11} E_{22} E_{33}	0	Any element has stiffness reduced by 90%
Gummadi and Palazotto (1998)	Fibre Matrix Delam	Max stress	Stiffness matrix terms, Q_{11}, Q_{12}, Q_{55}, Q_{66} Q_{22}, Q_{12}, Q_{44}, Q_{66} Q_{44}, Q_{66}	0	Any element has all plies failed
Puck and Schürmann (1998)	Fibre Inter fibre	Puck FF Puck IFF	Single fibre fracture affects all fracture plane resistances R_A	By eqn, see paper	Large deformation and fracture plane angle limits
Rotem (1998)	Fibre Matrix	Max stress Rotem	All properties All properties except fibre direction	0 0	First Ply Failure (FPF) for fibre is Final Failure (FF) After matrix FPF, fibre strengths are increased by 20%, FF at all lamina fail
Liu and Tsai (1998)	Ply	Tsai-Wu	E_m if positive transverse strain exists, E_f otherwise	0.15 for E_m, 0.1 for E_f	Each ply can fail in matrix then fibre, or in fibre only. Final failure when all plies have failed.
Singh and Kumar (1999)	Ply	Tsai-Hill	Moduli of dominant mode from Tsai-Hill equation	0	All plies failed
Knight, Rankin and Brogan (2002)	Ply	Max stress, max strain, Hashin, Chang-Chang or Tsai-Wu	All mechanical properties	varied, not 0	Computations stopped based on experiment
Xie and Biggers (2003)	Ply	Hashin	All stiffness properties	0	No final failure
Ambur, Jaunky and Hilburger (2004)	Matrix Shear Fibre	Hashin	E_{22}, ν_{12} ν_{12}, G_{12}, G_{13} E_{11}, E_{22}, ν_{12}, G_{12}, G_{13}, G_{23}	0, (approx)	Qualitative, use drop in load shortening, increase in damage and compare to experiment
Bogetti et al. (2004)	Ply	Max strain	Stiffness for property associated with failure	0 (approx)	Excessive deformation
Feih and Shercliff (2005)	Matrix Delam	Hashin Tong-Norris	E_2, G_{12}, G_{23} –	0.2 –	Analysis continued until delamination occured

Whilst capable of effectively capturing the reduction of material properties caused by damage, the limitations to a progressive failure approach must be considered. Due to the abundance of easily interchangeable failure criteria, and the efficiency of FE analysis, there is a danger in applying arbitrary or incorrect failure criteria, and then simply using the knockdown factor to "tune" the FE results to produce any desired solution (Hart-Smith 1998). Sound engineering judgment must be applied, so that each damage type being modelled is accurately represented by the failure criteria, and this requires a thorough grasp of the assumptions and limitations of all failure and damage conditions. As Hart-Smith (1998) argues, in many cases of progressive failure analysis, damage modes such as matrix cracking and fibre-matrix shearing are applied, with no attempt to correlate any prediction with experimentally observed damage.

Progressive failure analysis can only simulate degradation in material properties, and is unable to represent structural degradation that occurs due to some types of damage, particularly delamination. This becomes important in the analysis of compression loaded thin-walled structures, as the complex interaction between delamination initiation, substructure buckling, damage growth and even matrix cracking cannot be represented. An example of this is seen in Ambur et al. (2004), where predictions from progressive failure analyses in which delamination failure was ignored gave acceptable comparison with experimental data for specimens without delaminations, though less than satisfactory comparison, especially in out-of-plane displacement, for specimens exhibiting only minor delaminations.

2.2.4.3 Interface Elements

Interface elements are separate FE entities, either point-to-point or a continuous element layer, which are modelled between substructures of a composite material as a means of inserting a damageable layer for delamination modelling. Generally, the interface element functions by connecting the two substructures and transferring all tractions across the interface, until a particular criterion is reached, at which point the element stiffness properties degrade. Interface element behaviour is determined by the damage mechanics constitutive relationship between the relative displacement of the two connected substructures, and the traction generated between them as a result. A number of researchers have developed interface elements that utilise a variety of relationships, some of which are summarised in Table 3 with nomenclature taken from the references. The different models are compared across a few categories, including: type, approach to mixed-mode loading, whether additional constants or tests are required, and the types of structures analysed in the paper.

Table 2.4: Interface elements summary

Reference	Type	Mixed-mode formulation	Additional constants	Additional tests	Structures analysed
Cui and Wisnom (1993)	2 springs per node for 2D models	Mixed-mode loading not incorporated	–	–	2D beams in tension and 3-point bending
Hachenberg and Kossira (1993)	12 node interface, for use with 8 node "double node" shell	Delamination growth not incorporated	critical bending strain β_c	T-peel, ILS and peel test	2D specimens, 3D blade stiffened panels
Schellekens and de Borst (1993)	8 node line interface for 12 node shells	Mixed-mode loading not incorporated	–	–	2D mode I test specimen
Reedy, Mello and Guess (1997)	8 node hex interface for 4 node shells	Mixed-mode loading not incorporated	–	–	2D mode I and II specimens
Mi et al. (1998)	6 node line interface for 8 node shells	Modes I and II, use interaction exponent α for delamination growth	Mixed-mode: α	–	2D mode I, II, mixed-mode and overlap specimens
Petrossian and Wisnom (1998)	2 node spring for use with 2D shells	Linear interaction for delamination growth using modes I and II	–	FE tests required	2D beams and curved specimens
Wisheart and Richardson (1998)	6 node 2D line and 16 node 3D interface	Linear interaction for delamination growth using modes I and II	–	–	2D and 3D mode I, II, and mixed-mode specimens
de Moura et al. (2000)	18 node 3D hex for use with 27 node hex	Single mode softening, with displacements in modes I, II, III to define mixed-mode state	–	–	3D CAI plate test
Jansson and Larsson (2001)	2D plane strain damage formulation,	Linear addition of mode I and II SERR; then equate to experimental fracture toughness at given mixed-mode ratio	G as fn of mode ratio G(β)	Input data for G(β) equation	2D mode I, II and MMB specimens
Qiu, Crisfield and Alfano (2001)	4 node line interface for use with 2D shells	Interaction formulation of Mi et al. (1998)	Mixed-mode: α	–	2D mode I specimen
Borg, Nilsson and Simonsson (2002)	3 springs per node in 3D damage surface formulation	Mixed-mode power law relationships *f* and *g* for stresses and strain energy release rates into damage surface	8 constants Load:, α_0, α_i Energy: β_0, β_i	α_i and β_i chosen based on tests	3D DCB, ENF and MMB specimens
Camanho and Dávila (2002)	8 or 18 node 3D interface for 8 or 21 node bricks	Quadratic interaction for delamination initiation; Benzaggagh and Kenane (1996) fracture toughness criteria with $G_{shear} = G_{II} + G_{III}$ for growth	Mixed-mode: η for B-K criterion	Series of mixed-mode tests for η	2D DCB, 3D ENF and MMB specimens
Zou et al. (2002)	16 node non-cohesive interface for 8 node degenerated shell	Interaction formula (Eqn 1) with exponents α, β and γ for growth in modes I, II and III	Mixed-mode: α, β, γ	–	3D DCB and impact specimens
Zou, Reid and Li (2003)	2 interfaces, for 2D/3D solids and laminated shells	Damage surface formulation of Borg, Nilsson and Simonsson (2002), with *g* incorporated into another function ψ to control damage surface shrinkage rate	As for Borg, Nilsson and Simonsson (2002)		2D DCB and mixed-mode overlap specimen
Goyal et al. (2004)	8 node interface for 2D shells, with PFA applied	Parameter μ combining displacements in modes I, II,III; use μ in exponential softening relationship	Material: β, κ, e, mixed-mode: α	–	3D shear and compression panels with cutouts

2.2.4.4 Cohesive Elements

Cohesive elements are a type of interface element that use both damage mechanics and fracture mechanics to define the behaviour of an interface, and are increasingly being applied by researchers to model delaminations and debonds in composite structures. A cohesive zone material model, an example of which is given in Figure 2.4, defines the relationship between the gap opening (δ) and traction (τ) across the interface. After the element passes the strength limit (τ_c) of the material, the stiffness is reduced gradually. This continues until the interface has zero stiffness, at which point the substructures are completely delaminated, and the interface element acts only as a contact region to deny any physically impermissible cross-over of the two substructures. In the cohesive element formulation the work done in reducing the material stiffness to zero is equal to the fracture toughness (G_c). This not only incorporates fracture mechanics theories into the damage mechanics-based approach, but assists in alleviating some of the mesh density problems associated with stress-based analysis.

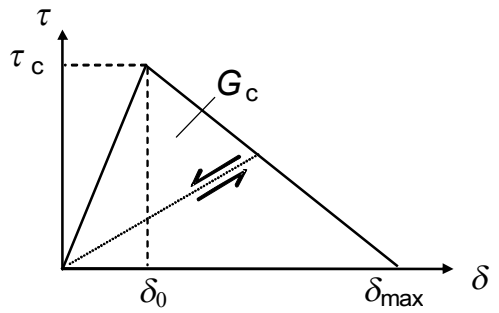

Figure 2.4: Cohesive zone bilinear material model

For delamination and debonding, cohesive elements have a number of important advantages over other modelling approaches, as they have the capacity to investigate both initiation and growth of damage in the same analysis, and to incorporate both strength and fracture mechanics theories. As opposed to classical fracture mechanics, the use of interface elements does not require the assumption of an initial damage size or propagation direction, and obviates the need to apply difficult and computationally expensive re-meshing to accommodate the propagating delamination front. However, cohesive elements require a fine mesh to remain accurate, and can become prohibitively inaccurate when larger mesh sizes are used, which makes their application to large structures problematic. Furthermore, the standard cohesive element formulation cannot account for an arbitrary crack front shape and so does not differentiate between shear damage in mode II and III directions, and in general the exact location of the crack front can be difficult to define due to the use of a cohesive-based definition to describe the quasi-brittle nature of composite failure.

2.2.4.5 Fracture Mechanics

Damage modelling for fracture mechanics analysis requires the definition of a pre-existing crack region in the numerical model. For delamination and skin-stiffener debonds, this involves separating the damaged region into two substructures and defining a contact region between them. A number of researchers have also recognised the importance of modelling the entire structure as two separate sublaminates, with a tying connection in the intact region and contact defined in the damage region, to avoid the error involved in fracture mechanics calculations at points of changing thickness (see, for example: Bruno & Greco 2001; Wang & Qiao 2004). However, it is important to note that an intact structure represented as two substructures joined using tying constraints would have different bending and interlaminar shear properties as compared to using a single laminate. In spite of this, the representation of a delamination or debond as a region of separate sublaminates is both necessary for fracture mechanics, and advantageous as it accounts for the structural degradation due to damage.

Accurate damage modelling of delaminations and debonds also requires the damage area to be grown during analysis. To date, fracture mechanics analysis has been limited in this respect due to the complexities involved in monitoring crack progression and a typical requirement for a fine mesh around the crack front, which usually combine to require either a highly dense mesh or computationally expensive re-meshing. Furthermore, fracture mechanics calculations are generally dependent on the shape of the crack front, particularly the determination of the correct mode mix ratio, and this can require complicated algorithms to monitor the crack front shape as the damage area progresses. These factors have tended to deter researchers from developing fracture mechanics approaches for modelling crack progression, and analyses have been limited to detecting the onset of crack growth only. However, an approach using fracture mechanics to model crack progression has recently been added to the commercial FE code ABAQUS/Standard (Abaqus) and is based on using fracture mechanics calculations to control a debonding mechanism between two surfaces in contact (*VCCT for ABAQUS User's Manual, Version 1.1* 2005). Though the literature available on the implementation of this approach is limited due to its commercial nature, the development does illustrate that efficient and robust methods are possible for incorporating fracture mechanics into crack propagation analysis.

2.3 Benchmarking Study

A study was conducted to benchmark the capability of several currently available commercial FE software codes to analyse postbuckling composite stiffened structures. This was done for a number of reasons, which included complementing the literature review with the current state of the art for commercially available analysis tools and providing an excellent starting point from which to reference the development of this work. The benchmark study was quite comprehensive, and covered four FE solvers – three implicit and one explicit, and three sets of experimental results for composite postbuckling multi-stiffener panels – two for undamaged and one with pre-damage. It must be noted that this study was conducted in 2004, and did not include more recent damage modelling technologies that have since become available in the various codes. A brief summary is presented here, and is focused on the lessons learnt, and the key aspects and issues in performing postbuckling analysis and representing composite damage. The reader is referred to Orifici et al. (2005) for a more thorough description of the experimental results, analysis procedures and numerical models.

2.3.1 Experimental Data

Experimental data was available from three separate tests of fuselage-representative postbuckling stiffened panels, and each were designated as a separate benchmark. Benchmark 1 (B1) was an undamaged 5-blade stiffened curved panel manufactured by Israel Aircraft Industries and tested at Technion Aerospace Structures Laboratory as part of the POSICOSS project (Abramovich et al. 2003). Benchmark 2 (B2) was an undamaged 4-blade stiffened curved panel manufactured and tested at the German Aerospace Center also within the POSICOSS project (Zimmermann, Klein & Kling 2006). For Benchmark 3 (B3), the Benchmark 1 panel was repaired and impacted at three locations to introduce a pre-damage, then re-tested as part of the COCOMAT project. The repair was performed by bonding aluminium angles around the four areas of fibre fracture in the stiffeners, and the B3 panel showed an almost identical stiffness in the load-displacement behaviour as the B1 panel. Within the COCOMAT project it was recognised that there were issues in repairing and re-testing a collapsed panel, such as the likely presence of extensive microcracking in the panel that would have occurred prior to collapse. However, it was thought that the impact damage regions would promote failure before the repair regions, and that there was still considerable value in performing the numerical analyses in order to assess the capabilities of various codes to represent pre-damage. The details of all three benchmark panels are summarised in Table 2.5.

Table 2.5: Benchmark panel specifications

Benchmark	B1 / B3	B2
Panel radius [mm]	1000	1000
Panel length [mm]	720	780
Arc length [mm]	680	419
Number of stiffeners	5	4
Stiffener height [mm]	15	13.25
Stiffener web lay-up	$[\pm 45, 0_2]_{3S}$	$[(45,-45)_3, 0_6]_S$
Skin lay-up	$[0,\pm 45, 90]_S$	$[0, \pm 45, 90]_S$
Ply thickness [mm]	0.125	0.125
Material	IM7/8552	IM7/8552

All benchmark test panels were encased in potting on both ends to ensure a homogenous distribution of the applied displacement, and various restraints were placed along the longitudinal panel edge for additional support, as shown in Figure 2.5 for the B1 panel. For B1, panel skin imperfections were measured using an LVDT probe. For B1 and B3, a moiré fringe pattern was used to observe the deformation pattern, whilst for B2 a photogrammetric technique was applied. In addition to the load and displacement data from the testing machine and the deformation pattern, Linear Variable Differential Transducers (LVDTs) and a large set of strain gauges were applied to all panels. The testing procedures for all panels involved some pre-loadings to settle nonlinearities, then quasi-static loading until collapse.

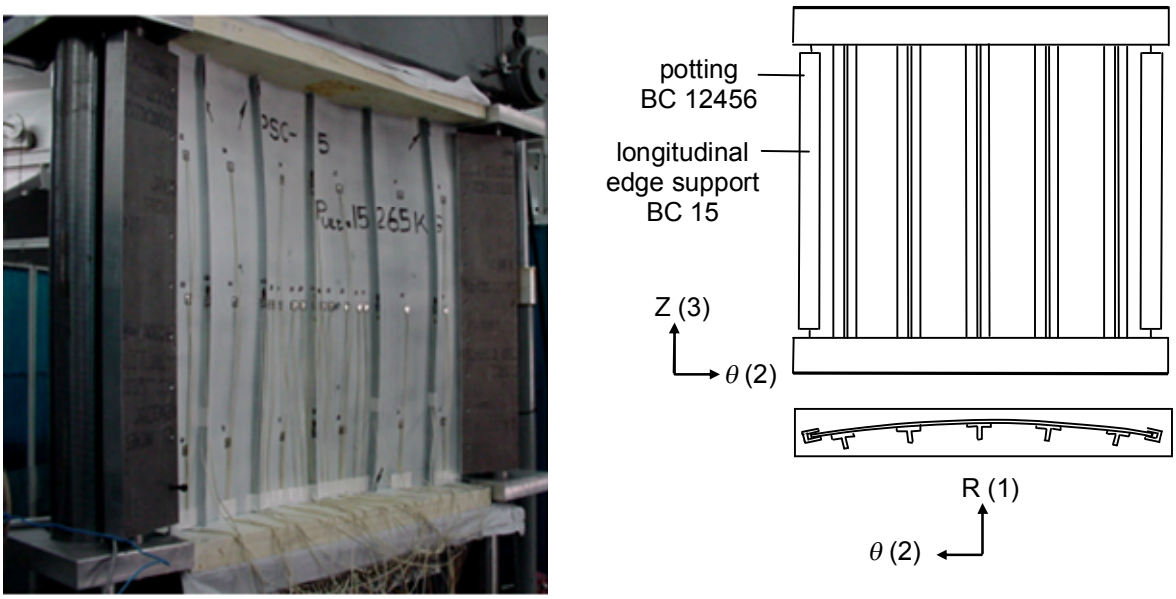

(a) *(b)*

Figure 2.5: B1 panel: (a) Experimental panel in test rig (courtesy of Technion) (b) Schematic of panel restraints with boundary condition (BC) definition

All panels showed behaviour common for postbuckling stiffened structures, and agreed with the observations summarised previously for other researchers. Local buckling patterns of small buckles between the stiffeners were seen, leading to the onset of global buckling patterns with buckles spanning the entire panel bays. Collapse of the panels was characterised by a loud crack, delaminations occurring generally in the stiffener at various locations, and a sharp drop in the load-carrying capacity of the panel. For the B3 panel, collapse was seen to be triggered by damage growth from one of the impact locations. An example load-displacement graph is given in Figure 2.6 for the B2 panel, which also gives several corresponding deformation patterns taken from the photogrammetric measurement system.

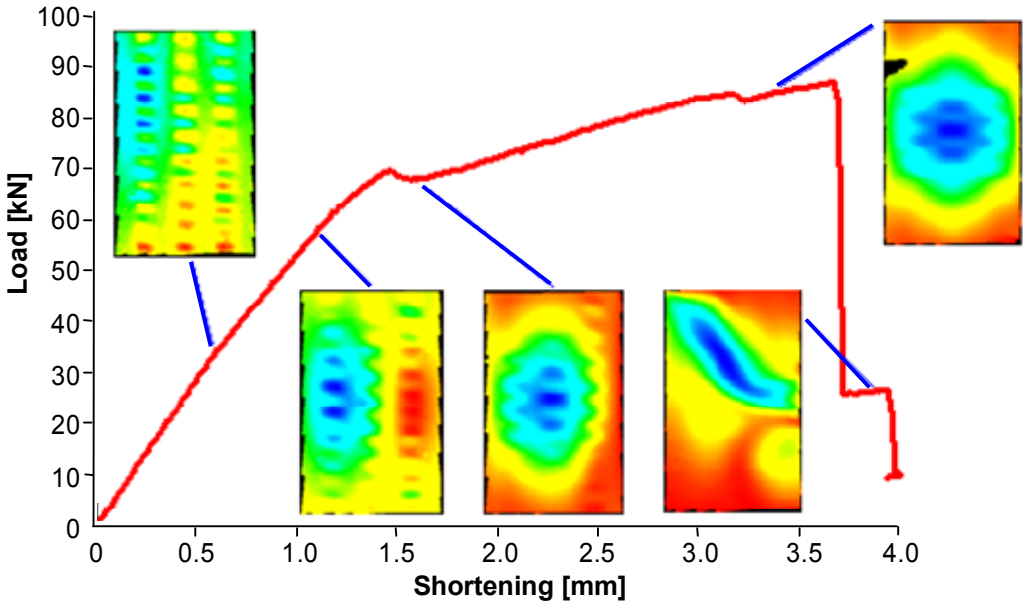

Figure 2.6: B2 load-displacement graph, with photogrammetry mode shapes superimposed

2.3.2 Numerical Analysis

All numerical models were created using 4-node shell elements, which apply a laminate material definition according to CLPT. An example FE model is given in Figure 2.7(a)-(b) for the B3 panel. The three impact sites of the B3 panel were modelled by splitting the intact laminate into separate sublaminates with a frictionless contact between them. A hexagonal delamination shape was applied with a maximum length and width of 60 mm, in order to match the roughly circular shape of the impact damage areas seen from the ultrasonic scan, shown in Figure 2.7(c)-(d). The location of the splitting interface was between plies 4 to 6, and was an approximation based on C-scans of the impact sites on the real panel. Across all panels, several FE codes were applied: implicit solvers MSC.Nastran (Nastran) v2001.0, Marc v2003r2 and Abaqus 6.4-3, and explicit solver LS-Dyna 970. Node-based displacements

were applied as boundary conditions, and the standard nonlinear solver of each code was applied. For the Abaqus models, both the standard solution procedure based on Newton's method and the modified Riks approach were applied with default parameters. Only results for the standard procedure are shown, as this was seen to give more reliable and accurate capturing of the postbuckling deformations, which is likely due to the panels being loaded in displacement control." A linear buckling analysis was also conducted in Nastran for the B1 panel, however the results did not compare well with the experiment in terms of predicted displacement and deformation shape at the onset of either local or global buckling. As a result of this, and the roughly comparable computational effort in running a nonlinear analysis up to the onset of global buckling, the application of linear buckling analysis was seen to be not suitable for this work.

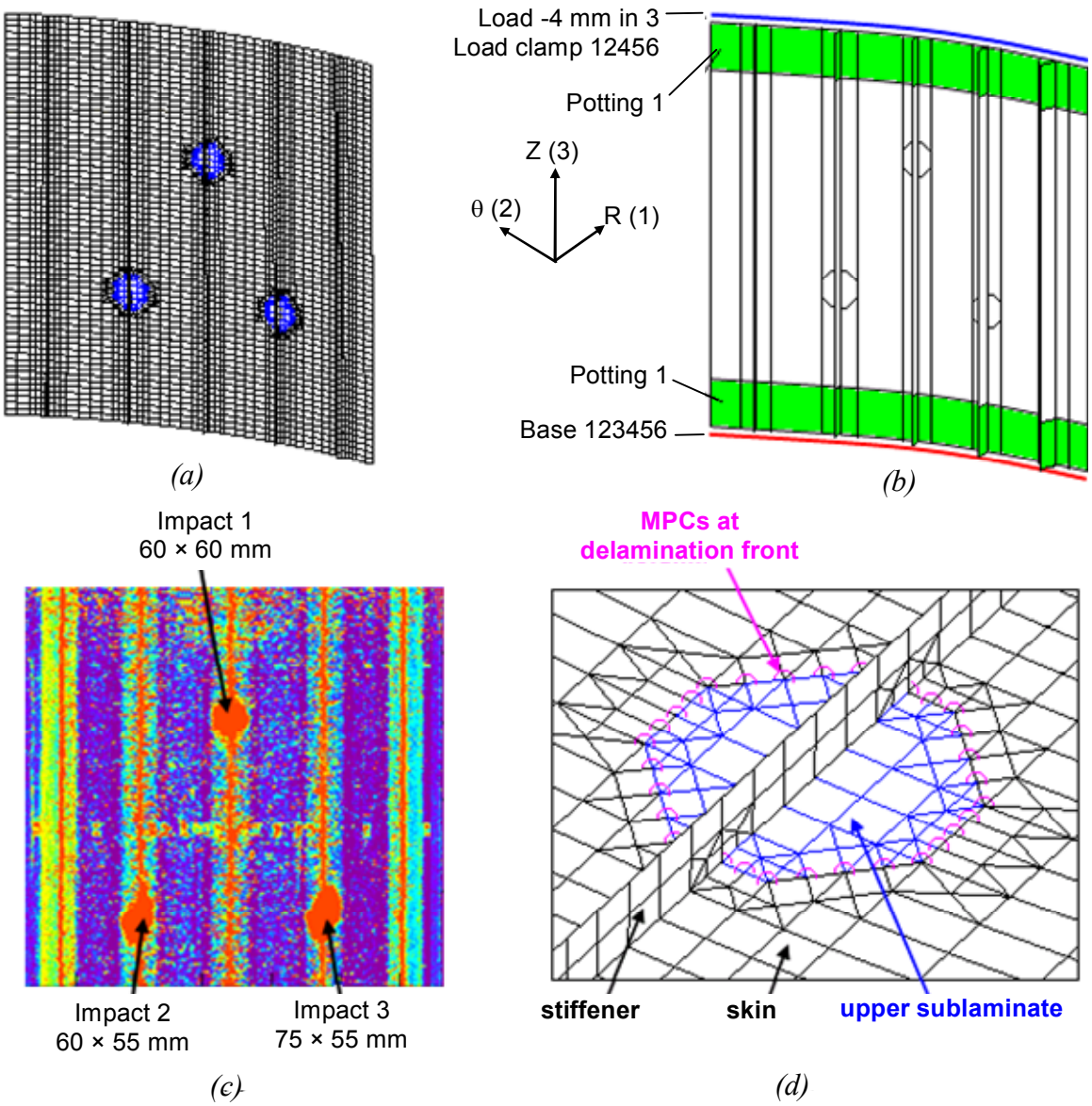

Figure 2.7: B3 panel: (a) FE model (MPCs not shown) (b) Boundary conditions (c) Experimental impact sites (d) FE model impact delamination modelling

Examples of the comparison between experiment and numerical results are given below for the benchmark study, where Figure 2.8 gives the load-displacement curves for the B1 and B3 panels, Figure 2.9 gives the B2 deformation patterns for the various analysis codes at different levels of stroke, or applied loading displacement, and Figure 2.10 gives the B2 load-displacement curves.

Comparison with experimental data for the benchmark cases demonstrated that all software codes could generate reasonably accurate predictions across most panel characteristics. Typically, FE predictions provided very good to excellent predictions of structural stiffness, buckling load and displacement, though in general the numerical models over-predicted the panel stiffness after the onset of global buckling. This indicated the importance of including progressive damage, which was not applied in any model. Additionally, the B3 numerical model did not take into account any matrix damage that would have been present in the test panel as a result of its previous collapse test for B1. Predictions of buckling shape varied, though in general very good comparison was seen in the local buckling and initial global buckling shape, though some models did predict secondary mode shape changes in postbuckling that were not present in the experiment.

Importantly, the collapse of the panels was only able to be predicted by models that included the critical damage mechanisms. The LS-Dyna used a degradation model based on the approach of Chang and Chang (1987) shown previously in Table 2.3, which monitors failure criteria for different in-plane damage modes and uses element deletion upon detection of failure. Using this approach, the LS-Dyna model was able to predict collapse due to the onset of fibre fracture in the stiffeners, which was the critical mechanism causing collapse in the experimental panels. However, due to the over-estimation of the panel stiffness, the predicted collapse did not compare well with the experimental results, which demonstrates that it is necessary to capture all of the critical damage mechanisms in order to get reliable collapse predictions. Though some analyses did show a large reduction in load in the deep postbuckling region, this was due to mode shape changes and not the delamination, skin-stiffener debonding and fibre fracture that caused collapse in the experimental panels.

The results of the benchmarking exercise reinforced the critical nature of accurately capturing boundary conditions, which were shown to be highly influential on the predicted mode shapes. Throughout all analyses, the importance of maintaining a high level of accuracy in the model definition and convergence tolerances of the nonlinear solver was also evident. In

particular, the nonlinear solution procedure, which includes the convergence tolerance and the stiffness update method, were seen to have an influence on results, and the defaults of the FE solvers generally needed to be modified to ensure a high level of precision was applied. Other results indicated that the inclusion of panel imperfections altered the deformation progression from local to global buckling, though had a negligible effect on the postbuckling region.

Comparing the software codes, the implicit solvers all gave very similar results, though the Abaqus and Nastran nonlinear solvers were found to use a more robust and efficient approach to handle convergence difficulties. LS-Dyna predictions showed very good comparison prior to global buckling, though gave the highest degree of overestimation in deep postbuckling. Analysis run times were also higher for LS-Dyna, with run times approaching a week common for the explicit solver, compared to a maximum of around eight hours for the implicit solvers.

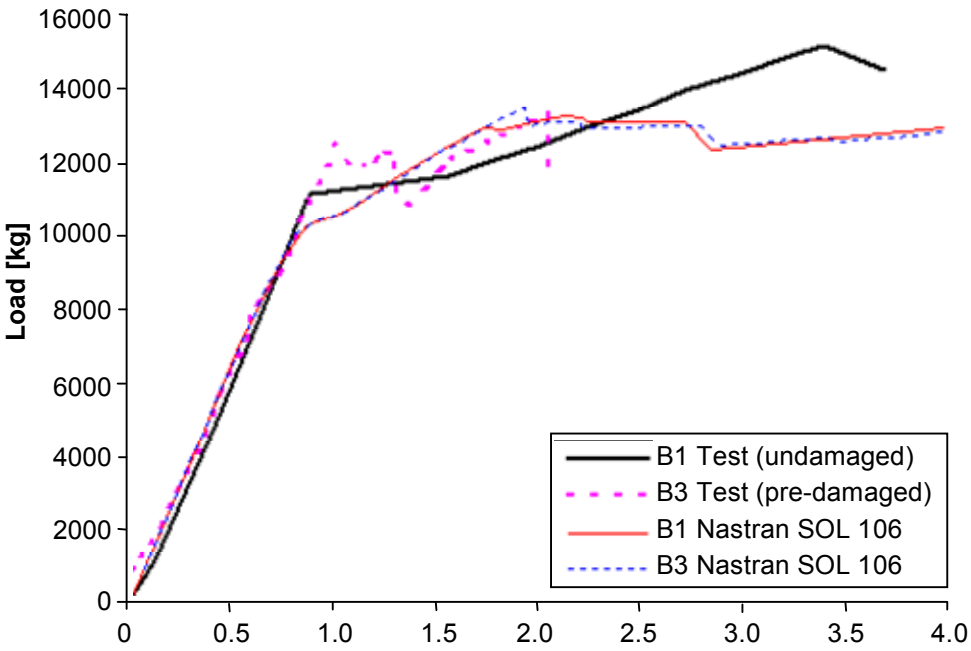

Figure 2.8: B1 and B3 load versus displacement, experiment and Nastran FE results

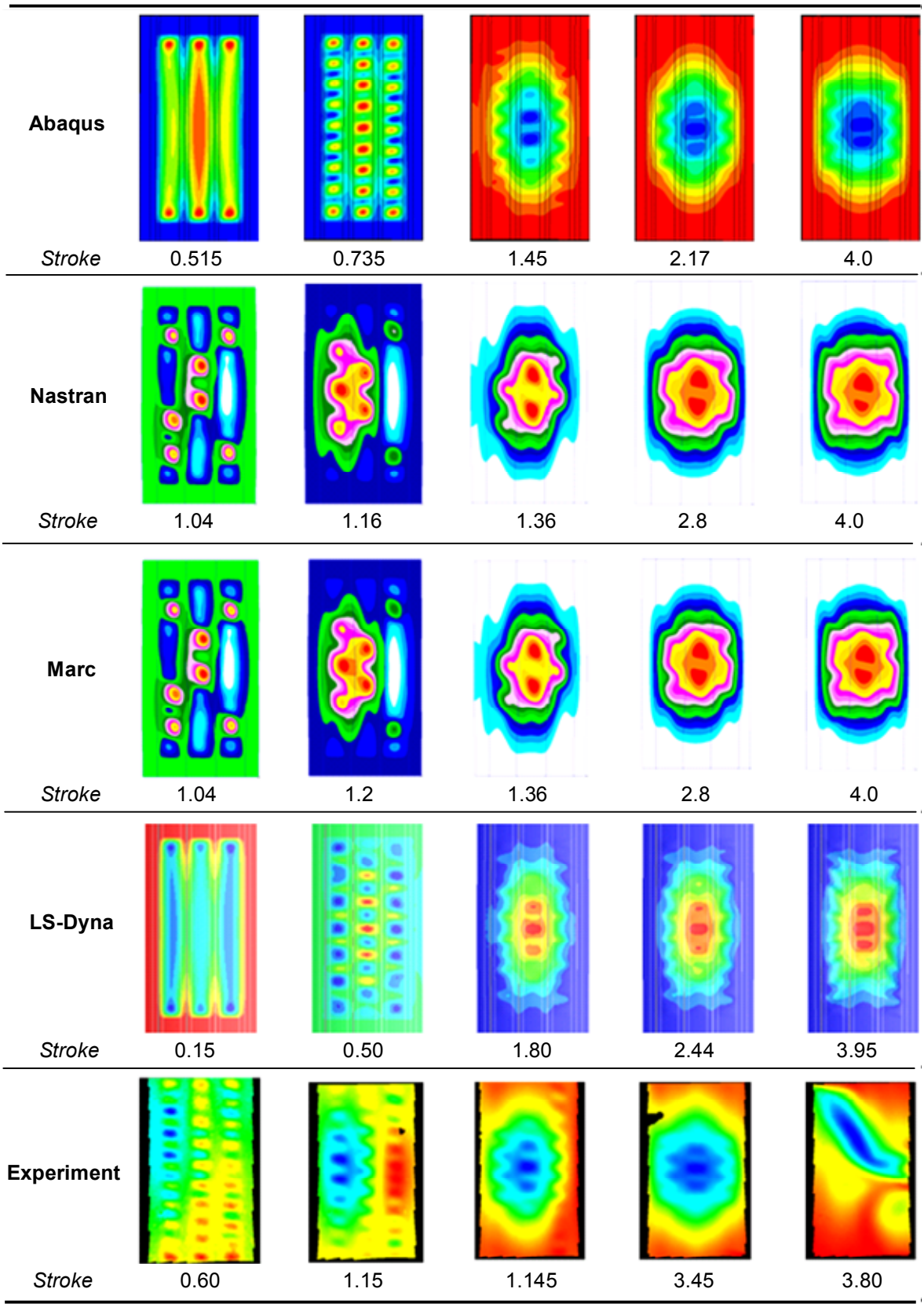

Figure 2.9: B2 mode shape progression, all FE models (stroke values in mm)

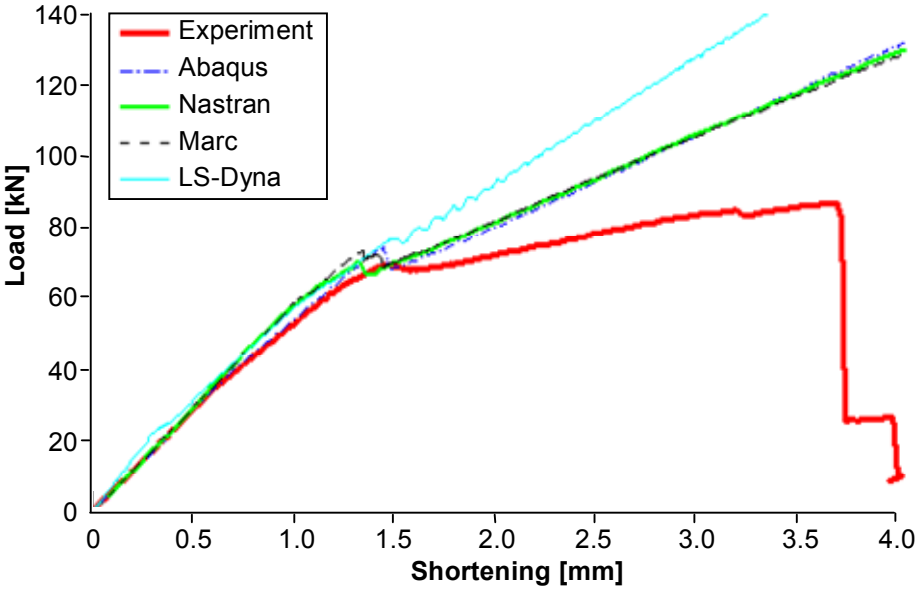

Figure 2.10: B2 load versus displacement, all FE solvers

2.4 Discussion

In this section, the current state of the art for postbuckling composite structure analysis presented in previous sections is discussed in the context of the current work. The intention of the discussion is to illustrate the way in which the literature review and benchmarking study informed the subsequent development. This will include discussions on the approaches for the structural analysis and damage modelling adopted, and a set of requirements and functions necessary for a complete analysis tool.

2.4.1 Structural Analysis

The various methods available for structural analysis, and the issues that become especially relevant for postbuckling structures, are both well developed and have been successfully applied by numerous researchers. The use of FE analysis, the choice between implicit and explicit solvers, and the postbuckling complexities of mode shape changes, geometric imperfections, frictionless contact, nonlinearity and boundary conditions are crucial to achieving accuracy in structural analysis. However, from a development point of view, the area of structural analysis offered less potential for improvements in accuracy, as compared to other less mature definitions such as material damage and degradation. So, this work did not focus on an improvement or alternative to the structural analysis aspects of postbuckling structures as these were considered adequately accurate, but rather concentrated the development on improving the definition of damage types and degradation models.

Following on from the discussion in Section 2.2.1, and the conclusions of the benchmarking study, the following approaches were used for structural analysis:

- Classical Laminate Plate Theory.
- Numerical methods over analytical methods, in a commercial FE software program.
- An implicit solution procedure.
- Methods for improved mode shape capturing and nonlinear definition available from the FE codes.
- Contact between sublaminates in a delamination, and a focus on modelling panel imperfections and boundary conditions as accurately as possible.

2.4.2 Damage Modelling

After reviewing the large variety of damage characterisation and modelling approaches in the literature, it was concluded that fracture mechanics presented an accurate option for the analysis of a pre-existing interlaminar damage region, whilst damage mechanics were naturally suitable for characterising both ply damage and the initiation of interlaminar damage. It was clear that an analysis approach combining all of these damage types would be highly attractive, as it would allow their development and possible interaction to be studied.

For the analysis of crack growth at a pre-existing interlaminar damage region, a point-based interface element was chosen as offering an attractive mix of ease of development and practical capabilities. Various “element” types such as a tie constraint, beam element or contact definition were highlighted as being feasible from a structural point of view, and amenable to implementing fracture mechanics calculations. Though cohesive elements remain an attractive alternative option for a number of reasons, it was thought that fracture mechanics were more applicable and gave a better representation of the physics involved in the crack growth process, and separately cohesive elements are now available in some commercially available FE programs.

For the inclusion of ply damage mechanisms in the model, it was decided to base the approach on the criteria developed by Hashin for monitoring fibre failure, matrix failure, and fibre-matrix shear failure (see Table 2.1). The Hashin criteria have been demonstrated to be deficient in a few areas, most notably in the omission of the beneficial effect of moderate transverse compression on the ply shear strength (Pinho et al. 2005). However, to date,

advanced failure criteria have only been shown to give a slight benefit in prediction of experimental results under only certain types of loading, and the Hashin criteria remain attractive for characterising ply damage due to their accuracy, phenomenological basis, and amenability to FE analysis (Kaddour, Hinton & Soden 2004; Pinho et al. 2005). Additionally, the progressive degradation methodology adopted was based on that proposed by Chang and Lesard (1991), which is presented Table 2.3 under the earlier reference of Chang and Chang (1987). Further detail on the approach developed is given in Chapter 5.

For the initiation of delamination and debonding in an intact structure, it was decided that strength-based criteria were more suitable than a fracture mechanics approach. This is due to the fact that fracture mechanics requires the assumption of a pre-existing crack, which is not suitable for analysis of an intact structure. Furthermore, strength-based failure analysis is a common approach applied in both industry and in research, and a large number of failure criteria have been proposed to predict delamination initiation from strength considerations (see for example the reviews on the subject by D'Ottavio and König (2006), Tong (1997) and Feih (2002)). However, no delamination initiation criterion has been shown to be either commonly applied by researchers or consistently more accurate than any other criterion. As a result, further investigation of an appropriate criterion was deemed necessary, and this is detailed in the following chapter.

2.4.3 Analysis Tool

One of the goals of the work was the development of an analysis tool to incorporate the features of the damage modelling approach. After the completion of the literature review and benchmarking study, it was possible to give a clearer definition of the required functionality of the tool for a complete analysis of a postbuckling composite structure. The following is a list of functions for the analysis tool that summarises the requirements of the designer or analyst applying the tool for different applications.

For all analyses:

- Use progressive failure analysis to degrade properties for in-plane damage modes.
- Detect final structural collapse. The condition for final collapse is undecided, though will most likely involve a combination of ply fibre failure and excessive deformations due to large debonding and delamination areas.

- In pre-processing, incorporate any required pre-damage, including impact damage and debonded regions manufactured using a Teflon inclusion.

For the analysis of intact structures:

- Detect the location of delamination or debonding damage initiation in the panel.
- Determine the failing ply interface for the damage.

For the analysis of an existing delamination or debonded damage region:

- Calculate SERR in all modes for all points around the delamination.
- Advance the crack front in the appropriate direction, based on the existing delamination shape, and the strain energy release rates.

2.5 Conclusion

A literature review has been conducted on all areas relevant to the analysis of postbuckling composite stiffened structures. Summaries of previous researchers' experience in structural analysis were presented, which included the appropriate plate theory, analytical or numerical methods, explicit and implicit solution procedures, and a variety of issues in structural analysis found in postbuckling analysis such as mode shape changes, imperfections, contact, nonlinearity and boundary conditions.

Moving from structural analysis to damage analysis, the damage types found from previous experimental investigations were summarised, and some of the theories and criteria used by previous researchers to characterise damage were listed. Following this, various methods applied by previous researchers to model the different damage types were summarised, and grouped into two broad categories of damage mechanics and fracture mechanics.

A benchmarking study was then conducted to complement the literature review with the current state of the art for commercially available tools for the analysis of postbuckling stiffened panels load to collapse. Three benchmark cases were described, and analysis was conducted using the implicit solvers in Nastran, Marc and Abaqus, and the explicit solver LS-Dyna.

Comparison with experimental data for the benchmark cases demonstrated that all software codes could generate reasonably accurate predictions across most panel characteristics.

Numerical predictions of stiffness and buckling were generally very good to excellent, though the postbuckling behaviour was slightly overestimated, which importantly was attributed to not taking damage into account in the analysis. Comparing software codes, the implicit solvers gave very similar results, with Abaqus and Nastran providing more efficient nonlinear solver algorithms. The explicit solver LS-Dyna did give good predictions of panel behaviour, though showed the most overestimation in postbuckling and significantly larger run times.

Based on the summaries of the literature review and benchmarking study, discussions were presented for structural analysis and damage modelling in the context of the development in this work. This included: recommendations for the structural analysis; a basic outline of various damage modelling approaches suitable for further development and investigation, and a set of functions for an analysis tool incorporating the damage modelling approaches.

CHAPTER 3

INTERLAMINAR DAMAGE INITIATION

From the literature review in Chapter 2, capturing the initiation of interlaminar damage was recognised as a critical aspect in the analysis of postbuckling blade-stiffened composite structures. This chapter presents the results of an investigation into such failure for a skin-stiffener interface of a fuselage-representative structure, loaded under typical postbuckling deformations.

In the experimental investigation, thin strips consisting of a skin and single stiffener were cut from a large stiffened panel to form T-sections. These sections were loaded until failure in two separate test rigs, which aimed to simulate the symmetric and antisymmetric loads on skin-stiffener interfaces in a postbuckling panel. Two-dimensional finite element models were analysed, and strength criteria applied in order to predict the initiation of delamination in these specimens. Based on these predictions, recommendations are made for the application of the 2D analysis approach to predict skin-stringer interface failure in large fuselage-representative structures [2].

3.1 Introduction

Blade-stiffened skin designs have the potential to produce highly efficient composite structures provided the large strength reserves available after structural buckling, in the postbuckling range, are exploited. In experimental tests of skin-stiffened composite structures in postbuckling, failure typically initiates at the interface of the skin and stiffener, either around the base of the stiffener or at the edge of the stiffener flange (Meeks, Greenhalgh & Falzon 2005). Delamination or debonding in the skin-stiffener interface typically leads to rapid and even explosive failure of the panel, as the damaged region spreads and leads to a detachment between the skin and stiffener (Starnes, Knight & Rouse 1985; Wiggenraad et al.

---

[2] Orifici, AC, Herszberg, I, Thomson, RS, Weller, T, Kotler, A & Bayandor, J 2007, 'Failure in stringer interfaces in postbuckled composite stiffened panels', in *12th Australian International Aerospace Congress*, Melbourne, Australia, 19-22 March.

1996; Zimmerman, Klein & Kling 2006). Failure usually occurs at nodal or anti-nodal lines in the structure, where either the bending or twisting moments are at their maximum (Stevens, Ricci & Davies 1995). Typical deformation patterns for postbuckling skin-stiffener interfaces are shown in Figure 3.1, which gives the antisymmetric loading at an anti-nodal line caused by buckling between stiffeners and the symmetric loading caused by global panel buckling (Abramovich & Weller 2006).

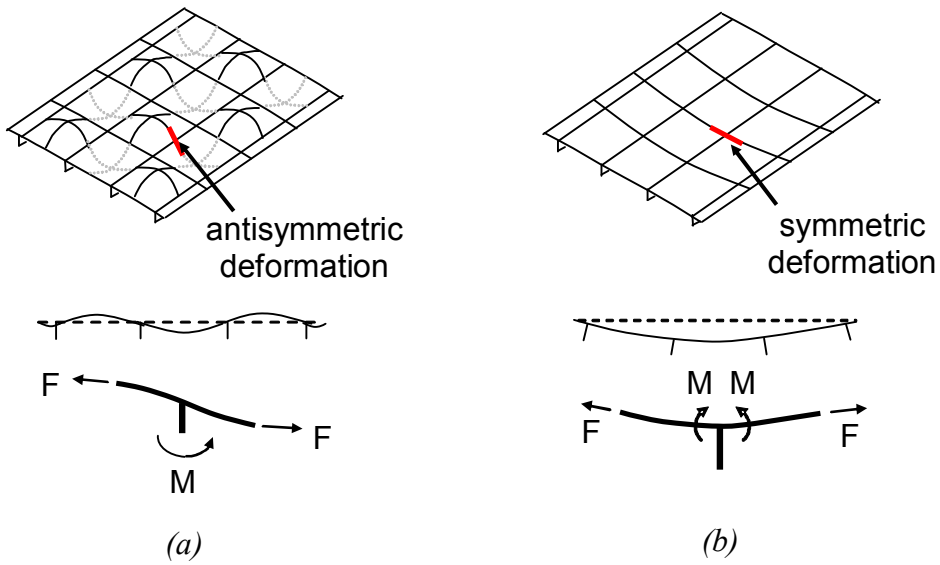

Figure 3.1: Deformation patterns in postbuckling skin-stiffener interfaces: (a) Local buckling (antisymmetric) (b) Global buckling (symmetric) (Abramovich & Weller 2006)

From the benchmarking study of the previous chapter, it was seen that relatively simple global modelling of such structures using shell elements leads to a good definition of the postbuckling shape in relatively short time. However, modelling such a structure in sufficient detail to determine failure in the modes observed experimentally would involve a very large number of elements with consequential very long solution times. In the interest of providing an efficient design tool, small elements of the structure (Figure 3.1) in the region of potential failure are considered. Detailed models of these small regions may be analysed rapidly to determine failure in the critical regions when they are deformed in the shape predicted by the global analysis. After the design process has been completed the global model may be used to verify the results.

A conclusion reached from the literature review presented in the previous chapter was that strength criteria are the most suitable choice for predicting the initiation of interlaminar damage in intact structures. In strength-based criteria the stress, or a similar parameter such as strain or force, in the critical directions are compared to material strengths and then combined

in a single value. These criteria are typically based on the through-thickness tensile, or peel stress, in combination with the through-thickness shear and longitudinal tensile stress, and differ mainly in the relative contribution of the peel stress, and the use of tensile or compressive longitudinal strength (see D'Ottavio and König (2006); Tong (1997)). In this work the damage propagation behaviour was not considered, and the initiation of interlaminar damage was taken as the specimen failure point. This approach was taken based on the literature review, which showed that in experimental investigations of compression-loaded stiffened structures, the initiation of interlaminar damage commonly led to instantaneous structural collapse.

3.2 Experimental Investigation

Co-cured skin-stiffened panels representative of a composite fuselage design were manufactured at Israel Aircraft Industries from IM7/8552 carbon fibre prepreg. These panels were cut into thin strips consisting of a skin and single stiffener, at nominal widths of 13 mm, 25 mm and 35 mm, and the remaining geometry is given in Figure 3.2. In the specimen manufacture, the plies in the blade were laid together, then laid in halves over the skin. This was done in three drop-off steps, and also caused an asymmetry in the orientation of the 45° layers.

The specimens were tested at the Aerospace Structures Laboratory at Technion in two test rigs to simulate the antisymmetric and symmetric postbuckling loadings shown in Figure 3.1. A brief summary of the experimental program and results follows. More details are presented by Herszberg et al. (2007).

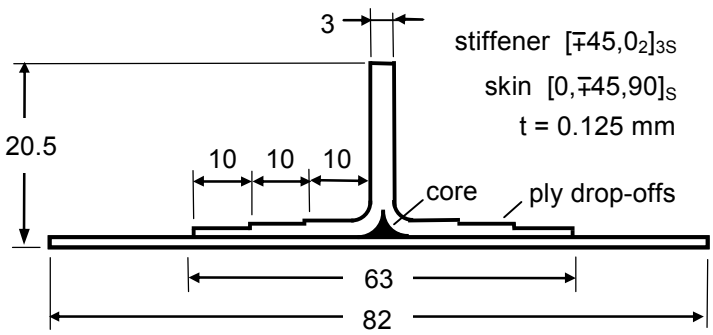

Figure 3.2: T-section geometry, all dimensions in mm (Abramovich & Weller 2006)

Antisymmetric tests were designed to simulate the loading condition generated at an anti-nodal line for a postbuckling stiffened panel, shown in Figure 3.1(a). In the test rig, given in Figure 3.3, the specimen was held by clamps on the end of the blade and skin. The skin clamps were on a rotating fixture, which was also connected by a horizontal bar and circular segment to a load cell. As the piston moved up, the blade and skin clamps translated, while the skin clamps also rotated around the axis of rotation due to their connection to the fixed load cell. The tests were conducted in displacement control with a loading rate of 2 mm/min.

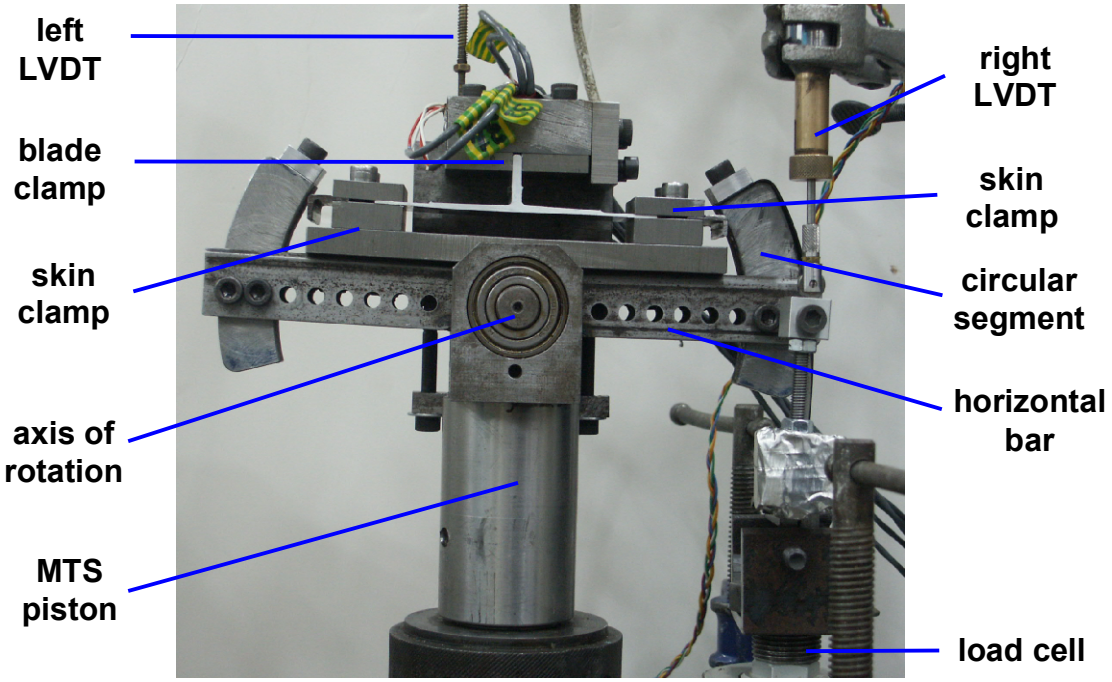

Figure 3.3: Antisymmetric test rig at Technion Aerospace Structures Laboratory (Herszberg et al. 2007)

As output from the test, the right and left LVDTs respectively measured the displacement of the circular segment and of the MTS machine at the blade fixture. The angle of rotation was calculated using the difference between the two LVDTs and the distance between the axis of rotation and the circular segment. The reaction force was taken at the load cell, and was multiplied by the distance between the axis of rotation and circular segment to give the applied moment. This moment was multiplied by the angle of rotation to give the applied energy, which was then normalised using the specimen width.

The symmetric tests were designed to simulate global buckling loading, as shown in Figure 3.1(b). These tests used a simplified version of the antisymmetric rig, where the skin clamps were connected to the MTS piston without the rotating assembly, and the blade clamp was

directly connected to a load cell. The piston moved downwards and pulled down the skin clamps, whilst the blade clamp remained stationary. As output, the load cell reaction force was multiplied by the displacement of the clamp fixture, taken from the difference between LVDTs on the piston and load cell. This gave the failure energy, which was again normalised using the specimen width.

Twenty-five antisymmetric and 14 symmetric tests were performed up to specimen failure, where failure in each test was defined as the point of first load reduction or observation of visible damage, which for most tests corresponded to the maximum load. The antisymmetric and symmetric results were similar, where failure was observed in three main failure types, shown in Figure 3.4. As the skin-stiffener joint was constructed using a co-cured manufacturing process, all interlaminar damage was in the form of delaminations. Of the three failure types, type 1 was the most common, and involved delamination in the bend of the skin-stiffener junction. Failure type 2 involved delaminations in the stiffener, either exclusively or in combination with cracks in the bend, and was seen occasionally, particularly for the antisymmetric tests. Type 3 failure occurred at the flange edge, and was not common as it appeared to have only resulted when the skin clamps were not properly tightened, so will not be considered further.

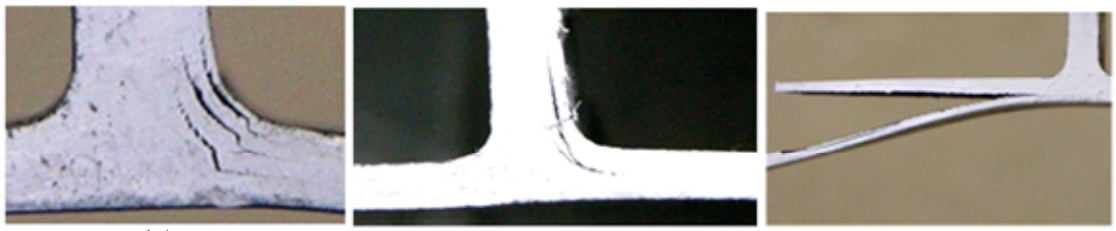

Figure 3.4: Failure types: (a) 1. Skin-stiffener bend (b) 2. Stiffener (c) 3. Flange edge (Herszberg et al. 2007)

For the symmetric tests, failure type 1 was predominant, with only a few samples showing failure types 2 or 3. For failure type 1, delamination cracks were seen at ±45°/0° interfaces, and typically there were significant cracks in three evenly spaced ±45°/0° interfaces through the thickness. Delaminations were contained on one side of the stiffener for each specimen, though the side varied between tests. In the vicinity of the middle of the bend, cracks would often appear to cross from an 45°/0° interface through the 0° plies and onto the 45°/0° interface on the other side. A scanning electron microscopy investigation appeared to indicate that failure initiated in the 0° plies and progressed to ±45°/0° interfaces on either side, though there was insufficient evidence to make a definitive conclusion.

For the antisymmetric tests, failure types 1 and 2 were both common, though type 2 showed significantly lower failure energies than type 1. For failure type 1, delaminations again formed mainly in +45°/0° interfaces on the tension side of the stiffener, though sometimes cracks migrated through the triangular core region to the other side of the stiffener, or down into the first +45°/−45° interface of the skin. Delaminations occurred in single interfaces close to the outer edge or in the middle of the bend, or in two or three evenly spaced interfaces through the thickness. Type 2 failures involved cracks that appeared to have initiated in the bend region and moved up into +45°/0° interfaces in the stiffener, as well as delaminations that appeared to have initiated in the central 0°/0° interface of the stiffener and spread to nearby +45°/−45° or less often +45°/0° interfaces.

In terms of the test output data, the normalised energy versus loading displacement or angle is given in Figure 3.5 and Figure 3.6 for the symmetric and antisymmetric tests respectively, where the shaded region represents the range of experimental results recorded. From this data, outliers were determined using the specimen stiffness and failure energy, where for this purpose in the antisymmetric tests the results for type 1 and type 2 failures were treated as separate data sets. In spite of the identification of outliers, there was still a considerable degree of experimental scatter, as is evident in the range of stiffness data and failure energies for both test rigs. Note that due to the normalisation the results are not separately classified using specimen width, and that all results for failure type 3 were already removed as outliers based on failure type.

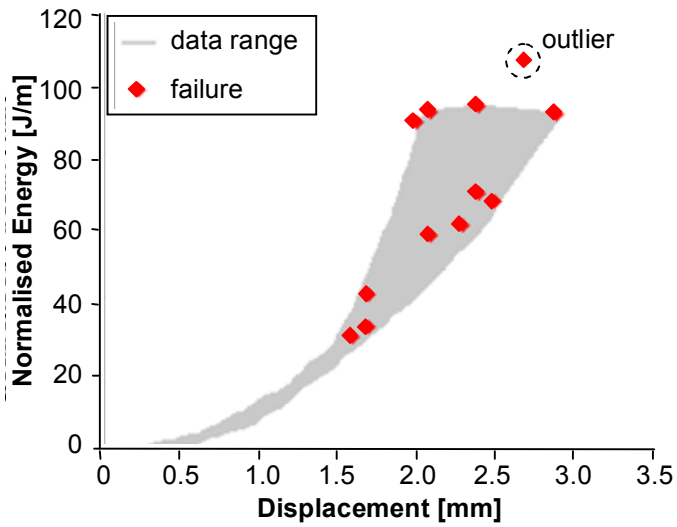

Figure 3.5: Symmetric tests, data range and failure energies, with outliers

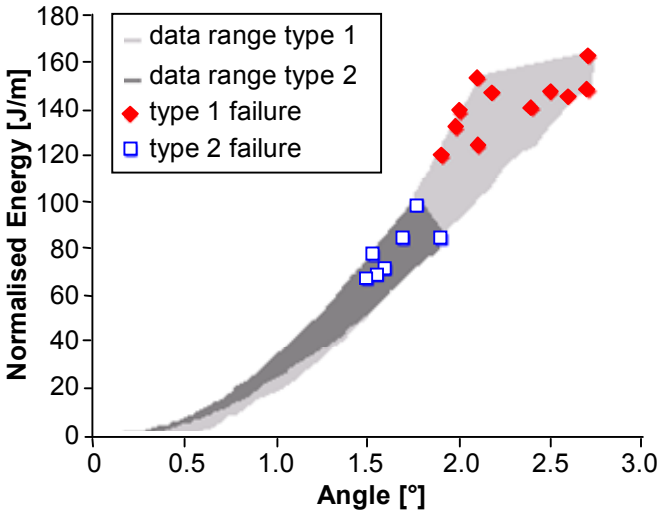

Figure 3.6: Antisymmetric tests, data range and failure energies, failure types 1 and 2, outliers removed

3.3 Numerical Analysis

An analysis approach was developed for the T-section specimens that involved monitoring a strength-based criterion for delamination in 2D FE models. The models used 2D generalised plane strain elements, which are 6-node elements consisting of a 4-node plane strain quadrilateral element with two additional nodes shared by all elements containing the out-of-plane displacement and rotations for the entire model. FE models were created of the antisymmetric and symmetric tests in MSC.Mentat for analysis in Marc (*MSC.Marc and MSC.Mentat User Manuals Version 2005r3* 2006). The generalised plane strain elements were validated as giving almost identical behaviour to 3D solid elements in separate analyses. The models were generated using the specimen geometry in Figure 3.2. Further detail is given in Figure 3.7, Figure 3.8 and Table 3.1. The material properties are identical to those described in a later chapter for separate analysis, and are given in Table 5.4.

Table 3.1: FE model nominal parameters, symmetric and antisymmetric models

	Symmetric	*Antisymmetric*
Number of elements	4491	4561
Number of nodes	4801	4846

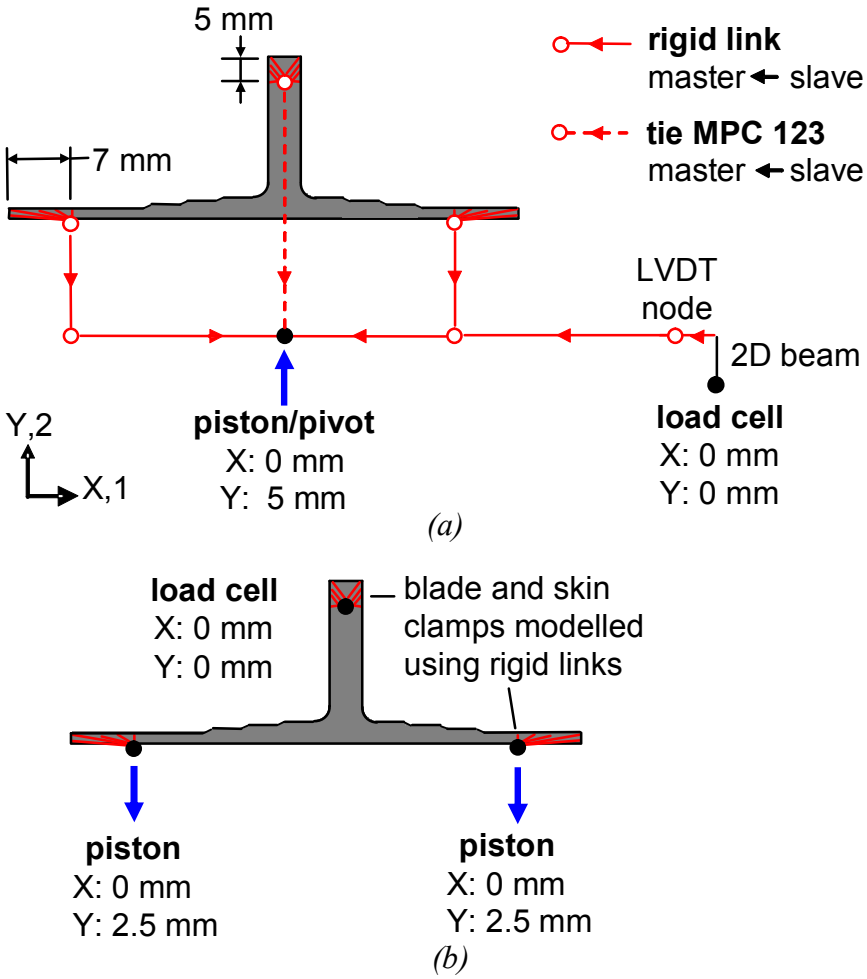

Figure 3.7: 2D FE models: (a) Antisymmetric (b) Symmetric tests

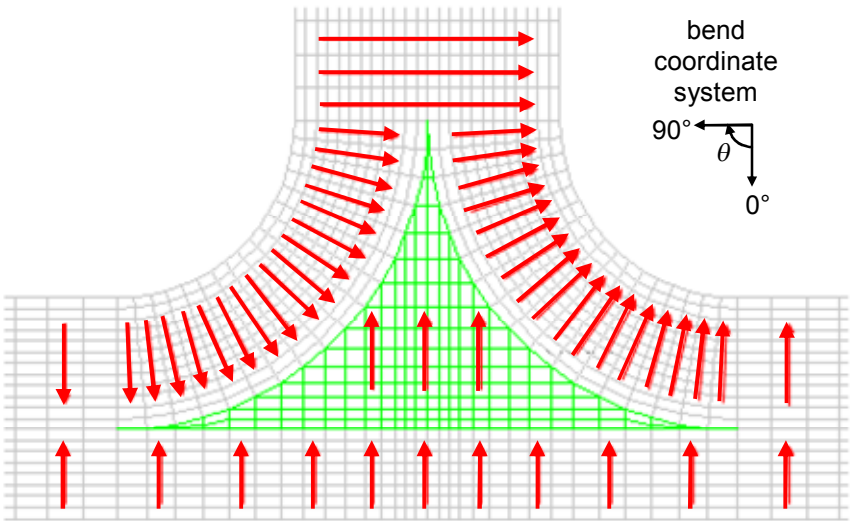

Figure 3.8: Skin-stiffener junction modelling showing element orientations

The mesh of plane strain elements in both models was identical, and was constructed using elements for every ply and aspect ratios lower than four. In both models, a small triangular region of resin material was included at the end of every ply drop-off, as shown in Figure

3.7(a), in order to represent the smoothing process applied on the excess resin in real test specimens to create a continuous surface. In the antisymmetric model, a system of rigid links and a 2D beam was used to replicate the rotating test rig shown in Figure 3.3. The 2D beam was given the properties of a nominal aluminium bar, and was required as a boundary condition was applied at the load cell node, which meant this node could not be made a slave node in a rigid link. The material properties of the specimens were taken from characterisation tests on IM7/8552 unidirectional specimens, and were the average of values taken from tests in three laboratories. The stiffness data were all generally within 5% and the strength data were within 10% of the mean except for the transverse tensile strength, where the variation between data sets was up to 25% from the mean. The material was assumed to be transversely isotropic, so that the through-thickness properties were assumed equal to the transverse properties. The elements in the triangular core region were given properties equal to the 0° plies, as in the real specimens this region was filled with rolled prepreg tape during manufacture.

In order to determine the initiation of delamination in the specimen, a user subroutine was written for the PLOTV routine within Marc. The PLOTV subroutine allows for the calculation of user-defined element output values, and is called by every integration point at every layer of each element. The subroutine takes as input the element global stresses and strains, and the stresses in the element orientation direction. As shown in Figure 3.8, orientations were assigned to each element to align the first material direction with the through-thickness direction, which greatly simplified the calculation of the failure criterion in the subroutine. Though various strength-based criteria were investigated, due to the fact that each criterion differed mainly in the addition of the longitudinal tensile component and that this component was almost negligible for the 2D specimens investigated, there was no noticeable difference between the criteria investigated. As a result, delamination predictions in this chapter will only be shown for the "degenerated Tsai" criterion (Feih 2002), which is given by

$$\left(\sigma_{\mathrm{x}}/X_{\mathrm{t}}\right)^2+\left(\sigma_{\mathrm{z}}/Z_{\mathrm{t}}\right)^2+\left(\tau_{\mathrm{yz}}/S_{\mathrm{yz}}\right)^2\geq 1, \tag{3.1}$$

where σ_{x}, σ_{z}, τ_{yz} and X_{t}, Z_{t}, S_{yz} are stresses and strengths in the longitudinal, through-thickness tensile and shear directions, respectively. Failure was deemed to occur when the average of all four integration point values in an element satisfied this criterion.

All models were analysed using the Marc 2005r3 nonlinear solver, with 50 increments, a convergence tolerance of 0.1 on load residuals and all other analysis parameters set to the program defaults. The analyses were run on a 2.4 GHz Dual Core AMD Opteron processor, with run times around 60 seconds. The results for the nominal models are presented in Figure 3.9 and Figure 3.10, which give the normalised energy versus loading displacement or angle and first failing element for the symmetric and antisymmetric tests.

For the nominal symmetric model, the specimen stiffness and delamination initiation prediction agreed well with the experimental values, with the predicted failure at 78.3 J/m giving good comparison with the experimental average failure value of 69.4 J/m. Delamination was predicted to occur at the innermost 0° ply within the bend at an angle $\theta = 67°$, where θ is the clockwise angle in the bend, and varied from 0° at the skin to 90° at the stiffener as shown in Figure 3.8. Though this location did not correspond exactly to the bend angle and ply interface seen in the experiment, the model did predict a type 1 failure, which was the dominant mode of failure in the symmetric tests.

For the antisymmetric tests, the nominal FE model was significantly stiffer than the test specimens, which resulted in the initiation of delamination being predicted much earlier than the test results. From inspection of the experimental video footage, it was noticed that in addition to the axial movement from the piston the specimen appeared to translate laterally. This is shown in Figure 3.11, where a displacement of approximately 1 mm can be seen by overlaying images from the test taken before the loading and just prior to failure. Based on this, the tie MPC shown in Figure 3.7(a) was removed and the blade clamp was loaded with 1 mm and 5 mm displacement in the X and Y directions respectively, and the results are shown in the "FE updated" curve in Figure 3.10. From this, it is clear that any lateral translation of the piston would have significantly reduced the stiffness of the FE model, and the updated model showed much closer correlation with the experiment than the nominal model.

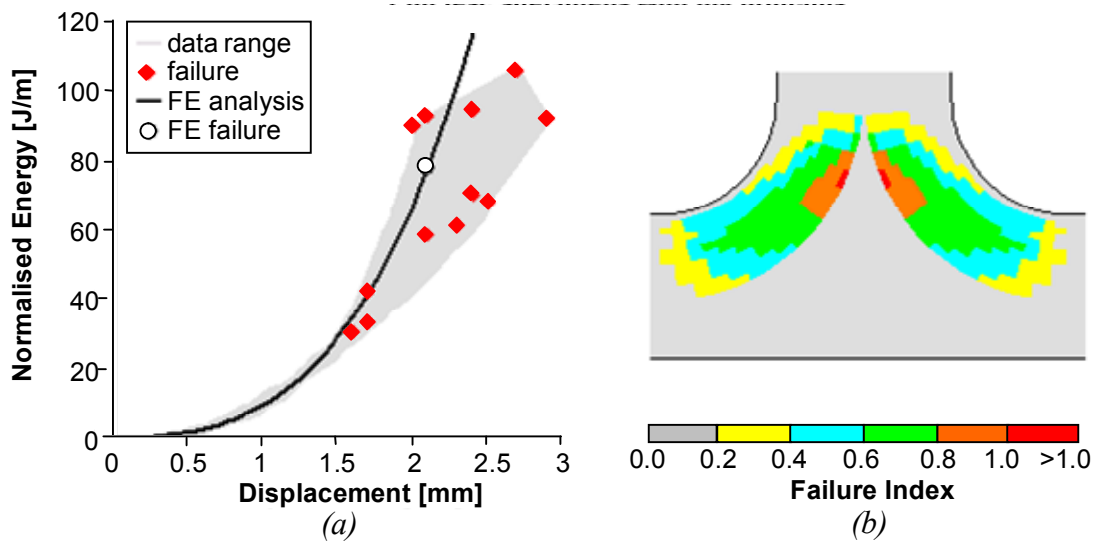

Figure 3.9: Symmetric specimen: (a) Normalised applied energy versus loading displacement (b) delamination failure index at first failure

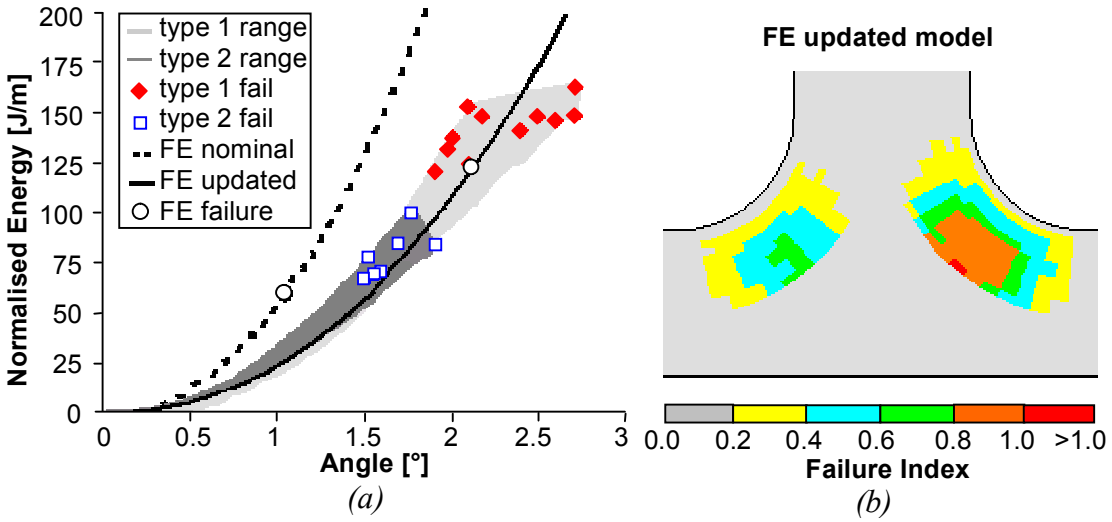

Figure 3.10: Antisymmetric specimen: (a) Normalised applied energy versus loading angle (b) delamination failure index at first failure

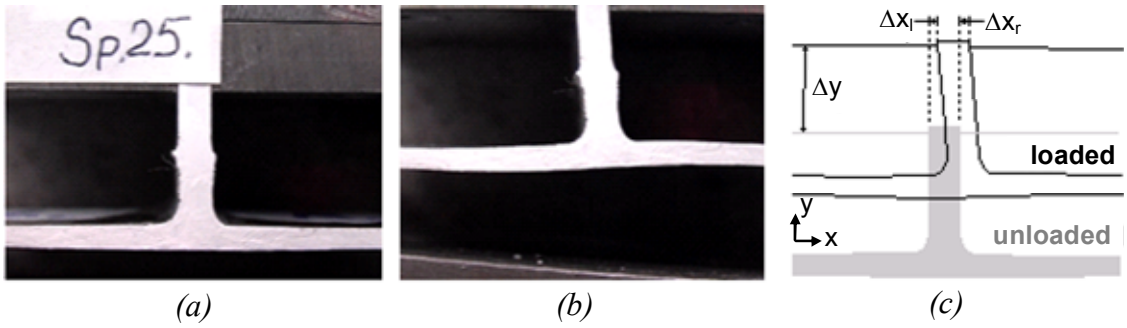

Figure 3.11: Lateral displacement of specimen under loading: (a) Unloaded (b) Loaded (c) Schematic taken from (a) and (b) showing y displacement of piston and x displacement measured at left and right stiffener edges

Failure in the updated model was predicted in the skin-stiffener bend at $\theta = 40°$, and occurred at the innermost ply closest to the core region. Though this location agreed well with a number of the type 1 bend failures seen in the experiment, the type 2 stiffener failures and the type 1 bend failures involving only the outermost ply were not predicted by the updated model.

From the nominal models, a number of parametric investigations were performed, in order to determine the sensitivity of the models to various parameters and to attempt to match the model more closely with the real specimens. The parametric investigations are summarised in Table 3.2, were the "Rig" column defines when the investigation was applied to the antisymmetric (A) or symmetric (S) test rigs.

Table 3.2: FE model parametric investigation

Investigation		Parameter	Nominal value	Variants	Rig
(1)	Core region property	Material of elements in triangular core	all 0° plies	all resin, mixtures of 0°/resin	A S
(2)	Strength values	through-thickness tensile and shear strengths	average values from characterisation tests	$Z_t \pm 50\%$ $S_{yz} \pm 50\%$	A S
(3)	Clamp geometry	Size of skin and blade clamps	skin clamps 7 mm blade clamps 5 mm	skin clamps 5-10 mm blade clamps 3-7 mm uneven skin clamps, ± 3 mm	A S
(4)	Clamp friction	coefficient of friction, skin and blade clamps	perfect contact (no friction included)	friction coefficient from $0.5 - 1\times10^6$	A S
(5)	Blade geometry	width of blade (blade ply thickness t_b)	3 mm (t_b = 0.125 mm)	3.408 mm (t_b = 0.142 mm)	A
(6)	Bend radius	Inner radius of skin-stiffener bend	2 mm	3 mm	A

From the results, the strength properties had the most significant effect on the failure predictions, especially Z_t, as the through-thickness tensile stress was dominant in all models. In general, an increase of 25% in Z_t typically resulted in an increase in failure energy of around 30% and 12% for the symmetric and antisymmetric models. The significance of this sensitivity is discussed in a later section. The effect of modifying the ratio between the two strength values is shown in Figure 3.12. Decreasing this ratio caused the failure location to occur closer to the middle of the bend instead of the core, and increased the failure index in the middle of the stiffener, both of which resulted in a pattern more closely resembling type 2 failure. This is due to the fact that for all models, the through-thickness tensile stress was highest at the interface of the bend and core, whilst the through-thickness shear stress was highest in the middle of the stiffener, as shown in Figure 3.12.

Other parameters were also found to have an important effect on the model behaviour, especially in delaying the onset of delamination. Introducing friction into the model reduced the stiffness and delayed the initiation of delamination, where it was seen that friction had a greater influence on the symmetric specimens. Modifying the clamp lengths had only a small effect on the results, though the use of uneven skin clamps did delay the delamination prediction, which was more pronounced for the symmetric tests. The core material was shown to have a negligible effect on the specimen stiffness and failure, and the use of an uneven distribution of 0° and resin elements only modified the failure location angle by around 10°. For the antisymmetric models, increasing the inner bend radius from 2 mm to 3 mm increased the failure energy by 21 J/m, with almost no effect on the specimen stiffness, as shown in Figure 3.13.

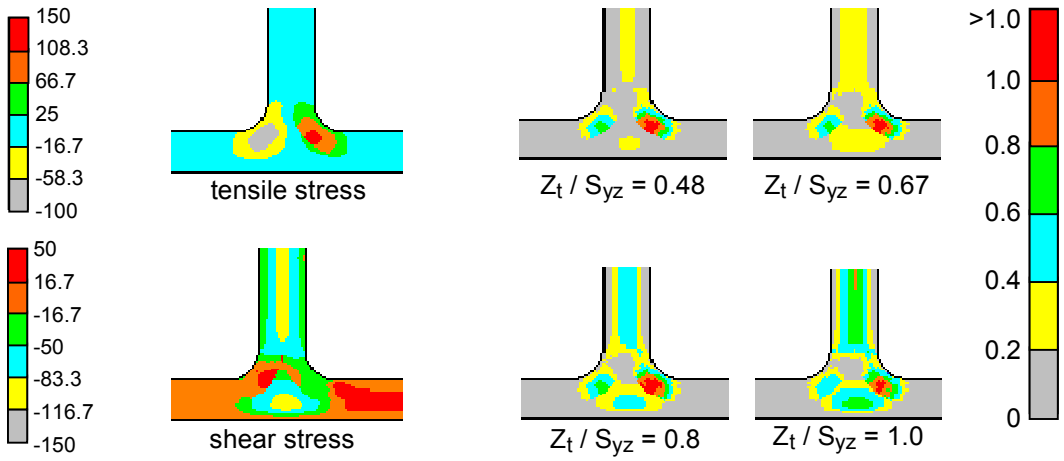

Figure 3.12: (a) Antisymmetric model through-thickness tensile and shear stress (b) Effect of Z_t / S_{yz} on the failure index at first failure

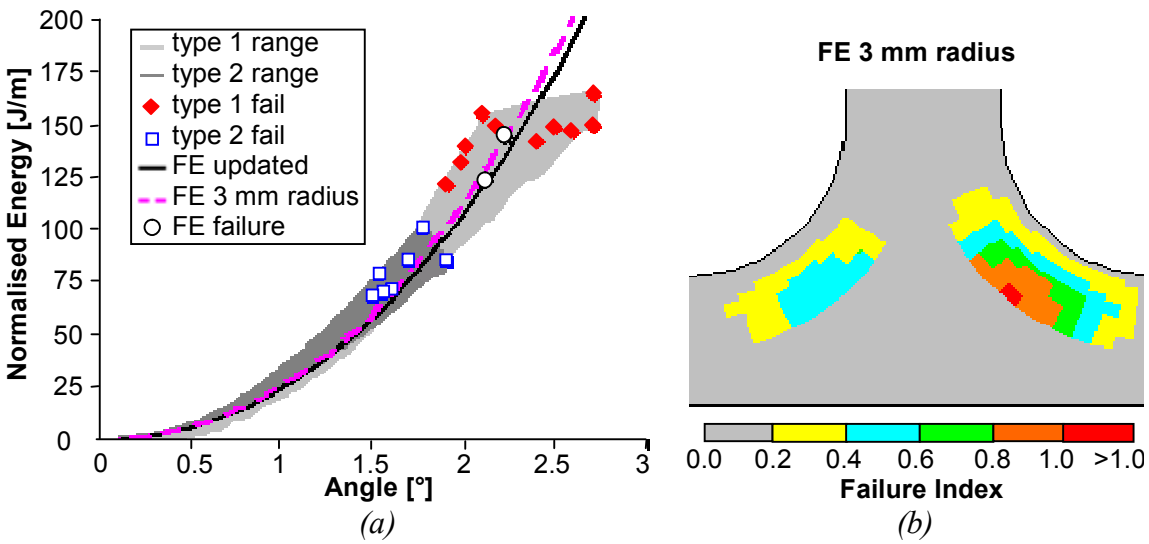

Figure 3.13: Antisymmetric specimen with 2 mm (updated) and 3 mm inner bend radius (a) Normalised applied energy versus loading angle (b) Failure index at first failure

3.4 Discussion

The large amount of experimental scatter compromised the comparison between the FE models and the experimental data, and was caused by a number of factors. Firstly, there was significant manufacturing variation in the specimens, which was evident in images of the test as differences in the bend radius, surface finish, geometrical symmetry, excess resin, and may also have included variation in void content. As the specimens were very thin, even small variations in geometry or material parameters would not be "averaged out" as for large specimens, and the behaviour would be considerably different. This would account for the situation in which nominally identical specimens gave different failure mechanisms.

There were also indications of irregularities with the boundary conditions, which included the clamps being of unequal geometry, not being tightened consistently, and not clamping the specimen enough to prevent slipping at high loads. The thin specimens would have been highly sensitive to boundary condition changes due to the relatively large unclamped region, which is reflected in the large variability in stiffness seen for both test rigs. Additionally, there may have been problems with the setup of the test rigs themselves, such as lateral movement allowed in the loading piston, fixtures not being parallel, or other energy absorbing mechanisms in the panel that would have caused the specimens to fail at higher loads than predicted in the FE models.

The material parameters were shown to have the most significant effect on the failure predictions. This is especially relevant as failure predictions were mostly dependent on the through-thickness tensile strength, which is a difficult parameter to obtain experimentally (Feih 2002). There are no standardised test methods for directly determining Z_t, and whilst some authors have proposed methods for determining through-thickness strengths (see for example Wisnom, Hill and Jones (1998)), these tests were not conducted within the COCOMAT project. For transverse tensile strength, standardised tests for Y_t typically show a degree of variance in the results. In the material characterisation tests for Y_t considered in this study, a variance of up to ±11% was seen in tests on the same material in the same laboratory and tests on the same material in all laboratories showed a variance of 27%. This highlights the difficulty in measuring the transverse tensile strength. As demonstrated, the application of this type of variance has a considerable effect on the failure predictions, which emphasises the necessity of taking material parameter variation into account in strength-based failure analysis. Though the assumption of transverse isotropy is common to obtain through-thickness properties, the accuracy of this assumption for this case remains largely uncertain.

Though the specimens failed within a large range of applied energies and in different failure modes, the failure values predicted using the approach were within the scatter band and were generally conservative. The location of delamination failure within the specimen also showed good agreement with the experiment for type 1 failures, though the strength approach was not able to determine the exact delamination interface. This is due to the fact that the approach considers stresses within the ply instead of between plies, and that the delamination strength values from characterisation tests may be better considered as laminate, instead of ply, properties.

The occurrence of type 2 stiffener failure in the antisymmetric tests was cause for concern as it corresponded to lower failure energies than type 1, and indicates that through-thickness shear became the dominant stress component for these tests. Whilst the reason for this type of failure is unclear, delamination in the middle of the stiffener under through-thickness shear is not a failure mechanism that is typically observed for skin-stiffened panel designs, and may be due to the particular test rig, specimen design or manufacturing process. Similarly, the strength approach could not predict the type 1 failures for the antisymmetric tests that involved only the outermost +45°/0° interface, as according to the FE model this was not a high stress region. This type of failure may have been due to a manufacturing variation such as a local defect in the bend radius or variation in the bend geometry.

The approach developed in this chapter will be extended in later chapters for the analysis of larger, more complex structures. This will involve using a global-local approach, where the complete structure is first analysed with a model based on shell elements to provide the ‘global’ displacement field, which is then used to input displacement boundary conditions onto a ‘local’ model. Further detail on this approach is given in Chapter 5, which includes a discussion on the mesh density, not investigated in this chapter, and the applicability of the ply thickness mesh refinement used. The application of the global-local approach to larger and more complex structures is given in Chapter 7.

It is important to note the limitations of investigating delamination initiation using 2D specimens. The T-section tests described in this chapter only consider loading within the cross-sectional plane, and do not incorporate any out-of-plane loads corresponding to the axial direction in a stiffened panel. Some authors, such as Meeks, Greenhalgh and Falzon (2005) have noted the 3D nature of the skin-stiffener debonding process, where axial compressive loading is significant and damage growth in the axial direction is possible. Whilst these

considerations are more relevant for capturing damage growth than for predicting damage initiation, they do highlight the necessity of taking 3D loadings into account in order to accurately capture all damage mechanisms. The criterion used to predict delamination in this work, the degenerated-Tsai equation, included a parameter for the axial loading component. Though this parameter had negligible influence on the T-section failure predictions due to their 2D nature, it is more relevant for 3D analyses such as the global-local procedure outlined in Chapter 5.

3.5 Conclusion

In this chapter, an approach to predict interlaminar damage failure in skin-stiffener interfaces of postbuckling composite structures was developed. This was based on an experimental investigation into failure mechanisms in skin-stiffener interfaces, and a numerical study that monitored a strength-based delamination criterion in 2D models.

In the experimental investigation, T-section specimens were formed by cutting thin strips consisting of a skin and single stiffener from a large stiffened panel. Two separate test rigs were developed, which aimed to simulate the symmetric and antisymmetric loads on skin-stiffener interfaces in a postbuckling panel. The specimens were loaded until failure in both tests rigs, and failure was characterised by delamination initiation leading to immediate collapse of the specimens. For the symmetric tests, the dominant failure mode was failure in the skin-stiffener junction bend, whilst for the antisymmetric tests in addition to failures in the bend a number of specimens also showed delaminations in the stiffener.

In the numerical analyses, 2D generalised plane strain FE models were analysed in Marc, and a user subroutine was written to apply a strength criterion for the prediction of delamination failure. The strength-based criterion was able to predict the failure of the specimens in the majority of cases, within the relatively large experimental uncertainties associated with the test results and the strength data used in the model. Further parametric investigations showed that the specimens were sensitive to a range of factors, including material strengths, geometrical variations, loading rig displacements and clamping friction, and that for the most part the scatter in results could be replicated by modifications to these parameters. The strength-based criterion used in this work will be extended to a global-local analysis approach that will use a global 3D shell model to input displacement boundary conditions on a local cross-section model, for application to large fuselage-representative structures.

CHAPTER 4

INTERLAMINAR DAMAGE PROPAGATION

While the previous chapter dealt with the prediction of interlaminar damage from an intact structure, in this chapter a degradation model developed to capture the growth of a pre-existing damage region is presented. The interlaminar damage degradation model was implemented in Marc via user-defined MPCs to control the connection of two shell element layers. Fracture mechanics calculations were performed using VCCT and used to control the failure of the MPCs. Gap elements with a user-defined orientation were also included to prevent penetration of the shell layers. The method for crack propagation was studied extensively, where it was found that a simple fail-release approach led to conservative results, and a novel modification method was developed and shown to give more accurate estimations of the strain energy release rate. The degradation model was validated using experimental results of fracture mechanics characterisation tests for mode I, II and mixed-mode I-II. Investigations were made to study the accuracy of the fracture mechanics calculation, which included an analysis of mode III specimens and studies into the accuracy of the VCCT [3, 4].

4.1 Introduction

As described in detail in Chapter 2, for composite stiffened structures in compression one of the most critical damage mechanisms leading to structural collapse is detachment of the skin and stiffener, typically initiated at a stiffener flange edge. In co-cured stiffened panels this detachment is caused by delamination growth at or near the skin-stiffener interface, and in secondary bonded panels usually involves adhesive debonding between the skin and stiffener in addition to delamination. The phenomenon of skin-stiffener separation can be considered analogous to that of interlaminar cracking, for which the use of fracture mechanics to predict

---

[3] Orifici, AC, Thomson, RS, Degenhardt, R, Bisagni, C & Bayandor, J 2007, 'Development of a finite element methodology for the propagation of delaminations in composite structures', *Mechanics of Composite Materials*, vol. 43, no. 1, pp. 9-28.

[4] Orifici, AC, Thomson, RS, Degenhardt, R, Büsing, S & Bayandor, J 2007, 'Development of a finite element methodology for modelling mixed-mode delamination growth in composite structures', in *12th Australian International Aerospace Congress*, Melbourne, Australia, 19-22 March.

crack growth has become common practice over the past two decades (O'Brien 1982; O'Brien 1998). This analogy is directly applicable between lamina in co-cured stiffened panels and is an approximation in the case of the adhesive layer in secondary bonded panels. In fracture mechanics analysis, the strain energy release rate, *G*, is compared to the interlaminar fracture toughness, G_C, to determine the onset of damage propagation. The components of *G* in the three crack opening modes are usually applied in single-mode criteria or combined in a mixed-mode criterion to determine the onset of propagation, and these generally require curve-fitting parameters taken from experimental testing.

The Virtual Crack Closure Technique (VCCT) is one of the most commonly applied fracture mechanics methods for determining the components of *G* along a crack front. The VCCT approach was proposed by Rybicki and Kanninen (1977) and is based on two assumptions: 1) Irwin's assumption that the energy released in crack growth is equal to the work required to close the crack to its original length; and, 2) that crack growth does not significantly alter the state at the crack tip. The use of VCCT is advantageous as it allows the strain energy release rates to be determined with simple equations from a single finite element analysis. Numerous researchers have applied VCCT to analyse the crack growth properties of pre-existing interlaminar damage in a range of structures, including fracture mechanics test specimens (Krueger, König & Schneider 1993; Li et al. 1997), bonded joints (Wahab 2000; Qin & Dzenis 2001), and both co-cured and secondary bonded skin-stiffener interfaces (Wang & Raju 1996; Li, O'Brien & Rousseau 1997; Johnson, Butkus & Valentin 1998).

In order to accurately represent interlaminar damage growth in composites, an approach is required for increasing the debonded area during the analysis. As discussed in Chapter 2, to date VCCT has been limited in this respect due to the requirement of a fine mesh of the order of the ply thickness (Krueger 2002) and the need for complicated algorithms to monitor the shape of the crack front. Cohesive elements offer an alternative approach for modelling skin-stiffener separation, and have the advantage of incorporating initiation and propagation of debonding (Mi et al. 1998; Camanho & Dávila 2002). However, as mentioned in Chapter 2, cohesive elements can become prohibitively inaccurate when larger mesh sizes are used, limiting their application to large structures. Furthermore, the standard cohesive element formulation cannot differentiate between mode II and III directions, and in general the exact location of the crack front can be difficult to define. So, in spite of its disadvantages, the VCCT approach remains attractive for application into crack growth analysis as it provides

information on the exact nature of the crack front and crack growth mechanisms, and is expected to retain an acceptable degree of accuracy with larger mesh sizes.

4.2 Model Development

4.2.1 Modelling Approach

A modelling approach was developed for the separation of two composite layers, and is summarised in Figure 4.1. In this approach, two layers of shell elements were identically meshed and connected with user-defined MPCs. The shell layers were nominally coincident, though separated by a distance of 0.002 mm in order to differentiate between opening and closing tying forces in the MPCs. The distance of 0.002 mm was a compromise between using extremely small values and maintaining precision in floating-point calculations, and was validated as having negligible effect on solution accuracy in separate FE analyses. The nodes of the shell elements were offset from the element mid-plane to the interface between the two shells using "dummy" or nominally zero-stiffness layers, shown in Figure 4.2. Placing the nodes at this interface obviated the requirement for complicated constraint equations that would have been necessary for nodes modelled at the shell mid-planes. The use of dummy layers avoided the use of plate offsets, which can give inaccurate results in geometric nonlinear analyses. However, errors were introduced in the interlaminar shear distribution as shown in Figure 4.3, though as the magnitude of this error was proportional to the dummy layer thickness (Yap et al. 2004) it was not expected to be significant. All FE models applied in this chapter were analysed with Marc v2005r3, and pre- and post-processed with MSC.Mentat (*MSC.Marc and MSC.Mentat User Manuals Version 2005r3* 2006).

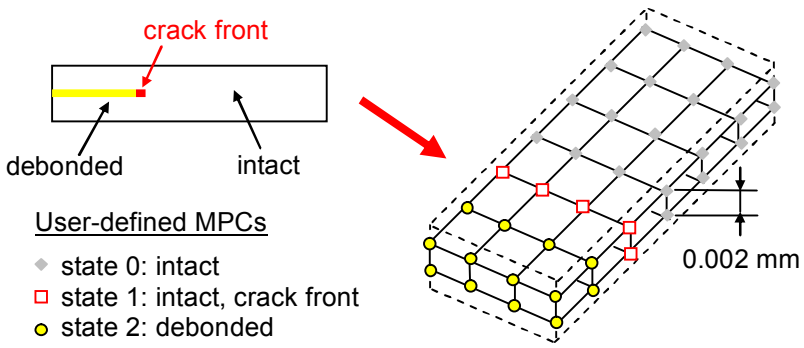

Figure 4.1: DCB modelling with user-defined MPCs

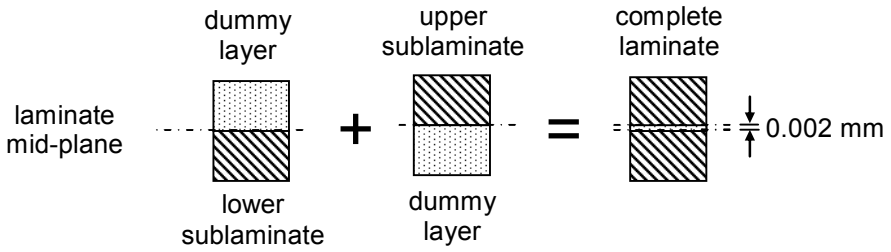

Figure 4.2: Laminate definition with dummy layers shown

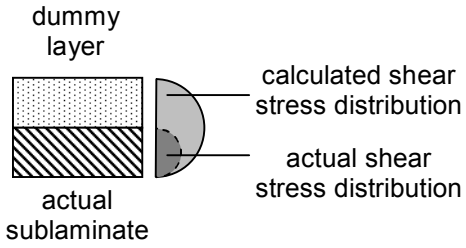

Figure 4.3: Error in interlaminar shear stress distribution due to zero-stiffness layers

Each user-defined MPC acted on a node pair of one node from each shell layer, with the lower node of each pair arbitrarily selected as the master node. The MPCs were given one of three "states", in order to represent the different constraint conditions within the structure. State 0 was for MPCs in the intact region, state 1 for MPCs in the intact region but on the crack front or border between intact and debonded regions, and state 2 for MPCs in the debonded region. Intact MPCs (states 0 and 1) applied a displacement constraint and debonded MPCs (state 2) applied no constraint between the two nodes. Note that only the displacements and not the rotations of the nodes were constrained, in order to maintain the correct bending of the separate shell layers, especially in the region of the crack tip. This constraint condition was validated with separate FE models of bending plates containing a debonded region, and is also in agreement with FE analysis and recommendations of other researchers (Wang & Raju 1996; Krueger 2002).

User subroutines were written to control the state of the MPCs in order to increase the debonded area during an analysis. The user subroutines were written in Fortran, and implemented in the UEDINC and UFORMSN subroutines provided in Marc. Both developed user subroutines performed functions dependent on the state of each MPC, and these were kept in an internal variable called a common block. The interaction of the two user subroutines within a nonlinear analysis increment is illustrated in Figure 4.4.

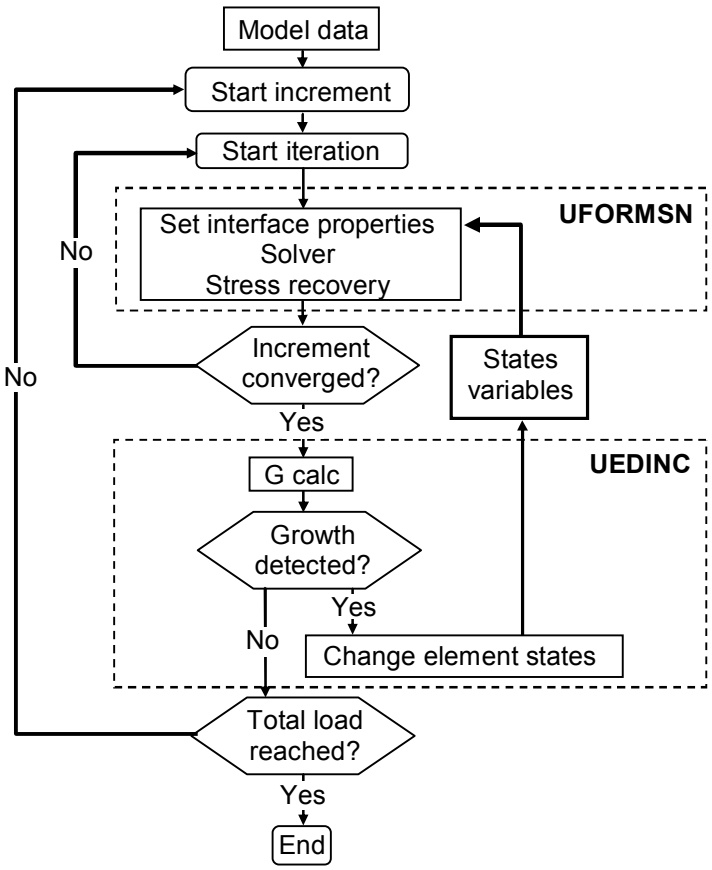

Figure 4.4: Nonlinear analysis flow with user subroutines for degradation modelling

The UEDINC user subroutine is a dummy routine provided in Marc that is called at the end of every increment in a nonlinear analysis. With reference to Figure 4.4, the developed UEDINC subroutine performed a loop over all user-defined MPCs to calculate the strain energy release rates at all MPCs on the debond front (state 1) and assessed whether the interface fracture toughness had been exceeded. A separate loop was then used to change the failing MPCs to debonded (state 2) and to change the corresponding MPCs for the new crack front. The strain energy release rate calculation was carried out using VCCT equations described in the following section.

The UFORMSN subroutine is provided within Marc to allow the definition of a user-defined MPC. The subroutine is called several times in every iteration for each user-defined MPC, and is used to provide the constraint matrix for the calling MPC. The constraint matrix is the matrix that relates the degrees of freedom of the slave node to the master node in the MPC node pair. In the developed UFORMSN subroutine the internal states variable was accessed, and the MPC properties were set to either intact for MPC states 0 and 1, or debonded for MPC state 2.

Additionally, gap elements were included in the interface layer, and were modelled between the same two nodes as the MPC. The gap elements were necessary in the interface layer in order to prevent physically impermissible penetration of the two sublaminates. A contact definition could not be used between the two sublaminate surfaces, as it is not possible in Marc to define a node that is subject to both tying and contact restraints, regardless of whether the two constraints are applied at different stages in the analysis. The gap element options in Marc allow for the definition of a "True Distance" gap, to maintain a minimum gap distance between two nodes, which in this work was set to 0.001 mm. The gap direction can be taken as the vector between the two nodes, or be set using the GAPU user subroutine in Marc. Using the default gap direction it is possible for two nodes on separate surfaces to move around each other in such a way that although the gap distance is maintained, the two surfaces pass through each other. In order to prevent this, a subroutine was written for the GAPU routine, which finds the shell element associated with each gap element, and then forms the shell normal direction using the updated nodal coordinates of the shell nodes. It should be noted that the GAPU subroutine is called in the Marc analysis procedure before the nodal coordinates have been updated with the displacements of the current increment, so that in the developed GAPU subroutine the gap direction is formed using displacements of the previous increment. However, as the increment sizes were generally very small it is not anticipated that this caused any significant errors in the contact definition.

4.2.2 Strain Energy Release Rates

The Virtual Crack Closure Technique is based on the Two-Step VCCT or Crack Closure Method (CCM). In CCM crack growth is analysed with two separate finite element analyses before and after crack extension, step 1 and 2 as shown in Figure 4.5 for the 2D case. CCM is based on Irwin's crack closure integral (Irwin 1958), which assumes that the energy released in crack extension is equal to the work required to close it again. From Figure 4.5, the force vector, **F**, holding the crack together is taken from step 1, and the displacement vector, $\boldsymbol{\delta}_u - \boldsymbol{\delta}_l$, between the upper and lower nodes upon crack extension is taken from step 2. The energy release rate is calculated as the energy released (the work done in closing) divided by the area of crack surface formed, ΔA. This area is the new crack surface area created as a result of the release of the crack node from step 1 to step 2. In the 2D example of Figure 4.5, ΔA is equal to $\Delta a \cdot 1$, or the crack growth length multiplied by a unit width, but generally this does not apply and the crack growth area must be determined. The equation for $\Delta\mathbf{G}$ or vector change in strain energy release rate is given by

$$\Delta \mathbf{G} = \tfrac{1}{2}\mathbf{F}\left(\boldsymbol{\delta}_u - \boldsymbol{\delta}_l\right)/\Delta A\,. \tag{4.1}$$

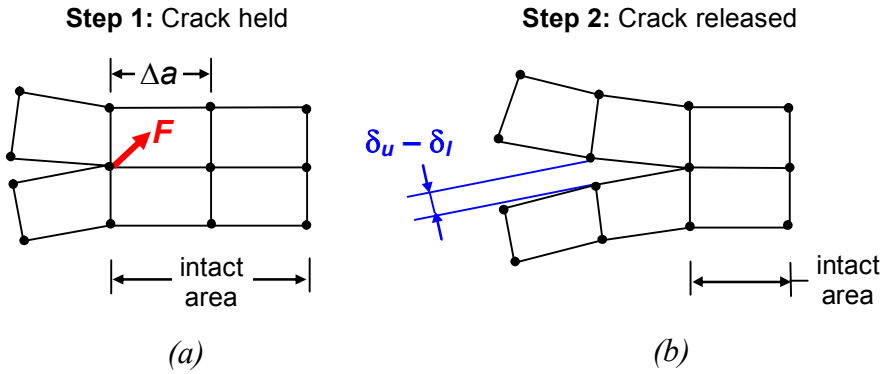

Figure 4.5: Crack closure method: (a) Step 1. Crack closed (b) Step 2. Crack extended

VCCT is based on the same assumption as CCM of Irwin's crack closure integral. Additionally, it is assumed that crack growth does not significantly alter the state at the crack tip, that is, the crack grows in a self-similar manner. This means that the displacements ahead of the crack tip in step 1 can be assumed to be equal to the displacements that will occur upon crack extension. This allows the calculation to be performed in a single FE analysis, which is particularly relevant here as the calculation is to be included as part of a propagation analysis.

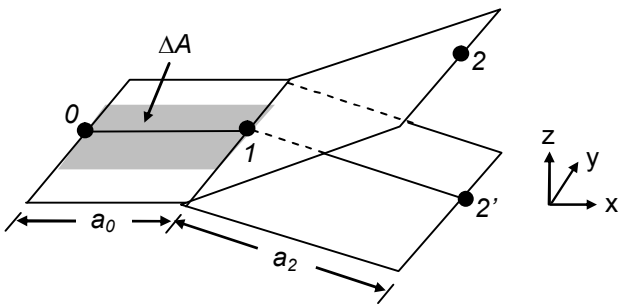

Figure 4.6: VCCT model with arbitrary rectangular shell elements

Figure 4.6 shows an example FE model for VCCT created using the proposed modelling approach, with rectangular shell elements of arbitrary length and width. In Figure 4.6, the upper and lower shell layers in the intact region are overlapping and are indistinguishable. For this type of model the VCCT equations needed to account for changes in element length in all directions. This required the correct crack surface area to be found using the appropriate nodal coordinates. Additionally, the displacements at the node ahead of the crack front were adjusted to account for changes in element lengths behind and in front of the crack front. This was done using linear interpolation, as suggested by Krueger (2002), so that the VCCT equations for arbitrary shell elements are given by (Wang & Raju 1996; Krueger 2002)

$$G_I = -\frac{1}{2}\frac{1}{\Delta A}F_{z1}(w_2 - w_{2'})\frac{a_0}{a_2},$$

$$G_{II} = -\frac{1}{2}\frac{1}{\Delta A}F_{x1}(u_2 - u_{2'})\frac{a_0}{a_2}, \qquad (4.2)$$

$$G_{III} = -\frac{1}{2}\frac{1}{\Delta A}F_{y1}(v_2 - v_{2'})\frac{a_0}{a_2},$$

where with reference to Figure 4.6: G_I, G_{II}, G_{III} are strain energy release rates in local mode I, II and III directions; ΔA is the virtual crack growth area; $\{F_x, F_y, F_z\}$, and $\{u, v, w\}$ are forces and displacements in the local x, y and z directions; a are distances from the crack front MPC; subscripts 0, 1 and 2 refer to values taken from MPCs of states intact, crack front and debonded; and, 2' is the lower node of the MPC in the debonded region. These equations are for shell elements constrained to each other only by displacements with rotations left free, and as such do not include any rotations or tying moments. This is in accordance with the constraint condition applied between the two sublaminates, which was explained previously.

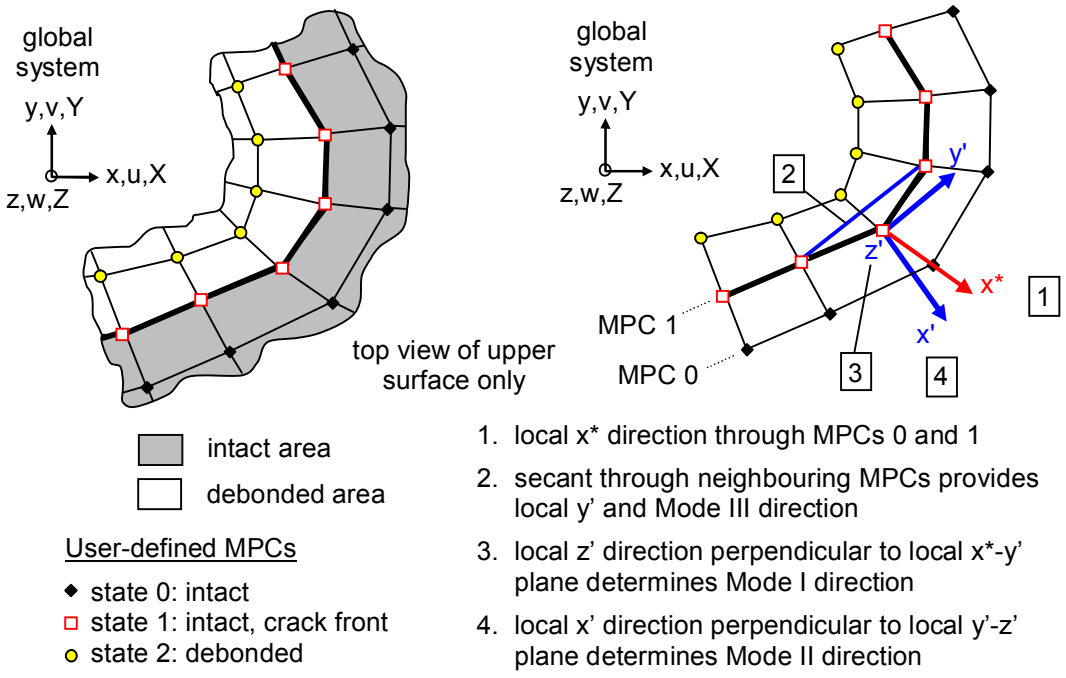

Figure 4.7: Determining the local crack front coordinate system for an arbitrary crack front, after Krueger (2002)

The local crack front directions were also required in order to apply VCCT to an arbitrary crack front. The method for determining the local crack front coordinate system was adapted from Krueger (2002), and is illustrated in Figure 4.7. This approach was based on locating the neighbouring nodes on either side of the crack front, which were used to form the local mode

III direction and to determine the local mode I and II directions. Using the local crack front coordinate system the forces and displacements were resolved into their correct mode I, II and III components, to reflect the true crack opening mechanisms acting locally on the crack front.

To incorporate the VCCT approach into a propagation analysis it was necessary to account for the wide variety of crack front shapes possible, shown in Figure 4.8. With reference to Figure 4.8, any crack front shape or crack type was defined as a crack front MPC in the centre of a maximum of four 4-noded shell elements. So any crack front MPC could have a maximum of four adjacent "side" MPCs and four "diagonal" MPCs. Crack types were classified according to the status of the adjacent side MPCs, and whether the MPC was on a structural edge. It was assumed that triangular elements were not used.

For each of the different crack front shapes it was necessary to define a set of displacements and areas for the VCCT calculation. The approach taken was based on applying the VCCT assumption of self-similar crack growth to the local crack front. The local crack front was defined as the central MPC with a maximum of two adjacent crack front MPCs depending on whether the central MPC was on a structural edge. Based on the propagation of the local crack front shape, the crack growth area was calculated and displacements were taken from the most appropriate of the surrounding MPCs. This is summarised in Figure 4.8, where in the "VCCT MPCs" column, the "displacements" MPC is the one from which displacements were taken, and the "new location" MPC is the one to which the central failing MPC was grown. This type of "locally self-similar" configuration still requires the global VCCT assumption that at all points on the crack front, crack opening displacements can be taken from the same increment as crack closing forces. The only exception to the locally self-similar configuration was for crack growth at a convex corner, crack type 10 in Figure 4.8, where the area was based on the growth of only the central failing MPC.

In order to determine the onset of failure, three approaches were implemented: single-mode failure criteria, and two mixed-mode failure criteria. These criteria are given by

Single mode:
$$\frac{G_I}{G_{IC}} = f_I, \quad \frac{G_{II}}{G_{IIC}} = f_{II}, \quad \frac{G_{III}}{G_{IIIC}} = f_{III}, \tag{4.3}$$

Power law:
$$\left(G_I/G_{IC}\right)^m + \left(G_{II}/G_{IIC}\right)^n + \left(G_{III}/G_{IIIC}\right)^p = f, \tag{4.4}$$

B-K:
$$\frac{\left(G_I + G_{II} + G_{III}\right)}{\left(G_{IC} + \left(G_{IIC} - G_{IC}\right)\left[\left(G_{II} + G_{III}\right)/\left(G_I + G_{II} + G_{III}\right)\right]^\eta\right)} = f. \tag{4.5}$$

Crack Type	Side MPCs	Pattern	VCCT MPCs	Area
1	1 intact 1 debond	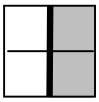	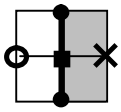	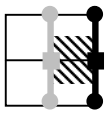
2	1 intact 2 debond		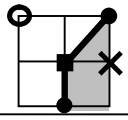	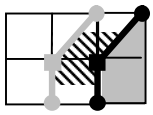
3	1 intact 3 debond	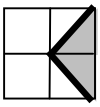	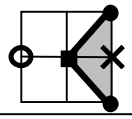	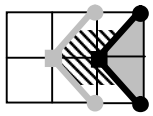
4	2 intact 1 debond		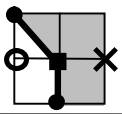	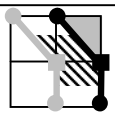
5	2 intact 2 debond	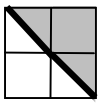	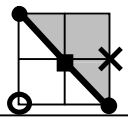	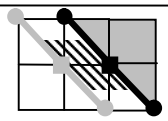
6	3 intact 1 debond	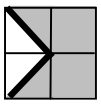	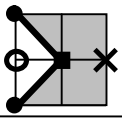	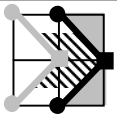
7	1 intact 1 debond (on edge)	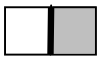	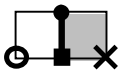	
8	1 intact 2 debond (on edge)		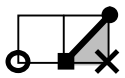	
9	2 intact 1 debond (on edge)	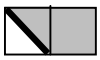	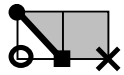	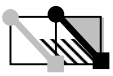
10*	0 intact 2 debond	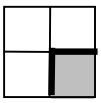	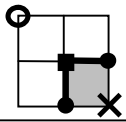	
11	2 intact 0 debond	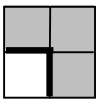	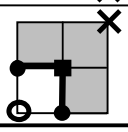	

* Non self-similar crack growth assumption

Side MPCs: MPCs directly adjacent to central crack front MPC (■)

Pattern: intact; debonded; crack front

VCCT MPCs: new location; displacements; local crack front

Area: crack area; old crack front; new crack front

Figure 4.8: Crack front pattern, VCCT MPCs and crack growth area for each crack type

The single mode failure criteria compare the strain energy release rate to the material fracture toughness in each of the three crack opening modes, and express this as a failure index, $f_{I,II,III}$. The mixed-mode criteria implemented were the Power law and B-K (Benzeggagh &

Kenane 1996) criteria, which take into account all crack opening modes and combines them into a failure index *f*. For all criteria, failure is deemed to occur when any failure index reaches 1 or above. The Power law criterion requires three curve-fit parameters, *m*, *n*, and *p*, which are usually given the same value, α, and can be set to represent a linear (α = 1) or a quadratic (α = 2) relationship. The B-K criterion requires one curve-fit parameter, η. Standards exist for experimental characterisation of mixed mode I-mode II fracture toughness, from which it is possible to extract the curve-fit parameters to some extent, though currently there are no test configurations in literature for mixed-modes I-III or II-III.

4.2.3 Propagation Modelling

The propagation method is the way in which the crack front was advanced once the crack growth criteria were satisfied. During the degradation model development, it was found that the propagation method had a significant influence on solution accuracy and crack growth behaviour. Despite the VCCT approach being used extensively for almost thirty years, the relationship between propagation method and solution accuracy, especially with reference to the VCCT assumption of self-similarity, has not previously been studied. In this work, four different propagation methods were investigated, in order to compare the sensitivity of the solution to the choice of propagation approach. These methods are detailed below and shown in Figure 4.9 and Figure 4.10. Note for the following discussion that the VCCT calculation is performed at every crack front MPC, "failure" is where the crack growth criteria have been satisfied at an MPC, and "release" of an MPC is a change to the debonded state 2.

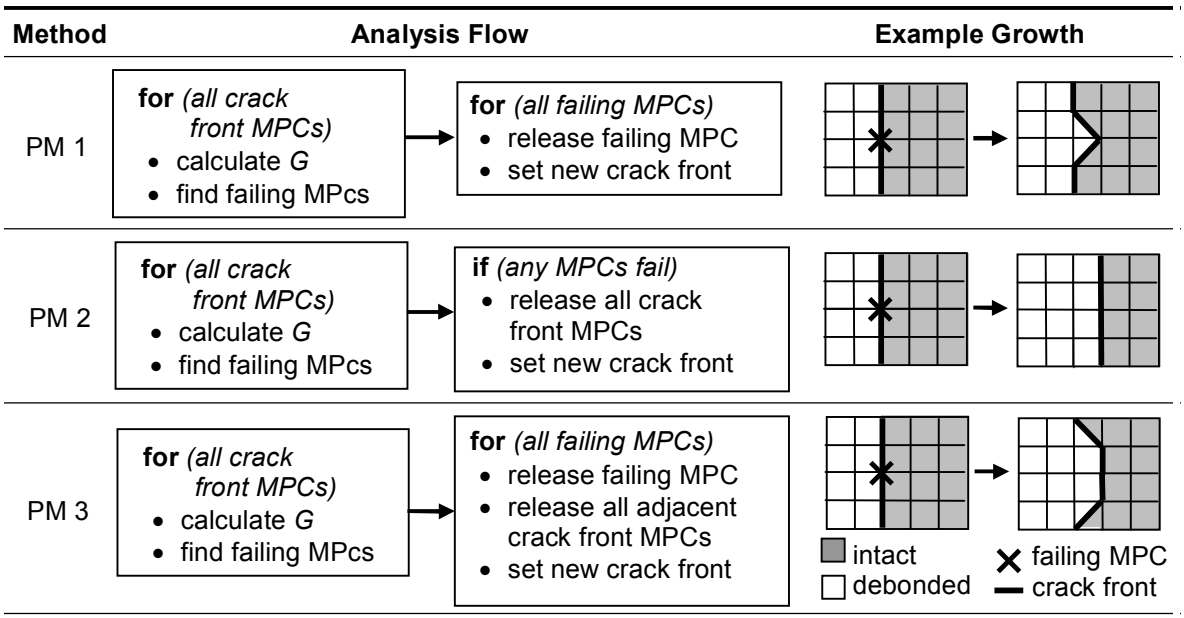

Figure 4.9: Analysis flow and example growth for propagation methods 1, 2 and 3

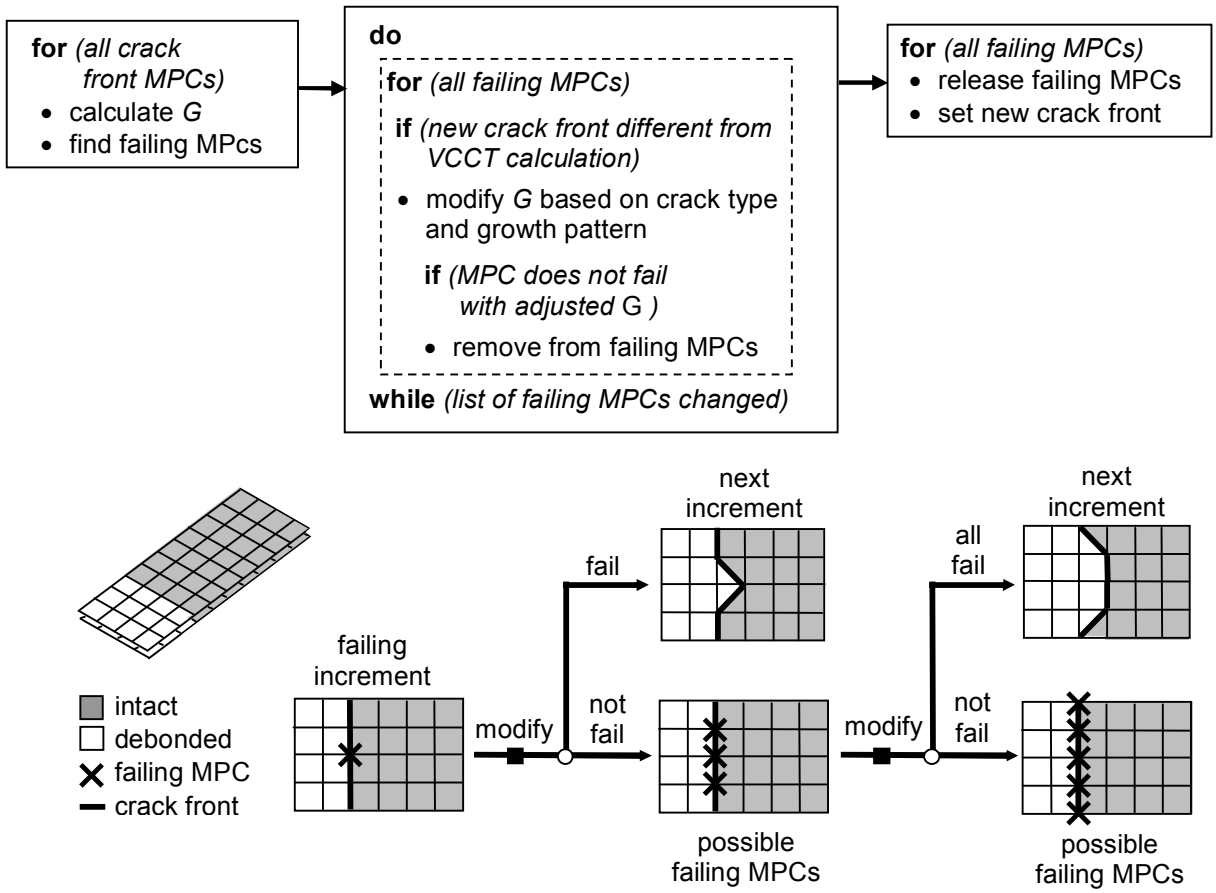

Figure 4.10: Analysis flow and several example growths for propagation method 4

Propagation Method 1 (PM 1) was the simplest approach, where each failing MPC was released, and the adjacent intact MPCs modified to become crack front MPCs. This is the approach that has recently been implemented in commercial FE codes, such as the "VCCT for ABAQUS" technology within Abaqus. However, as part of the development in this work, it was found that this approach could lead to conservative results under some loading conditions. This was due to the fact that as a result of the crack propagation, the assumption of similarity before and after crack growth could be violated. An example of this is illustrated in Figure 4.9, for a simplified double cantilever beam specimen with large elements. For a DCB specimen under a peeling load, at some point in the analysis failure is detected at only the centre node. This is quite possible, as it is known both theoretically and experimentally that unidirectional DCB specimens develop the highest strain energy release rates in the centre of the crack front, due to anticlastic curvature (Davidson 1990; Brunner 2000). Applying PM 1, this MPC is released, so that the new crack front is as shown in Figure 4.9. However, this type of crack growth is different from the self-similar growth assumed in the VCCT calculation. So, the displacements that result inside the new crack area due to an MPC released in this manner are much less than that in the previous increment that was used for the VCCT

calculation. This means that the energy released in crack growth would be much less than that calculated using VCCT and would probably fall under the threshold fracture toughness, in which case the crack growth should not have occurred.

Propagation Method 2 (PM 2) enforced global crack growth, in order to maintain the assumption of self-similar growth. Upon failure at any MPC along the crack front, the entire crack front was grown, that is, all current crack front nodes were released and the adjacent intact MPCs changed to crack front MPCs. This ensured that for the failing MPC, the states of the crack tip before and after crack growth were very similar, which upheld the VCCT assumption. This approach was conservative as it forced crack growth on MPCs that had not failed, which underestimated the fracture toughness of the material. However, for single-mode fracture tests, the strain energy release rates are nearly constant for the majority of the crack front, with the exception of the edges, at which edge effects become significant (Davidson 1990). So, in spite of its conservatism PM 2 was still applicable and was valuable for comparison with the other methods.

Propagation Method 3 (PM 3) enforced local crack growth, as an approximation in maintaining the assumption of self-similar growth. Any failing MPC was released, and additionally the adjacent crack front nodes that made up the local crack front shape were also released, irrespective of whether these nodes had also failed themselves. This ensured that the local crack front shape was preserved, which assumed that the propagation of only the local crack front shape was enough to maintain similarity in the crack opening displacements before and after crack growth. As with PM 2, this approach was conservative as the crack front was grown at locations at which the fracture toughness was not passed, so that a greater crack area was created than that which the material should have been able to withstand.

Propagation Method 4 (PM 4) involved the addition of a separate loop into the fracture mechanics calculation, shown in Figure 4.10. This additional loop was run between the strain energy release rate calculation and the MPC release, and assessed whether for each failing MPC the energy released in crack growth would correspond to that calculated using VCCT. This was based on an assessment of the shape of the local crack front to be created in the following increment. So, as in the example given for PM 1, if the local crack front created differed from that for self-similar growth, then the strain energy release rate values were modified to take into account the difference in energy to be released upon crack growth, and the failure criteria were applied again. Further detail on this process is given in the following

paragraph. If the failing MPC was deemed to have failed again considering the actual energy to be released, then the MPC was released in the next increment. However, if the energy to be released no longer satisfied the failure criteria, then this MPC was removed from the list of failing MPCs. After the additional loop was completed, if the list of failing MPCs was changed, the loop was restarted, and all remaining failing MPCs rechecked with the same procedure. When the additional loop was completed with no change to the list of failing MPCs, then the subroutine continued, and released all the required MPCs, or no MPCs if all of the failing MPCs had been removed.

The modifications that were made to the strain energy release rate are given in Figure 4.11, and were the result of considerations for crack growth displacement and area with respect to the difference between the assumptions in the VCCT calculation and the actual crack propagation. For the difference in displacements between the assumed and actual crack propagation, an extensive study of two-step parametric analyses was conducted, similar to CCM steps. The models used in the parametric studies for mode I, II and III crack growth were taken from the validation analyses that are detailed in the following section. Though the parametric studies are summarised in Figure 4.11, a more thorough description of the investigations is given in Appendix A. The modification factors were also investigated in mixed-mode specimens, and the results of these studies are also presented in Appendix A.

From the parametric studies, it was found that for any failing MPC, differences in crack opening displacement between two steps of arbitrary global crack growth could be classified according to only the local crack front shape. The different changes to the local crack front shape were then grouped into growth types according to the number of MPCs in the local crack front being released between increments. From Figure 4.11, growth types 1 and 2 involved release of respectively one, two and three of the local crack front MPCs, with the central failing MPC always released. Based on these growth types, the resultant difference in crack growth area from that assumed in the VCCT calculation was determined, using the assumption that the sizes of all surrounding elements were roughly equal.

As a result of these considerations, an approximate and conservative modification factor f_m was determined for each growth type of each crack front shape, as shown in Figure 4.11. This factor was the value that the strain energy release rates were divided by in order to reflect any difference in released energy as a result of differences in displacement or area caused by a non-assumed growth pattern.

Crack Type	Growth Type I Pattern	f_{m_I}	$f_{m_{II}}$	$f_{m_{III}}$	Growth Type II Pattern	f_{m_I}	$f_{m_{II}}$	$f_{m_{III}}$
1	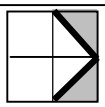	2.5	1.0	1.0 1.5*	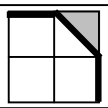	1.5	1.0	1.33 1.0*
2	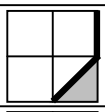	2.0	1.0	1.0	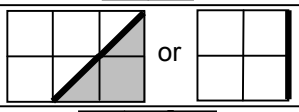	1.0	1.0	1.0
3	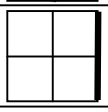	1.5	1.33	1.0		1.33	1.0	1.0
4	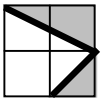	6.0	1.0	2.0	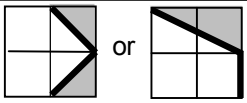	2.0 3.0 +	1.0	1.33
5		6.0	1.33 1.0*	1.5	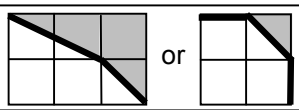	2.0 1.0*	1.0	1.33 1.0 +
6	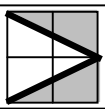	2.0	1.33	2.0	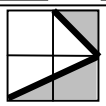	3.0	1.0	1.33 1.0*
7		1.33	1.0	1.5	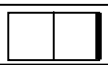	1.0	1.0	1.0
8	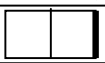	1.33	1.33	1.0		1.0	1.0	1.0
9	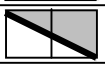	5.0	1.33	1.0	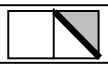	1.0	1.0	1.0
10	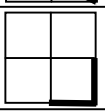	2.0	1.33	1.33		2.0	1.0	1.0
11	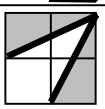	3.0	1.0	4.0 2.0*	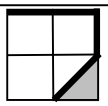	3.0	1.0	1.0

* Choice between values made based on whether crack growth occurs at other MPCs in model
\+ Choice between values made based on which crack front node is released

Pattern: intact debonded crack front

Figure 4.11: PM 4 f_m values, for each crack front type and growth type

4.2.4 Automatic Cut-Backs

Functionality was implemented into the degradation model to allow control over the increment size during the analysis. Two aspects of the crack growth process were monitored in order to ensure an appropriate increment size was used: failure ratio G/G_c and the number of failing MPCs per increment. The failure ratio was determined for each failing MPC, where values greater than one corresponded to the amount of "overshoot" or excess strain energy release rate in the increment. At the end of each increment, the failure ratio of each failing MPC and the number of failing MPCs were compared to pre-set maximum allowables. These pre-set values were stored in an external data file, which is explained in further detail in the following chapter. When the maximum failure ratio or maximum number of failing MPCs

was passed a cut-back, or decrease in increment size, was triggered, using a reduction factor that was also a pre-set variable. Monitoring of the two cut-back criteria could be prevented by setting the pre-set allowables to zero.

The increment size, or time step, was controlled using the UTIMESTEP user subroutine in Marc. This subroutine is a dummy routine that is called after every opportunity in which the time step could have been modified by the Marc solver. In the developed degradation model, the UEDINC subroutine monitored the cut-back criteria at the end of every increment, and used an internal variable to trigger any necessary cut-backs. The UTIMESTEP subroutine monitored this internal variable, and was used to decrease the time step by the pre-set reduction factor. Typical values that were used for the allowables were a maximum failure ratio of 2.0, a maximum number of failing MPCs corresponding to the majority of the crack front, and a reduction factor of 0.5, though these values were problem-specific. An example is given in Figure 4.12 of the output written to the Marc *.out* file upon a time step reduction using the developed UTIMESTEP subroutine. In the example shown, the modification was due to the maximum failure ratio being passed, and this output was slightly modified for cut-backs due to the maximum number of failing MPCs.

```
             failure to converge to tolerance

             increment will be recycled
utimestep:   timestep control activated from uedinc
timestep cut back due to high failure index

             time increment has been changed to   1.00000E-03
             previous time increment              2.00000E-03
             due to user subroutine utimestep

             increment cut-back number      1
```

Figure 4.12: Example output written to .out *file for increment size cut-back using the automatic cut-back functionality*

4.3 Experimental Comparison

In this section, results are presented for the validation of the interlaminar damage degradation model using experimental results for fracture mechanics characterisation tests. This includes comparison with mode I, mode II and mixed-mode I-II tests. For each test series, the experimental results are compared to numerical predictions, and the results are discussed in terms of the capacity of the degradation model to represent the interlaminar damage propagation occurring.

4.3.1 Experimental Results

In the DCB test, shown in Figure 4.13(a), a specimen with a pre-cracked region is pulled apart to generate mode I peeling crack growth. Experimental tests were performed at DLR on DCB specimens in order to determine the mode I fracture toughness of the unidirectional carbon fibre prepreg material IM7/8552 (Kling & Degenhardt 2006) in accordance with the German standard (*Determination of Interlaminar Fracture Toughness Energy - Mode I - G_{IC}* 1996). The specimen details are summarised in Table 4.1 and Figure 4.13(a), where in the material lay-up "//" is used to denote the location of the delamination in the pre-cracked region. Note that in contrast to the completely unidirectional laminate specified in the standard, a multi-directional laminate was used, as multi-directional laminates find far greater application in aerospace design. A quasi-isotropic lay-up was used that was symmetric about a central 0°//0° interface, which ensured that the crack growth occurred at this interface, and avoided problems with variability in characterising off-axis interfaces due to fibre bridging and other effects (Andersons & König 2004). The use of a quasi-isotropic laminate was expected to minimise any additional anticlastic curvature, according to recommendations for testing multi-directional laminates by Davidson (1990).

Nine DCB specimens were manufactured at Aernnova for testing at DLR, with the delamination at the central 0°//0° interface generated using a Teflon insert. Hinged plates were bonded to the delaminated edges to assist with load introduction, which involved the upper hinge being held whilst the lower hinge was pulled down in displacement control. For each test, the applied load and loading displacement were available from the testing machine as output, and were used to determine the experimental mode I fracture toughness. The test procedure involved an initial pre-load cycle to generate a "natural" crack front, and then final loading until the total crack length was approximately 100 mm. The load-displacement results for all tests are given in Figure 4.14(a), where the results for test #7 are highlighted. The results for test #7 were used as the basis for comparison with numerical analyses, as it gave a very good representation of the average of all test results, both in specimen behaviour and the experimental fracture toughness of 243 J/m^2. For specimen #7, crack growth initiated at an applied displacement of approximately 1.5 mm, or 106 N, and the loading was stopped at an applied displacement of around 13.2 mm. At the final applied displacement the crack had grown from an initial length of 49.2 mm to 127.4 mm.

The ENF test, shown in Figure 4.13(b), involves loading the pre-debonded structure in three-point bending, which causes crack growth due to shear forces resulting from the different

flexural behaviour of the upper and lower laminates. Experimental tests were performed at DLR on ENF specimens manufactured at Aernnova, in order to determine the mode II fracture toughness of the unidirectional carbon fibre prepreg material IM7/8552 (Kling & Degenhardt 2006) using the German standard (*Determination of Interlaminar Fracture Toughness Energy - Mode II - G_{IIC}* 1996). In accordance with the standard, the tested specimens from the DCB experiments were re-used, in order to obtain a pre-crack generated in mode I crack opening. All details are given in Table 4.1 and Figure 4.13(b).

Nine ENF specimens were loaded in three-point bending until the onset of crack growth, at which point the test was stopped. For each test, the applied load and loading displacement were available from the testing machine as output, and were used to determine the experimental fracture toughness in mode II. The test procedure involved loading the specimen with the mode I pre-crack in bending until the crack growth onset was determined. There was some scatter in the experimental results, as is typical for ENF testing (Andersons & König 2004), though the structural stiffness of all tests was very close. Though the mode II fracture toughness values varied between 318 J/m^2 and 820 J/m^2, in the middle of this range there were three very close tests results, within a range of only 32 J/m^2. From these, the results for test #2 were very close to the average for the three specimens, and also gave close comparison with the average of all ENF tests, so were subsequently used as the basis for comparison with numerical results. The load-displacement results for all specimens are given in Figure 4.14(b), and the result for specimen #2 is highlighted. For specimen #2, crack growth initiated at an applied displacement of approximately 1.43 mm, or 622 N, and the experimental mode II fracture toughness was 517 J/m^2.

In the MMB test, shown in Figure 4.13(c), an end notched specimen is loaded in three-point bending by a central roller that is connected to an end loading hinge, so that the specimen undergoes simultaneous mode II bending and mode I peeling crack opening. MMB tests were performed at RWTH Aachen University to investigate the mixed-mode I-II properties of the woven fabric prepreg 950-GF3-5H-1000 (Büsing and Reimerdes 2006) using the American standard (*Standard Test Method for Mixed Mode I-Mode II Interlaminar Fracture Toughness of Unidirectional Fiber Reinforced Polymer Matrix Composites* 2001). The proportion of each loading action, the mixed-mode ratio $G_{II} / (G_I + G_{II})$ or G_{II} / G_T, was controlled by the distance between the load application points, known as the lever arm, c. Three mixed-mode loading ratios were tested, 25%, 50% and 75%, with the corresponding lever arm lengths calculated according the standard, and included with the specimen parameters in Table 4.1.

Eighteen MMB specimens were tested, consisting of six tests each for 25%, 50% and 75% nominal mixed-mode ratios. MMB specimens were loaded in three-point bending until increased loading led clearly to a reduction in the reaction load of the specimen, at which point the test was stopped. The applied load and loading displacement output from the testing machine were used to determine the experimental total fracture toughness, which was then split into its components using equations in the testing standard. The experimental results for all tests showed very good agreement at each mixed-mode ratio, both in terms of the structural stiffness and delamination onset load. The results for test specimens #5.5, #4.3 and #3.1 were close to the averages for the 25%, 50% and 75% tests respectively, so were used as the basis for comparison with numerical results. The load-displacement results for the MMB tests are given in Figure 4.15(a), with the results for specimens #5.5, #4.3 and #3.1 highlighted. Based on the tests, the experimental fracture toughness values were used to curve-fit coefficients α and η for the Power law (assuming $m = n = p = \alpha$) and B-K criteria. Previous experimental results for pure mode I and mode II tests conducted at RWTH Aachen University on the same material (Büsing and Reimerdes 2006) were included in the curve-fitting data, and the results are shown in Figure 4.15(b). Note that the experimental mixed-mode ratios for MMB varied slightly from the nominal values.

Table 4.1: Geometry and material details for DCB, ENF and MMB tests, dimensions in mm

	DCB	*ENF*	*MMB*
Length, L	250	100	100
Width	25	25	25
Teflon insert	25 × 25 × 0.02	–	–
Pre-crack, a_o*	50	30	30
MMB lever arm, c	–	–	25%: 77.2 50%: 42.1 75%: 30.0
Material	Unidirectional tape IM7/8552	Unidirectional tape IM7/8552	Woven fabric 950-GF3-5H-1000
Lay-up	$[(0,90,+45,-45)_{2S}$ // $(0,90,+45,-45)_{2S}]$	$[(0,90,+45,-45)_{2S}$ // $(0,90,+45,-45)_{2S}]$	$[0_5$ // $0_5]$
Ply thickness	0.152	0.152	0.35
Total thickness	4.864	4.864	3.5

* Approximate value taken from DCB Test #7

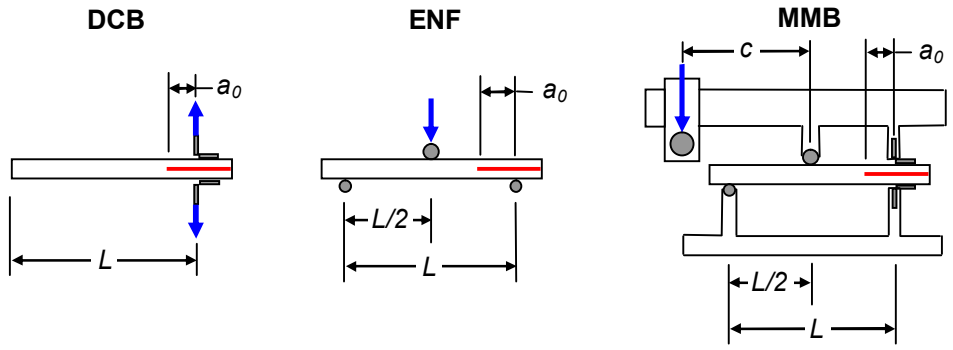

(a) *(b)* *(c)*

Figure 4.13: (a) DCB, (b) ENF and (c) MMB experimental test setups

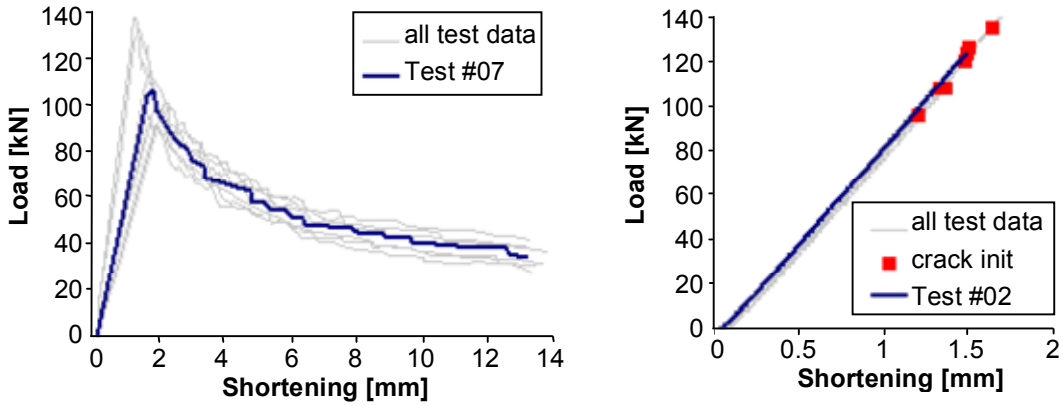

(a) *(b)*

Figure 4.14: Applied load versus displacement (a) DCB tests (b) ENF tests

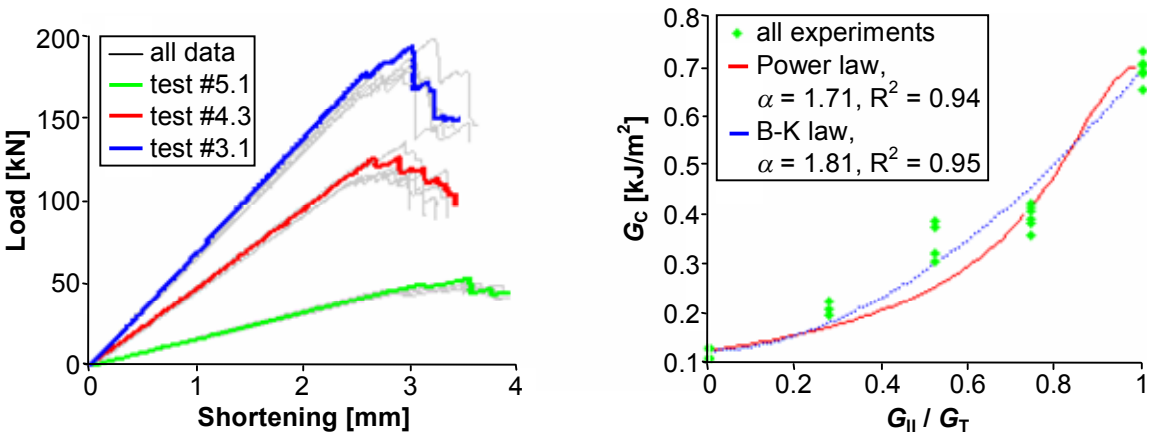

(a) *(b)*

Figure 4.15: (a) Applied load versus displacement, MMB tests (b) Woven fabric 950-GF3-5H-1000, curve-fitting fracture toughness values for mixed-mode failure criteria

4.3.2 Numerical Analysis

Finite element models were generated at four mesh densities, and were characterised according to the element length in the direction of crack growth: 5 mm, 2.5 mm, 1.25 mm and 0.125 mm. The 0.125 mm model was created in accordance with Krueger (2002), in which element lengths of the order of the ply thickness are recommended with VCCT. All models consisted of a pre-crack region of only gap elements between sublaminates, a crack growth region with the user defined MPCs, and the remainder of the structure tied with standard pin-jointed MPCs, as shown in Figure 4.16 for the ENF 2.5 mm model. The length of the crack growth region, or region of user-defined MPCs in which crack could be modelled, varied for each test series, and was based on the crack growth seen in the experiment. All models were based on a regular grid of square elements of the characteristic length, though the 0.125 mm models and some ENF and MMB models used a mesh transition scheme to larger elements after the crack growth region in order to reduce model size. In Figure 4.16 the load and boundary condition (BC) definition for all models is given, and an example of the mesh transition scheme can be seen in the top figure. Note that in Figure 4.16, slight modifications were made to the DCB hinge plate length, ENF specimen length and MMB lever arm distance, in order to match the initial experimental stiffness. This can be considered similar to determining the effective support conditions, and was necessary so that the boundary condition modelling did not affect the comparison of crack growth prediction.

Table 4.2: DCB, ENF and MMB model details

DCB model [mm]	**5**	**2.5**	**1.25**	**0.125**
Nodes	614	1056	3660	10,562
Shell elements	500	936	3460	10,456
User-defined MPCs	132	462	1722	4422
Gap elements	–	–	–	–
ENF model [mm]	**5**	**2.5**	**1.25**	**0.125**
Nodes	612	798	2846	18,698
Shell elements	616	1033	4008	27,515
User-defined MPCs	132	132	525	3417
Gap elements	186	341	1344	8991
MMB model [mm]	**5**	**2.5**	**1.25**	**0.125**
Nodes	466	1660	3638	20,142
Shell elements	537	2057	4298	19,519
User-defined MPCs	132	462	441	3618
Gap elements	162	572	903	402

The DCB tests were given the most extensive analysis treatment, and were used to investigate a range of parameters. The ENF and MMB analyses were based on the conclusions reached from the DCB tests, and so used a reduced set of investigations and were principally focused

on assessing the capability of the degradation model to represent crack growth under the different loading regimes. All models were run using the nonlinear solver in Marc, with a full Newton-Raphson procedure applied and the Marc default tolerance of 0.1 on load residuals. For all tests, the 5 mm, 2.5 mm and 1.25 mm models were run for the full displacement loading, while the 0.125 mm models were only run up to a displacement around 0.1 mm past the crack initiation point to reduce run times.

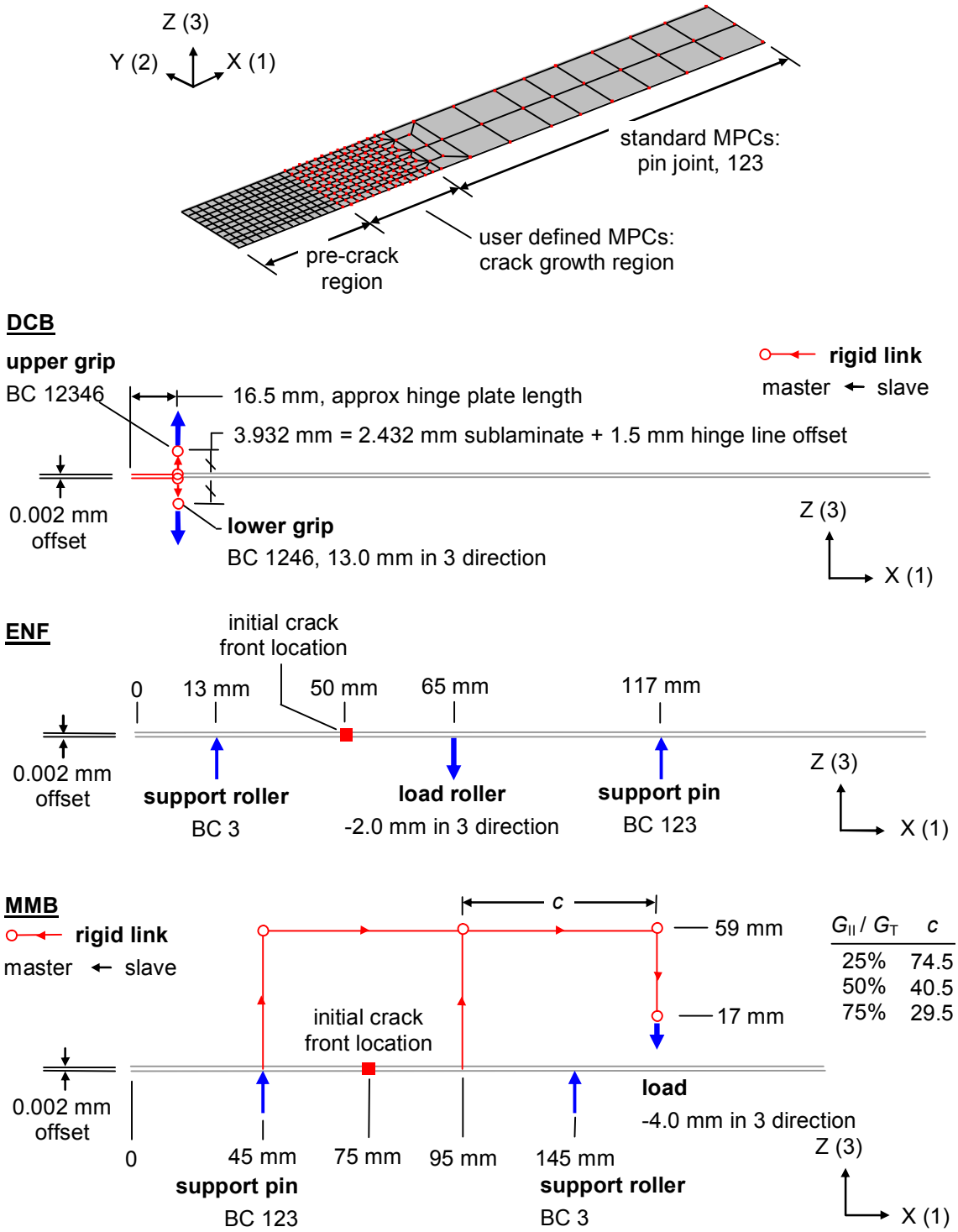

Figure 4.16: DCB, ENF and MMB modelling, ENF 2.5 mm model shown in top figure

For the DCB models, the four mesh density models were each run with the four propagation methods on an Intel 1000 MHz Pentium III CPU, and the single-mode failure criteria given in Equation 4.3 were applied. Analysis results for the DCB tests are presented below, where Figure 4.17 and Figure 4.18 are typical comparative curves for applied load versus displacement, Figure 4.19 is a comparison of the strain energy release rate before any crack growth, and Figure 4.20 illustrates the effect of both mesh density and propagation method on crack progression. Table 4.3 is a summary of all DCB analysis results, where P_{max} is the maximum load reached, a_{max} is the total crack length at 13 mm displacement, and P_{init} is the load at initiation, which is given for 0.125 mm models. Table 4.4 is a summary of all analysis times, where t is the total analysis time, inc is the total number of increments, and t_{inc} is the average time per increment.

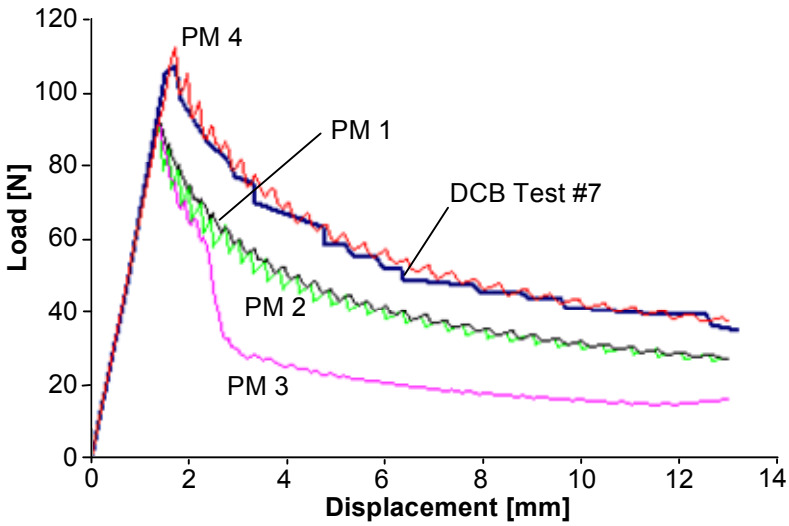

Figure 4.17: Applied load versus displacement, DCB Test #7 and 2.5 mm model with PMs 1-4

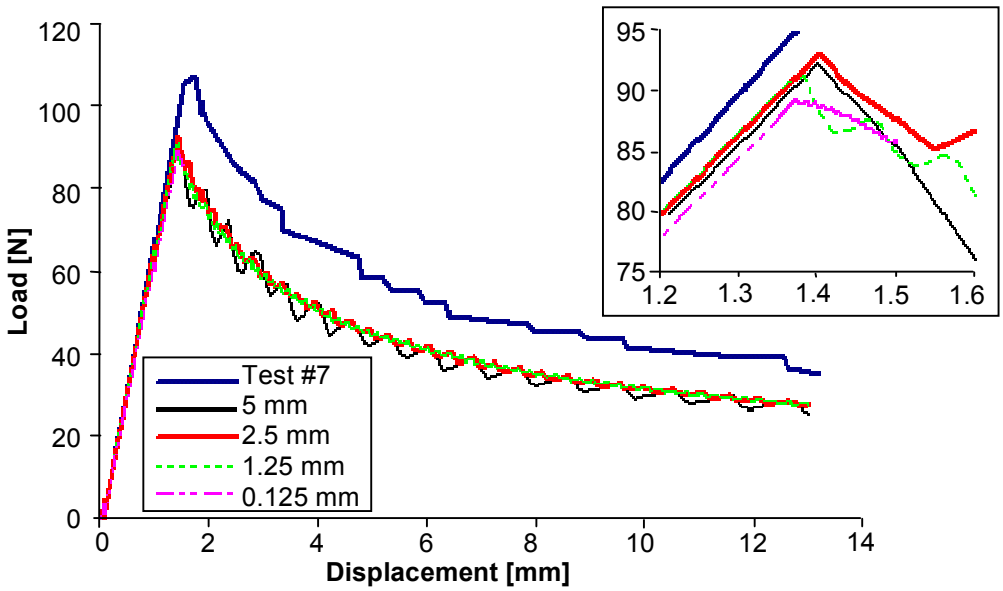

Figure 4.18: Applied load versus displacement, DCB Test #7 and PM 1, all FE models

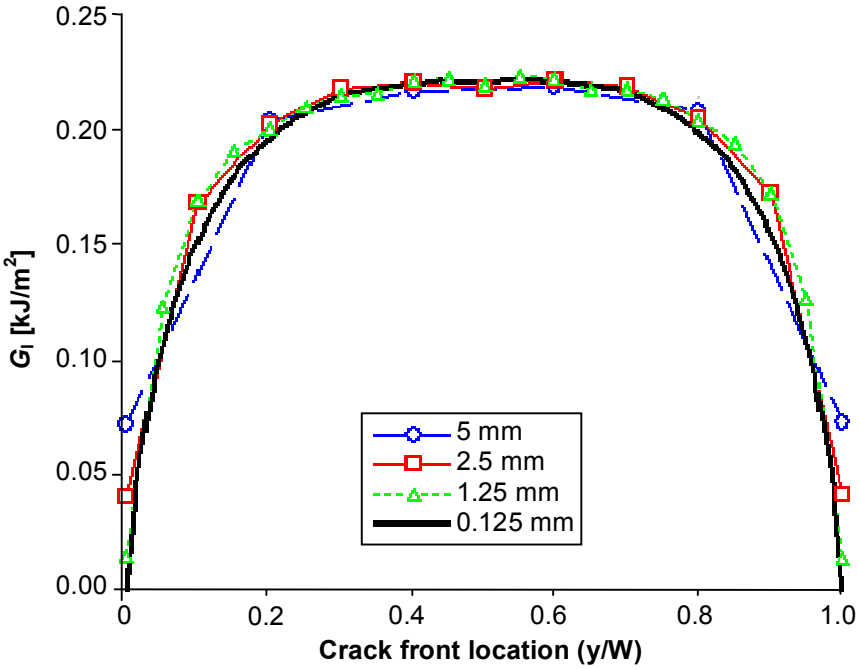

Figure 4.19: DCB strain energy release rate at 1.3 mm applied displacement, all FE models

Table 4.3: FE analysis summary, for all FE models and all propagation methods

PM	5 mm		2.5 mm		1.25 mm		0.125 mm		DCB Test # 7	
	P_{max} [N]	a_{max} [mm]	P_{max} [N]	a_{max} [mm]	P_{max} [N]	a_{max} [mm]	P_{init} [N]	a_{max}* [mm]	P_{max} [N]	a_{max} [mm]
1	92.4	130	93.2	127.5	91.4	128.8	89.2	–	108	127.4
2	92.4	130	93.2	127.5	90.7	127.5	89.2	–		
3	92.4	>150	93.2	>150	90.7	>150	89.2	–		
4	112.1	120	113.0	117.5	111.9	116.3	109.2	–		

* Analyses for PMs 1, 2 and 3 only run to 1.5 mm. Analysis for PM 4 only run to 1.8 mm.

Table 4.4: FE analysis time summary, for all FE models and all propagation methods

PM	5 mm			2.5 mm			1.25 mm			0.125 mm		
	T [hr]	*inc*	t_{inc} [s]	t [hr]	*inc*	t_{inc} [s]	t [hr]	*inc*	t_{inc} [s]	t* [hr]	*inc*	t_{inc} [s]
1	0.57	121	16.9	1.69	235	25.9	16.0	586	98.4	11.7	151	279.2
2	0.52	121	15.4	1.15	235	17.7	11.7	586	71.7	8.16	151	194.6
3	0.59	121	17.5	1.79	235	13.8	13.8	586	84.7	9.69	151	231.0
4	0.51	121	15.1	2.00	235	18.8	18.8	586	115.5	9.57	151	228.1

* Analyses for PMs 1, 2 and 3 only run to 1.5 mm. Analysis for PM 4 only run to 1.8 mm.

For the ENF and MMB models, the models were run with PM 1 and PM 4 on a 2.4 GHz Dual Core AMD Opteron processor, and all three failure criteria were applied. Analysis results are presented below, where Figure 4.21 and Figure 4.22 are typical comparative curves of applied load versus displacement for the ENF and MMB models, Figure 4.23 gives the distribution of *G* along the crack front for both models, and Figure 4.24 shows the deformed shape and crack length of the MMB 50% model at 3 mm applied displacement.

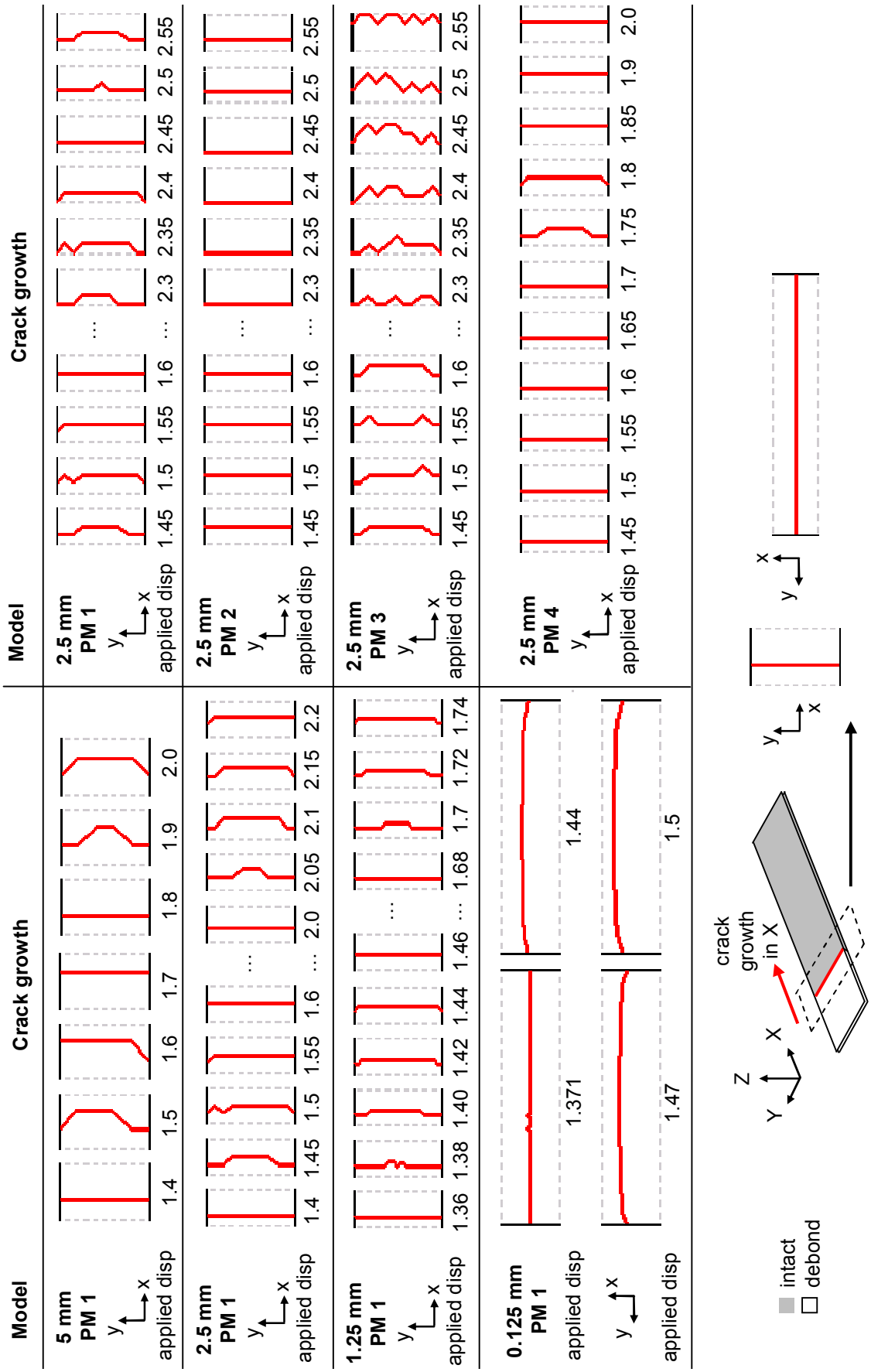

Figure 4.20: DCB model, crack growth progression with applied displacement for: left – PM 1 with all models; right – 2.5 mm model with all propagation methods.

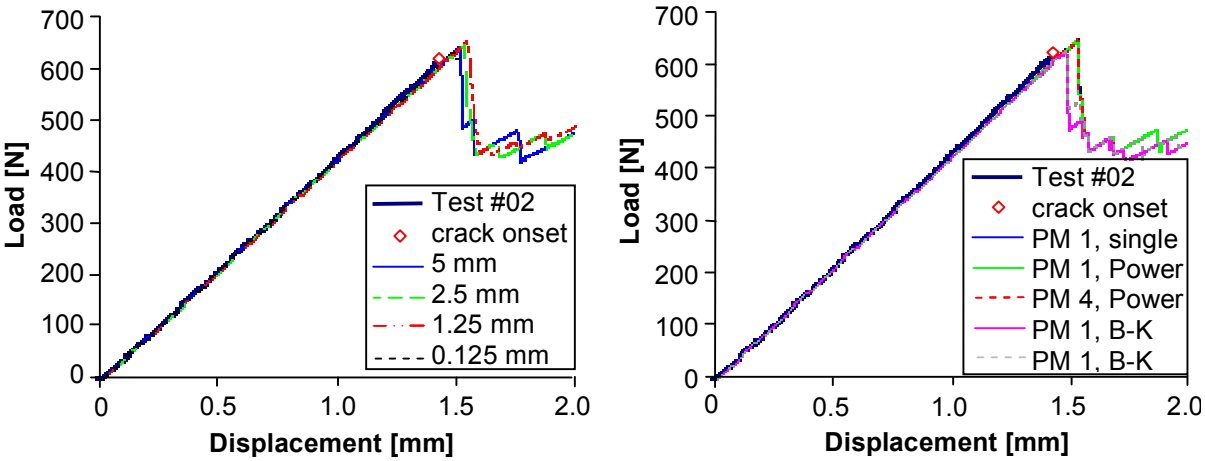

(a) (b)

Figure 4.21: ENF models, applied load versus displacement: (a) PM 1, Power law, varying mesh density (b) Varying propagation method

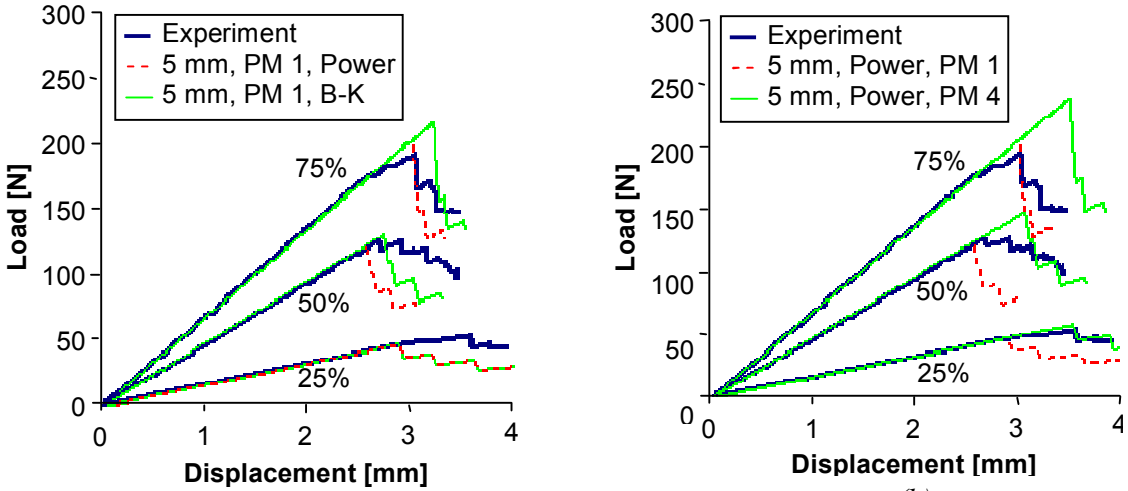

(a) (b)

Figure 4.22: MMB models (varying G_{II} / G_T), applied load versus displacement: (a) Varying failure criterion (b) Varying propagation method

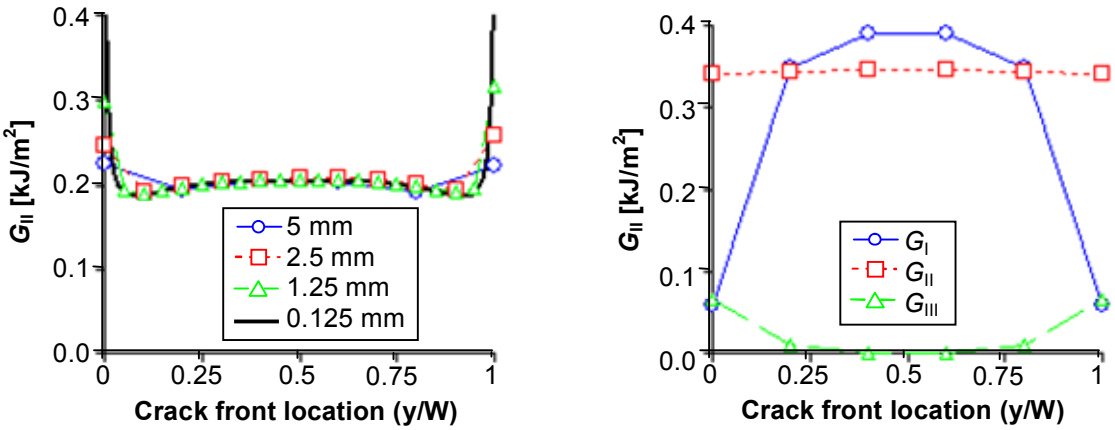

(a) (b)

Figure 4.23: G distribution along crack front: (a) ENF, all models (b) MMB 50% 5 mm

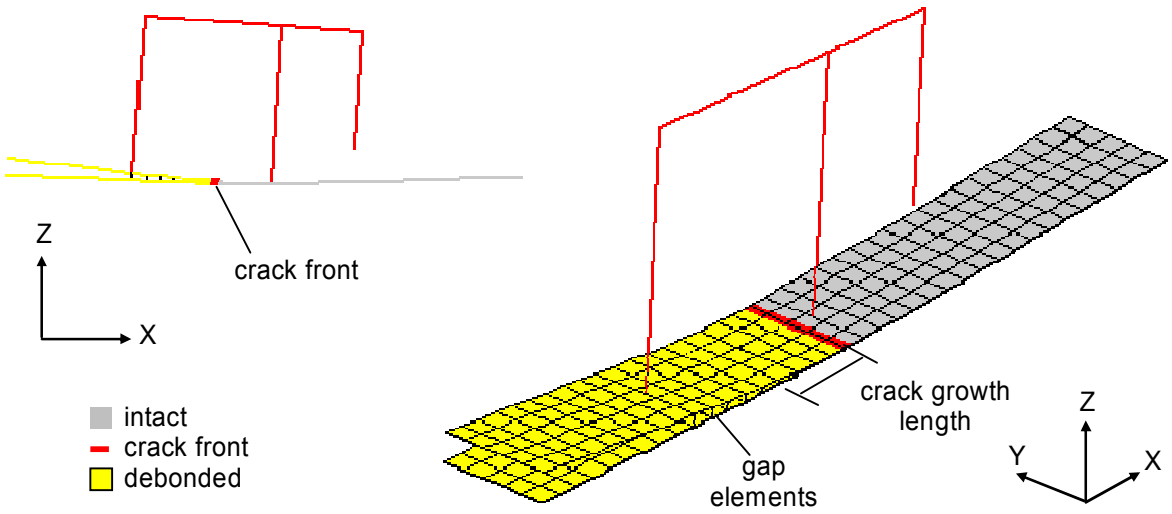

Figure 4.24: MMB 25% 5 mm model, deformed shape and crack growth, 3 mm displacement

All models displayed similar behaviour regardless of test type or propagation method, which involved an initially linear region leading up to the initiation of crack growth, and crack growth characterised by reductions in the load-carrying behaviour corresponding to advances in the crack front. For all 5 mm, 2.5 mm and 1.25 mm models, the crack advanced as a straight crack, and alternated between a stationary full width straight crack and a jagged crack front in crack growth. This behaviour was reflected in the "saw-tooth" appearance of all load-displacement curves that was the most pronounced for the 5 mm model, and in general the straight and jagged crack fronts corresponded to increasing and decreasing load-displacement behaviour respectively. The drop in load upon crack growth corresponded to the distance of crack advance and the number of MPCs released, so the use of smaller elements resulted in a smoother load-displacement curve. The sequence of failing MPCs along the crack front was usually identical between growth steps for each different mesh density and propagation method, and this sequence was largely symmetrical for all models.

Across all results, the degradation model gave very good predictions of the crack growth initiation and strain energy release rate values of each specimen. The values for load and displacement at crack onset were within 13% for all DCB models, and within 10% for ENF and MMB models. For the MMB models, the failure predictions appeared to be related to the mode-mix ratio, and were more accurate for the 25% models, as shown in Figure 4.22. The calculations of strain energy release rate across the crack front accurately captured the correct crack opening actions, and in particular the mode-mix ratios of the mixed-mode bending models agreed very well with the experiment. The mesh density did not significantly affect the overall structural response and crack propagation behaviour for any model. There were slight differences in the exact crack propagation shapes and strain energy release rate

distributions between models, most noticeably for the 5 mm model, though from the load-displacement results these did not affect the global specimen response of any model.

The crack growth behaviour also appeared to be realistically represented by the degradation model, across all models. For the DCB 0.125 mm models, PMs 1, 3 and 4 all showed crack growth from the initially straight crack front into a curved or "thumbnail" shape, and crack propagation then continued in this thumbnail shape. For the ENF models, failure was first determined at the specimen edges, which caused a small region of crack growth to form at both edges. This "subcritical" crack growth did not affect the linearity of the load-displacement curve, or result in the growth of the remainder of the crack front. Though no information on the crack front shape was available from the tests performed, DCB thumbnail crack front and ENF subcritical crack growth are phenomena that are well known both theoretically and experimentally, and are due to the anticlastic curvature of the structure (Davidson 1990; Davidson 1996; Brunner 2000). The MMB models also showed a curved G distribution which produced first failure in the specimen centre, and this similarly was attributed to anticlastic curvature. Additionally, the ENF models all showed rapid crack growth at the onset of propagation, and this appeared to reflect the unstable crack growth behaviour that is commonly seen in ENF testing (O'Brien 1998).

In terms of the different failure criteria, for the ENF models the use of a mixed-mode criterion instead of the single-mode criteria reduced the failure load and displacement and showed improved comparison with experiment, so appeared to more realistically represent the mixed-mode conditions at the crack front. This was especially true in crack propagation, where it was common that the jagged crack front developed a significant mode III component. This always occurred at a non-straight crack front, typically at the corner between two straight crack front sections, and this led at times to MPCs failing in pure mode III conditions. The application of the different mixed-mode criteria had varying results, with the B-K criterion giving earlier and more accurate predictions of crack growth for the ENF models, though this situation was reversed for the MMB 50% and 75% models, and the two criteria gave identical results for the MMB 25% models. This was related to the curve-fit equations for each criterion, seen in Figure 4.15(b), which though generally giving similar predictions for G_C across all mixed-mode ratios, showed divergence at mode mix ratios of 50% and 75%, and gave very similar predictions at 25%. So, whilst it is possible to recommend the use of mixed-mode over single-mode criteria, no mixed-mode criterion offered any clear advantage for the specimens investigated.

For all models, the selection of the increment size was critical in order to ensure that the load was not increased disproportionately to the crack growth. That is, the increment size had to be small enough so that any crack growth required could take place before the load was increased enough to cause additional growth. The result of this was that the increase in mesh density doubly penalised the total analysis time due to the increase in both computational expense and required number of increments. This can be seen in Table 4.4, which summarised the analysis times for the DCB models. In this table the t_{inc} value is an attempt to give a more realistic appreciation of the computational expense for each model, and though this value does not account for iterations, the number of iterations was fairly constant between increments.

Though the influence of the propagation method varied across the test specimens, the comparative graphs shown in Figure 4.17, Figure 4.21(b) Figure 4.22(b) give a good representation across all test results. For the DCB results, in which all the propagation methods were applied, PM 1 predicted the load at crack growth initiation within 13%, captured the load-carrying behaviour in crack growth very well, and gave excellent comparison with the final crack length. As no change to the initiation criteria was made in PMs 2 and 3, these methods gave identical predictions for crack growth initiation. PM 2 gave almost identical behaviour to PM 1 for the entire loading, though with run times that were slightly less than PM 1 and the shortest of all propagation methods. The identical behaviour between PMs 1 and 2 was due to the fact that the crack front shape and location remained identical for the times in which the crack was stationary, in spite of the two approaches giving a different sequence of failing MPCs. In contrast, PM 3 gave results that significantly underestimated the load-displacement behaviour, with a slight increase in analysis time. The underestimation of PM 3 was surprising as it was expected to be less conservative than PM 2 given that it involved less MPCs being forced to fail. However, from inspection of the crack front progression, it was seen that in contrast to PMs 1 and 2 that essentially propagated a straight crack front, PM 3 resulted in the propagation of a jagged crack front shape consisting of a series of corners and edges. This configuration of crack front had less structural stiffness than the straight crack front, and critically the jagged edges were more likely to initiate further crack growth, which only worsened the underestimation problem. PM 3, unlike PM 2, enforced crack growth in a manner that was not representative or realistic for DCB specimens, and so an incorrect crack front was generated and propagated.

PM 4, in which the strain energy release rates were adjusted based on the new crack front, was applied to all DCB, ENF and MMB models, and gave good to excellent comparisons across all test results. For the DCB results, the maximum applied load was within 5 % and the total crack length was within 9 % for all mesh density models, though the predictions of total crack length were slightly less accurate than for PM 1 and PM 2. The modification process in effect added a delay to the onset of crack growth, which appeared to alleviate the conservatism shown in PMs 1, 2 and 3. Figure 4.25 shows the initiation of crack growth with PM 1 and PM 4, which clearly highlights the improved prediction of the actual strain energy released upon crack growth and the overestimation of the simple fail-release approach of PM 1. For the ENF models, PM 4 gave almost identical results to PM 1, which is not surprising given that the mode II modification factors were almost all equal to one. For the MMB models, the use of the modification factors in PM 4 resulted in a delay in the failure predictions of around 15%-20% for both the displacement and load at the initiation of crack growth. This modification gave improved predictions for the 25% and 50% models, though led to overestimation for the 75% models. In spite of this, all models consistently showed that the crack opening displacement after crack growth remained largely dependent on the shape of the local crack front, and that the modification factors applied in PM 4 continued to provide a conservative and realistic reduction of the assumed energy released in crack growth.

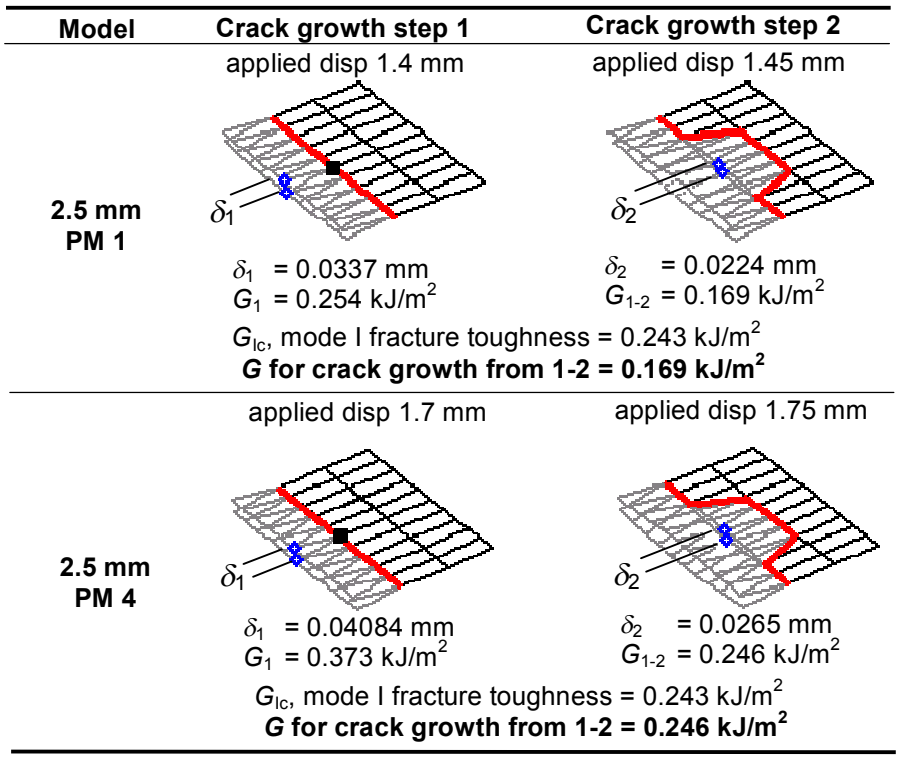

Figure 4.25: Crack growth initiation for PMs 1 and 4, showing the difference between assumed and actual strain energy release rates for both methods

4.3.3 Discussion

The modification factors for PM 4 found from the parametric studies varied across the different crack growth modes, and this influenced the results of the models. For mode I, the parametric studies revealed a considerable influence between the energy released in crack growth and the shape of the local crack front after crack growth. However, in mode II and mode III, the energy released was not affected by the local crack front to the same degree, and most modification factors for modes II and III were mainly 1.0 or close to 1.0. This was particularly evident for the mode II crack growth, in which only a small number of local crack fronts in propagation actually influenced the mode II opening displacement upon crack growth. The variance in the result comparison seen in the MMB specimens across the different mixed-mode ratios further illustrates the difficulty in applying an approach that is suitable across the entire crack opening regime. These results indicate that the modes may not be as separable as envisaged, and that the interaction of the modes and the mode mixity itself may be a contributing factor in determining the correct energy released in crack growth.

It is important to recognise that for PM 4, the correlation between local crack front shape and energy released in crack growth may not be applicable to all other types of structures and all other types of crack growth. The crack opening displacements created upon crack growth would not only be influenced by the local crack front shape, but also by any crack growth around the entire crack front, as well as by structural effects such as the proximity of any stiffeners or flange edges and the general deformation of the region. Though the parametric studies conducted to determine the modification factors were quite extensive, the conclusion that the local crack front shape could be used to represent all of these effects may be specific to some aspect of the specimens investigated such as the specimen configuration, boundary conditions or material properties. In all of the parametric studies the lowest reduction factor was taken for each set of local crack front investigations, and whilst this ensured the conservatism of the approach, in some cases the low factor did not represent the majority of results and would still lead to overestimation in the VCCT calculation. Based on these considerations, the performance of PM 4 was further evaluated using results for small and large stiffened structures, which is detailed in Chapters 5 and 7. However, from all analyses it is evident that the simple fail-release approach can violate the self-similar assumption leading to overestimation of the energy released at crack growth, and that PM 4 offers a simple and effective approach for increasing the accuracy of the VCCT calculations.

More generally, the results indicated that the VCCT approach can remain accurate for large mesh sizes, and can be used to make predictions on the load-carrying capacity and structural response. This is a critical requirement for the degradation model in order to be applicable to large skin-stiffened structures. The results indicate that the approach is suitable for obtaining detailed information on the crack initiation and crack shape, though this does require significant computational effort. It must be noted that many researchers have found VCCT to give mesh-dependent results, especially for the so-called "bi-material" interface between two dissimilar sublaminates (Krueger 2002). In the following section, a numerical investigation is made into asymmetric laminates in order to study the effect of a bi-material interface on the VCCT results. Though mesh-dependency for asymmetric laminates would be problematic as these types of interfaces are common in stiffened structure designs, approaches such as mesh density studies and a comparison with a ply-thickness element length model can be applied to mitigate these issues, as demonstrated in the analyses in this chapter.

4.4 Numerical Investigations

A series of numerical investigations were performed, in order to further demonstrate and assess the capabilities of the degradation model and modelling approach. These included the following investigations:

- A full description of the results for the edge crack torsion (ECT) specimen, which is the mode III fracture mechanics characterisation test previously mentioned.
- A comparison with damage and fracture-based elements in the Abaqus FE code: the "VCCT for Abaqus" approach and the cohesive element.
- A study of asymmetric laminates, looking at the strain energy release rate values, to investigate the effect of a bi-material interface on the mesh-dependency of VCCT.

4.4.1 Mode III: Edge Crack Torsion

4.4.1.1 Introduction

There are currently no standards or accepted test procedures for investigating mode III fracture toughness, due to the difficulty in developing methods that generate pure mode III loading (O'Brien 1998). One of the most promising is the edge crack torsion test, shown in Figure 4.26, in which a $[90/(+45/-45)_n]_{2S}$ laminate with a full-length mid-plane delamination is loaded in a special test rig so as to generate torsion along the delamination (Lee 1993). The

ECT test does however have several problems, including significant edge effects, a mismatch between experimental and analytical values of the stiffness constant D_{66} (Zhao & Wang 1998), and the need to determine the transverse shear stiffness G_{23} (Camanho and Dávila 2002).

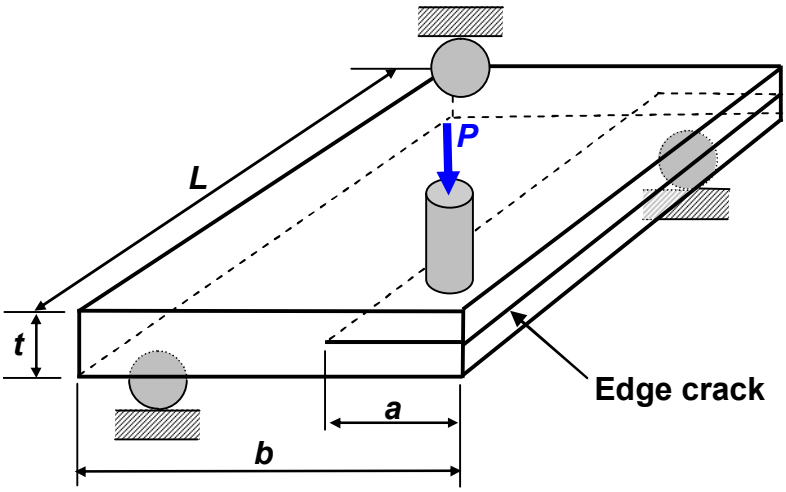

Figure 4.26: Mode III ECT configuration

4.4.1.2 Numerical Analysis

The ECT specimen was taken from Zhao & Wang (1998), in which a numerical model was created for experimental tests performed in Lee (1993). An overview of the specimen configuration was given in Figure 4.26, and details of the parameters are given in Figure 4.27 and Table 4.5.

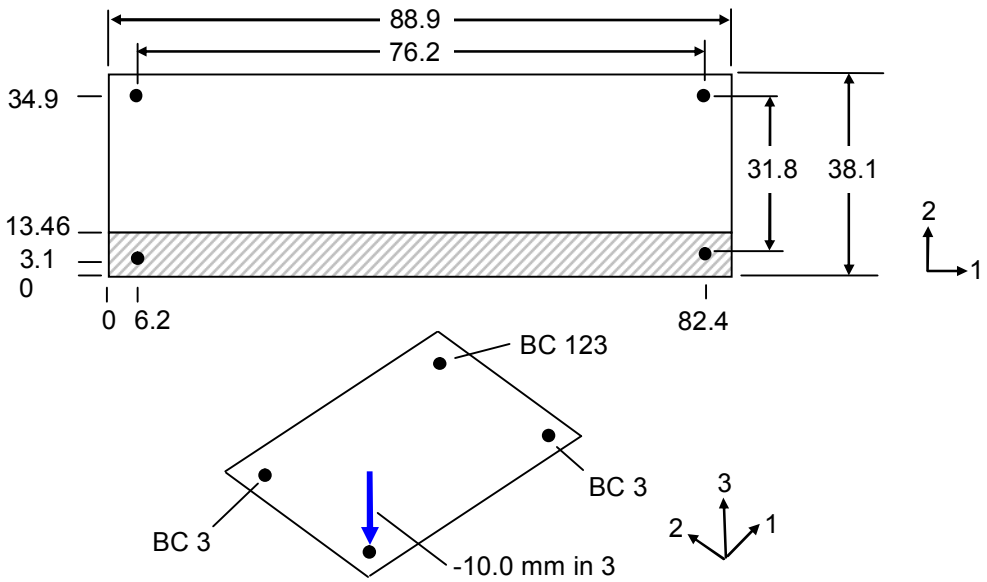

Figure 4.27: Geometry and support conditions for ECT tests, dimensions in mm

Table 4.5: Material specifications for ECT tests, from Lee (1993)

Lay-up	$[(90,(+45,–45)_3)_S$ // $(90,(+45,–45)_3)_S]$
Ply thickness	0.13 mm
E_{11}	165 GPa
E_{22}	10.3 GPa
$G_{12} = G_{31}$	5.5 GPa
G_{23}	4.023 GPa
$\nu_{12} = \nu_{23} = \nu_{31}$	0.28

From the experimental tests, a value of G_{IIIC} = 1.14 kJ/m^2 was determined, with crack growth initiating at 6.2 mm applied displacement. In the reference numerical analysis from literature, the VCCT was used in a 3D solid element FE model to determine the strain energy release rate distribution along the crack front. Additionally, the mode I opening displacement (local Z direction) of the nodes in the delaminated region were tied together, in order to prevent penetration of the two sublaminate surfaces.

An FE model was generated that was based on a 2.5 mm regular grid mesh, though some of the element lengths were modified slightly in order to accommodate the exacts support and crack length dimensions, as shown in Figure 4.27. The model used 1080 four-node bilinear thick-shell elements, 555 gap elements, and 444 user-defined MPCs. The boundary conditions are also shown in Figure 4.27, where roller supports were used around the specimen, except for additional supports on the non-loaded side, which were necessary in order to prevent rigid body rotations in the FE model. This, however, differed from experiment in which only rollers were used, and did have some influence in the values of strain energy release rate in the vicinity of the supports.

For the ECT analysis, the 2.5 mm model was run with both PM 1 and PM 4, with a linear mixed-mode failure criterion (Equation 4.4 with $m = n = p = 1$). The two analyses were run to 8 mm displacement load on an Intel 3.2 GHz Pentium 4 CPU. As for the DCB and ENF analyses, the Marc nonlinear solver was used, with a full Newton-Raphson procedure applied and the default tolerance of 0.1 on load residuals. Analysis results are presented below, where Figure 4.28(a) is the load-displacement, Figure 4.28(b) is the strain energy release rate distribution of the crack front in comparison with results from the reference VCCT analysis, and Figure 4.29 is the final deformed shape and crack growth area.

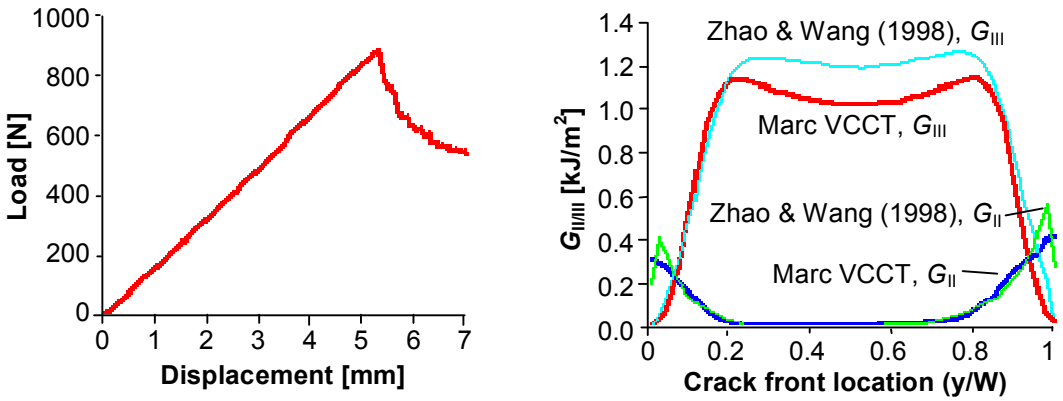

Figure 4.28: ECT model: (a) Applied load versus displacement, 2.5 mm model (b) Strain energy release rates across the crack front at crack growth onset

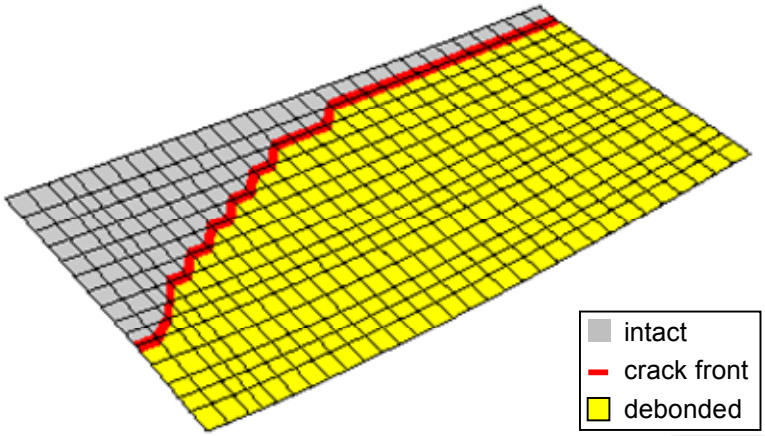

Figure 4.29: Final deformed shape and crack growth region, ECT

In the numerical model, crack growth initiated at an applied displacement of 5.25 mm, which compared well with the 6.2 mm value taken from experiment. The strain energy release rate results also compared well with the reference values, where it must be noted that the values shown in Figure 4.28 were taken from the onset of failure for each model, and so represent different values of applied displacement. In spite of this, the distribution of both the mode II and III strain energy release rates showed very good agreement. Following the onset of crack growth, the load-carrying capacity of the panel was reduced, in the same manner as was seen for the DCB and ENF specimens. However, unlike the DCB and ENF specimens, the numerical results showed that an asymmetric crack front developed, with little crack growth occurring on the loading side, though it is not known whether this was due to the influence of the boundary condition definition in the numerical model. Regardless, the results further demonstrated the capability of the degradation model to represent interlaminar crack growth in any mode loading during an analysis.

4.4.2 Abaqus Comparison

Models were generated for Abaqus 6.6.1 using the 2.5 mm mesh as described previously, applying the "VCCT for ABAQUS" (Abaqus VCCT) technology and the Abaqus cohesive element (Abaqus cohesive) (*ABAQUS Version 6.6 Documentation* 2006; *VCCT for ABAQUS User's Manual, Version 1.1* 2005). The parameters of both of these models are given in Table 4.6, where: a linear interaction was assumed for the power law; supplier data for a standard resin was used for the cohesive element stiffness and strengths; the viscosity parameter was selected taken from Abaqus sample problems (*ABAQUS Version 6.6 Documentation* 2006); and program defaults were used for all other parameters. Figure 4.30(a) gives a comparison of the load-shortening curves for the Abaqus VCCT and Abaqus cohesive models with the 2.5 mm PM 1 and PM 4 results given previously. A comparison of the strain energy release rates for the Marc VCCT PM 1 and Abaqus VCCT 2.5 mm models is given in Figure 4.30(b).

Table 4.6: Non-default analysis parameters, Abaqus VCCT and Abaqus cohesive models

Abaqus VCCT		*Abaqus cohesive*	
Mixed-mode law	Power law	$E_{33} = E_{12} = E_{23}$	3.0 GPa
Power law coefficient a_m	1.0	Damage initiation criterion	Max stress
Power law coefficient a_n	1.0	N_{max}, $S_{max} = T_{max}$	8.3 MPa
Power law coefficient a_o	1.0	Viscosity parameter	1×10^{-4}

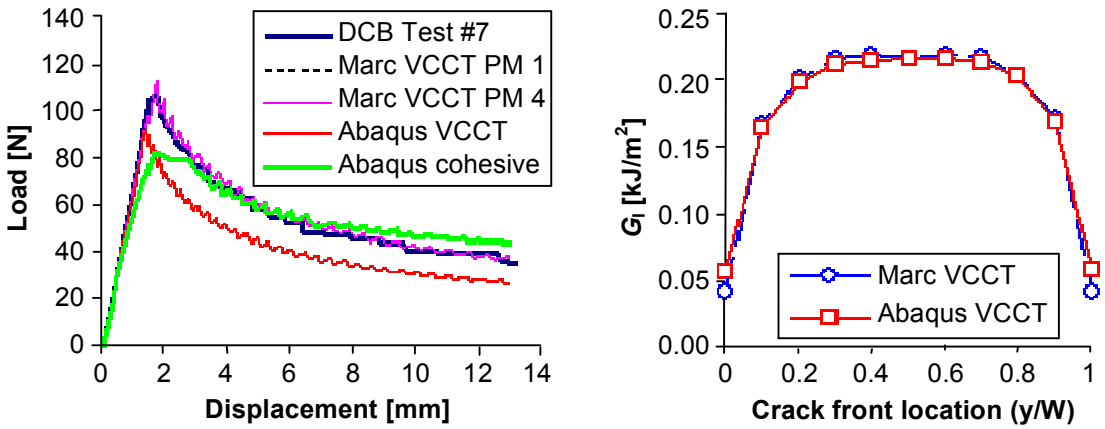

(a) *(b)*

Figure 4.30: Marc VCCT, Abaqus VCCT and Abaqus cohesive comparison: (a) Applied load versus displacement (b) Strain energy release rate at 1.3 mm displacement, 2.5 mm mesh,

From Figure 4.30, and the results for crack growth behaviour not shown, the Abaqus VCCT and Marc VCCT PM 1 models both described very similar behaviour, with the load-shortening curves almost identical. This is due to the fact that both approaches apply a very similar adaptation of VCCT in the FE analysis, where in contrast to the developed Marc approach using MPCs, Abaqus VCCT is based on a contact definition. However, both

approaches apply the same VCCT equations at the end of the increment, so gave very similar values of strain energy release rate. There were some differences between the strain energy release rate calculations for non-straight crack fronts, though these did not affect the global load-carrying predictions. These conclusions have also been further demonstrated in other models of DCB specimens and other fracture mechanics characterisation test specimens. The almost identical nature of all comparisons validates a large part of the implementation of VCCT in the developed Marc approach. Furthermore, the results also demonstrated the increased accuracy of PM 4 over the simple fail-release approach in PM 1 and Abaqus VCCT, which was seen to be more significant for mode I dominated problems such as the DCB test.

In terms of the cohesive element, the load-shortening curve is similar to the VCCT results, especially in the initially linear region before the onset of softening in the cohesive layer at around 1 mm loading. For this 2.5 mm mesh, the Abaqus viscosity parameter was required in order to achieve convergence, and the influence of this parameter is evident in the appearance of a delay in the results, especially around the onset of crack growth corresponding to the turning point on the load-shortening curve. The results appear to indicate that either the viscosity parameter (1×10^{-4}) was too large or that the mesh density was not fine enough to achieve accurate results with cohesive elements. However, it should be noted that no studies were made into an appropriate mesh density or viscosity parameter, and there was no application of any advanced meshing techniques to attempt to achieve an optimum mesh density of either the cohesive layer or the shell elements. Though it is expected that further study of these parameters would improve the cohesive element results, these were not investigated in this work due to the focus on validating and comparing the developed method.

4.4.3 Asymmetric Laminates

In the previous models, the VCCT approach gave mesh-independent results for both load-shortening behaviour and strain energy release rate calculations. However, as previously mentioned, a bi-material interface has been found by other researchers to cause the VCCT equations to give mesh-dependent results (Krueger 2002). The lay-up of the previous model was a quasi-isotropic symmetric laminate, so it was not possible to determine the effect of a bi-material interface on the developed VCCT approach.

To investigate the effect of asymmetric sublaminates on the VCCT calculations, the four mesh density models investigated previously were used, and the lay-up was modified to give different asymmetric laminates. The lay-ups studied are given in Table 4.7, where all other

parameters were identical to those given previously. From this, the quasi-isotropic lay-up was from the previous analyses, and the "0-90" laminate consisted of the lower sublaminate with all 0° plies and the upper sublaminate with all 90° plies. The Design 1 (D1) and Design 2 (D2) laminates were taken from the skin-stiffener interfaces of the COCOMAT Design 1 and Design 2 stiffened panels. These laminates were included as they were relevant to later analyses of COCOMAT single-stiffener flat panels and multi-stiffener curved panels. The strain energy release rates across the crack front for all mesh densities are given in Figure 4.31 for the 0-90 and D1 laminates and Figure 4.32(a) for the D2 laminate. Figure 4.32(b) shows the effect of mesh refinement on the strain energy release rate value at the centre of the crack front, which is plotted against the element length per mm in the crack growth direction.

Table 4.7: Lay-up definition for asymmetric laminate investigation.

Sublaminate	quasi-isotropic	0-90	Design 1	Design 2
Upper	$[0,90,+45,-45]_{2S}$	$[90]_{16}$	$[0_6,(-45,+45)_3]$	$[90_2,0_2,-45,+45]$
Lower	$[0,90,+45,-45]_{2S}$	$[0]_{16}$	$[90,+45,-45,0]_S$	$[+45,-45,0,90]_S$

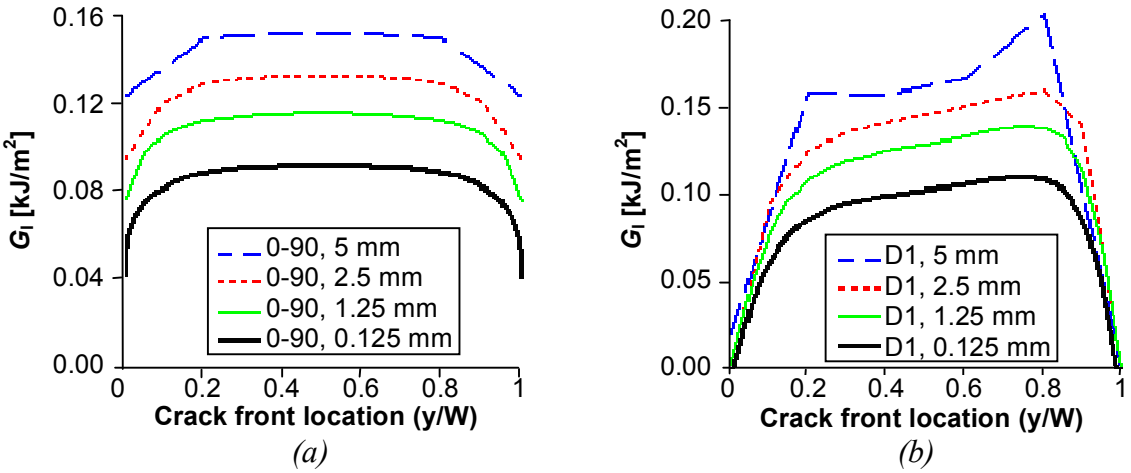

Figure 4.31: Strain energy release rate across crack front, all models: (a) 0-90 (b) D1

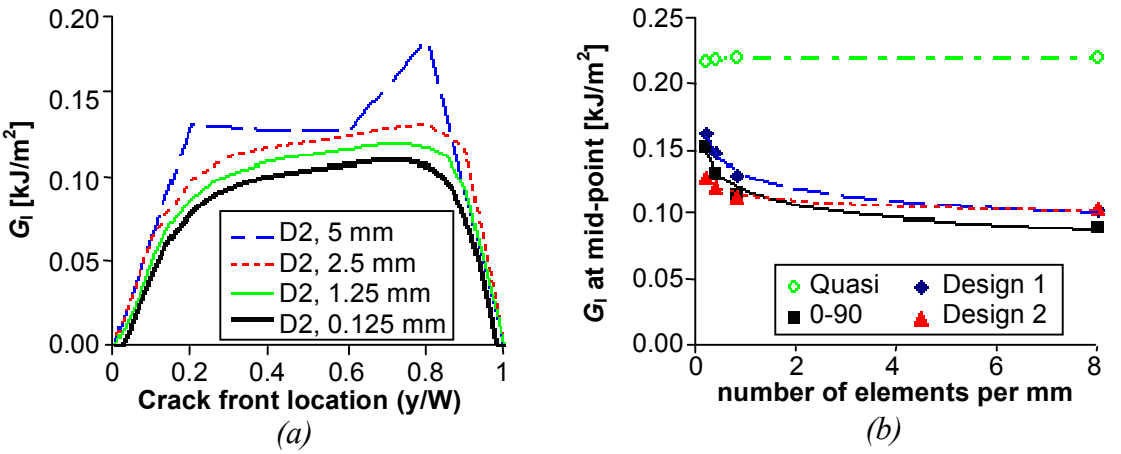

Figure 4.32: Strain energy release rate (a) across crack front, D2 (b) at the crack front mid-point versus the number of elements per mm

The results indicate that there was a significant influence of laminate asymmetry on the mesh-dependency of the VCCT calculation. This can be seen from all of the results of this investigation, where increasing the mesh density (decreasing the element length) continually reduced the calculated values of strain energy release rate. The results did show qualitative convergence, as the shape of the distribution across the crack front converged with decreasing element length. However, though elements of the order of the ply thickness are recommended in order to achieve mesh-independent results (Krueger 2002), the convergence results in Figure 4.32(b) indicate that a compromise can be found between accuracy and computational cost. Though the load-displacement curves and behaviour in crack growth was not studied, it is clear that the higher strain energy release rates of larger elements will cause premature crack growth, and hence the fracture properties of the structure will be conservatively estimated.

Results from preliminary investigations have indicated that the mesh-dependency of asymmetric laminates is related to the ratio between the axial and transverse stiffness values of the ply material. Specifically, results from early investigations have shown that mesh-dependency is significantly reduced in the analysis of fabric composites, in which the axial and transverse stiffness values are nominally equal, in contrast to the unidirectional tape composites used here in which the axial stiffness is roughly two orders of magnitude greater than the transverse stiffness. This further indicates that the mesh-dependency of the VCCT calculations should be investigated for each structure analysed. In spite of this, the qualitative convergence of the strain energy release rate distributions and the conservative overestimation of values for large element sizes suggest that the developed approach remains suitable from a design point of view, and that expensive mesh sensitivity studies would only be necessary in the final stages of the design process.

4.5 Conclusion

A degradation model to capture the propagation of delaminations in composite structures has been developed. The model was implemented for nonlinear FE analysis with user subroutines in Marc. In the approach, user-defined MPCs were applied to control the connection of two shell element layers. At the end of every increment, fracture mechanics calculations were performed using VCCT and any failing MPCs were released for the next increment. Gap elements were also included to prevent penetration of the shell layers, and a user subroutine was written to maintain the correct gap distance using the shell layer normal direction.

As part of the development, an extensive study was conducted into the method of crack propagation used with VCCT, and it was found that a simple fail-release approach could lead to overestimation of the crack growth as it allows for the fundamental VCCT assumption of self-similarity to be violated. A novel approach was proposed that linked the shape of the local crack front following crack growth to reduction factors for the strain energy release rate. This approach was supported by extensive parametric studies in all crack opening modes, and was shown to give more accurate estimations of the strain energy release rate.

The degradation model was compared to experimental results of DCB, ENF and MMB fracture mechanics characterisation tests for mode I, II and mixed-mode I-II, respectively, where results were taken from testing within COCOMAT. The simple fail-release approach was shown to give accurate results in all comparisons, though did give slightly conservative results for mode I crack opening. In comparison, the novel modification approach was shown to significantly improve the mode I predictions, and had an important though minor effect on the mode II and mixed-mode I-II results. In general, all analyses demonstrated the ability of the degradation model to represent the propagation of a pre-existing debond during numerical analysis, and to use this in order to accurately predict the load-carrying capacity of a structure.

Investigations were made into the accuracy and applicability of the degradation model, and included application of the model to mode III crack growth in an ECT specimen, comparisons with Abaqus, and studies into the effects of a bi-material interface. It was shown that the approach developed was applicable for the analysis of crack growth behaviour and strain energy release rate distribution under mode III crack opening conditions. It was also shown that the degradation model with the simple fail-release approach gave almost identical results to the Abaqus VCCT implementation, and that these approaches overestimated the strain energy release rates in comparison with the novel modification approach. There was also good comparison with the Abaqus cohesive element, though the results did indicate that further improvement to the cohesive element results might have been possible through investigating the mesh density and viscosity parameter. For a bi-material interface, the VCCT calculations were shown to be mesh-dependent when the sublaminates bounding the interface layer were not symmetric, though the results did indicate that it is possible to obtain results of adequate and conservative accuracy without resorting to prohibitively small element sizes.

CHAPTER 5

ANALYSIS METHODOLOGY

In this chapter a complete methodology for the collapse analysis of postbuckling composite structures is presented. The methodology incorporates the analysis approach for interlaminar damage initiation given in Chapter 3, and the degradation model for interlaminar damage propagation presented in Chapter 4. First, a degradation model developed to capture in-plane damage within the composite ply is summarised. Then, the methodologies developed in previous chapters are extended for the analysis of large postbuckling structures. This includes coupling the local cross-section analysis with a global analysis of an entire structure, selecting a location for the skin-stiffener damage interface, and representing pre-damage due to impact. The program subroutines and external files are then listed, followed by an overview of the way in which the approach can be applied to the design and analysis of composite postbuckling structures. The validation of the analysis methodology using experimental results for single-stiffener specimens is then presented.

5.1 Analysis Methodology

In Chapter 2, a methodology for the collapse analysis of postbuckling composite structures was discussed, and consisted of predicting the initiation of interlaminar damage, capturing the propagation of interlaminar damage, and capturing in-plane ply damage. In this section, a complete methodology is presented, in which the approaches developed in previous chapters are extended, and further functionality is developed for the analysis of postbuckling composite structures up to collapse.

5.1.1 Ply Degradation

A degradation model was developed for capturing in-plane damage occurring within the plies of the composite material. From the literature review in Chapter 2, a large number of failure criteria and ply degradation models were identified. For failure criteria, there is a clear difference between fully interactive criteria like Tsai-Wu (1971), which represent general lamina failure using a single criterion, and criteria that distinguish between the different ply

failure modes. Though there continues to be considerable debate between the two approaches (see for example, the failure exercise of Kaddour, Hinton and Soden (2004)), the failure-mode based criteria are generally considered more suitable, particularly for ply degradation, due to the additional information provided by the consideration of the separate failure mechanisms.

In terms of the failure mechanisms considered, fibre-reinforced composite plies can display failure in the fibre and matrix, with separate mechanisms in tension, compression and shear. For fibres, tensile failure occurs due to the accumulation of individual fibres failing in tension, and is commonly predicted with simple limit-based equations using tensile strength parameters from experimental coupon tests. Fibres in compression fail due to microbuckling of the fibres, and though some authors have developed criteria and approaches for handling this, simple strength-based limit equations are still commonly applied (Kaddour, Hinton & Soden 2004). Failure under in-plane shear occurs along the fibre-matrix interfaces, and though no consistent approach has been applied, Hashin (1980) proposed a quadratic interactive criterion that combines longitudinal and in-plane shear stresses. Matrix failure is decidedly more complex, where cracking typically initiates at defects or fibre-matrix interfaces, and failure occurs at the critical fracture plane through the matrix, which is dependent on the combination of loads acting on the material (Puck & Schürmann 1998). Though a considerable amount of development on this subject is available in the literature, for example in the identification of the critical failure plane angle and a number of different matrix failure modes (Puck & Schürmann 1998; Cuntze & Freund 2004), or the application of in-situ material strengths and incorporation of fracture mechanics considerations (Pinho et al. 2005), the criteria of Hashin (1980) have shown a reasonable degree of accuracy in all loading conditions, and continue to be widely applied (Kaddour, Hinton & Soden 2004; Pinho et al. 2005; Ambur et al. 2004).

On the basis of these considerations, and the survey of failure criteria and degradation models presented in Chapter 2, a degradation model was implemented in Marc, and is summarised in Table 5.1. The model combines the failure criteria and degradation models of Hashin (1980) and Chang and Lesard (1991), and is largely based on the recent implementation of these two approaches by Goyal et al. (2004). Note that σ_{11}, σ_{22}, τ_{12} and X, Y, S_{12} are stresses and strengths in the fibre, in-plane transverse and shear directions, S_{23} is the through-thickness shear strength (assumed equal to S_{12} for a transversely isotropic ply), and subscripts T and C refer to tension and compression. The degradation model consists of the criteria used to

distinguish between the different in-plane failure mechanisms, and the selected properties reduced for each criterion upon detection of failure.

Table 5.1: In-plane failure criteria and property reduction

Failure type	Criterion	Properties reduced
Fibre, tension	$\left(\sigma_{11}^2/X_T^2\right)^{\frac{1}{2}} \geq 1$	E_{11}, E_{22}, G_{12}, G_{23}, G_{31}
Fibre, compression	$\left(\sigma_{11}^2/X_C^2\right)^{\frac{1}{2}} \geq 1$	
Matrix, tension	$\left(\sigma_{22}^2/Y_T^2+\tau_{12}^2/S_{12}^2\right)^{\frac{1}{2}} \geq 1$	E_{22}
Matrix, compression	$\left(\frac{\sigma_{22}}{Y_C}\left(\frac{Y_C^2}{4S_{23}^2}-1\right)+\frac{\sigma_{22}^2}{4S_{23}^2}+\frac{\tau_{12}^2}{S_{12}^2}\right)^{\frac{1}{2}} \geq 1$	
Fibre-matrix shear, fibres in tension	$\left(\tau_{12}^2/S_{12}^2\right)^{\frac{1}{2}} \geq 1$	G_{12}, G_{31}
Fibre-matrix shear, fibres in compression	$\left(\sigma_{11}^2/X_C^2+\tau_{12}^2/S_{12}^2\right)^{\frac{1}{2}} \geq 1$	

The ply damage degradation model was implemented in Marc using the HYPELA2 and UEDINC user subroutines in Marc. The HYPELA2 subroutine was used to define a stiffness matrix and stress state for a hypoelastic material, and the UEDINC subroutine is a dummy subroutine called at the end of every increment, as detailed previously. In the degradation model, each integration point at each layer of every element was given three binary variables to define its failure state in the three in-plane failure modes, where 0 was defined as intact and 1 defined as failed. A fourth variable was added to control the reduction of stresses at the failing integration point. The UEDINC subroutine was used at the end of each increment to evaluate the failure criteria for each damage type as a decimal value. Upon satisfaction of any failure criterion, the corresponding binary variables were permanently set to 1, and the fourth variable was set to 1 for the next increment only. The HYPELA2 subroutine was used to define the stiffness matrix, and this was dependent on the damage variables and reductions in corresponding properties according to Table 5.1. The knockdown factor applied in this work was 0.1, which was a compromise between using a value close to zero to represent complete stiffness loss and a value large enough to avoid numerical convergence issues. The HYPELA2 was also used to control the stress state at the integration point, and so was used in coordination with the fourth internal variable to trigger the appropriate stress reduction at softening. This was necessary as the softening reduced the stiffness whilst the strain was held constant, which required a corresponding reduction in stress.

During the analysis, the output from all failing integration points was written to the *.out* Marc output file. This included the binary failure indices and the decimal criterion values from the most recent calculation. An additional output variable was defined in order to assist with quick post-processing, by combining the three failure indices into one value in a binary manner. This was implemented using the PLOTV user subroutine in Marc, and is defined in Table 5.2, where *f*, *m* and *s* are the binary failure indices for fibre, matrix and fibre-matrix shear failure modes and the associated integer output variable is given. There were a few issues with the implementation in this manner, one of which was the fact that the PLOTV subroutine was called before the UEDINC subroutine, so that the output variable was calculated using the values of the previous increment. Furthermore, in the instances that not all of the integration points in an element failed, the output variable of the entire element did not reflect the true element damage state. As a minor point, the user-defined variable tended to overestimate the damage state graphically, as it was used to identify failure at any point in the element throughout the whole composite laminate. In spite of this, the user-defined output variable did allow a good appreciation of the ply failure in the structure, especially for identifying the occurrence of fibre failure, and the output variable was always checked against the raw output in the *.out* file to ensure the damage behaviour was being properly interpreted.

Table 5.2: User-defined output variable for in-plane ply failure

Failure	*f*	*m*	*s*	Output variable
no failure	0	0	0	0
fibre-matrix shear	0	0	1	1
matrix	0	1	0	2
matrix + fibre-matrix shear	0	1	1	3
fibre	1	0	0	4
fibre + fibre-matrix shear	1	0	1	5
fibre + matrix	1	1	0	6
fibre + matrix + fibre-matrix shear	1	1	1	7

5.1.2 Global-Local Analysis

In Chapter 3, an approach was presented for predicting interlaminar damage in intact structures that was based on using finely detailed models of the skin-stiffener interface. To adapt this approach for large, postbuckling structures, it was necessary to employ more coarsely resolved models, as well as be able to apply the correct postbuckling deformations to the finely detailed models. These considerations suggested the use of a two-step analysis procedure, in which the first step used coarse shell models of the entire structure and was used to determine the complete postbuckling deformation history, and the second step applied the deformations from the first analysis to finely detailed models to predict damage initiation. In

Marc, using the results from one analysis as the boundary conditions of another is known as a "global-local" analysis, and this technique was incorporated into the analysis methodology.

The global-local procedure developed for the analysis of postbuckling composite structures is detailed below.

- A "global" results file (*.t16* file in Marc) was generated for the complete structure using a coarse model, which in the models applied in this work consisted of thick shells and a fairly coarse meshing scheme. The incrementation of the global analysis was not important as the local analysis used interpolation between increments. However, in Marc, the element thickness (element post code 20) was required for any analysis results file to be used in a global-local boundary condition. The ply-based degradation model could also be applied in the global model, so that the effects of in-plane damage could be incorporated into the global deformation field.
- A "local" model was created, with care that the global coordinates of the local model were identical to the global model. In particular, the use of 2D elements in the local model was avoided as 2D elements in Marc are defined with a range of different degrees of freedom, which may not have corresponded to the degrees of freedom in the global model. In this work, shell elements were used in the global model and solid elements were used in the local model.
- A global-local boundary condition was created for a number of nodes in the local model. In Marc, for every node in the local model with a global-local boundary condition, the solver searched the global result displacement field for a point on the structure with identical global coordinates (within a tolerance). The displacement history of that point was then input onto the local node, with interpolation if the global point did not lie on a global node. Though the number of local nodes that were necessary to replicate the deformation of the global cross-section was not pre-defined, in this work a general rule of thumb was to use the global-local boundary condition on the local nodes that most closely matched nodes in the global model. An example of this is given in Figure 5.1, where there are 21 nodes in the global skin-stiffener interface (nominally coincident nodes are counted together), and these are used to locate the global-local boundary conditions on both ends of the local model.
- The local analysis was run, which required adding an extra parameter in the Marc run command to identify the global results file. The local model was run with the user subroutine presented in Chapter 3 for predicting the onset of interlaminar damage.

- The local model could then be modified to place it at another location within the global model. This was repeated a number of times in order to identify the point at which interlaminar damage was predicted to occur first in the global model. This process required an aspect of experience and judgement to avoid unnecessary runs of local analysis models. In general the global results file was inspected to determine locations of maximum deformation or stress, which typically occurred at nodal and anti-nodal lines in the structure.

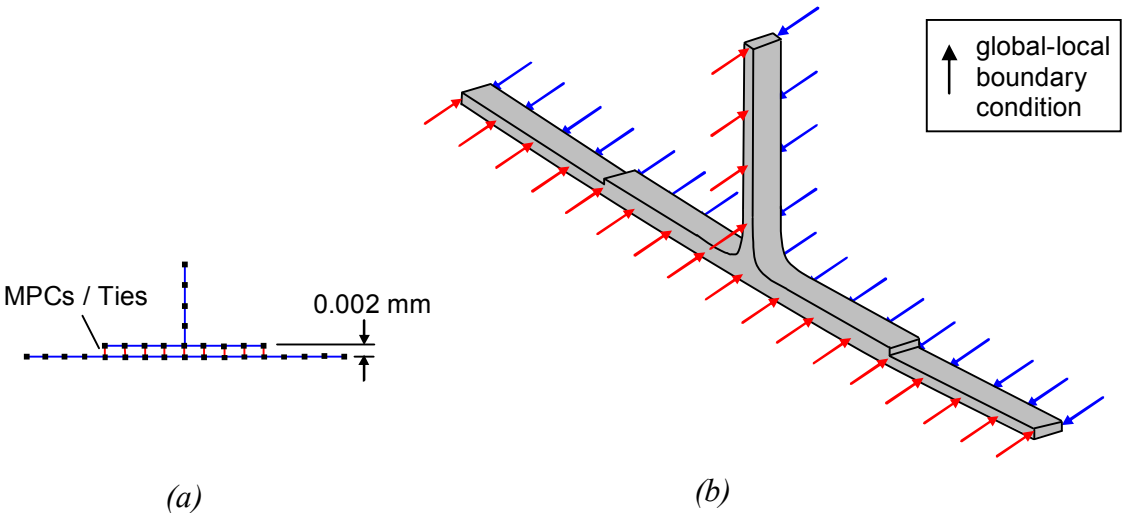

Figure 5.1: Example skin-stiffener interface: (a) Global model (b) Local model with global-local boundary conditions shown

5.1.3 Interface Location

In Chapter 4, a degradation model for the propagation of an existing interlaminar damage region was developed. In order to apply this degradation model for the analysis of composite structures, it was necessary to decide at which location within the composite laminate to model the damage interface. One approach for this decision would be to conduct a detailed analysis of the skin-stiffener cross-section to determine the most likely debonding interface, in the manner demonstrated using 2D elements in Chapter 3. However, the previous analysis demonstrated that this approach may not be able to pinpoint the exact failing interface in every instance, and is best considered as an indication of laminate failure in general. Additionally, any analysis conducted in this manner would be necessarily dependent on an exact knowledge of interlaminar material properties, which becomes problematic for strength-based criteria and prohibitive for fracture mechanics criteria, due to the difficulty in experimental characterisation of interlaminar properties. Separately, another approach for selecting an appropriate interface location would be to use results from preliminary

experimental studies, though this approach would require testing for each material and structure investigated, so was not considered appropriate. So, the selection of an appropriate interface was made on a semi-empirical basis, and represented a compromise between the most likely, most critical, and most practical location for debonding and debond analysis.

As a result of these considerations, and in consideration of the focus of this work for an industry-ready analysis methodology, it was decided to model the structural degradation due to debonding with a damage region at the skin-stiffener interface, for the following reasons:

- As discussed in detail in the literature review in Chapter 2, many researchers investigating postbuckling composite structures have concluded that skin-stiffener debonding is a critical damage type. Locating the interface element layer at the skin-stiffener interface allows direct control of the properties of this crucial connection.
- In experiments, the stress concentrations at the geometry change between the stiffener flange and skin and the different bending properties of the two structural elements typically result in debonding initiation at or very close to the stiffener interface.
- In experiments of skin-stiffened structures, debonds that initiate at the skin-stiffener interface typically migrate at some stage to other ply interfaces in the vicinity, and have even resulted in multiple cracks at several interfaces. However, in general, this type of debonding is centred around the skin-stiffener interface, and modelling a single damage site there would represent a worst-case scenario for crack growth.

One problem with the use of the skin-stiffener interface is the issue of accurate and representative material properties at this location. Material characterisation tests for the strength and toughness of composite materials are usually performed at an interface between two ply layers, or a ply-ply interface. This is appropriate when the skin and stiffener are co-cured, or manufactured as one piece, as this creates a ply-ply interface between the skin and stiffener. However, it is common practice within aircraft structural manufacture to assemble separately fabricated skin and stiffener parts using an adhesive, which results in a ply-adhesive-ply interface. The properties of this type of interface are not as well understood, especially with reference to the behaviour of the interface under debonding conditions. Though there are several experimental tests planned within the COCOMAT project to investigate the properties of this type of interface, it is anticipated that the selection of the interface element layer location at the skin-stiffener interface will continue to be slightly

problematic from a material characterisation point of view. However, as previously noted, material characterisation problems are unavoidably present for any interface.

5.1.4 Impact Analysis

Impact events on composite structures typically lead to delamination and ply damage modes throughout the laminate, for example as described in Greenhalgh et al. (1996) where impacts on skin-stiffened structures caused a range of effects that varied depending on the structure surrounding the impact site. Though characterising impact damage was beyond the scope of this work (see, for example, Bayandor et al. (2003) for work on this topic), it was necessary to incorporate impact damage into the complete analysis methodology so that postbuckling stiffened panels with impact-induced pre-damage could be analysed. This was achieved using the ply damage model described previously.

In the ply degradation model, the damage at each integration point was controlled using three internal state variables. At the start of each analysis, the initial values of these internal state variables were read into the solver from an external text file. By modifying these damage variables in the external file, it was possible to represent the ply damage modes initially present throughout the laminate as a result of impact. This could be used in addition to a pre-defined delamination region, which was set up in the model in the same manner as described in Chapter 3. The definition of impact damage in this manner was greatly assisted by the suite of pre-processing functions developed, which are detailed in the following chapter. It must be noted that with the current analysis methodology, it was not possible to implement multiple delaminations throughout the laminate cross-section.

5.1.5 Subroutines and External Files

As previously described, all aspects of the developed methodology were implemented in Marc using subroutines to provide the required functionality. All the Marc subroutines developed were contained in a single Fortran file, which was compiled to give a single executable, *damage.exe*. This file needed to be included in the analysis working directory, and referenced using the "-pr damage" parameter in the "run_marc" run command for any analysis. A complete list of all subroutines used is given below, where a thorough description of the more complex subroutines is given in the corresponding sections throughout this work.

- USDATA: This is a Marc subroutine called at the beginning of the analysis, which is provided to define any user-defined variables. This subroutine was used to read in all the information stored in external data files, which was then stored in a series of internal variables within common blocks. The use of the common blocks meant that these internal variables could be accessed and modified by any subroutine throughout the analysis, which allowed for the transfer of information between subroutines.
- UFORMSN: This is the Marc subroutine used to define the constraint matrix for any user-defined MPCs.
- HYPELA2: This Marc subroutine was used to define hypoelastic material properties, which was used in the in-plane ply failure approach.
- UEDINC: This is the dummy subroutine provided in Marc that is called at the end of every increment, which was used extensively to monitor and control all aspects of the analysis approach.
- PLOTV and UPSTNO: Marc subroutine used to calculate any user-defined element and node variables respectively, which were then available in the *.t16* results file.
- UTIMESTEP: This subroutine is provided in Marc to allow control of the time step, and was used in the interlaminar crack growth degradation model to maintain an appropriate increment size.
- UACTIVE: This is the Marc subroutine used to activate and de-activate elements. This subroutine was applied in the interlaminar crack growth degradation model, and was used to ensure that the gap elements were only activated between nodes of debonded user-defined MPCs.
- GAPU: This is the Marc subroutine used for each gap element to provide the gap direction and closure distance.
- Additional subroutines were written to provide common utility functions, such as calculating the angle, orientation or cross-product of two vectors, and assisting with reading data from the external files.

In addition to the Fortran executable, the analysis approach used a series of external data files containing all the user-defined and other information necessary for the various subroutines. These external data files are listed below, where < > is used in place of the job name. Though it was desirable to limit the amount of external files required for the analysis, the use of separate files was necessary in a number of instances to allow for user input and provide the initial data for a number of internal variables used by the various subroutines.

- <>_*u-data.csv*: This file contained all the user-defined data necessary for the analysis methodology. This included: the nominal ply stiffness values used for the in-plane ply failure analysis; the ply strength properties used by both the in-plane damage and delamination initiation approaches; fracture toughness values and mixed-mode criterion parameters for the interlaminar damage growth analysis; and, a series of parameters and toggles used to control various aspects of each subroutine, including toggling the use of each approach, selecting the various criteria, setting parameters such as allowables and reduction factors, and controlling the amount of output written to the *.out* file. It was typical to save a common version of this data file for the database, which was then copied and modified for each particular job.
- <>_*u-gaps.txt*: This file contained a list of all gap elements in the model. For each gap element, the gap state and node numbers were also listed, and were used to determine which gap elements needed to be activated and de-activated between increments.
- <>_*u-lyrs.txt*: This file contained the layer orientations at every ply for each composite material in the model.
- <>_*u-mats.txt*: This file listed each element and its corresponding material number, which was used in combination with the orientation data to determine the ply orientations for every element in the model.
- <>_*u-quads.txt*: This file listed each shell element and its four corresponding nodes, which was used to create the shell plane and normal directions necessary for the gap elements
- <>_*u-states.txt*: This file listed all the information needed for the user-defined MPCs. For each MPC, the state, neighbouring MPCs and dependent and independent nodes were listed. The state data was used to define any initially debonded regions, and the corresponding crack front nodes.
- <>_*u-ufl.txt*: This file listed the in-plane failure indices and stress reduction trigger for every integration point in the model. As there were four integration points, per layer, per element, this file could be quite large. The failure indices were used to define any initially softened elements, which was particularly relevant to define pre-damage due to impact in the manner previously described in Section 5.1.4.
- <>_*run.bat*: This was a batch file that contained the "run_marc" command used to run any analysis, and any additionally parameters such as including the Fortran executable and the global results file in a global-local analysis. This file was not strictly necessary for the functionality of the approach, but was used to run jobs quickly and without having to open a separate command window.

5.1.6 Overview

The analysis methodology developed allows for a complete analysis of the postbuckling and collapse behaviour of composite structure designs, including the effects of damage. The features of the methodology make it suitable in both a design and comparative analysis context. In a typical design scenario, various configurations of a particular design are considered, and a design goal is formulated to evaluate each configuration. Alternatively, in comparison with experiment, numerical models are generally used to make pre- and post-test simulations, and conduct parametric studies in order to investigate the sensitivities of the configuration. The methodology developed allows for the use of damage as a design parameter in both of these analysis scenarios, and was specifically developed to be suitable for the analysis of large, postbuckling structures undergoing collapse.

The methodology also allows for the analysis of specimens that were intact or that had pre-defined damage regions, which include Teflon-induced debonding and impact-induced damage sites. This makes it suitable for certification and damage tolerance purposes, as it allows for realistic estimations of structural behaviour including the effects of the critical composite damage mechanisms. The application of the developed methodology is further illustrated in Figure 5.2, which gives a flow chart of analysis procedures for intact and pre-damaged structures, and the interaction between intact and pre-damaged models.

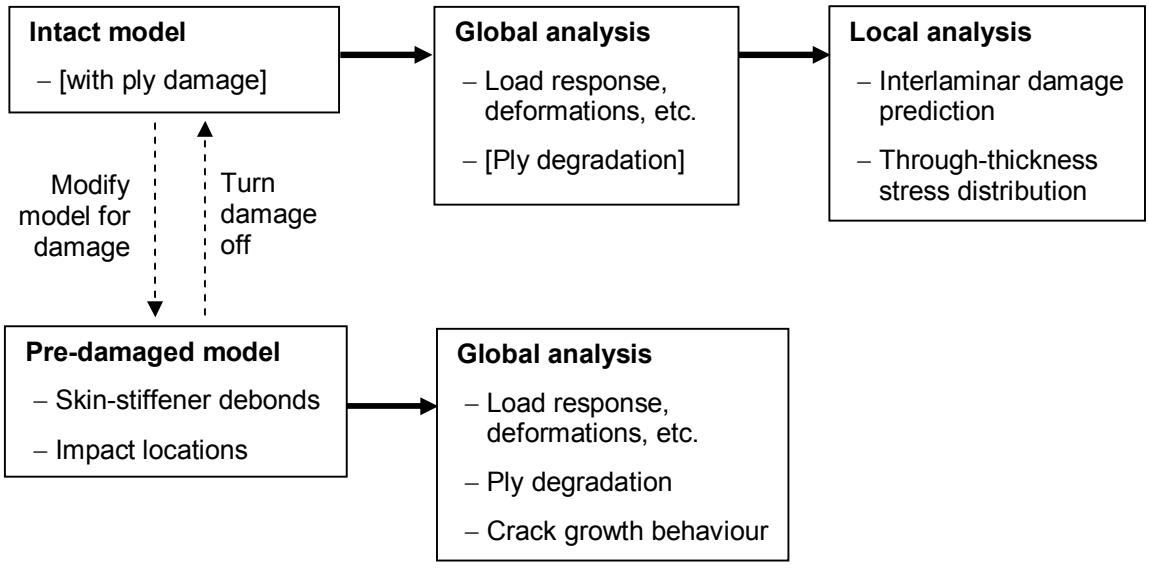

Figure 5.2: Developed methodology analysis procedure for intact and pre-damaged models

5.2 Validation

In this section, results are presented for the validation of the analysis methodology using experimental results from collapse tests of single-stiffener specimens. These specimens used the COCOMAT D1 and D2 configurations, where each configuration had both undamaged and pre-damaged specimens tested. For each test series, the experimental results are compared to the numerical predictions, and the results are used to validate the different aspects of the developed analysis methodology.

The specimens consisted of a flat skin and secondary-bonded single stiffener and were manufactured and tested at Aernnova. Four specimens were tested, which consisted of the D1 and D2 designs in undamaged (intact) and pre-damaged (debond) configurations. The debond regions were created by replacing the bonding adhesive with a strip of Teflon across the width of the stiffener flange. The length of the debond relative to the panel free length (~25%) and the focus on full-width debonds were chosen to ensure that crack growth would be observed prior to panel collapse. Though likely to be larger and more severe than defects encountered in real structures, this type of debond was necessary given the use of the results for validation of the developed approach. More realistic damage types, both smaller relative lengths and partial debonds, were the focus of other experimental investigations within the COCOMAT project (Abramovich 2007), and will be used in future comparison and validation studies.

The specimens were encased in potting to ensure an even distribution of the applied load. In experimental testing, a range of data collection devices were applied, which included strain gauges, video recordings and LVDTs on the stiffener, skin and between the loading grips. For the debond specimens, a system was used in which thin metallic paint strips were applied at the debond edges and changes in the electrical current were monitored to predict the onset of debond growth. Specimen details are summarised in Table 5.3 and Figure 5.3.

Table 5.3: D1 and D2 single-stiffener specimen details, all dimensions in mm

Parameter	**D1**	**D2**
Total length, L	400	500
Free length, L_f	300	400
Width, b	64	112
Skin lay-up	$[90,\pm45,0]_S$	$[\pm45,0,90]_S$
Stiffener lay-up	$[(\pm45)_3, 0_6]_S$	$[\pm45,0_2,90_2]_S$
Material	IM7/8552	IM7/8552
Ply thickness, t	0.125	0.152
Stiffener height, h	14	28.91
Stiffener width, w	32	56
Debonded length, d (debond specimens only)	80	105

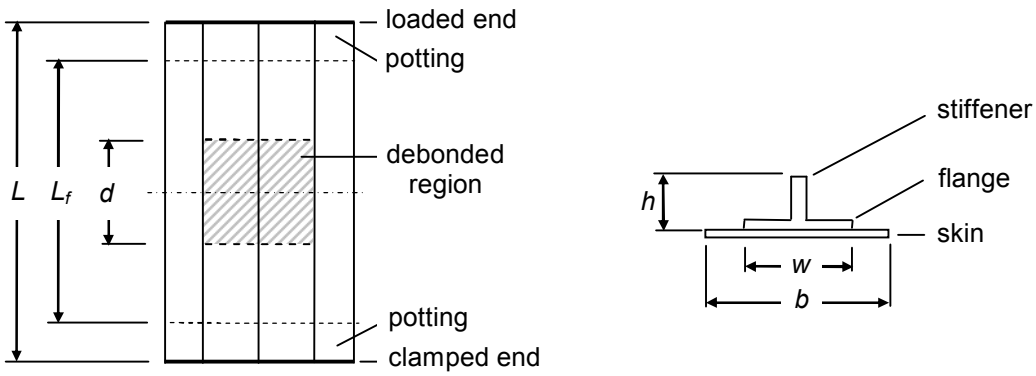

Figure 5.3: Single-stiffener specimen geometry

5.2.1 Intact Specimens

5.2.1.1 Experimental Results

For the intact specimens, experimental results are summarised below, where Figure 5.4 gives the applied load-displacement curves, and Figure 5.5 shows images taken during testing of the D1 and D2 specimens. There were three specimens tested for both D1 and D2 configurations, and there was good agreement for each configuration in terms of structural stiffness and specimen behaviour. Under compression, the D1 specimens all showed a buckling pattern of eight buckling half sine waves, leading to collapse caused by ply damage around the loaded or clamped ends. The D2 specimens buckled into an asymmetric pattern of an inwards and outwards half wave, and failure occurred near the centre of the specimen, though closer to the loaded end. All specimens displayed explosive failure at collapse, where the failed specimens showed a wide range of damage types, which included fibre fracture in the stiffener, and matrix cracking and delamination around the skin-stiffener interface. However, the development of all ply damage types was instantaneous, and it was not possible to determine the sequence of damage progression.

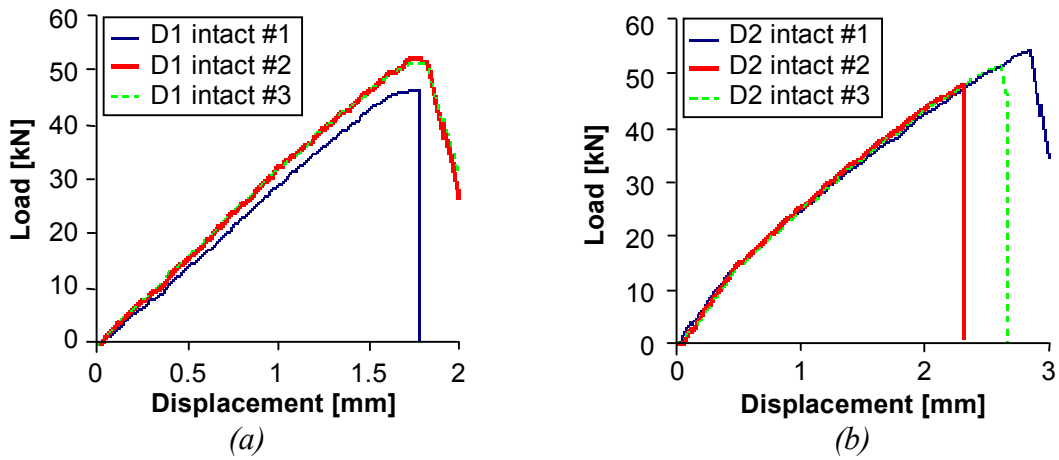

Figure 5.4: Single-stiffener intact specimens, load-displacement: (a) D1 (b) D2

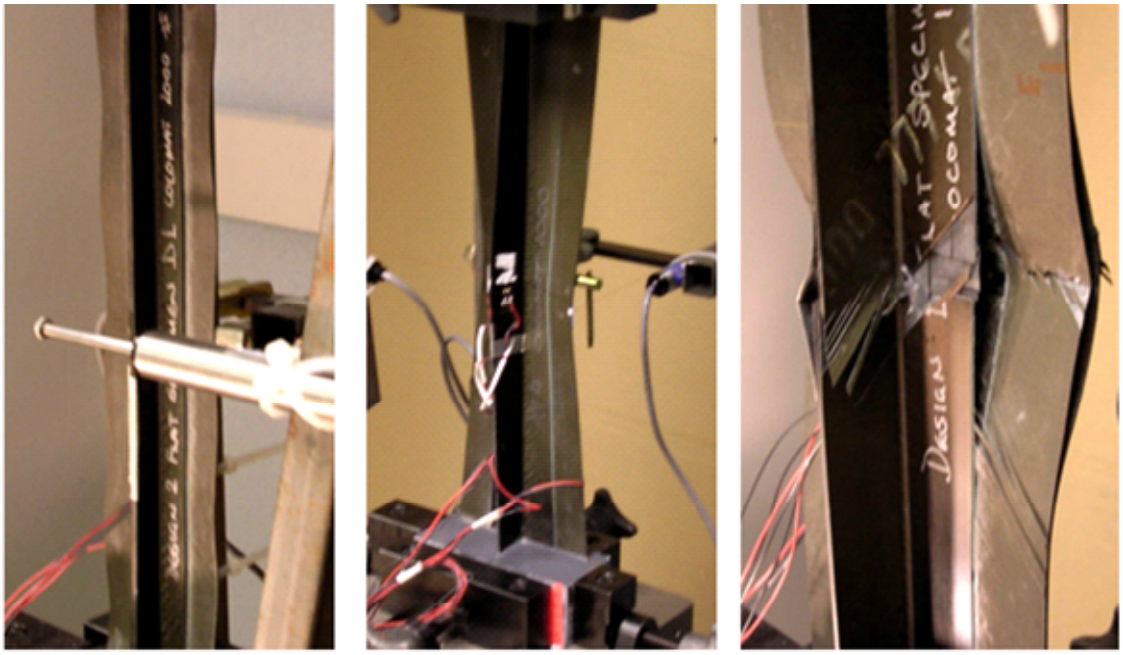

(a) (b) (c)

Figure 5.5: Single-stiffener intact specimens: (a) D1 antisymmetric buckling pattern (b) D2 antisymmetric buckling pattern (c) example damage at failure (D2 test #1) showing fibre fracture, matrix cracking and skin-stiffener debonding (courtesy of Aernnova)

5.2.1.2 Numerical Analysis

Finite element models were created for global and local analysis of both specimen types. The global models consisted of a regular grid of shell elements, where the flange and skin were modelled using separate but coincident shell element layers with dummy plies connected by pin-jointed tying constraints. This was done so that the intact models could be re-used for the debond specimens, where the debond analysis is detailed in a later section. Figure 5.6(a) gives the load and boundary condition definition for the global model, where the applied load varied between the D1 and D2 specimens and was based on the displacements applied in the experiments. The local models were generated using solid brick elements at a ply-level mesh refinement, as shown in Figure 5.6(b) for the D1 specimen. The local models used 8 elements along the length of the specimen, corresponding to a cross-section 4 mm thick, and applied a global-local boundary condition to the nodes on the two end faces of the cross-section that corresponded to the 21 nodes in the global cross-section (as shown in Figure 5.14(a) for the debond specimens). The material properties for all models are given in Table 5.4, where properties were taken from material characterisation tests performed by other COCOMAT partners. A summary of all FE models is given in Table 5.5.

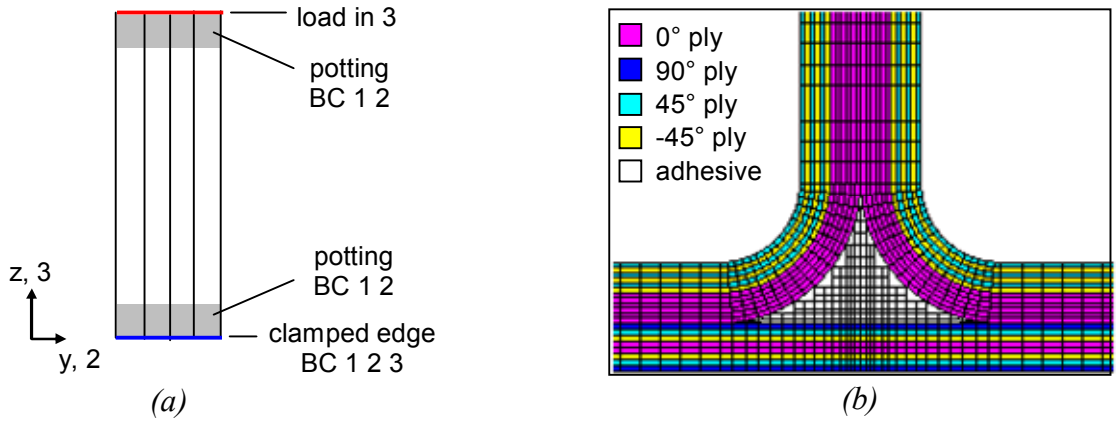

(a) *(b)*

Figure 5.6: Single-stiffener specimen: (a) Global model, load and boundary conditions (b) Local model skin-stiffener interface with material definition (D1 model shown)

Table 5.4: Material properties for carbon unidirectional tape IM7/8552

Stiffness property	Value	Strength property	Value
E_{11} [GPa]	147	X_t [MPa]	2379
E_{22} [GPa]	11.8	X_c [MPa]	1365
ν_{12}	0.3	Y_t [MPa]	39
G_{12} [GPa]	6.0	Y_c [MPa]	170
G_{23} [GPa]	4.0	S_{xy} [MPa]	102
G_{31}* [GPa]	6.0	S_{yz} [MPa]	78

* assumed

Table 5.5: Single-stiffener specimen FE model details

Model	Nodes	Elements		MPCs / Ties
D1 global	2430	2240	shells	729
D1 local	27,644	22,648	solids	–
D2 global	3030	2800	shells	909
D2 local	34,376	27,736	solids	–

All models were run in Marc v2005r3 using the nonlinear solver with a full Newton-Raphson procedure and a load residuals tolerance of 0.01. For the local models, the degenerated Tsai criterion was applied to detect the onset of delamination, and is given by

$$\left(\sigma_x / X_t\right)^2 + \left(\sigma_z / Z_t\right)^2 + \left(\tau_{yz} / S_{yz}\right)^2 = f \,, \tag{4.1}$$

where: $\{\sigma_x, \sigma_z, \tau_{yz}\}$ and $\{X_t, Z_t, S_{yz}\}$ are stress and strengths in the longitudinal, through-thickness tensile and through-thickness shear directions; and, f is a failure index such that delamination occurs when f is greater than or equal to one, and failure in an element was deemed to occur when the average f of all the element integration points was greater than one.

Analysis results are presented below, where Figure 5.7 gives the load-displacement curves, Figure 5.9 shows the deformation and ply damage development, and Figure 5.8 gives the local model deformation shape and delamination prediction.

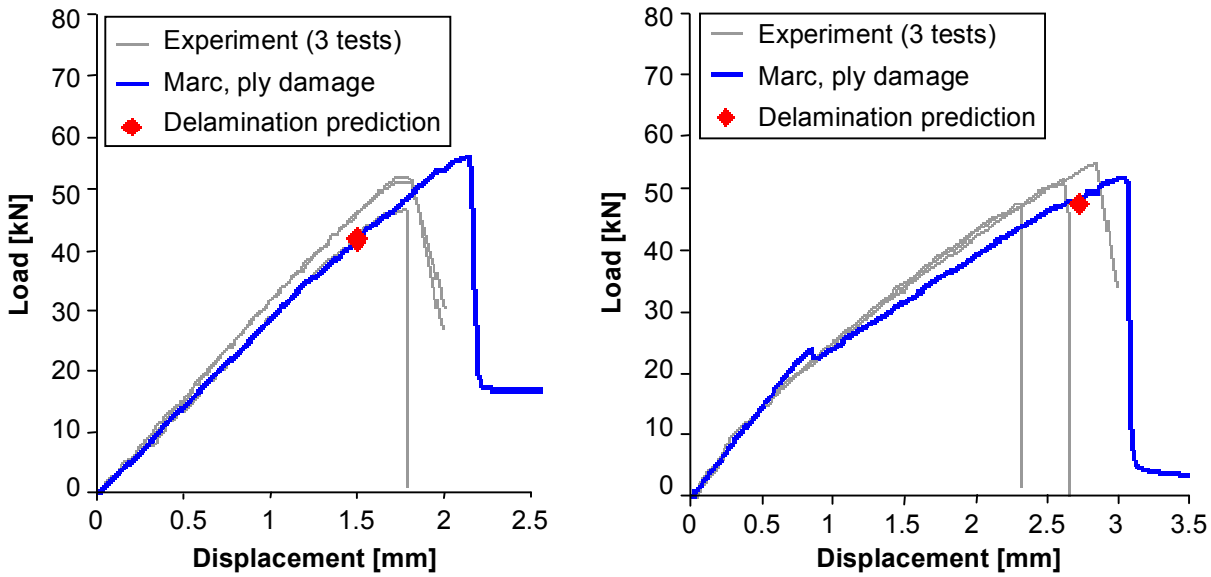

Figure 5.7: Single-stiffener intact specimens, applied load versus displacement, experiment and FE predictions: (a) D1 (b) D2

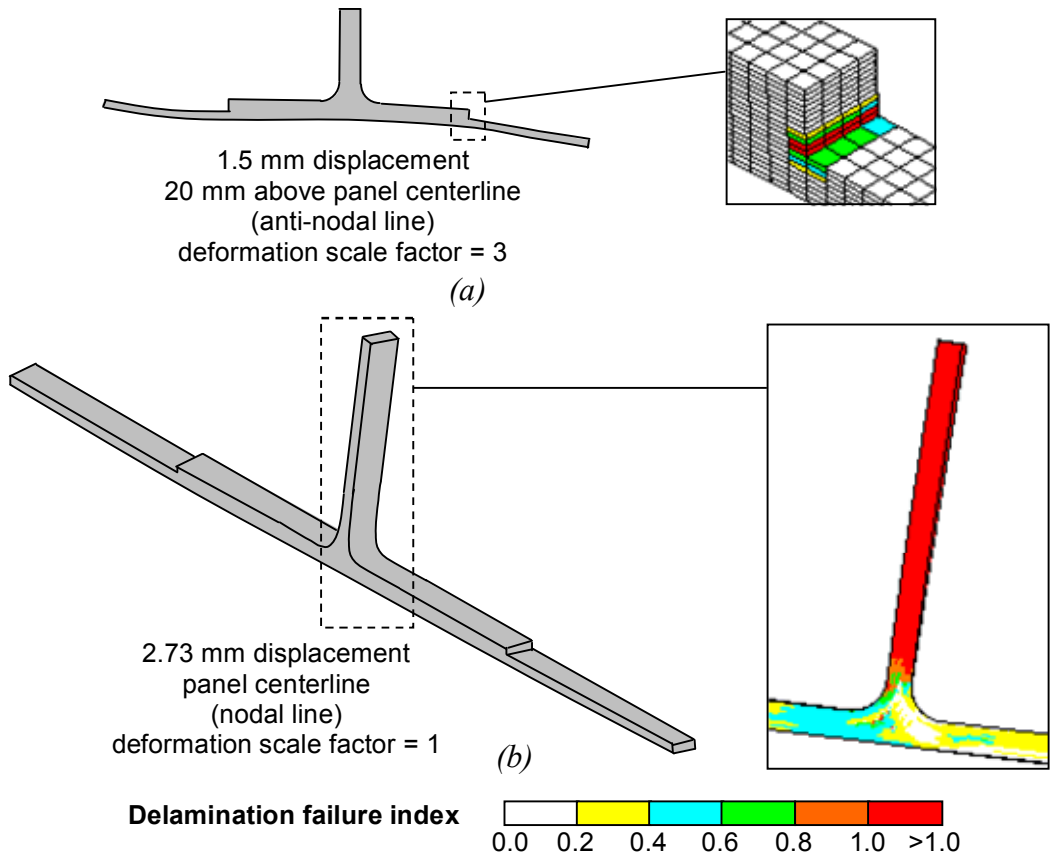

Figure 5.8: Single-stiffener intact specimens, local delamination prediction at applied displacement: (a) D1 (b) D2

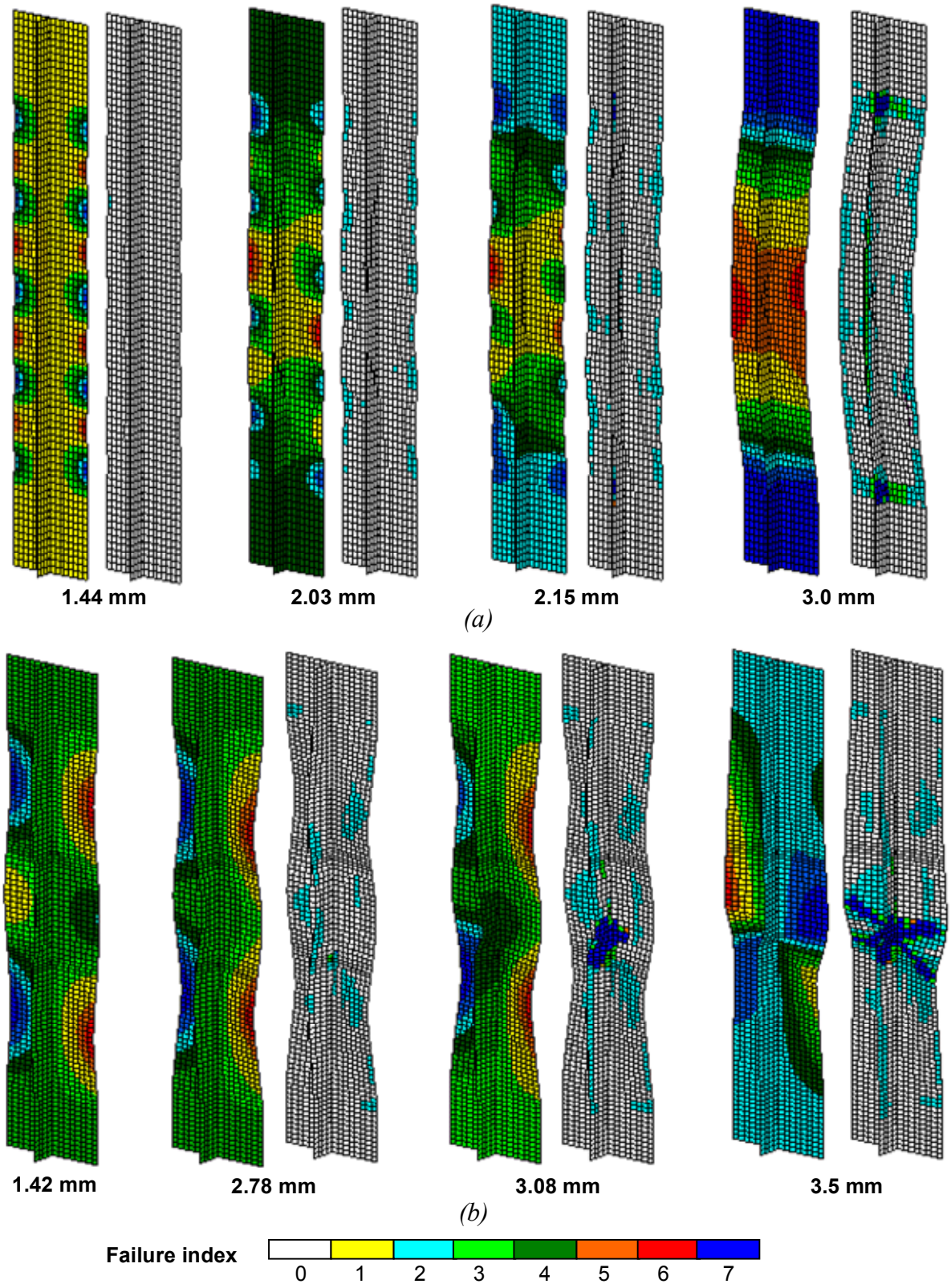

Figure 5.9: Single-stiffener intact specimens, out-of-plane fringe plot and ply damage failure index at various applied displacement levels: (a) D1 (b) D2

For the intact specimens, the D1 model gave very good correlation with the specimen stiffness, and showed eight buckling half sine waves, which correlated well with the experimental pattern. The D2 model predicted three half waves, and whilst this was different from that seen experimentally, the stiffness also gave very good correlation with the test data. For both models, delamination was predicted to initiate in the local models prior to the onset of fibre failure in the stiffener, where the latter led to collapse in the numerical models. The experimental collapse values gave closer comparison with the local failure predictions, which indicated that skin-stiffener debonding triggered collapse, though this was not able to be determined in the experimental specimens due to the instantaneous nature of the failure.

In the D1 specimen, debonding was predicted to occur at an anti-nodal line, where the buckling deformations were at a maximum, whilst the D2 specimen showed debonding at a nodal line due to a high degree of twisting in combination with transverse shear, as seen in Figure 5.9 and Figure 5.8. Though the debonding and fibre fracture locations did not exactly correspond to the damage sites seen in the experiment, this was the result of the different displacement patterns and the fact that due to the periodic nature of the buckling patterns the failure indices at all of the other nodal and anti-nodal lines were very close. However, the comparison in Figure 5.7 clearly shows that the developed analysis methodology was capable of predicting the load-carrying capacity of the specimens, and the collapse predictions were realistic and within the experimental scatter of the results.

The use of the strength-based criterion was seen to give accurate predictions for the initiation of delamination. However, as mentioned in Chapter 2, in order to achieve reasonable results it was necessary to apply a number of approaches aimed at mitigating the well-known stress singularity issues. Firstly, failure was determined on an element basis, where an average of the failure indices at all integration points in the element was taken. This can be considered as introducing a characteristic length into the analysis, and using ply thickness element lengths is both common and advantageous in this regard as it implicitly accounts for the dependence of the delamination strength on the ply thickness (D'Ottavio & König 2006). Though not demonstrated in this work, mesh refinement studies or previous modelling experience would be required in order to ensure that the element sizes were large enough to effectively "average out" the singularity at the flange edge, whilst being small enough to capture the stress field accurately.

Another approach that was necessary due to strength-based considerations in the local model was to use eight elements in the axial, or cross-section thickness, direction. The global-local boundary condition was applied on only the outside nodes of each end of the cross-section, and the inner four elements only were used to monitor the failure index. The outer elements were not considered to avoid the spuriously high stresses that were recorded at the nodes with the boundary condition applied. The onset of delamination was then deemed to occur when a line of elements through the four inner cross-section elements had failed. These two approaches of using element average stresses and avoiding the boundary condition problems ensured that the failure predictions were much less influenced by the stress singularity effects, and that the real delamination-causing effects such as maximum bending or twisting at the anti-nodal and nodal lines could be accurately captured.

There are also a number of issues that are important for the applicability of the developed interlaminar damage detection approach. As the approach is strength-based, a dependence on element size is unavoidable, so that mesh sensitivity studies will generally always be required, and stress peaks at geometry and boundary conditions changes must always be taken into consideration. Importantly, whilst the comparison with experimental results for the T-section specimens in Chapter 3 did validate the prediction of damage initiation in the skin-stiffener junction, failure at other locations in the skin-stiffener interface, in particular delamination initiating at the flange edge, was not strictly validated using the results shown. Similarly, the analysis in Chapter 3 was performed with 2D elements on specimens that were essentially 2D in nature, so that the capability of the approach to predict failure in the presence of significant 3D effects was also not strictly validated. However, in spite of these issues, the comparison with experiment in both Chapter 3 and in this chapter did demonstrate that the developed methodology was capable of accurately representing the load-carrying capacity and specimen behaviour, as well as providing realistic predictions of the collapse load.

5.2.2 Debond Specimens

5.2.2.1 Experimental Results

The debond specimens were nominally identical to the intact specimens, except for a full-width debond located centrally in the skin-stiffener interface, and were statically loaded in compression until collapse. The experimental results are summarised below, where Figure 5.10 gives the applied load-displacement curves, and Figure 5.11 shows images taken during testing of the D1 and D2 specimens. There were six D1 specimens tested and nine D2

specimens tested, where three of the D2 specimens showed significantly different structural stiffness and were excluded from Figure 5.10(b), though in general the results showed good consistency for each configuration. All debonded specimens gave similar results, which involved local buckling of the debond region, lateral deflection of the stiffener, growth of the debond in the skin-stiffener interface, and final collapse as shown in Figure 5.11.

Following the collapse testing, an investigation into the crack growth in the skin-stiffener interface was conducted, using one specimen each from the D1 and D2 configurations. Ultrasonic scans of the collapsed specimens were conducted, to determine the extent of debonding in the skin-stiffener interface, and results are given in Figure 5.12. The specimens were then cut approximately 10-15 cm ahead and behind of the initial crack location at both ends of the pre-damaged area, except for the D1 specimen, where the left edge was cut at the initial crack location. The cutting separated the skin and stiffener in these regions, as the skin-stiffener interface was detached due to either the initial Teflon insert of crack growth during testing. The separate skin and stiffener segments, from the left (L) and right (R) debond edges of the D1 and D2 specimens were then inspected visually, both to assess the quality of the bonding and to compare the fracture surfaces of the two specimens, and the results are shown in Figure 5.13.

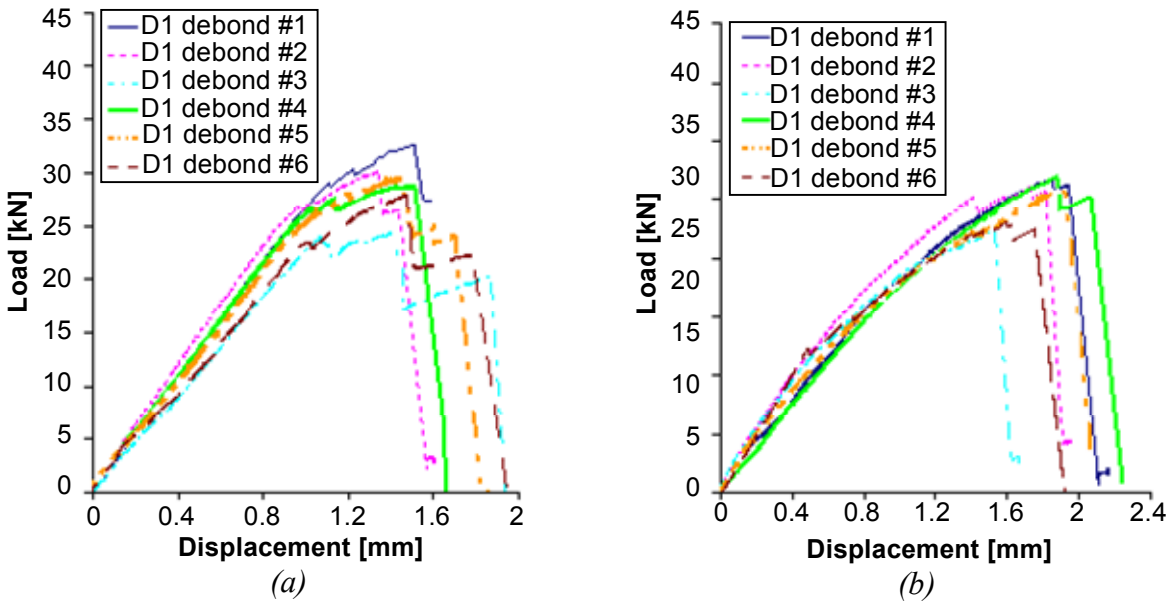

Figure 5.10: Single-stiffener debond specimens, load-displacement: (a) D1 (b) D2

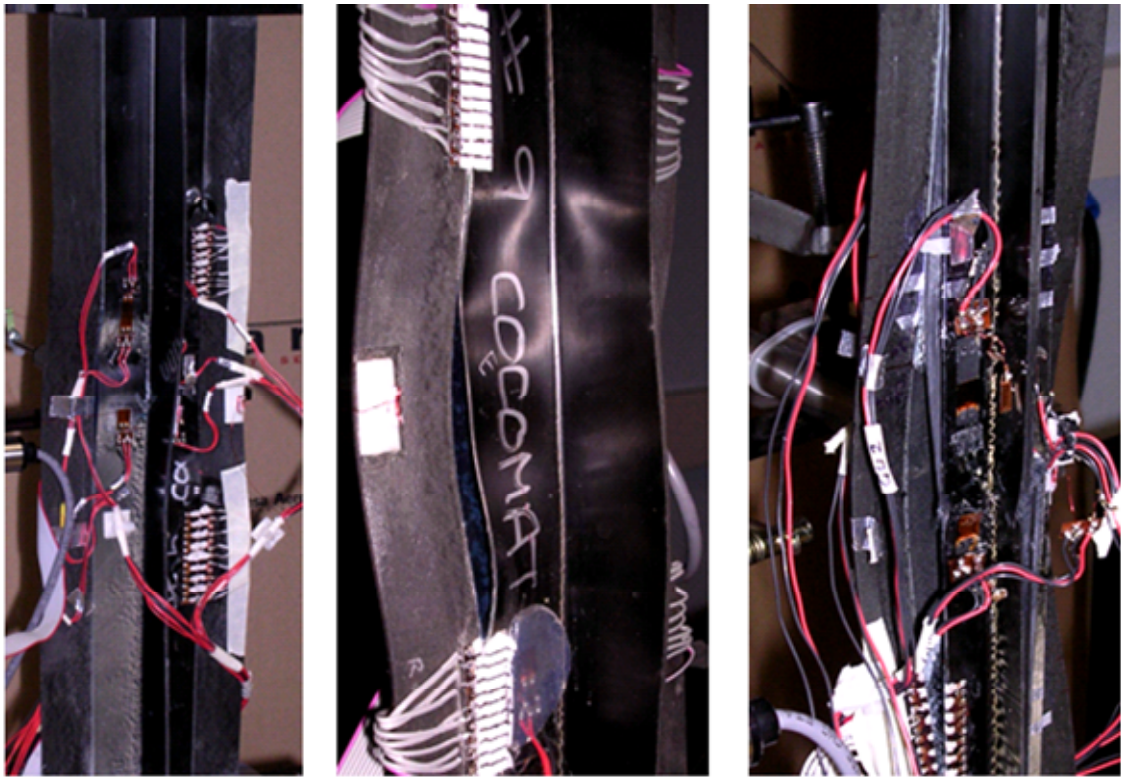

(a) (b) (c)

Figure 5.11: Single-stiffener debond specimens: (a) Deformation before failure (D2 Test #6) (b) D2 asymmetric buckling (D2 Test #8) (c) Damage at failure: skin-stiffener debonding, stiffener delamination and fracture (D1 Test #3) (courtesy of Aernnova)

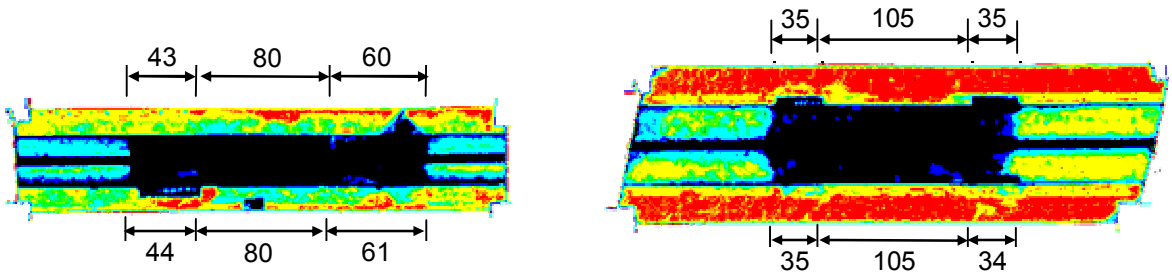

(a) (b)

Figure 5.12: Debond specimens, ultrasonic scans after collapse, lengths in mm (a) D1 (b) D2

Under compression loading, the skins of all specimens buckled away from the flange in a single half-wave that covered the entire flange width. Flange buckling varied between designs, where the D1 specimens gave mostly symmetrical flange buckles consisting of single half-waves buckling away from the skin, and the D2 specimens gave two types of behaviour involving antisymmetric patterns, one with multiple half-waves per flange both buckling away from the skin (see Figure 5.11(b)), and the other with single half-waves buckling on one side away and on the other side with the skin.

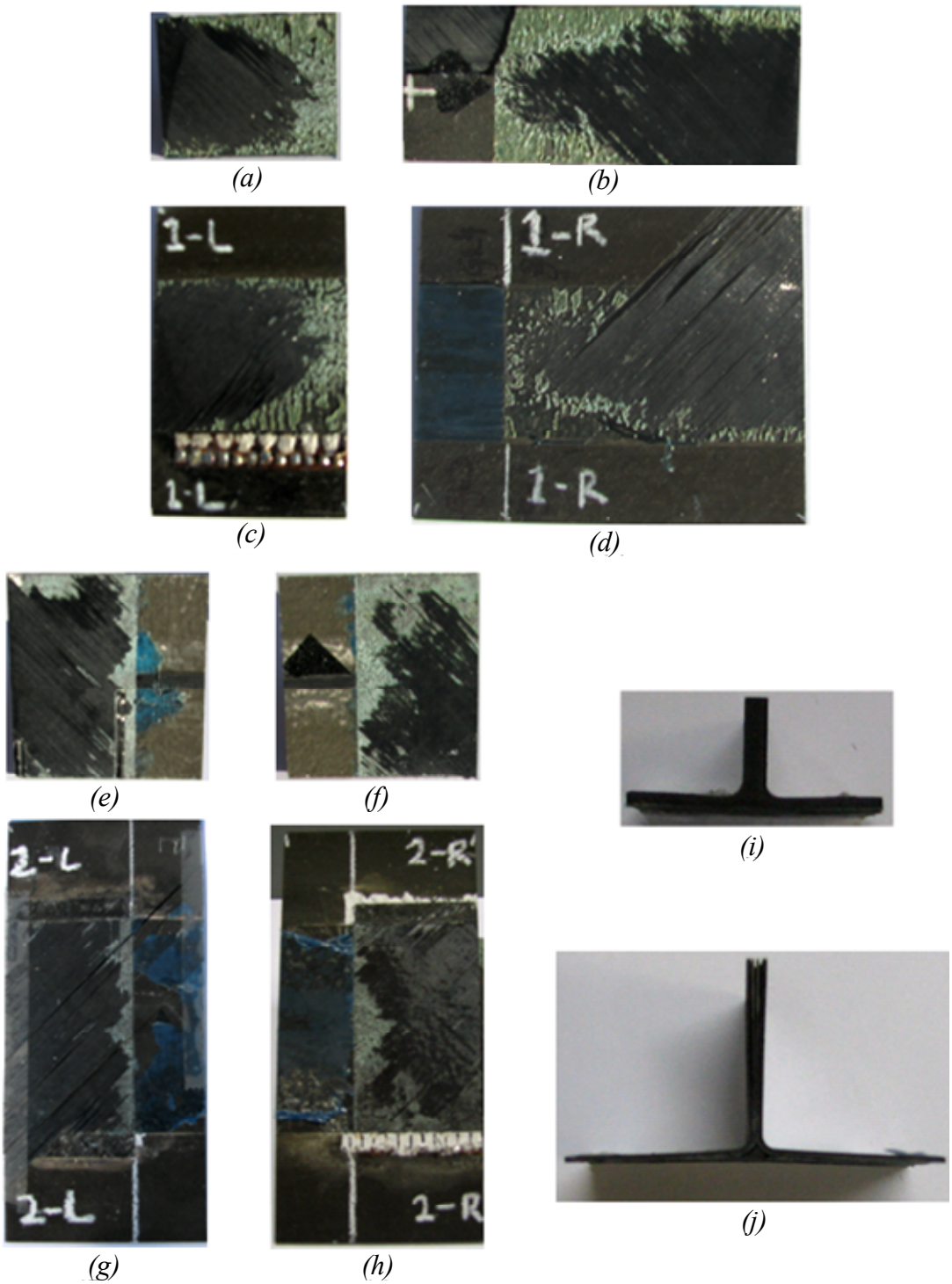

Figure 5.13: Debond specimens segments: (a)-(b) D1 stiffener L-R, (c)-(d) D1 skin L-R, (e)-(f) D2 stiffener L-R, (g)-(h) D2 skin L-R, (i) D1 stiffener (j) D2 stiffener

The growth of the debonded region was characterised by visual observation, cracking noises, and jumps in the load, LVDT and strain output. Debond growth was also detected using a system of metallic paint strips connected in parallel to an electric circuit, where crack growth through the system ruptured strips sequentially and reduced the voltage in the circuit, so that the voltage levels could be used to characterise the debond length. Crack growth typically

progressed in a stop-start manner, where load increases caused small finite crack growth steps, though for some specimens cracking was heard without any visual indications that damage was progressing underneath the flange. For the D1 specimens, crack growth typically initiated at around 1.0 mm compression and then continued in stages until collapse at around 1.4 mm compression. The D2 specimens generally gave less crack growth, and though occurring over a period of around 0.4 mm compression typically only had two or three small increases in debond length before collapse.

Collapse of the specimens was characterised by fibre fracture and delaminations in the stiffener, growth of the skin-stiffener debond, and matrix cracking in the stiffener, flange and skin. From the test results, it is thought that the lateral deflection of the stiffener caused delaminations in the central +45°/0° interfaces of the stiffener, which led to catastrophic failure involving fibre fracture in the 0° stiffener plies and extensive growth of the debond in and around the skin-stiffener interface, though further post-test specimen analysis is required.

The investigation into the skin-stiffener interfaces of the collapsed specimens revealed significant differences between the D1 and D2 specimens. The bonding of the adhesive in the D2 specimen appeared to be of much higher quality than in the D1 specimen. This can be seen in Figure 5.13, where the surfaces visible on the crack faces indicate the interface at which cracking occurred in the specimen. For the D2 specimen, though there was an initial region of adhesive visible, the fracture surface was dominated by the ply material, which indicated that fracture occurred initially by debonding the skin and stiffener before the crack moved to an adjacent interface between two plies. For the D1 specimens, the ply material was seen mainly underneath the stiffener, and there were significant regions of adhesive visible in the areas underneath the flanges. This means that the D2 specimen would have had a significantly tougher skin-stiffener interface than the D1 specimen, as the fracture toughness values for failure of the adhesive bonding are generally an order of magnitude smaller than for fracture between two plies (Baker, Dutton & Kelly 2004).

From the inspection of the specimens, it appears that the most likely reason for the difference in bonding quality of the two specimens was the difference in distortion of the flanges in the manufacturing process. In curing, the asymmetric flanges ($[(\pm 45)_3, 0_6]_S$ for D1 and $[\pm 45, 0_2, 90_2]_S$ for D2) led to distortion, causing the D1 specimens to bend inwards and the D2 specimens to bend outwards. This “springback” behaviour was noted by Aernnova during manufacture, and special moulding tools to account for this were developed. However, from

Figure 5.13 (i) and (j), it can be seen that the tooling may not have fully corrected the problem, as the D1 stiffeners appeared to show inwards bending due to springback, while the D2 stiffeners appeared fairly straight or even slightly bent outwards. This would mean that when the skins and stiffeners were pressed together during bonding there would have been less pressure applied underneath the flanges of the D1 stiffeners, which would have had a significant effect on the bonding process. Furthermore, the adhesive fracture surfaces themselves appear different, with the D2 adhesive regions characterised by fine and tightly packed voids, whilst the D1 specimens had larger and more loosely spaced void regions. The D1 adhesive surface also appears to have a glossier appearance, particularly evident in Figure 5.13(d), which further indicates that the adhesive did not bond well with the regions underneath the D1 flange. These observations reinforce the conclusion that skin-stiffener bonding of both specimens was different, mainly underneath the stiffener flanges, and that this was likely due to the different curing behaviour of the two specimens.

5.2.2.2 Numerical Analysis

Finite element models were created for global analysis of both specimen types, and were taken from those used previously for the intact specimens, where the load and boundary condition, material properties and FE models were previously summarised in Figure 5.6(a), Table 5.4 and Table 5.5 respectively. For the debond models, user-defined MPCs were used in the skin-stiffener interface, and the debonded region was created by setting their initial states to 1 and 2 for crack front and debonded, as shown in Figure 5.14 for the D1 specimen. Additional material parameters were required for the fracture properties and are given in Table 5.6. These properties were taken from tests performed within COCOMAT, except for the η coefficient for the mixed-mode failure law, which was taken from literature results from Hansen and Martin (1999) for mixed-mode testing on the same material.

All models were run in Marc v2005r3 using the nonlinear solver with a full Newton-Raphson procedure applied, and a tolerance of 0.01 on load residuals. For both D1 and D2 specimens, propagation methods 1 and 4 were applied, as described in Chapter 4. However, for both specimens, an updated set of modification factors were determined for PM 4, as during the analysis it was seen that the modification factors developed from the fracture mechanics characterisation coupons in Chapter 4 were actually quite conservative. Using the original PM 4 approach, the first 25 instances of crack growth in both D1 and D2 models were studied, in order to determine more appropriate factors for the single-stiffener specimens. The

results of this investigation are summarised in Table 5.7, where the crack and growth types were defined in Chapter 4, and full details of the investigation are given in Appendix A.

Table 5.6: Fracture properties for carbon unidirectional tape IM7/8552

Fracture property	Value
Mixed-mode criterion	B-K
$G_{I\,c}$ [kJ/m^2]	0.243
$G_{II\,c}$ [kJ/m^2]	0.514
$G_{III\,c}$ * [kJ/m^2]	0.514
B-K coefficient, η *	4.6

* assumed

Table 5.7: Single-stiffener specimen PM 4 f_m factors from first 25 instances of crack growth

Model	Crack type	Growth type	Number of occurrences	Updated modification factor (original)		
				$f_{m\,I}$	$f_{m\,II}$	$f_{m\,III}$
D1	1	1	3	6.0 (2.5)	3.0 (1.0)	1.5 (1.5)
	1	2	1	8.0 (1.5)	2.0 (1.0)	1.0 (1.33)
	2	1	10	10.0 (2.0)	3.0 (1.0)	1.33 (1.0)
	2	2	3	2.33 (1.0)	1.5 (1.0)	1.0 (1.0)
	7	1	4	100.0 (1.33)	2.0 (1.0)	1.33 (1.5)
	7	2	1	5.5 (1.0)	1.5 (1.0)	1.0 (1.0)
	8	1	3	4.0 (1.33)	1.5 (1.33)	1.0 (1.0)
D2	1	1	4	2.0 (2.5)	1.33 (1.0)	1.0 (1.5)
	2	1	9	5.0 (2.0)	3.5 (1.0)	1.0 (1.0)
	3	1	4	1.33 (1.5)	1.0 (1.33)	1.0 (1.0)
	7	1	8	1.5 (1.33)	1.0 (1.0)	1.0 (1.5)

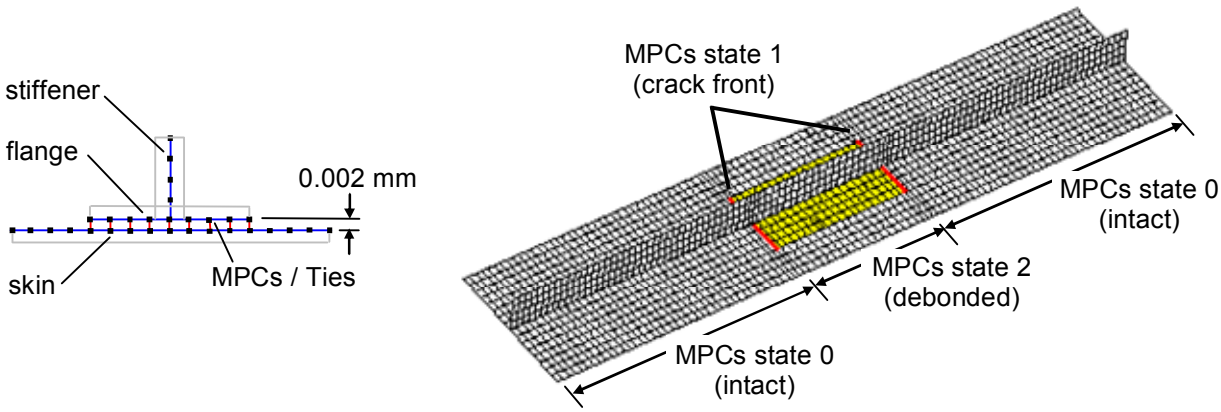

(a) *(b)*

Figure 5.14: Single-stiffener specimen global FE model: (a) Skin-stiffener interface (dummy plies not shown) (b) User-defined MPC definition (D1 model shown)

Analysis results are presented below, where: Figure 5.15 gives the load-displacement curves; Figure 5.16 shows the buckling deformation pattern, where the gap elements can be seen across the skin-stiffener interface; Figure 5.17 illustrates the growth of the debonded area, viewed from the skin side; Figure 5.18 gives the strain energy release rate distribution at the upper and lower edges of the debonded area just prior to crack growth onset for the D1 PM 4 and D2 PM 4 models; Figure 5.19 gives the results of a mesh density study that used the nominal mesh outlined previously and investigated two additional meshes of reduced element size at the crack front; and, Figure 5.20 illustrates the ply damage mechanisms present at collapse of the specimens.

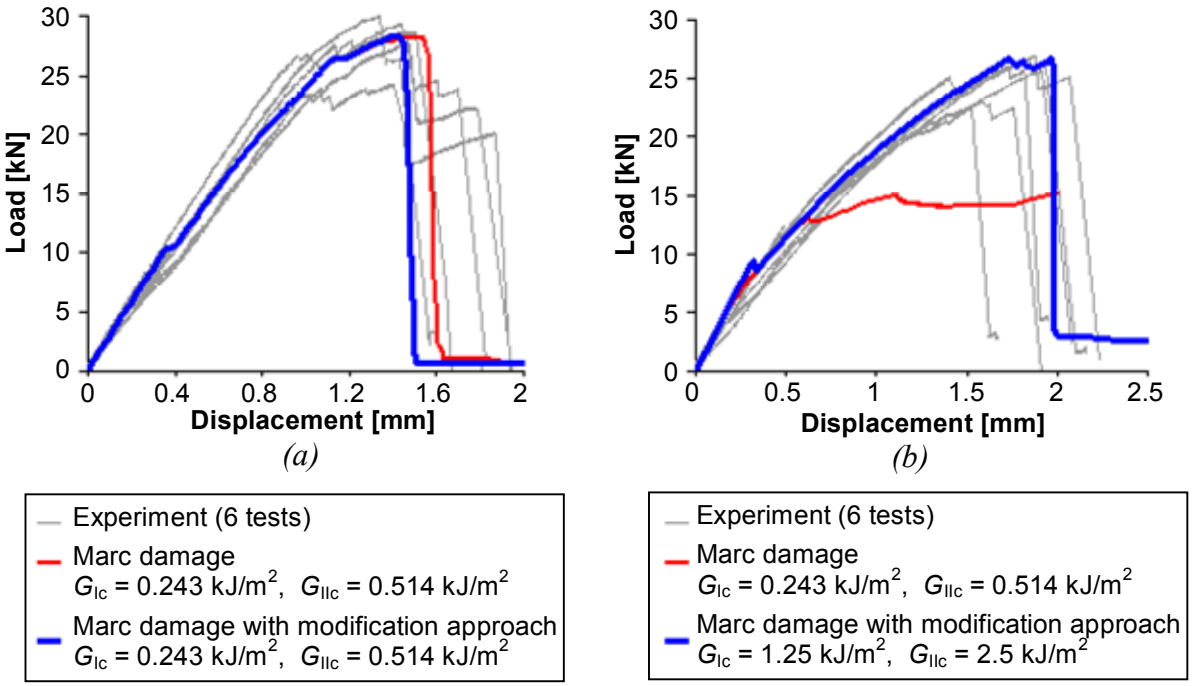

Figure 5.15: Single-stiffener debond specimens, load-displacement: (a) D1 (b) D2

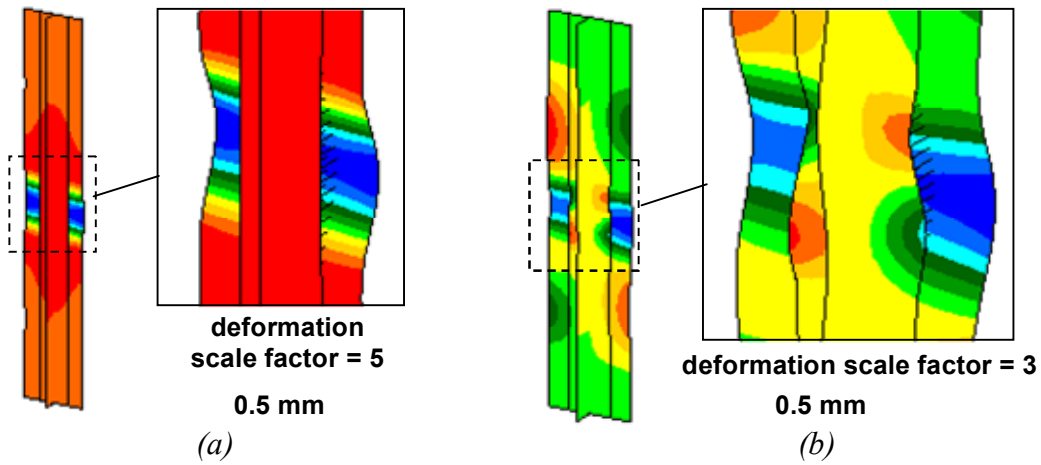

Figure 5.16: Single-stiffener debond specimens, buckling deformation pattern at applied displacement: (a) D1 (b) D2

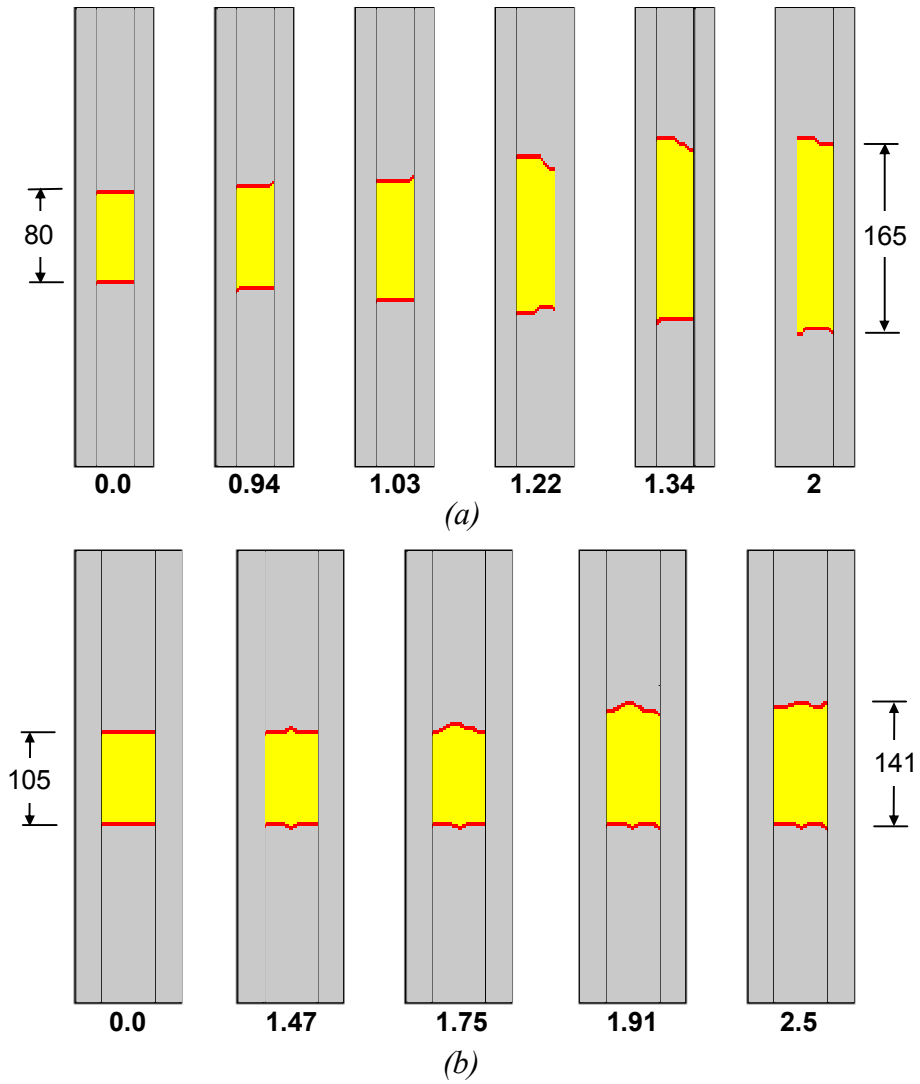

Figure 5.17: Single-stiffener debond specimens, debond growth at applied displacement, with PM 4: (a) D1 (b) D2 with G_{Ic} = 1.25 kJ/m^2, G_{IIc} = 2.5 kJ/m^2, (all values in mm)

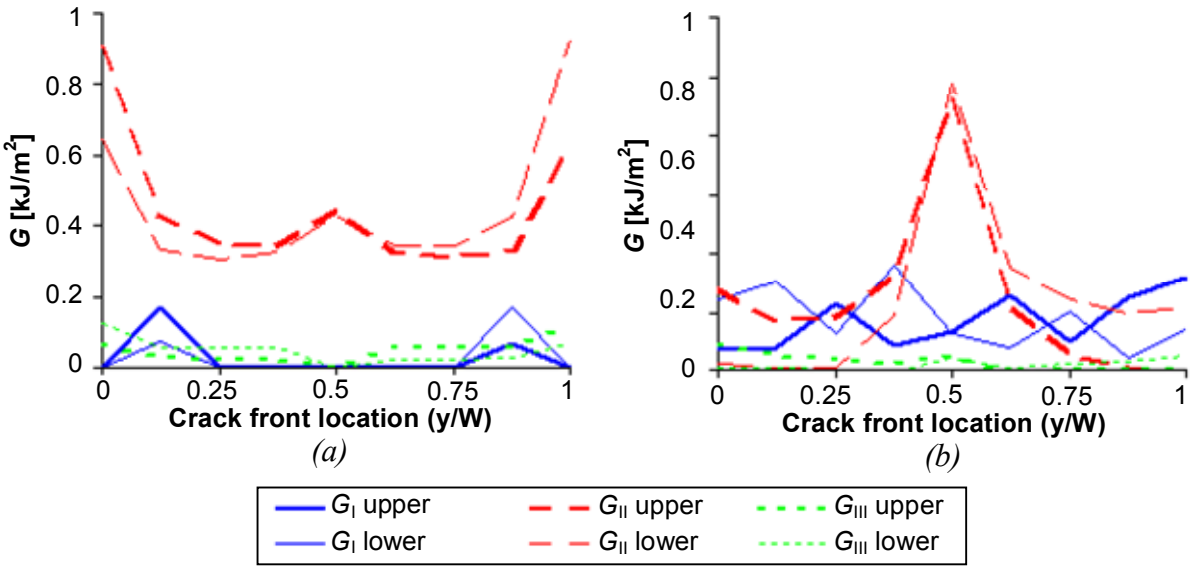

Figure 5.18: Single-stiffener debond specimens, strain energy release rate distribution at onset of crack growth: (a) D1 PM 4 (b) D2 PM 4

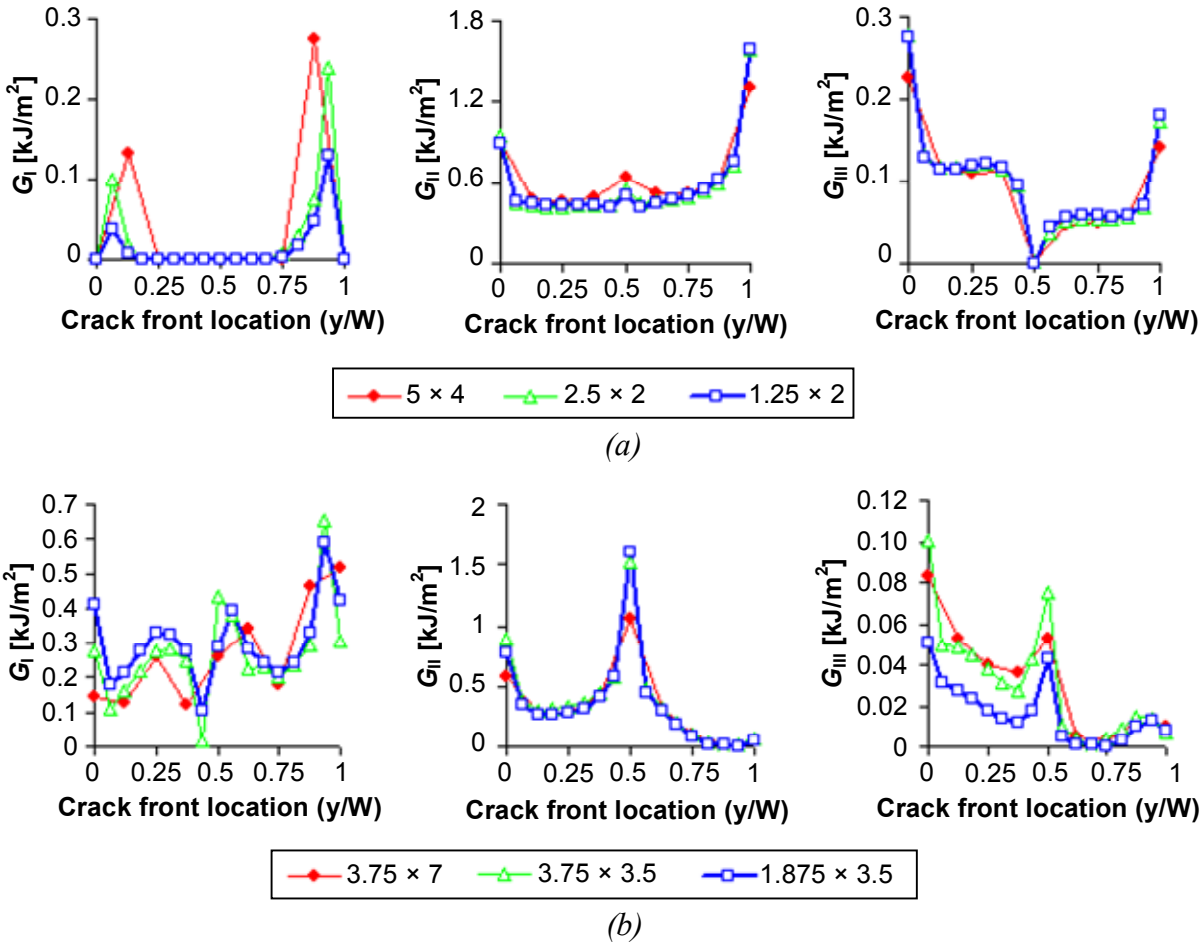

Figure 5.19: Single-stiffener debond specimens, strain energy release rate at different element sizes (in mm) at the crack front: (a) D1 lower debond edge (b) D2 upper debond edge

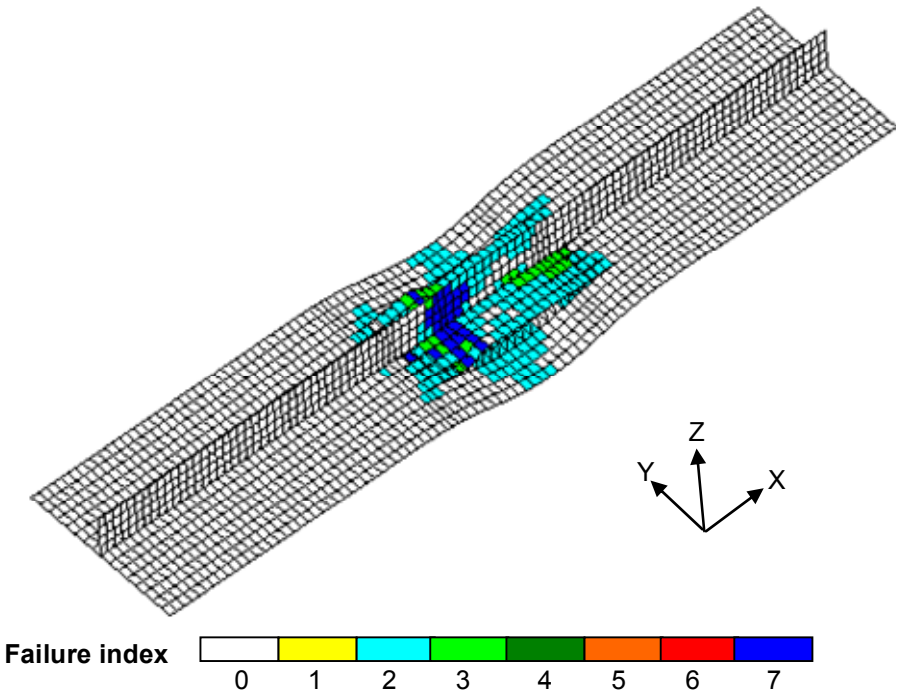

Figure 5.20: Single-stiffener debond specimens, ply damage at collapse (D2 model shown)

For the debond specimens, the D1 specimen showed skin buckling away from the stiffener in a single half wave, which appeared to show good correlation with the experimental shape. The D2 model displayed an asymmetric pattern of two half waves for each flange, which agreed well with the initial experimental shape, though the experimental buckling pattern of four and five half waves per bay seen under further compression, as shown in Figure 5.11(b), was not matched by the model. In spite of this, the stiffness for both models gave excellent correlation with the experiment, particularly in relation to the degree of variance in the test results.

In general, both model configurations displayed similar behaviour, where crack growth initiated at some point after buckling of the debonded area, the debonded area increased in size under further compression in conjunction with small amounts of matrix cracking, and this continued until the onset of fibre fracture in the stiffener, as shown in Figure 5.20. As seen in previous chapters, the occurrence of crack growth in the numerical model was generally characterised by reductions in the load response of the specimen, where the size of the load drop was related to the number of failing MPCs being released. Both these aspects compared very well with the experimental specimens, and indicated that the numerical models were accurately representing the specimen behaviour and load response in crack growth.

In terms of the propagation methods, from inspection of the opening displacements in crack growth for both the D1 and D2 models, it was again clearly seen that the displacements at a failing MPC in the increment following its release were generally much less than those assumed in the VCCT calculation. This justified the use of the modification approach in PM 4, where the strain energy release rates were reduced according to the local crack front shape, as described in Chapter 4. Additionally, crack growth using the simple fail-release approach of PM 1 tended to occur continuously causing only slight reductions in the load response, whereas crack growth using PM 4 occurred in a more stop-start fashion, which appeared to replicate the crack jumps and large load drops seen in the experiment results.

The D1 model was run with PM 1 and PM 4, that is, without and with the modification approach applied to strain energy release rate values. The results, given in Figure 5.15(a), show that the D1 model was not overly sensitive to the propagation method, and that the delay in crack growth introduced by the modification approach led to fibre fracture in the stiffeners occurring at lower values of axial compression. This was due to the fact that the increase in debonded area had a relaxing effect on the stresses in the specimen.

In comparison with experiment, the D1 model gave excellent predictions of the crack growth behaviour, using the nominal fracture toughness values given in Table 5.6 that were found from fracture mechanics characterisations tests. This can be seen in Figure 5.15(a), where the load-displacement curve of the D1 PM 4 model shows close comparison with the experimental results during crack growth. For the D1 models, the collapse of the specimen due to fibre fracture resulted in a significantly larger reduction in stiffness than was seen in the experiment, though as the behaviour of the specimen following collapse was of no interest this was not considered as important.

For specimen D2, the nominal fracture toughness parameters resulted in significant underestimation of the experimental fracture toughnesses, so that considerably more crack growth was predicted using the nominal values than was seen in the experiment. In order to improve this underestimation, the fracture toughness values were systematically increased until the crack growth initiation more closely matched the experimental results. From this, it was found that the fracture toughness parameters needed to be increased to around five times their nominal values, and these results were given in Figure 5.15(b). The significance of this result is discussed in the following section. With the increased fracture toughness values, the model gave very good predictions of the behaviour in crack propagation, and the applied load and displacement at final specimen collapse.

The D1 PM 4 model predicted crack growth to occur first at diagonally opposite corners of the debonded area, as shown in Figure 5.17(a), at axial compression values of 0.79 mm and 0.90 mm. These two instances of crack growth were sub-critical, in that they did not lead to growth along the rest of the crack front, in the same manner as was seen for ENF specimens in Chapter 4. From the strain energy release rate distribution in Figure 5.19(a), crack fronts of both the upper and lower debond edges were slightly antisymmetric and were clearly mode II dominated. Following the sub-critical crack growth, stable and continuous crack growth was then seen to occur from around 0.94 mm axial compression.

The D2 PM 4 model predicted sub-critical crack growth to occur first underneath the stiffeners, as shown in Figure 5.17(b), at axial compression values of 1.44 mm and 1.46 mm. From the strain energy release rate distribution in Figure 5.19(b), the mode II component was dominant under the stiffeners, though the rest of crack front showed both mode I and II components, with the mode III component again negligible. Stable crack growth was seen to occur from around 1.74 mm axial compression. For this model, the use of PM 4 did have a

noticeable delaying effect on the crack propagation, which was generally around 0.15 mm to 0.30 mm in axial compression and led to a corresponding increase in applied load.

From the mesh density investigation presented in Figure 5.19, the strain energy release rates showed good convergence with decreasing element size, and in general a reduction in strain energy rate values was seen for smaller elements. This meant that the nominal models predicted slightly higher strain energy release rates, which agreed with results previously presented in Chapter 4, and was not considered significant as it meant that the nominal models were the most conservative.

For the numerical models, the difference in crack growth behaviour between the D1 and D2 specimens gave good correlation with the nature of the experimental skin-stiffener interfaces observed from post-test inspection. In the numerical analysis, the D1 specimens gave excellent comparison with experiment using the fracture toughness values taken from experiment, whilst the D2 specimens required these values to be increased by a factor of five in order to achieve good comparison. This indicates that the fracture toughness of the two specimens was different, and that the D2 specimens had a tougher skin-stiffener interface. This agrees with the observations made from inspection of the D1 and D2 fracture surfaces, where it was seen that the bonding of the D1 specimens was quite poor, particularly under the stiffener flange, as a result of flange bending in curing.

The fracture toughness values applied in this analysis were determined from experimental tests that characterised the crack growth properties between two 0° plies in a quasi-isotropic laminate. In comparison, crack growth for the single-stiffener panels occurred either through the adhesive itself, between the adhesive and the external skin or stiffener ply (of any ply angle), or between plies close to the skin-stiffener interface via interlaminar migration. For the latter case, the crack would likely have migrated to a +45/-45° interface as the large angle difference is the most energetically favourable (Davidson 1996), and though could also have been at a 90°/+45° or -45°/0° interface, would almost certainly not have been at any of the 0°/0° interfaces. Clearly, none of the actual crack growth scenarios correspond to the characterisation specimen, so it is necessary to assess the applicability of the characterised value.

The post-test inspection of the skin-stiffener interfaces indicated that failure for the D1 specimens occurred primarily by adhesive failure between the adhesive and an external ply. In contrast the D2 specimen behaved more like properly-designed joints (Baker, Dutton and Kelly 2004), in that failure was not seen in the bonded connection, and instead due to the strength of the bonding failure was forced to occur in a neighbouring ply-ply interface. From the numerical results the characterised fracture mechanics values gave better correlation with the poorly bonded D1 skin-stiffener interface. This appears to indicate that the characterised fracture toughness values are more suitable to represent adhesive failure than crack growth at a ply-ply interface. One reason for this is that the fracture toughness for crack growth between plies of different angles is higher than that between two 0° plies (Andersons & König 2004). This type of information has direct relevance to the investigation of D1 and D2 large multi-stiffener panels in Chapter 7 and separately within the COCOMAT project, though does indicate that in general experimental investigations on small-scale specimens may be required in order to characterise the properties of any skin-stiffener interface.

5.2.3 Discussion

In general, the nature of the secondary bonded skin-stiffener interface is the most critical factor affecting the comparison with experimental results for both specimens. As previously mentioned, all of the crack growth properties were determined from investigations of a ply-ply interface, and though the assumption of analogous behaviour in the ply-adhesive-ply interface is necessary, the accuracy of this assumption in general remains largely unknown. In particular, this uncertainty is not only relevant for the fracture toughness values, but also for the law governing mixed-mode behaviour and the mixed-mode parameters. Additionally, it must be remembered that there is considerable uncertainty associated with fracture toughness values in general, where a large amount of variance is typically seen in experimentally determined values, particularly in mode II and mixed-mode I-II tests. Though this uncertainty would have affected both specimen configurations equally, it is important to recognise that the crack growth predictions are dependent on parameters that are themselves difficult to determine.

Another critical factor is the ability of the analysis software to accurately capture the correct deformation shape. The difficulty in obtaining the correct displacement patterns can be partially explained by the large amount of variance that was seen in the experimental results, especially for the D2 configuration, which illustrates the sensitivity of the buckling patterns

for these specimens. Additionally, the shell element used did not correctly account for the transverse shear through the thickness, and the use of the dummy plies also introduced transverse shear errors as previously explained, all of which would have had an influence on the predicted deformation shape. However, accurate mode shape capturing can be problematic for all buckling analyses, and this is especially true for structures loaded into the postbuckling range until collapse.

In spite of these issues, the results demonstrated the advanced capabilities of the analysis methodology for investigating the crack growth properties and propagation behaviour. Importantly, the methodology allowed for the behaviour of the specimen during crack propagation to be analysed. This provided a far more complete picture of the crack growth behaviour than current analysis practices in which the first instance of growth along a crack front is generally taken as the failure load. Using the developed approach, the way in which the crack propagated over time could be studied, where it was seen that the first instance of crack growth usually did not lead to propagation of the entire crack front, and that growth typically occurred in a stop-start fashion throughout the loading. This illustrates the way in which the developed methodology represented a marked improvement on the high degree of conservatism associated with current design practices, and provided a more realistic and accurate analysis of the specimen behaviour.

The results of the analysis also further validated the application of the modification approach to strain energy release rates developed to overcome issues with the self-similar VCCT assumption. This was seen both qualitatively from an investigation of the crack opening displacements for the single-stiffener specimens and quantitatively in comparison with experiment where the modification approach produced more realistic crack growth behaviour. It is important to note that the most accurate results for the single-stiffener specimens were found using the new modification factors found from the crack opening displacement investigation. This indicates that appropriate modification factors may be structure-dependent, which would require separate investigations for each structure analysed. However, the results of the analysis clearly indicated that the original factors were both conservative and necessary, and that even without the additional investigation the modification approach gave more accurate and realistic results for crack propagation.

5.3 Conclusion

An analysis methodology was proposed that combined the damage modelling approaches developed in the previous chapters into a coherent system for the collapse analysis of postbuckling composite structures. Additional functionality was added and included developing a degradation model for in-plane ply damage and defining a global-local approach to input global deformations on local cross-section models. A full description of the program functionality and various user subroutines was given, and the application of the methodology for both design and analysis of postbuckling structures was discussed.

The developed analysis methodology was then validated using experimental results for collapse tests of single-stiffener specimens based on the COCOMAT Design 1 and Design 2 panels. Experimental results were presented for intact specimens and specimens pre-damaged with a film insert, for both D1 and D2 designs. Results from the analysis methodology were then compared to the experimental data, and it was shown that the developed approach gave very good predictions across all aspects of specimen behaviour, and in particular the critical damage mechanisms leading to specimen collapse were accurately captured. Though there were some issues regarding the strength-based approach, the fracture toughness of the bonded skin-stiffener interface, and in capturing the correct displacement patterns, overall the results experimentally validated the developed approach and illustrated its advanced capabilities for the analysis of the damage mechanisms in composite postbuckling structures.

CHAPTER 6

ANALYSIS TOOL

In this chapter, the incorporation of the analysis methodology developed in previous chapters into a user-friendly software tool is presented. This involved combining the approach for predicting interlaminar damage initiation, the degradation model for representing interlaminar crack growth and the degradation model for capturing in-plane ply failure mechanisms. The software tool was implemented in Patran as a menu system that provided a series of pre- and post-processing functions for the analysis of postbuckling composite structures in Marc.

6.1 Introduction

The analysis tool was developed as a user-friendly package for the collapse analysis of composite structures taking degradation into account. As part of this, there were a range of capabilities that were necessary for the tool to be applicable across different analysis scenarios. The most obvious scenario was the analysis of intact or pre-damaged postbuckling designs, which was commonly used as pre- and post-test simulations of experimental results. Another important scenario was in the design of postbuckling structures, where parametric investigations were performed to select specimen configurations favourable for either experimental investigation or real world application. For both of these scenarios, it was necessary that the analysis tool was easy to use, required minimal knowledge of the various degradation models, and provided the functionality to investigate the various composite damage mechanisms in postbuckling structures.

6.2 Analysis Tool Functionality

The analysis tool was implemented as a menu system within Patran, and was intended to act as a complement to the model definition and analysis in Patran. In this way, the user would define the mesh, boundary condition, material, property and load case data for the model using the standard Patran functions, and would use the tool to define the damage regions and properties, run the analysis, and assist in the post-processing of the results.

The tool was created with the same "feel" as the Patran menu structure, which involved creating the menu and sub-menu system with the same style and functionality. This ensured that the tool was consistent within the Patran framework, and provided the user with a natural and comfortable extension of the existing software package. Additionally, all menus and sub-menus of the tool included a help function that opened a text box of information, to provide the user with details on each function and the way in which it formed part of the complete menu system. Another technique used to aid user-friendliness was "greying-out" or disabling certain options until they became necessary, which assisted the user by making the options and process clearer and less cluttered, as well as preventing erroneous input.

6.2.1 Main Menu

The main menu of the analysis tool was labelled "Marc Damage" and was located in the Patran toolbar as a pull-down menu, as shown in Figure 6.1. The tool consisted of a help option and four main sub-menus to provide functions necessary to define the damage regions, define the model properties, generate and run the files needed for analysis, and post-process the results. These sub-menus are described in the following sections.

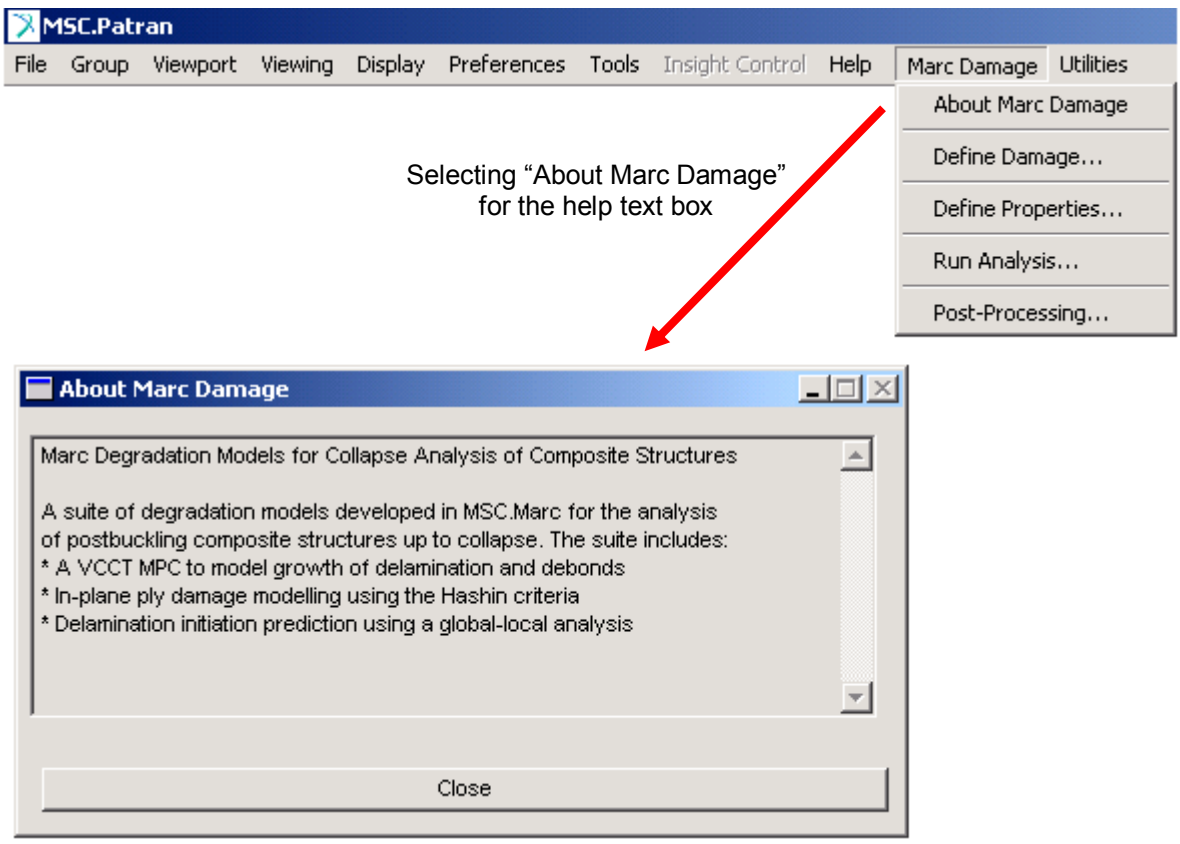

Figure 6.1: Analysis tool menu system in Patran with help text box displayed

6.2.2 Define Damage Sub-Menu

The Define Damage sub-menu is given in Figure 6.2, and was developed to provide functions necessary to set up the model for use with the composite damage degradation models. The functionality of this sub-menu is explained below:

- The "Create MPCs" frame allowed the user to create MPCs between sets of independent and dependent nodes, where an MPC was created between each independent node and the closest dependent node.
- The "Create groups" frame was used to define various groups of elements necessary to characterise the damage within the model. This included defining the total set of MPCs in which interlaminar damage propagation would be modelled, the MPCs used to form any initial debonded region, the shell elements in which the in-plane damage mechanisms would be captured, and the set of elements that would be used to define any elements softened as a pre-damage.
- The "Show groups" button was included to display the model with separate colouring for each of the separate groups, to allow quick visual interpretation of the defined damage regions. An example of a model with different damage regions is given in Figure 6.3.
- For the softened elements, a separate form was used that extracted the material groups from the elements selected, and allowed the user to define at which layer of each material group softening would be included. The softening was implemented in the model as matrix cracking in the selected elements at the designated layers, though further editing of this definition prior to the analysis to include the other damage mechanisms was also possible.

6.2.3 Define Properties Sub-Menu

The Define Properties sub-menu, shown in Figure 6.4 and Figure 6.5, was implemented to allow the user to import or enter in all of the required properties and parameters controlling the damage analysis. The sub-menu was used to create a data file, which was an external file with particular formatting that contained all analysis parameters and which the degradation models read as input at the start of the analysis.

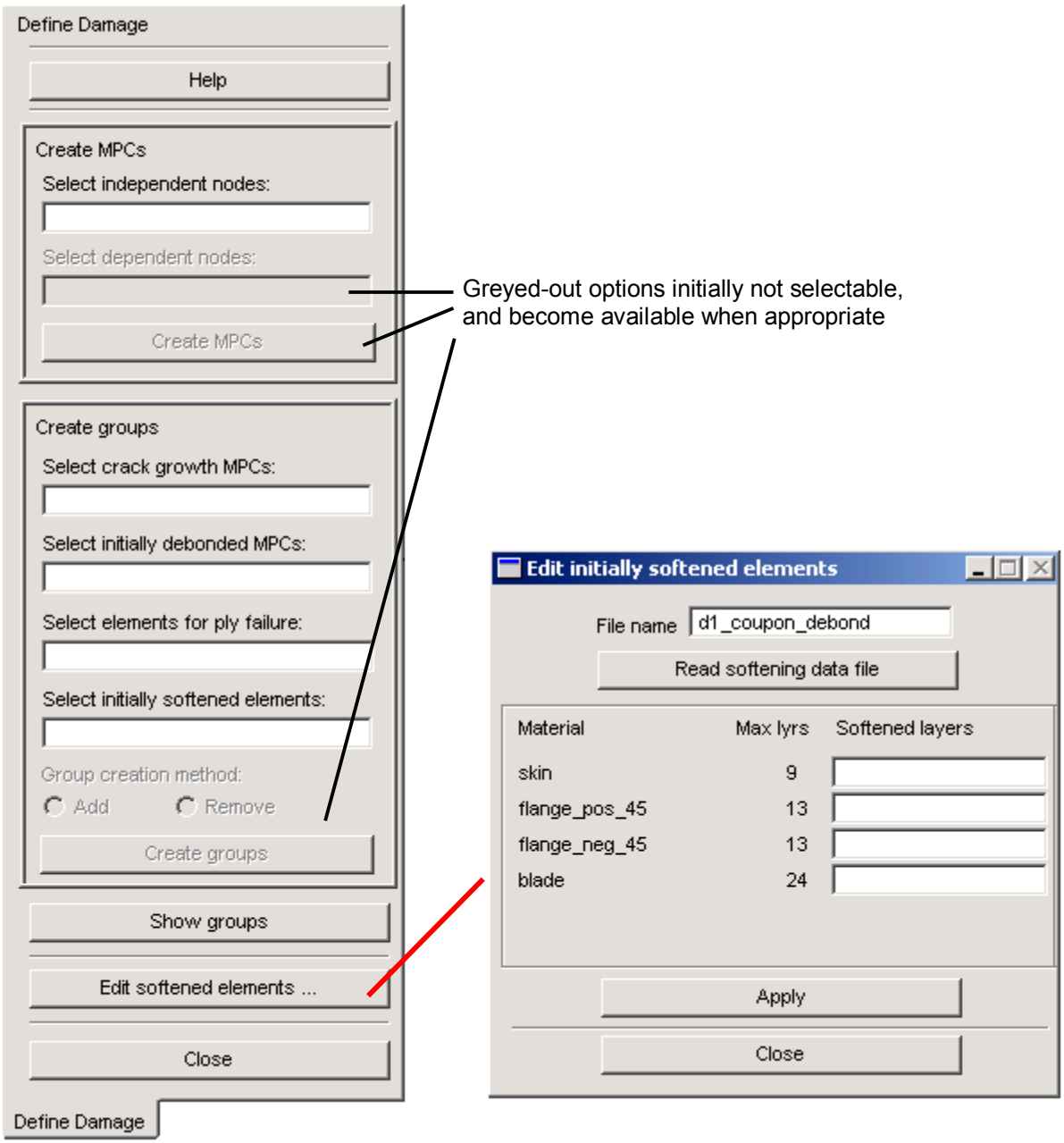

Figure 6.2: The Define Damage sub-menu with the form for element softening shown

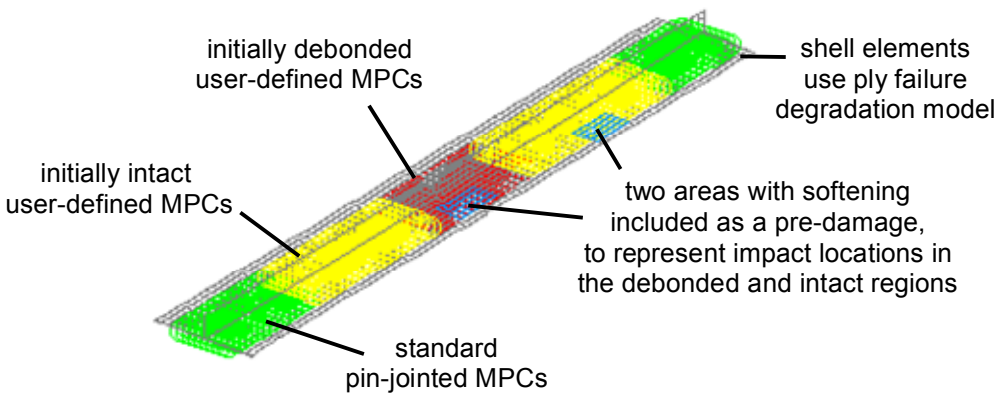

Figure 6.3: Example model (single-stiffener specimen) showing damage definition

The functionality of the Define Properties sub-menu is explained below:

- The "Read Existing" form, shown on the right in Figure 6.4, allowed the user to import property values from a previously-defined data file or from material data already entered into the Patran database.
- The "Material" form provided for manual entering of the stiffness, strength and fracture properties. There were seven stiffness properties (E_{11}, E_{22}, ν_{12}, G_{12}, G_{23}, G_{31}) required to define the 2D orthotropic materials with ply damage, nine strength properties (X_T, X_C, Y_T, Y_C, Z_T, Z_C, S_{12}, S_{23}, S_{31}) for the 3D failure theories, and the fracture properties as shown in Figure 6.5.
- The "Control" form allowed for the entering of parameters controlling the way in which the various degradation models operated, as shown in Figure 6.5. Note that in the tool developed, the use of the mixed-mode law (B-K, Power or single) and the PM 4 modification scheme were included as options, and the option was also provided to control the writing of ply damage failure indices to the output file.
- The "Preview values" button opened a text box summarising all the input parameters as entered, and was generally used prior to writing values to the external data file.
- The "Save to file" button created the external data file <job name>_*u-data.csv*.

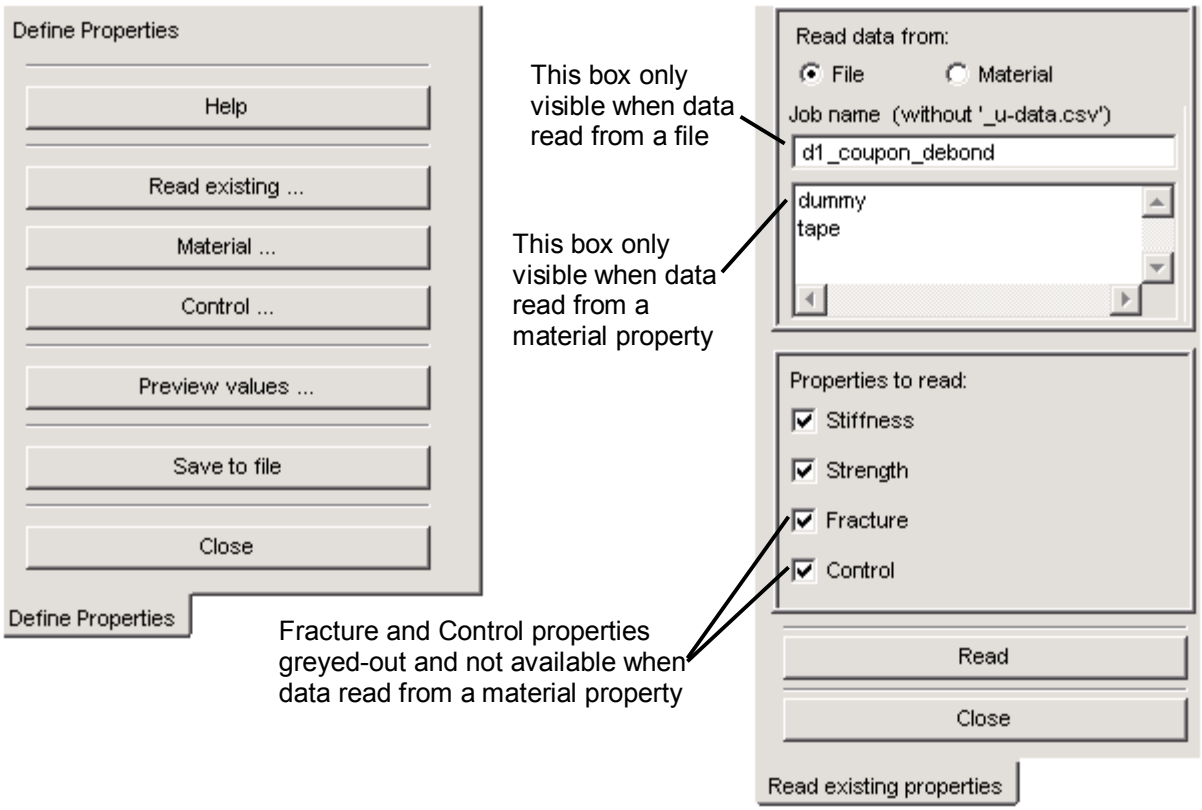

Figure 6.4: The Define Properties sub-menu with form for reading property data

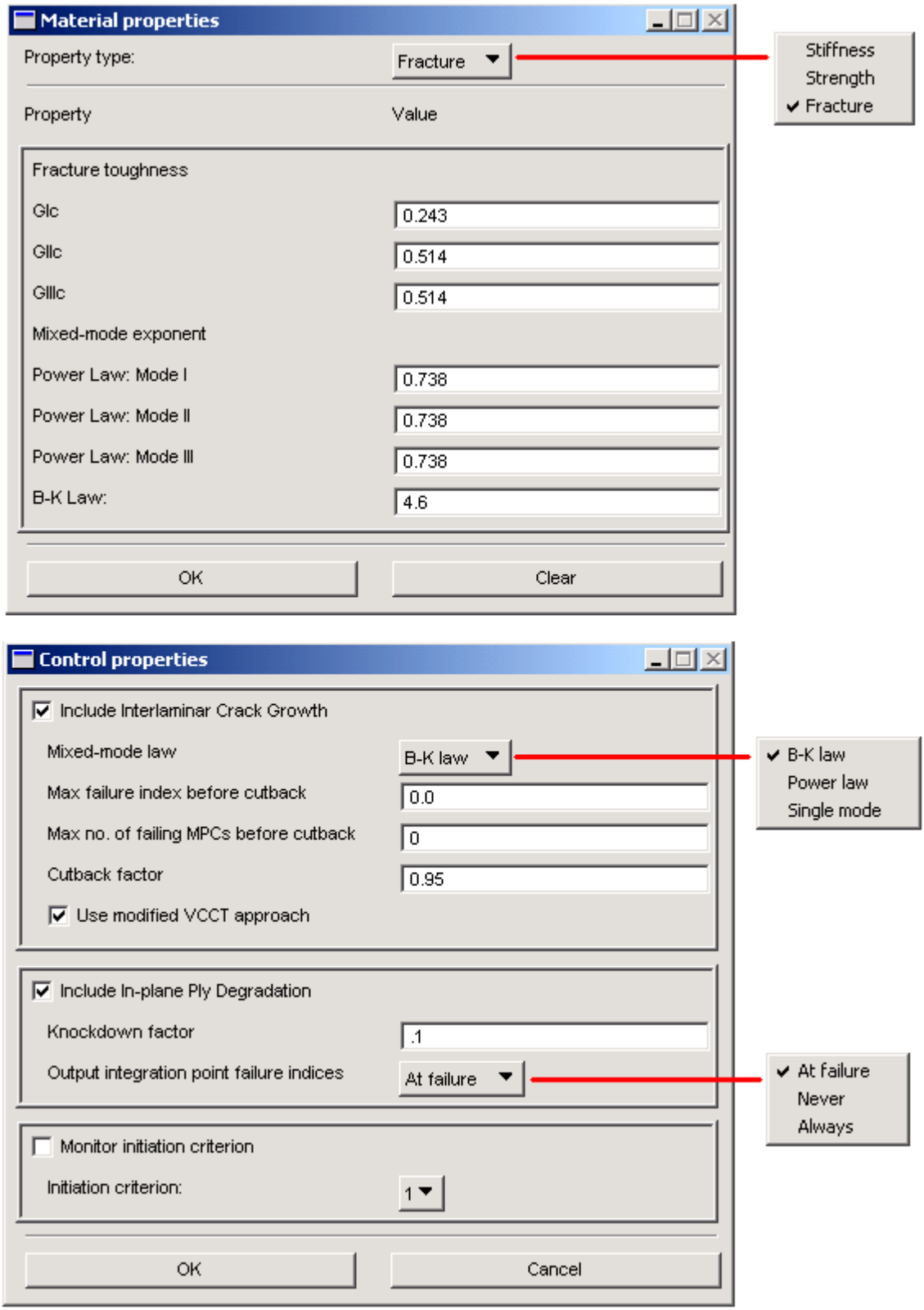

Figure 6.5: Forms from the Define Properties sub-menu for material and control properties

6.2.4 Run Analysis Sub-Menu

The Run Analysis menu, given in Figure 6.6, allowed the user to generate and run an input file for analysis with the degradation subroutines. In this sub-menu, the input file was first created using the "Create job" form shown in Figure 6.7. This form provided the user with the analysis options most commonly required such as the load case, incrementation and output parameters. The form used the Patran analysis translator to create an input file, which was then modified to incorporate any degradation models selected. This process included adding the gap elements and nodes for the interlaminar damage propagation analysis, and adding the hypoelastic material in the required element properties for the in-plane ply failure analysis. Additionally, all the external text files necessary for the subroutines were generated, which were read in as input at the start of the analysis as described in previous chapters. Following the creation of a job using this form, the job name appeared in the Run Analysis sub-menu. Using this sub-menu the job could be spawned, and options were given for renaming or creating a new data file for the job, deleting all job external text files after completion, and nominating the global post file for a global-local analysis.

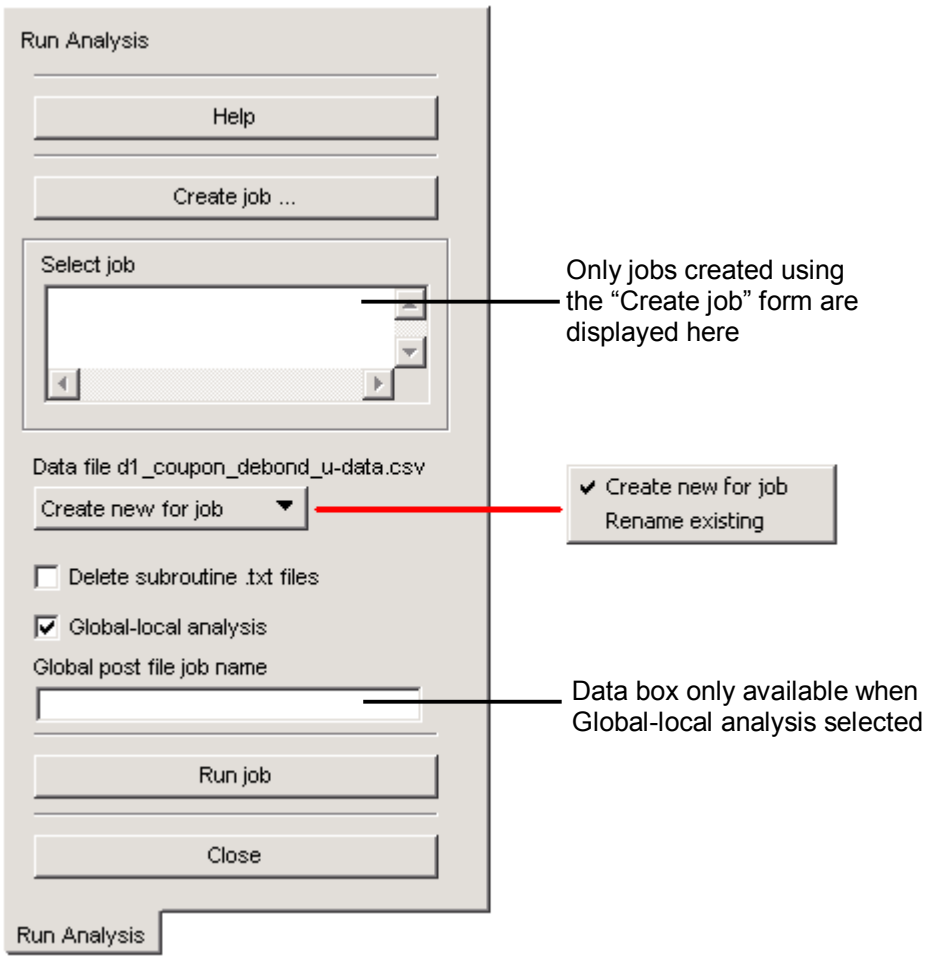

Figure 6.6: The Run Analysis sub-menu

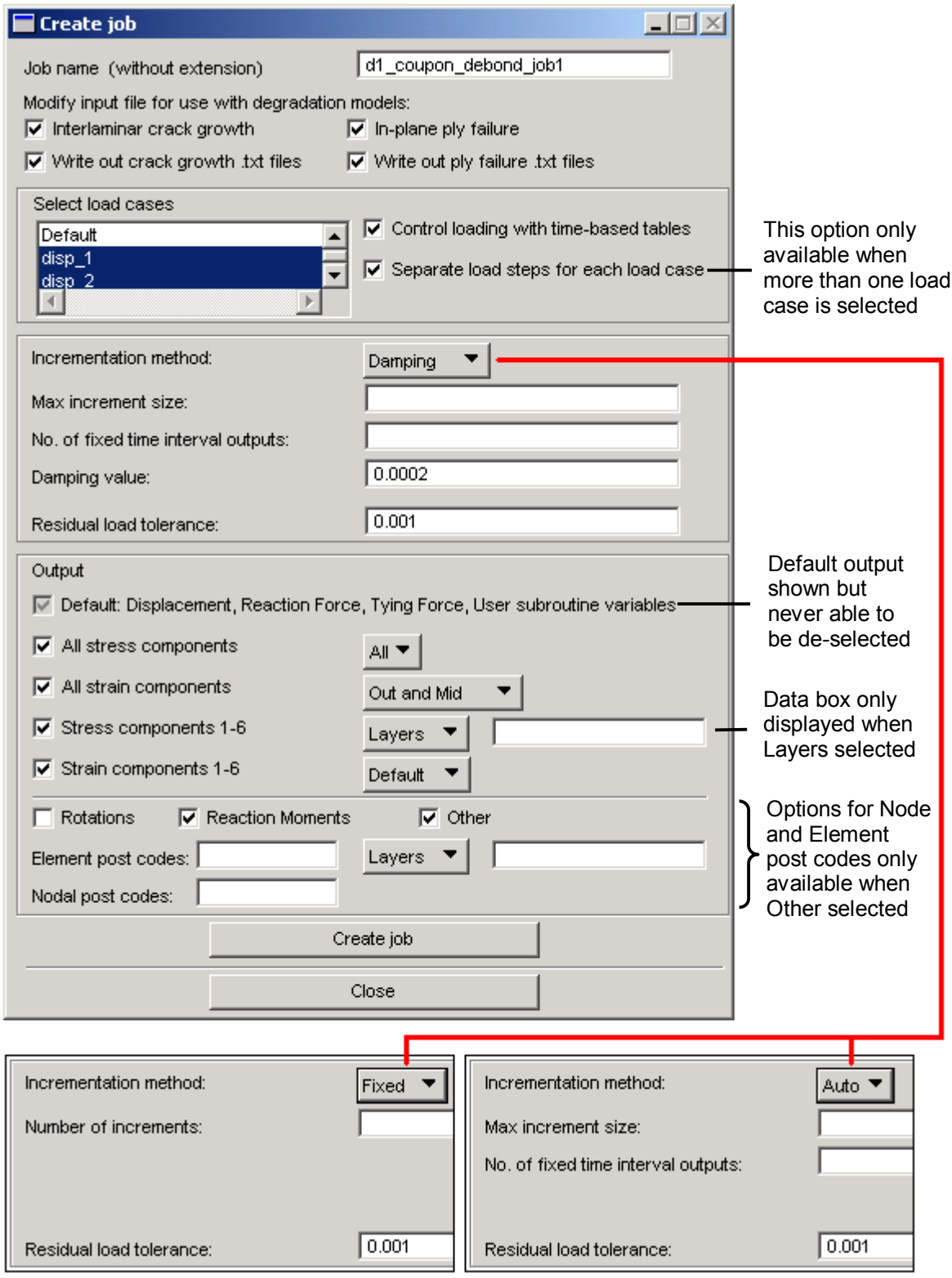

Figure 6.7: The Create job form from the Run Analysis sub-menu

6.2.5 Post-Processing Sub-Menu

The Post-Processing sub-menu, shown in Figure 6.8, provided a number of utility functions to assist in post-processing the results from the damage subroutines. The functionality of the sub-menu is detailed below.

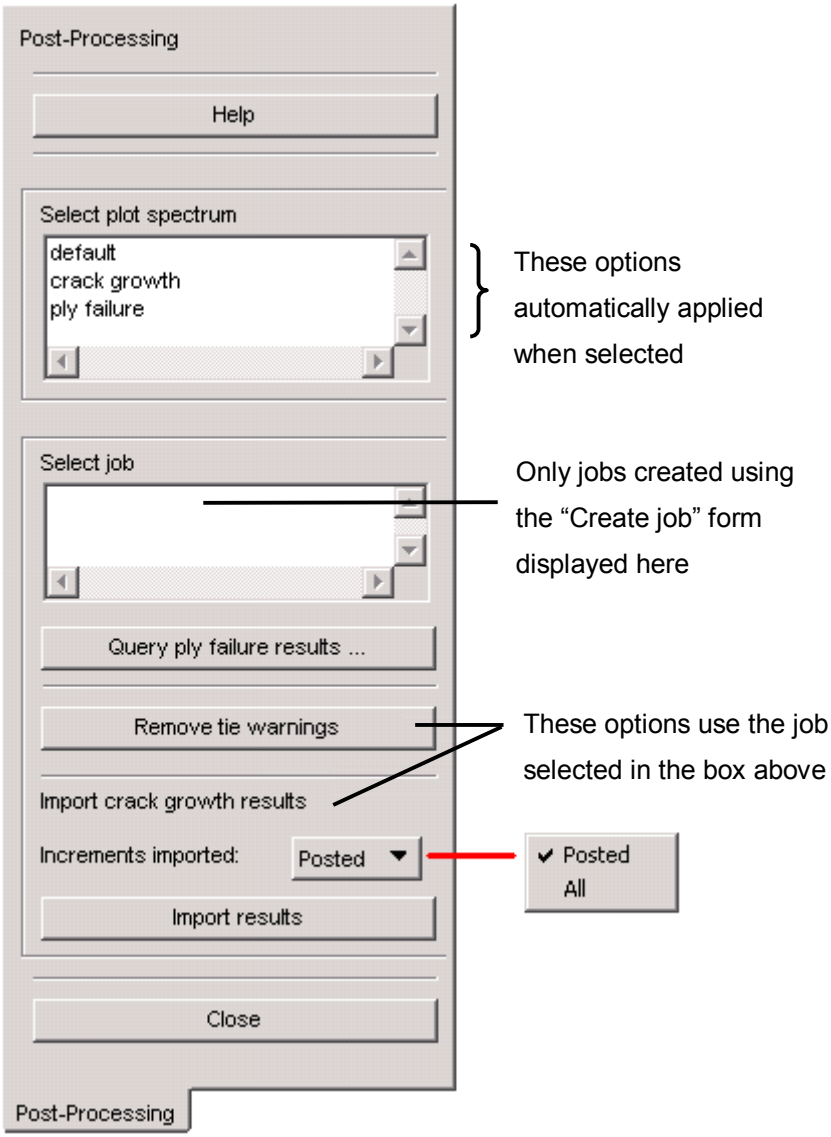

Figure 6.8: The Post-Processing sub-menu

The "Select plot spectrum" option provided preset colour spectrum and data range templates to assist with viewing results using the Patran option of post-processing results. These were used to match the user-defined output variables, where the crack growth preset was set up for three values ranging from 0 to 2, and the ply failure preset was created for eight values from 0 to 7.

The "Query ply failure results" form, shown in Figure 6.9, was used to post-process the ply failure data written to the output file. The selected *.out* file was first read, which involved importing the ply failure results output at the end of every increment. These values could then be searched using the data boxes below, where up to nine results could be displayed simultaneously. The results displayed included the ply angle, in-plane failure toggles *f*, *m* and *s* (set to either 0 for intact or 1 for failed) and the failure indices e_f, e_m and e_s (0 for intact, ≥ 1 for failed). There were three methods for searching and displaying results, which depended on whether any of the results were averaged. The first, shown in Figure 6.9, involved no averaging, and searched for results at a specified increment, element, integration point and ply layer. There was also the option to average all integration point values at a specified increment, element and ply, which removed the "lyr" data box from the form. Finally there was the option to average all values at a specified increment and element, which removed the "pt" data box, "lyr" data box and "angle" output value. There was also a "Legend" button, which displayed a separate form giving the definitions of all terms used in the results.

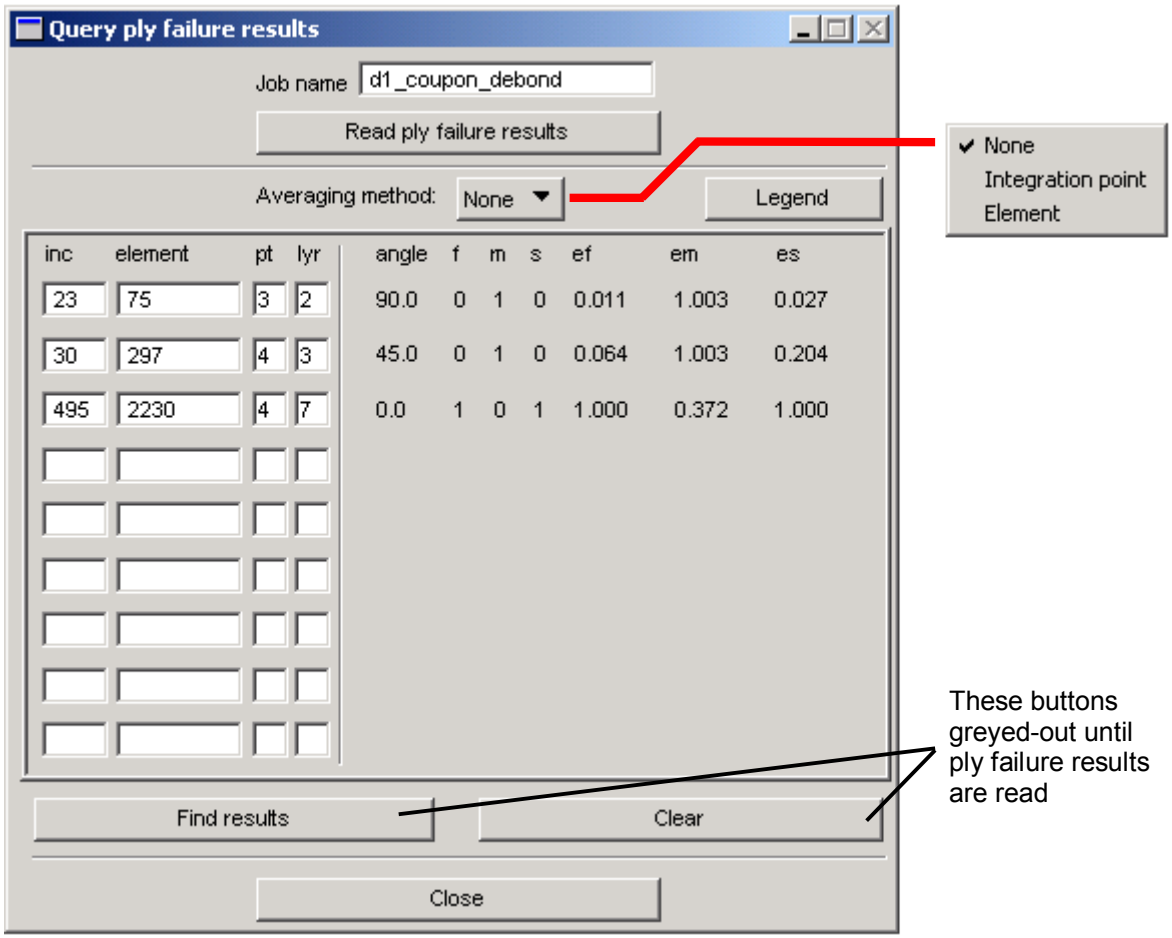

Figure 6.9: The Query ply failure results form from the Post-Processing sub-menu

The “Remove tie warnings” option in the Post-Processing sub-menu was used to remove erroneous warning data in the *.out* file. In Marc v2005r3 there was an error in the code, so that as each MPC was written to the output file, incorrect warning messages were generated for every MPC previously defined. As a result, the erroneous warning output increased exponentially with the number of MPCs, so that even for a small number of MPCs the size of the output file became excessively large and difficult to manage. The option was therefore provided to remove these warnings, which typically reduced the size of the *.out* file from over 100 MB to under 10 MB.

The “Import crack growth results” option in the Post-Processing sub-menu was included so that the strain energy release rate results written to the output file at the end of every increment could be imported into Patran. This meant that the strain energy release rate results were available in the Patran database for further post-processing, such as plotting graphs and displaying the data graphically on the model. As the Marc solver had the option to include results in the Marc *.t16* results database in a reduced number of increments, but the crack growth degradation model gave output at the end of every increment, the option was provided to select which increments the results from the *.out* file would be imported.

6.3 Conclusion

A user-friendly software tool was developed that incorporated the analysis methodology presented in previous chapters. This involved combining the approach for predicting interlaminar damage initiation, and the degradation models for interlaminar crack growth and in-plane ply failure. The tool was implemented as a menu system within Patran, and was used as a complement to the standard Patran pre- and post-processing functions. The menu system contained a series of sub-menu systems, which were used to define the damage regions and properties, run the analysis, and assist in the post-processing of the results. The tool was applicable to both design and analysis, as it incorporated the effects of damage in the analysis of postbuckling composite structures.

CHAPTER 7

APPLICATION TO DESIGN AND ANALYSIS

In this chapter the use of the analysis methodology and software tool for the design and analysis of postbuckling composite structures is demonstrated. Analyses that were performed within the COCOMAT project as part of the design process for intact and pre-damaged panel configurations are summarised, and are used to demonstrate the advanced capabilities of the developed approach. Following this, experimental results for intact and pre-damaged panels are presented, and the application of the analysis methodology for the collapse analysis of such structures taking degradation into account is shown. All examples of design and analysis of intact and damaged panels were taken from the COCOMAT project, and in particular the Workpackages to which this work directly contributed[5].

7.1 Introduction

For the design of postbuckling structures within COCOMAT one of the key philosophies was a research-based focus on generating results suitable for studying damage growth and validation of the software tools. Though there were structures designed along industry-based parameters that were more representative of damage in real structures, in this work only designs from the research-based philosophy are covered. This design philosophy was focused on investigating the degradation mechanisms critical for compression-loaded structures, principally skin-stiffener debonding. For this, the structures and laminates were based on real aircraft designs, but were modified to induce the composite damage mechanisms in a stable and controllable manner so that they could be studied. Examples of this philosophy include promoting interlaminar damage by grouping 0° plies together and not using ply drop-offs at flange edges, reducing stiffener pitch to limit the sensitivity of the panels to buckling mode shape changes, and selecting designs for manufacture and testing based on their damage properties and the likelihood of stable damage growth.

---

[5] Orifici, AC, Thomson, R, Degenhardt, R, Kling, A, Rohwer, K, & Bayandor, J 2008, 'Degradation investigation in a postbuckling composite stiffened panel', *Composite Structures*, vol. 82, no. 2, pp. 217-224.

COCOMAT Designs 1 and 2 were investigated in the work described in this chapter, so are summarised below as a reference. Both designs were for fuselage-representative composite panels loaded in compression only, where D1 was proposed by DLR from a research-based philosophy and D2 was proposed by Aernnova from an industrial perspective. Both designs used resin potting at the panel ends to ensure an even application of the end loadings, and D2 used a longitudinal edge restraint to constrain the radial (out-of-plane) displacements along the panel side. Though some aspects of the two designs were presented previously as they were used as the basis for the single-stiffener specimens, the designs are fully summarised below to avoid confusion.

Table 7.1: D1 and D2 panel details, all dimensions in mm

Parameter	**D1**	**D2**
Number of stiffeners	5	4
Total length, L	780	520
Free length, L_f	620	400
Arc length, W	560	624
Panel geometry	Curved	Curved
Radius, R	1000	1000
Stiffener pitch, b (between stiffeners)	132	156
Skin lay-up	$[90,\pm45,0]_S$	$[\pm45,0,90]_S$
Stiffener lay-up	$[(\pm45)_3, 0_6]_S$	$[\pm45,0_2,90_2]_S$
Ply material	IM7/8552	IM7/8552
Adhesive	FM 300	FM 300
Ply thickness, t	0.125	0.152
Stiffener height, h	14	28.91
Stiffener width, w	32	56

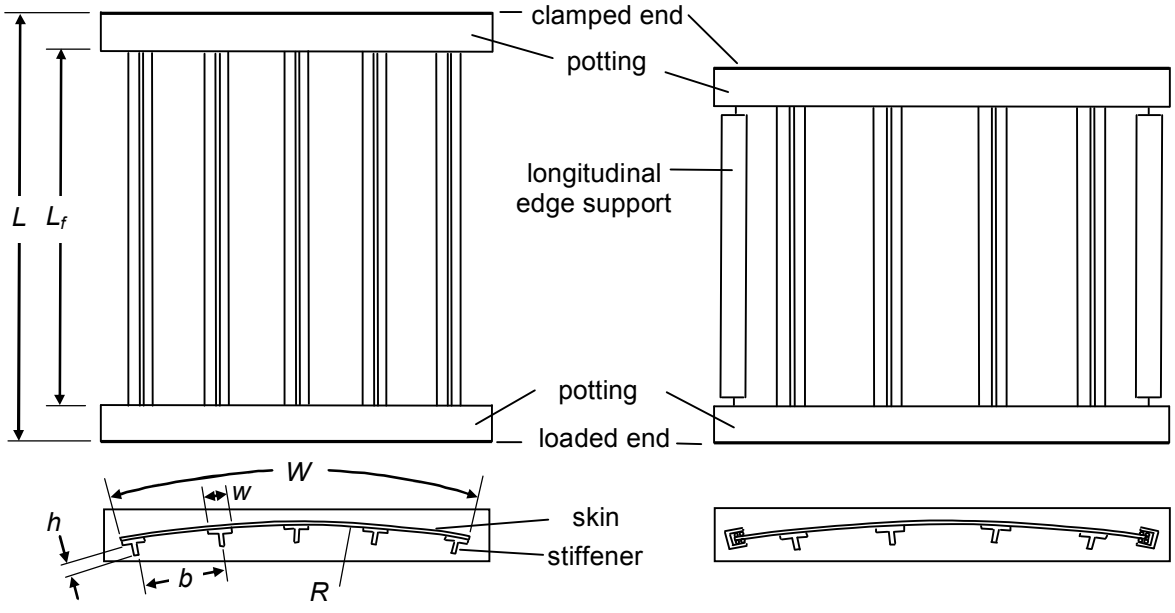

Figure 7.1: Panel geometry: (a) D1 (b) D2

7.2 Design

In this section, the application of the analysis methodology and software tool to the design of composite postbuckling structures is demonstrated. This includes the design of intact structures, where the onset of skin-stiffener separation typically leads to instantaneous collapse, and pre-damaged structures, where the pre-damaged region can show some growth before the onset of collapse.

7.2.1 Intact

COCOMAT Workpackage (WP) 2.3 involved the design and analysis of intact panels for manufacture and testing. As part of the design process for WP2.3, various proposals for COCOMAT Designs 1 and 2 were investigated, prior to the selection of the final designs. This process is summarised below, to act as a reference so that the application of the developed analysis methodology within current design practices can be demonstrated.

For COCOMAT Design 1, a nominal panel design was taken from POSICOSS, and three design variations were proposed. These variations, V12, V15 and V16, all used identical material and boundary conditions, though had variations in the geometry and outer stiffener heights, as shown in Table 7.2. For the definition of the geometry terms see Figure 7.1. The V12 design used four stiffeners with the outside two made 6 mm (43%) taller and stiffer than the nominal design, whereas the V15 and V16 design both used the nominal stiffener size, but differed in using five and six stiffeners respectively.

Table 7.2: D1 panel parameters, all design proposals, all distances in mm

Parameter	**Panel design**		
	V12	*V15*	*V16*
Panel length, L	780	780	780
Panel free length, L_f	660	660	660
Panel radius, R	1000	1000	1000
Stiffener pitch, b	132	132	132
Number of stiffeners	4 (2 inner, 2 outer)	5	6
Panel arc length, W	420	560	698
Material system	IM7/8552	IM7/8552	IM7/8552
Skin lay-up	$[90, \pm 45, 0]_S$	$[90, \pm 45, 0]_S$	$[90, \pm 45, 0]_S$
Stiffener height	inner: 14 outer: 20	14	14
Stiffener web lay-up	inner: $[(45,-45)_3, 0_6]_S$ outer: $[(45,-45)_3, 0_8]_S$	$[(45,-45)_3, 0_6]_S$	$[(45,-45)_3, 0_6]_S$
Ply thickness	0.125	0.125	0.125
Stiffener width, w	32	32	32

Finite element models were generated for all panel proposals in both Nastran and Abaqus, though as the two analysis codes gave very similar results only the Nastran results will be shown. All models were analysed with a full Newton-Raphson procedure, with the default nonlinear parameters used, except for tighter tolerances of 1×10^{-3} and 1×10^{-7} for load and work residuals respectively. For all models, use was made of an analysis tool developed previously at the CRC-ACS, Compdat (Yap et al. 2002), to calculate strain energy release rates at all the skin-stiffener interfaces. The values of G in its mode I and II components were used in a power law mixed-mode failure criterion, previously given as Equation 4.4, with the mode III contribution ignored. The mixed-mode failure index was used to determine the likelihood of skin-stiffener debond initiation. As fracture mechanics characterisation tests had not been performed at the time, values of G_{Ic} and G_{IIc} were taken from literature (Schön et al. 2000a; Schön et al. 2000b) and are given in Table 7.3, where a linear relationship ($m = n = 1$) was assumed for the mixed-mode law. The material properties used for the strength and stiffness values were identical to those previously presented in Table 5.7 in Chapter 5.

Table 7.3: IM7/8552 fracture toughness values for design, taken from literature

Property	**Fracture toughness (J/m^2)**	**Reference**
G_{Ic}	220	Schön et al. 2000a
G_{IIc}	630	Schön et al. 2000b

For D1, the load-shortening graphs for designs V12, V15 and V16 are given in Figure 7.2. All designs showed a local buckling mode shape of 15 longitudinal half sine waves per bay (similar to those shown in the leftmost image of Figure 7.21), which developed between 0.53 mm and 0.57 mm axial compression. The global buckling patterns of all panels were symmetrical with buckling inwards towards the centre of curvature. The V12 panel, with three stiffener bays, developed a single central global buckle at around 1.25 mm axial compression, whilst the V15 and V16 panels, with four and five stiffener bays respectively, showed two global buckles in the outer stiffener bays developing at around 1 mm axial compression. The V12 panel transitioned from local to global buckling via an antisymmetric mode, and both the V12 and V16 panels showed a change to a secondary global buckling shape. The results of the debond predictions using the mixed-mode failure criterion are also shown in Figure 7.2. Debonding was predicted to initiate at the edge stiffeners in design V12 and at the centre stiffeners for V15 and V16. The axial compression values for failure were very consistent across the three designs ranging from 1.39 mm to 1.44 mm. In general, the predicted failure was mode I dominated.

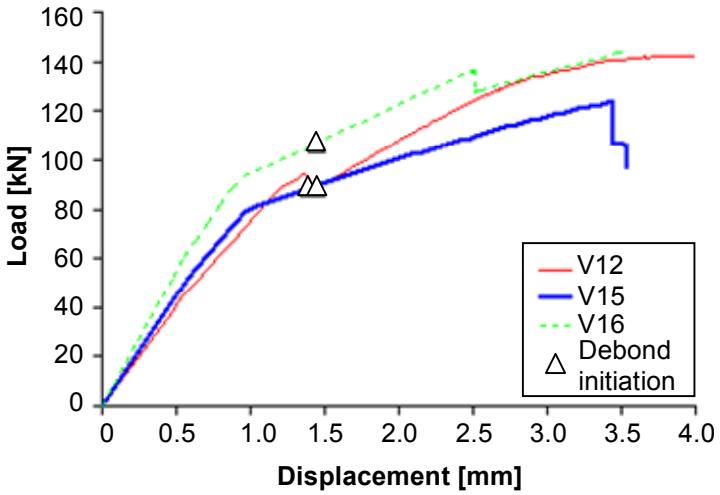

Figure 7.2: Load-shortening and debond predictions, D1 proposals

As a result of the structural and fracture mechanics analyses on all proposed D1 panels, panel design V15 was recommended from a research-based perspective as being best suited for experimental investigation of skin-stiffener debonding. For this panel, the postbuckling behaviour was stable with a progressive change from local to a symmetric global buckling mode. The panel also exhibited a large stable global postbuckling zone from 0.96 mm to 3.45 mm axial compression, and stiffener debonding was predicted to initiate clearly after global buckling. Finally, in separate investigations the V15 panel showed the least sensitivity to the mixed-mode power law exponents for the debonding predictions.

In contrast, the V12 panel analysis predicted that debonding would initiate in the outer stiffeners first, which raised the possibility that debond initiation could lead to catastrophic failure of the panel. Additionally, the progression from local to global buckling via an antisymmetric global mode demonstrated less stable global buckling behaviour. Debond initiation was predicted to coincide with the change from local to global buckling, which would make the accurate detection of initiation difficult during testing.

Separately, the V16 panel analysis predicted a reduced postbuckling zone as compared with the V15 panel, due to the secondary mode shape change occurring at 2.5 mm axial compression. This postbuckling mode shape change would not only be complicated by the existing skin-stiffener debond, but would affect the investigation into debond growth. The debond initiation prediction for the V16 panel was also more sensitive to the power law exponents, which would make validation of degradation models more difficult.

For COCOMAT Design 2, a similar process was followed, with a nominal panel design and three design variations proposed by Aernnova. The three design variations, V21, V22 and V23, were analysed in Nastran and the strain energy release rate values at all skin-stiffener interfaces were investigated using Compdat in the same way as for the D1 panels. The results of the analyses are presented in Figure 7.3. From the analysis, skin-stiffener debonding was predicted to occur at all of the inner stiffeners almost simultaneously, and all designs showed a large number of different global postbuckling mode shapes developing throughout the compression loading. On the basis of this analysis, it was concluded that none of the designs were particularly suitable for experimental investigation into skin-stiffener debonding. Following this, a subsequent panel design was proposed, which represented a modification to the V21 design, and was initially designated V21r. This design employed a reduced stiffener pitch, with all other parameters as given previously. The analyses using Nastran and Compdat were repeated, and the results are shown in Figure 7.3 and Figure 7.4. From these results, the revised design gave a stable postbuckling region with three half waves per bay, and debonding was predicted to occur on both sides of only the central stiffener. On this basis, D2 proposal V21r was recommended from a research perspective as being best suited for investigating skin-stiffener debonding.

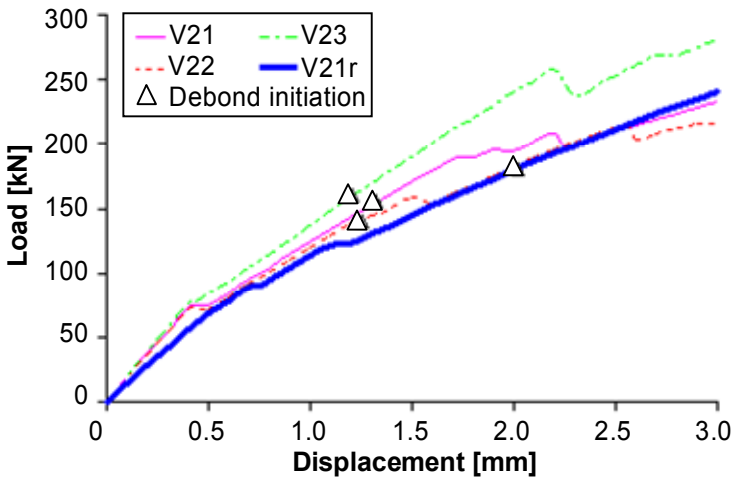

Figure 7.3: Load-shortening and debond predictions, D2 proposals

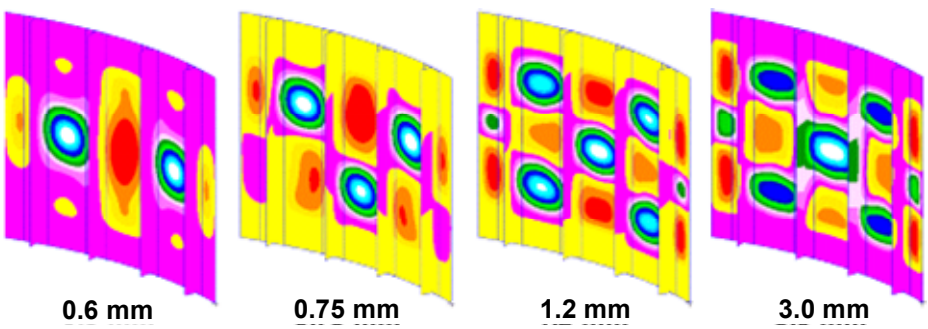

Figure 7.4: D2 proposal V21r, out-of-plane displacement at applied axial compression

Based on the two recommendations, D1 proposal V15 and D2 proposal V21r were selected for manufacture and testing, and were designated as COCOMAT Design 1 and Design 2.

To demonstrate the applicability of the developed methodology for the design of postbuckling structures, the analysis performed for the D2 design procedure was repeated using the developed software tool. Finite element models in Marc were created for global and local analyses, in the same manner as described in previous chapters. The global models consisted of shell elements in a regular grid mesh, with parameters and details given in Table 7.4. The local model was created using solid brick elements for each ply, and was applied in a number of locations corresponding to various nodal and anti-nodal lines in the global models. The local model used was taken from the local model presented in Chapter 5 for the D2 single-stiffener specimens, though was modified to account for the panel curvature.

Table 7.4: D2 panel, FE model details

Model	**Nodes**	**Elements**
D2 global	6413	6032 shells
D2 local	34,376	27,736 solids

The global model gave behaviour very similar to the previous Nastran analysis, which involved a local buckling mode of five longitudinal half waves leading to a global buckling mode of three half waves per bay, as shown in Figure 7.5. The onset of global buckling occurred at 1.16 mm axial compression, and the collapse of the panel was predicted to occur due to fibre fracture at the middle of the panel edges at around 2.67 mm axial compression. From the analysis of the local model at various locations it was found that the critical debond initiation location was at the panel centreline at the inner stiffeners, which with reference to Figure 7.5 corresponded to an anti-nodal line, or location of maximum displacement. The deformed shape and debond initiation prediction are shown in Figure 7.6, where debonding was predicted to occur when the average delamination failure index was greater than 1.0 for a line of elements through the cross-section.

As shown in Figure 7.7, the developed analysis approach (labelled “Marc”) compared very well with the previous Nastran analysis, which was especially significant given that the original approach used fracture mechanics theories whilst the developed methodology used a strength-based approach to detect the onset of skin-stiffener debonding. From the results, it was again clear that debonding was predicted to occur early after global buckling, and the stable postbuckling region was beneficial for experimentally investigating the debonding behaviour, which confirmed the conclusions reached in the previous analysis.

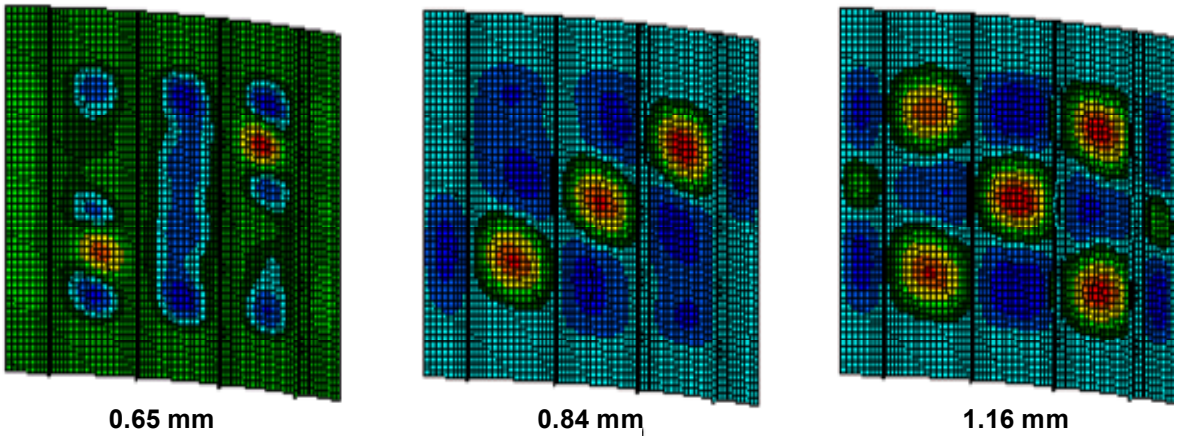

Figure 7.5: D2 global model, out-of-plane displacement at applied axial compression

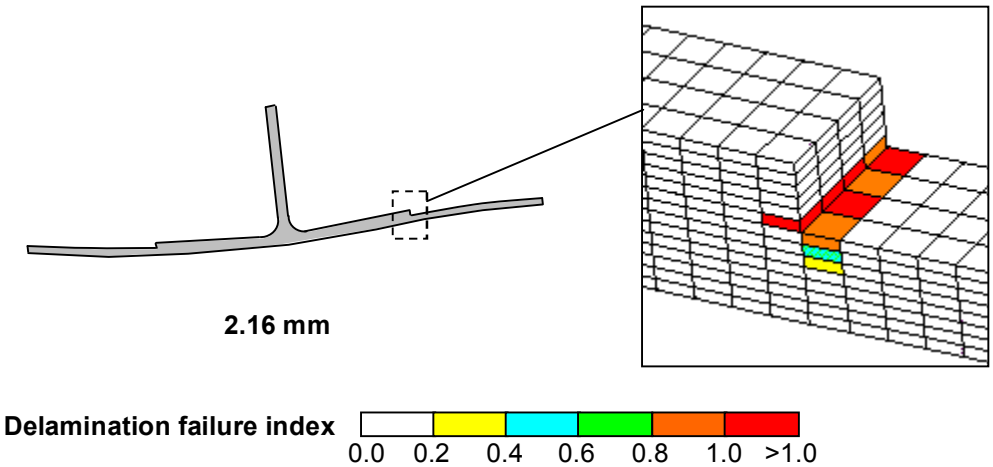

Figure 7.6: D2 local model, debond initiation prediction

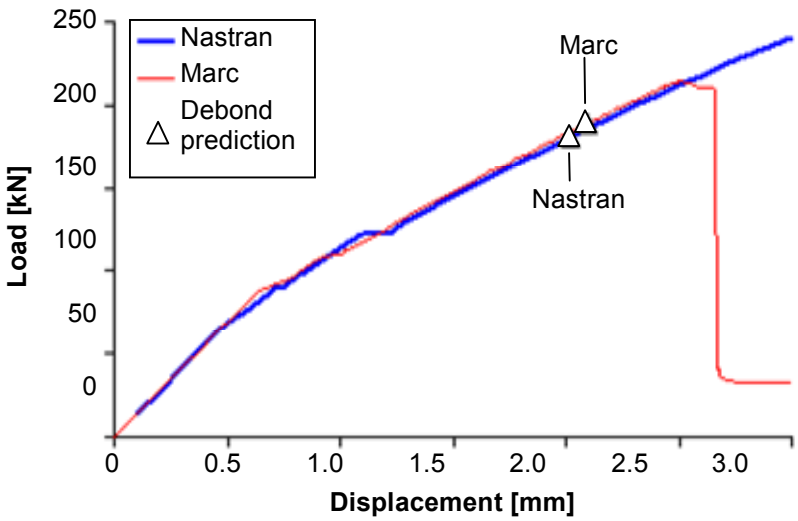

Figure 7.7: Load-shortening and debond predictions, D2 Nastran and Marc models

7.2.2 Pre-Damaged

In a similar manner to COCOMAT WP2.3, WP5.2 involved the design and analysis of pre-damaged panels for manufacture and testing. For this, the panels designed in WP2.3 were used, and the type, size and location of damage were investigated using the analysis methodology developed in this work to select a damage configuration for each design.

For the D1 panels, there were four panels that were selected for pre-damage, corresponding to two different damage configurations tested in static and cyclic loading. For this design, it was decided to implement a pre-damaged skin-stiffener debond, through the use of Teflon inserts between the skin and stiffener in manufacture, and to only implement one damage region per panel. As an initial step in the selection of the size and location of these Teflon inserts, DLR proposed two damaged configurations, summarised in Figure 7.8. These corresponded to a 100 mm and 200 mm debonded area, located in the centre of the panel under the central stiffener.

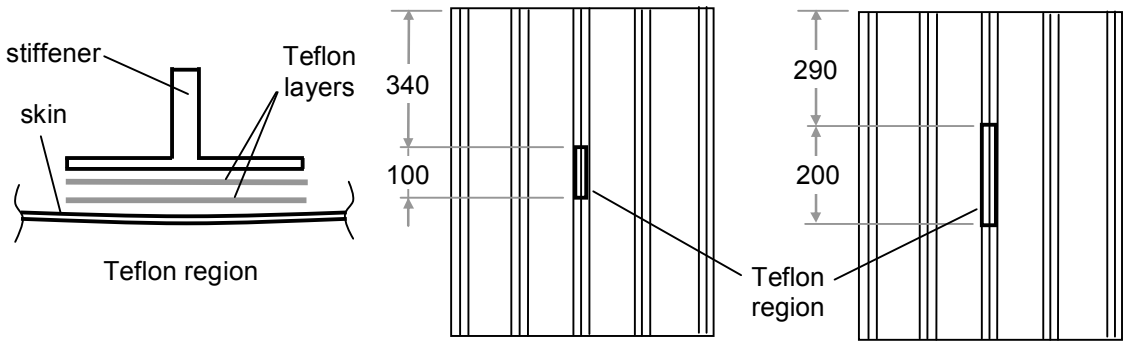

Figure 7.8: D1 proposed damage configurations: 100 mm and 200 mm damage region

Using the developed analysis tool, the proposed configurations were analysed under compression. Following this, several other configurations were analysed. These were based on the 100 mm configuration, and involved offsetting the debond region from the panel centre (called location 1) to two other positions (locations 2 and 3), and using one of the off-centre stiffeners instead of the central stiffener. The centre location 1 design and five subsequent proposals are defined in Figure 7.9.

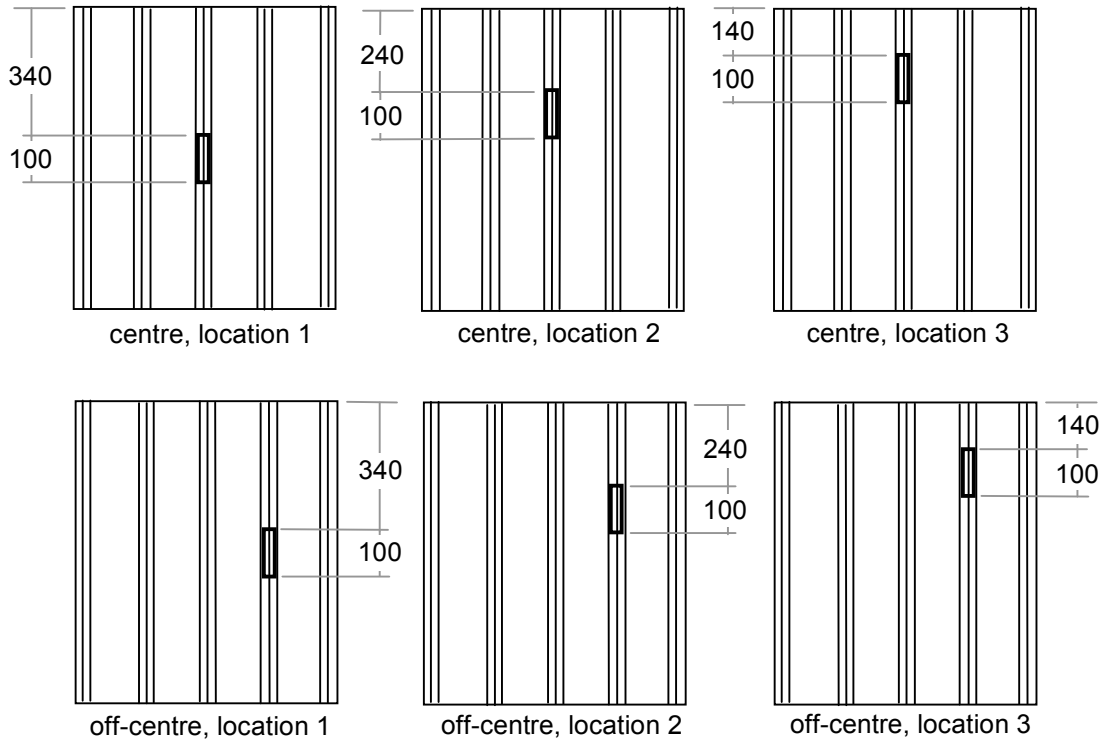

Figure 7.9: Damage configuration proposals using the 100 mm Teflon debond and modifying the location and stiffener used

All damage configurations were analysed using the methodology developed and demonstrated in Chapter 5, which included the degradation models for in-plane damage and interlaminar damage growth. The material properties were previously given in Table 5.4 and Table 5.6. The FE model for both the centre and off-centre models consisted of 5772 thick shell elements, 6004 nodes and 395 user-defined MPCs. The skin-stiffener joint of the stiffener containing the debond was modelled using two sublaminates, and all other skin-stiffener joints were modelled using a single shell element. This was the only difference between the centre and off-centre stiffener models. The different location models were created by setting the states of the user-defined MPCs accordingly.

The results for the DLR proposals are presented below, where Figure 7.10 shows both the load and debond length versus applied displacement and the radial displacement at 3.0 mm axial compression. It should be noted that the analyses were only run to 3.0 mm axial compression and were not continued until panel collapse, as this was not necessary in order to compare the panel configurations from a design perspective and would have increased the computational time considerably. The debond lengths were calculated using the average debond edge locations based on nodal coordinates. From these results, the 100 mm configuration showed crack growth initiation at 1.2 mm compression coinciding with the

onset of global buckling. The global buckling shape consisted of a central buckle over the centre stiffener, with buckling towards the centre of curvature. Crack growth was predicted to occur at both ends of the debonded region throughout the analysis, and was generally symmetric about the panel centreline. The crack growth for this configuration occurred almost exclusively without any mode I component, as crack growth was driven by the shear opening modes II and III. At the end of the 3 mm compression, the size of the debonded area had increased from 100 mm to almost 180 mm. The 200 mm configuration also showed crack growth initiating around global buckling at 1.1 mm compression, with a single central global buckle over the centre stiffener. Crack growth was again symmetric, and occurred at both ends of the debonded region. However, for this configuration there was much less crack growth predicted throughout the analysis, and at the end of the 3 mm compression the size of the debonded length had only increased from 200 mm to 210 mm.

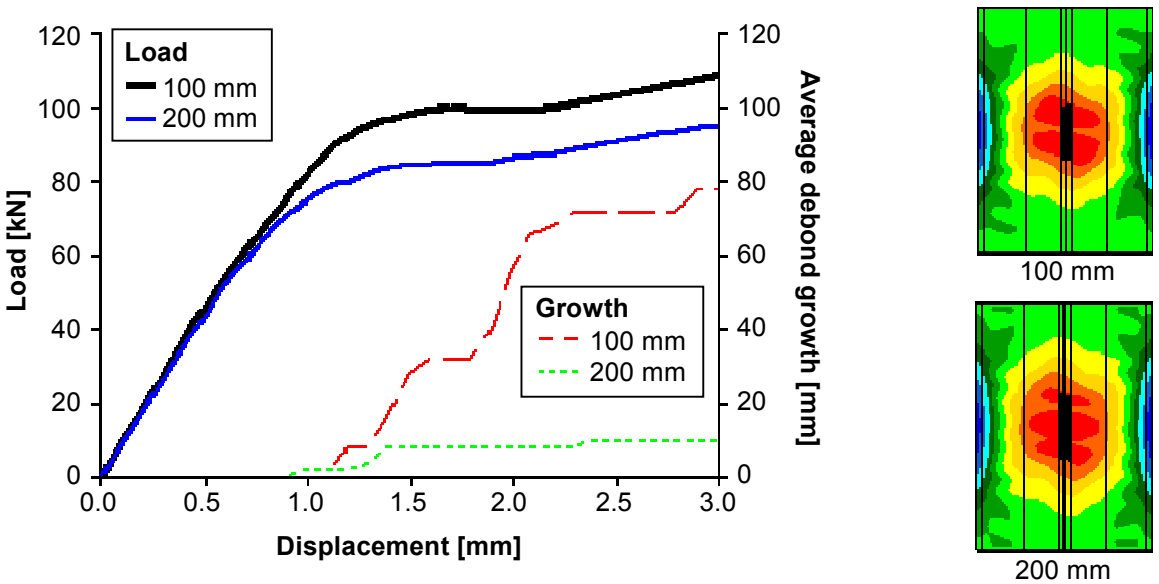

Figure 7.10: DLR 100 mm and 200 mm damaged configurations: (a) Load and debond length versus end shortening (b) Radial displacement and debond at 3.0 mm applied compression

For the additional configurations, offsetting the debond 100 mm to location 2 did not affect the global buckling shape, though gave more crack growth than the location 1 design that was focused on the debond edge closer to the centreline. Offsetting the debond a further 100 mm to location 3 changed the global buckling shape considerably, and also showed a significantly increased crack growth due to the higher proportion of mode I opening displacements at the crack front. For the debond under the off-centre stiffener, the centreline debond caused a change to an asymmetric global buckling pattern, as the weaker off-centre stiffener buckled

inwards first. The model with the debond at location 2, shown in Figure 7.11, gave a similar asymmetric global buckling shape, though under compression a more symmetric pattern developed with inward global buckles in the outer stiffener bays and an outwards buckling region over the centre stiffener. This displacement shape caused significantly higher mode I component at the crack front of the debond than the location 1 design, and as such increased crack growth was seen towards the end of the compression, to give a total crack length of 290 mm. For the debond at location 3, a single central global buckle was again seen, though the diagonal debond placement caused additional mode I opening, and at 3 mm compression the debonded region had extended to cover most of the stiffener length. For all off-centre stiffener models, crack growth initiation was generally coincident with the onset of global buckling, as was seen for the centre stiffener models.

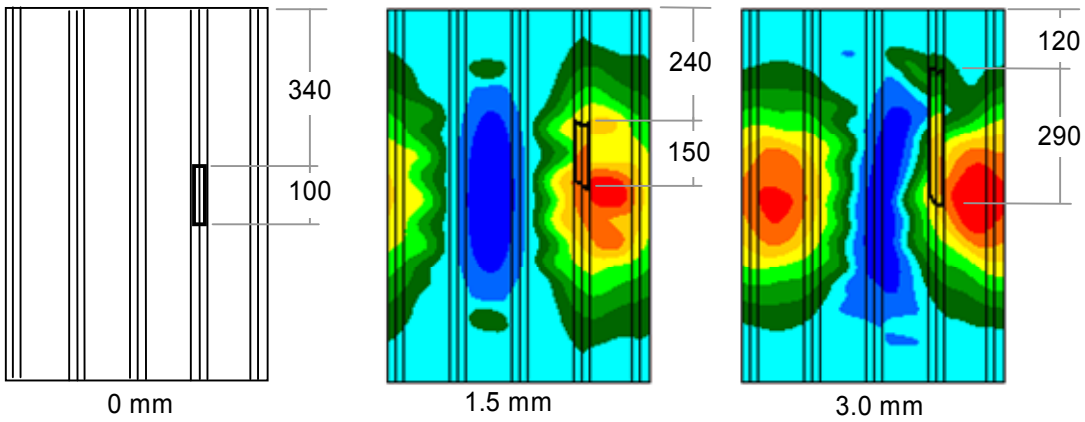

Figure 7.11: Off-centre location 2 design, out-of-plane displacement and debond size at applied compression values

In terms of using the analysis to make recommendations, the 100 mm DLR configuration with the debond under the centre stiffener showed a significant amount of crack growth occurring in a stable manner throughout the compression, making it suitable for experimental investigation. The 200 mm configuration, however, only showed limited crack growth, and it was concluded that this configuration would offer no new information on crack growth, and was not recommended. Of the additional configurations, the off-centre location 2 design was recommended, as it provided stable crack growth, and involved a different global buckling mode shape and a considerably higher mode I component. This would allow for the investigation of crack growth at a different mode mixity, and also of the debond behaviour under an asymmetric buckling shape.

Based on these recommendations, the 100 mm DLR proposal (centre location 1) and the centre location 2 configurations were accepted as the two configurations for pre-damaged D1 panels. This process demonstrated the way in which the developed analysis tool provided for the collapse analysis of postbuckling structures, and highlighted the advanced analysis capabilities possible by taking degradation into account.

7.3 Analysis

In this section, the analysis methodology and software tool are demonstrated for the analysis of postbuckling composite structures, in particular for post-test simulations. Again, the capabilities of the tool are shown to be applicable for both intact and damaged panel analysis. The panels presented in this section were manufactured by Aernnova and tested at DLR.

7.3.1 Intact

To demonstrate the capability of the developed tool for the analysis of intact postbuckling composite structures, experimental results for a D2 panel will be presented, and compared to the analysis results using the developed approach.

A D2 panel was manufactured according to the specimen details given previously, which consisted of a 4-stiffener curved panel encased in resin potting on the ends and with a longitudinal edge restraint along the sides to restrain the out-of-plane displacements. Imperfection data was measured using the 3D photogrammetric measurement system ATOS, and is given in Figure 7.12(a). Ultrasonic and thermographic scans were taken prior to loading, and no damage was visible in the untested panel. During the test, the applied load and displacement were taken from the testing machine and an axial LVDT, respectively. Displacement data for the entire panel was continuously monitored using the high speed optical measuring system ARAMIS. Thermographic scans were also taken during the test, at load levels before and after buckling, and following collapse, as shown in Figure 7.12(b).

Under compression, the panel developed a range of buckling mode shapes, as shown in Figure 7.13. Global buckling occurred at 0.47 mm axial compression and corresponded to one buckle in the outer stiffener bays. The buckles were not symmetric, and appeared to be influenced by the imperfection pattern, which showed a region of initial displacement towards the centre of curvature at a panel corner. One of the global buckles was offset from the panel centreline

towards this corner, and the bay with this offset buckle developed a second buckle at 0.57 mm axial compression. Under further compression the panel displayed a range of complex mode shape changes, which included a global buckle in the centre stiffener bay at 0.65 mm, and a second buckle in the other outer stiffener bay at 1.37 mm. The periodic thermographic scans showed that no damage occurred in the panel prior to the onset of collapse. Panel collapse occurred at 1.84 mm axial compression, or 174 kN applied load, and was characterised by fibre fracture in the stiffener and delaminations under all four stiffeners, as seen in Figure 7.12(b).

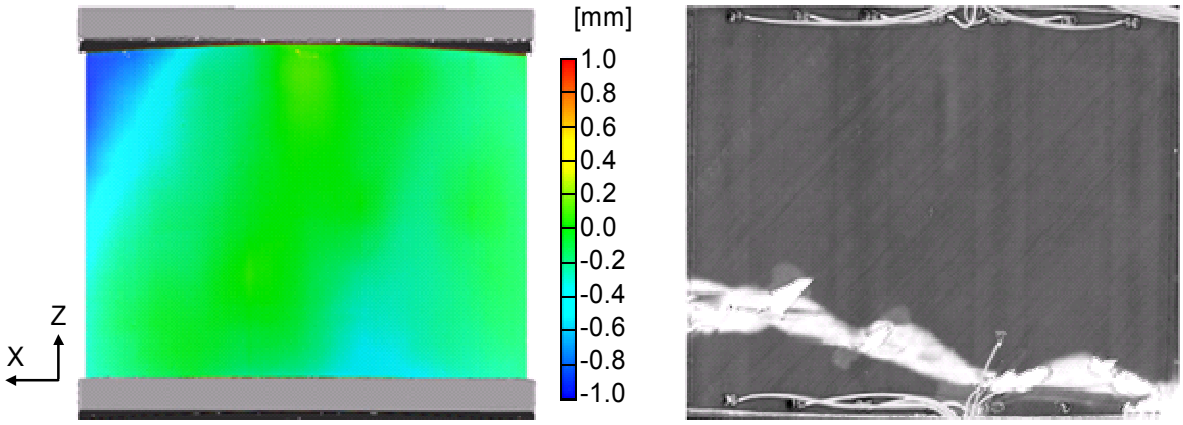

Figure 7.12: D2 panel (a) imperfection data (b) thermography scan after collapse (scans taken from the panel skin side) (courtesy of DLR)

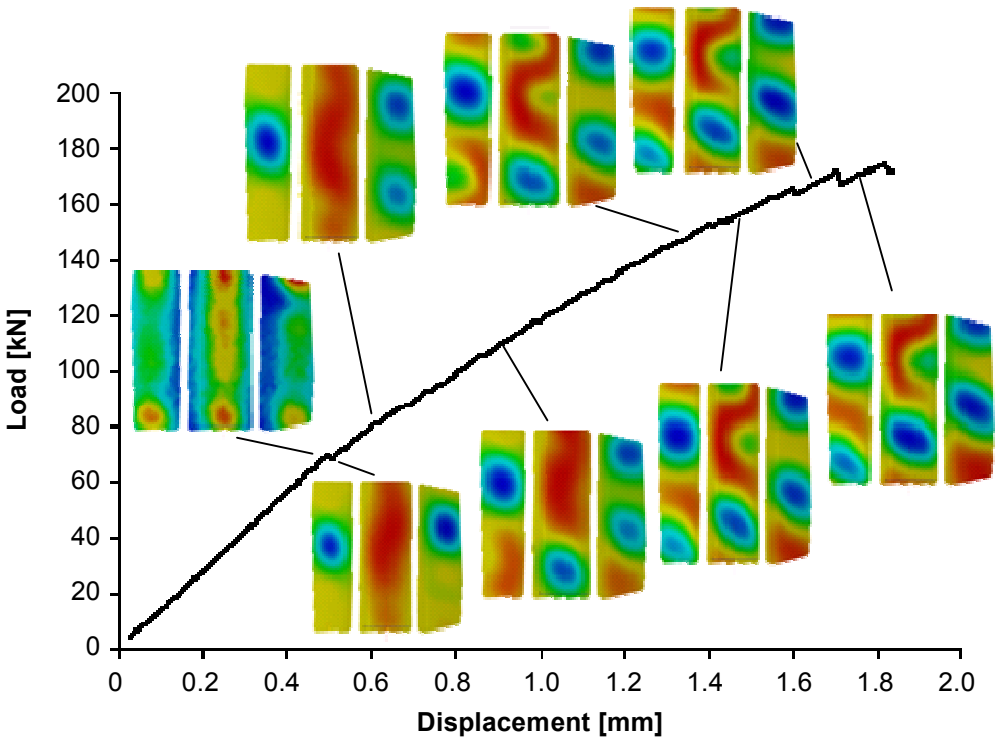

Figure 7.13: D2 experimental load-shortening, with radial displacement contours (stiffener side) (courtesy of DLR)

For the numerical analysis, FE models were created using the nominal and imperfect geometry. For the material properties, a different set of stiffness and strength values to those applied in the design analyses were used, as they had become available from new characterisation tests performed by DLR, and these are given in Table 7.5 (Degenhardt et al. 2007). For the imperfect model, the imperfection pattern seen in Figure 7.12(a) was approximated by modifying a triangular region of nodes in the panel corner on the unloaded end. This approach was taken as more sophisticated software tools for incorporating the measured imperfection data were not available at the time. The local model used was taken from the design studies presented previously. The results for both models are given in Figure 7.13 and Figure 7.14, where debond initiation was predicted to occur at 1.92 mm for both nominal and imperfect models, which preceded the onset of fibre fracture in both cases.

Table 7.5: Material and fracture properties for carbon unidirectional tape IM7/8552

Stiffness property	**Value**	**Strength property**	**Value**	**Fracture property**	**Value**
E_{11} [GPa]	142.5	X_t [MPa]	1741	Mixed-mode criterion	B-K
E_{22} [GPa]	9.7	X_c [MPa]	854.7	G_{Ic} [kJ/m^2]	0.243
ν_{12}	0.28	Y_t [MPa]	28.8	G_{IIc} [kJ/m^2]	0.514
G_{12} [GPa]	5.1	Y_c [MPa]	282.5	G_{IIIc}* [kJ/m^2]	0.514
G_{23}* [GPa]	4.0	S_{xy} [MPa]	98.2	B-K coefficient, η*	4.6
G_{31}* [GPa]	5.1	S_{yz}* [MPa]	78		

* assumed

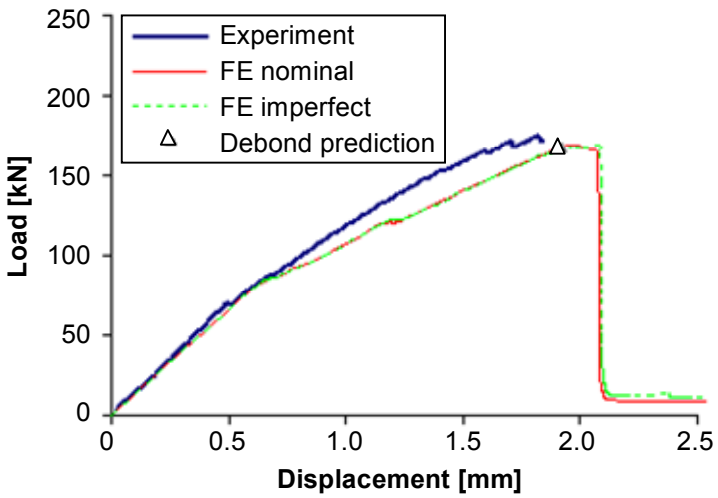

Figure 7.14: D2 panel, load-shortening and debond prediction, experiment and FE models

From the results, the nominal and imperfect models were almost identical, with the load-displacement, deformation pattern, and failure prediction all giving very similar results. The results of the analyses were also very similar to those previously presented in the design

process for the D2 panels, particularly the deformation pattern given in Figure 7.5. The models showed buckling of five to six half sine waves per stiffener bay from about 0.65 mm axial compression, where under further compression one or two half waves became dominant and showed larger deformation. There was continual change of the buckling shape until around 1.22 mm compression, at which point a stable and symmetric buckling pattern developed of three half waves per bay, as shown in Figure 7.15(a), and this continued until the onset of fibre fracture in the stiffeners at around 2.08 mm compression. It is interesting to note that the FE models had a lower stiffness than the experimental panel, as typically FE models tend to overestimate stiffness. This is due to difference in the deformation shapes, where the complex asymmetric buckling pattern seen in the experiment (Figure 7.13) gave a higher structural stiffness than the symmetric pattern predicted by the numerical models (Figure 7.15).

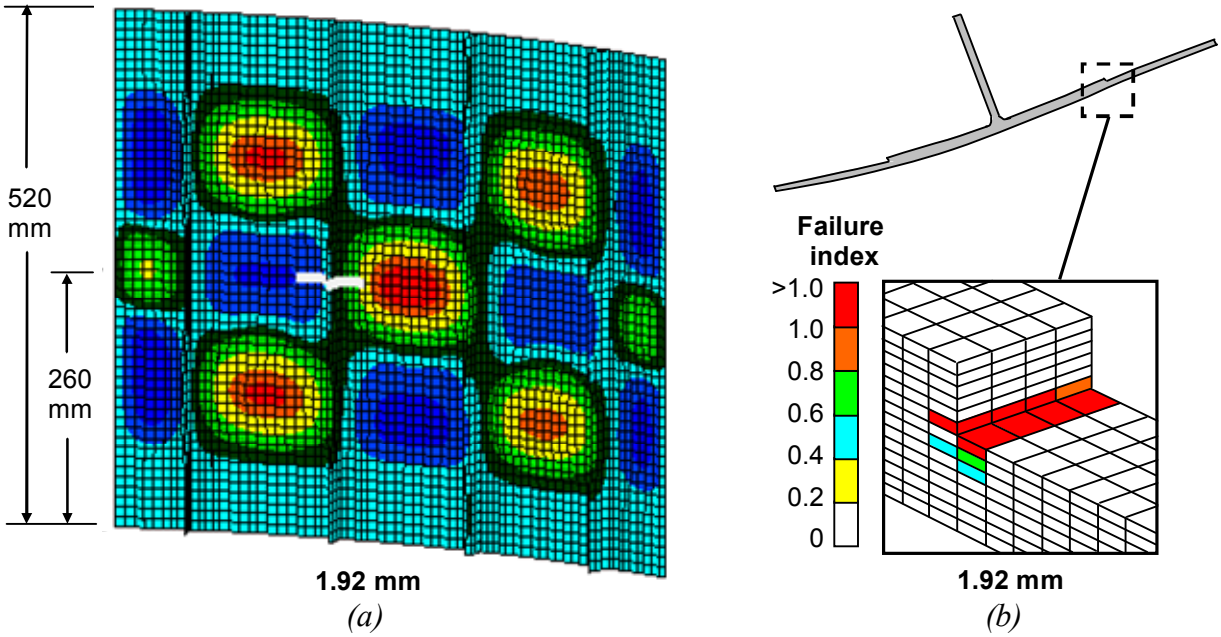

Figure 7.15: D2 panel, (a) global model with local location shown (b) local model

In comparison with experiment, both the nominal and imperfect models were not able to predict the exact asymmetric buckling patterns seen experimentally, and the predicted structural stiffness was lower than the experimental value, particularly in the postbuckling region. In spite of this, the panel behaviour and onset of buckling were predicted quite well. The predicted initiation of debonding also compared very well with the experimental collapse of the panel, though the exact location of failure was not predicted as this was dependent on the deformation. However, investigation of local models at other locations revealed that the interlaminar damage was predicted to occur at multiple locations throughout the panel within

a small range of compression values up to the point at which fibre fracture occurred. These locations included anti-nodal and nodal lines, where the anti-nodal lines such as that shown in Figure 7.15 gave failure at the flange edge due to high peel stresses, and the nodal lines of minimum displacement failed in the region underneath the stiffener due to high shear stresses.

7.3.2 Pre-Damaged

In this section, results from a pre-damaged panel are presented and compared to analysis results using the developed approach. Though the COCOMAT pre-damaged panel designs have not yet been manufactured and tested, experimental results were available for an intact panel that developed damage under cyclic loading, before being statically loaded to collapse. The results for this test have been published by Degenhardt et al. (2007).

A D1 panel was manufactured according to the specimen details given previously, and consisted of a 5-stiffener curved panel encased in resin potting on the ends. All data recording devices were as described for the D2 panel, and involved photogrammetric, ultrasonic and thermographic scans, shown in Figure 7.16, and LVDT and test machine data. In testing, the panel was loaded with 2000 cycles up to 1.08 mm compression, 1700 cycles up to 1.93 mm compression, then statically until collapse. The cyclic loading corresponded to loads just before global buckling, and 95% of the expected displacement at collapse, where the collapse displacement was taken from a previous test on another D1 panel. The experimental results are presented below, where Figure 7.17 shows photographs of the panel during testing with out-of-plane-fringe images overlaid, and Figure 7.18 is the load-displacement curve with corresponding out-of-plane displacement fringe images.

Under loading the panel developed a local buckling pattern at around 0.75 mm axial compression of 13 to 15 longitudinal half waves per stiffener bay, leading to global buckling at around 1.0 mm axial compression. The global buckling pattern was symmetric and consisted of an inwards buckle (towards the stiffener side) located over the centre stiffener and outwards buckles in the outer stiffener bays. Under further compression the central buckle moved to one of the inner stiffener bays creating an asymmetric pattern.

In cyclic loading, the periodic thermographic scans were used to monitor damage, and no damage was seen in the panel after the first 2000 cycles. After 400 cycles at the higher cyclic load, skin-stiffener debonding became evident at two locations in the centre and an inner stiffener. These areas were seen to grow under further cyclic loading, so that at 3700 cycles,

when the cyclic loading was completed, the damage was as shown in Figure 7.16(b). This corresponded to a debonded area of 2016 mm^2 under the centre stiffener and 1920 mm^2 under the inner stiffener, which were considered as the pre-damaged regions for the static loading.

Under static loading the same local and global buckling patterns seen in cyclic loading developed, though some opening of the debonded regions was evident by 2.5 mm axial compression. At around 2.5 mm axial compression the debonded areas showed a rapidly increased damage growth and opening displacement, which caused a large reduction in the load-carrying capacity of the panel, as seen in Figure 7.17. The damage growth process was seen again at around 2.81 mm axial compression, where growth of the debonded area led to an increase in the skin-stiffener opening, and also caused some fibre fracture and matrix cracking in the regions around the debonds. Collapse of the panel occurred at 3.31 mm axial compression and corresponded to significant fibre fracture through the centre stiffener.

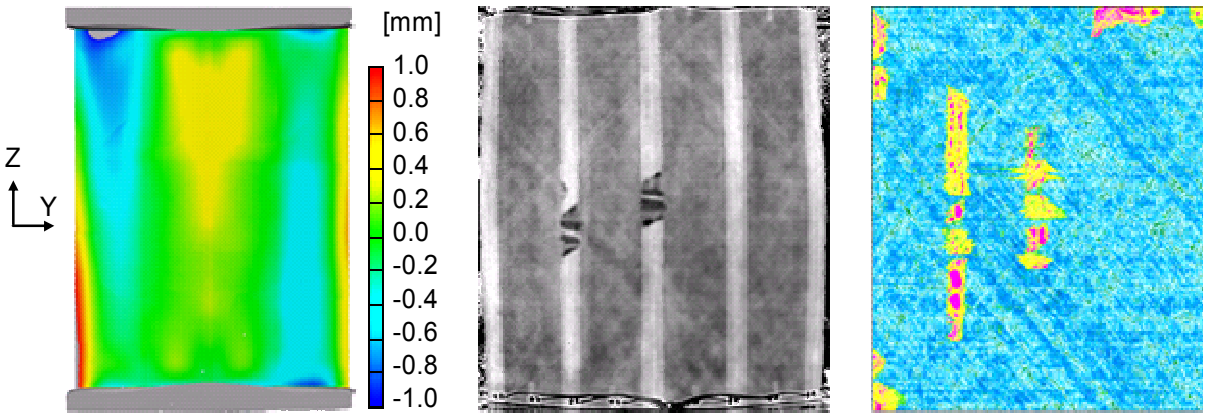

Figure 7.16: D1 panel: (a) imperfection data (b) thermography scan after 3700 cycles (c) ultrasonic scan after collapse (scans taken from the panel skin side) (courtesy of DLR)

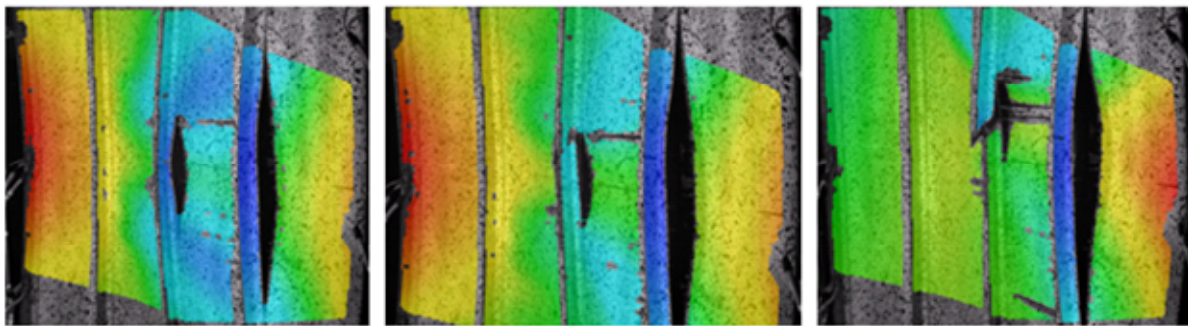

Figure 7.17: D1 test images with radial displacement contour overlays, showing debond progression (courtesy of DLR)

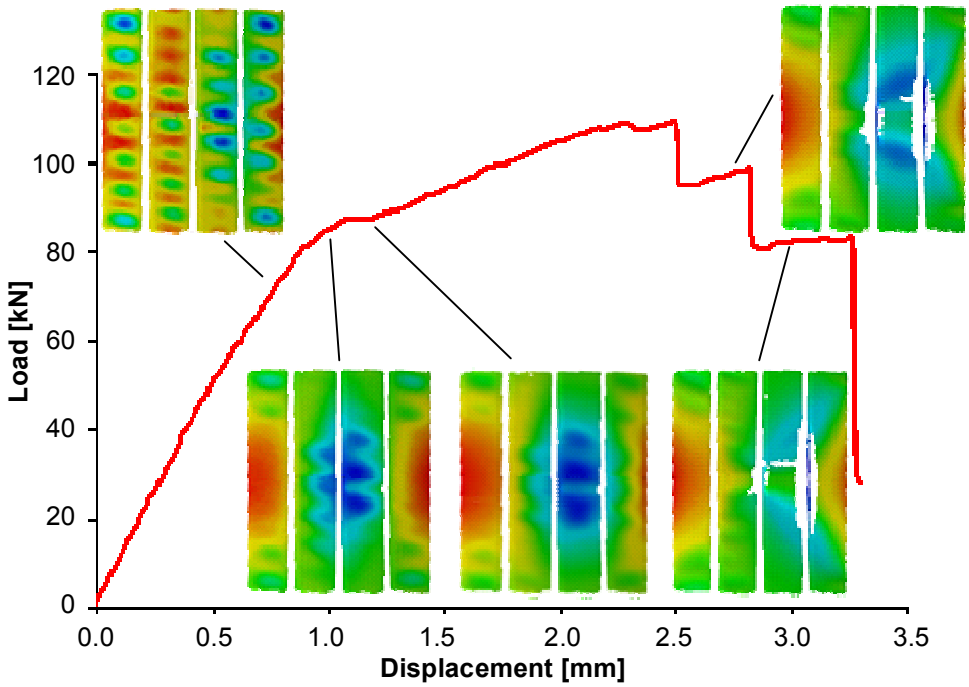

Figure 7.18: D1 experimental load-shortening, with radial displacement contours (stiffener side) (courtesy of DLR)

In the numerical analysis, the D1 panel debonded model detailed in the previous section was used, though the user-defined MPCs were included in the centre and an inner skin-stiffener joint in order to model debond growth. The pre-damaged debonded regions were taken from the thermographic scans of the damage, seen in Figure 7.16(b), and were adapted to the regular grid mesh of the model to most closely match the area and shape of the experimental damage sites, as shown in Figure 7.19. It was assumed that the cyclic loading only resulted in skin-stiffener debonding, and any other damage such as matrix cracking that could have been present in the experimental panel prior to static loading was not considered. The pre-damaged model was run with the PM 4 approach for strain energy release rates, with the modification factors found from the single-stiffener D1 specimens in Chapter 5.

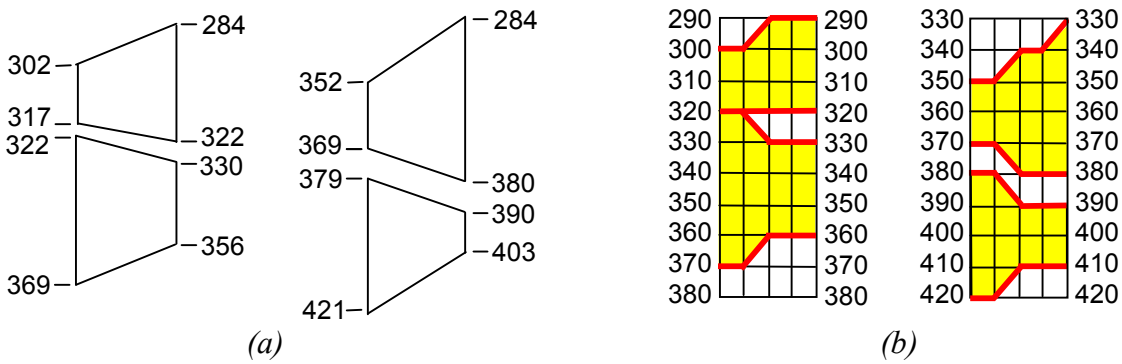

Figure 7.19: D1 cyclic test pre-damage: (a) Schematic representation, (b) Mesh-based approximation, distances given in mm to inside of potting on non-loading side

The results of the analysis are presented below, where Figure 7.20 is the load response with the length of the debonded areas under the centre and off-centre stiffener also shown. As for the design analysis in the previous section, the lengths of the debonded areas were calculated using the average debond edge locations based on nodal coordinates. As the initial pre-damaged configuration consisted of two separate debond regions under the two stiffeners, shown in Figure 7.19, the average of the two regions was used as the debond length. Figure 7.21 gives the out-of-plane deformation, Figure 7.22 illustrates the debond growth, and Figure 7.23 gives the failure index and out-of-plane displacement in the final deformed configuration, where gap elements can be seen across the debonded skin-stiffener interfaces.

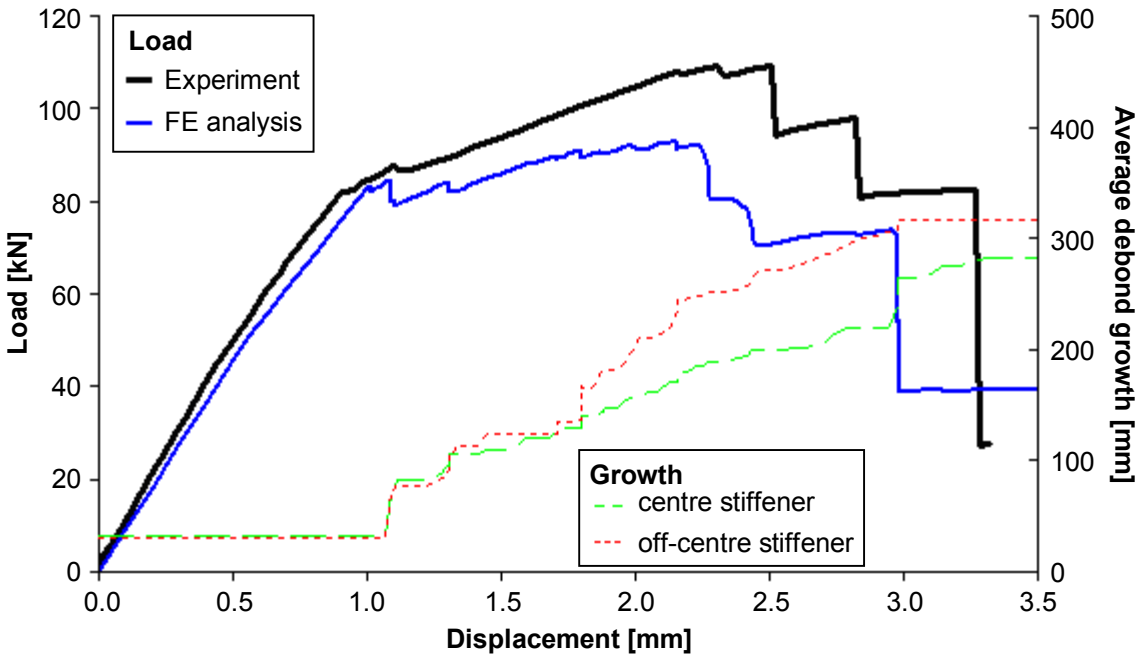

Figure 7.20: D1 panel, experiment and FE load-displacement results, and FE debond length predictions

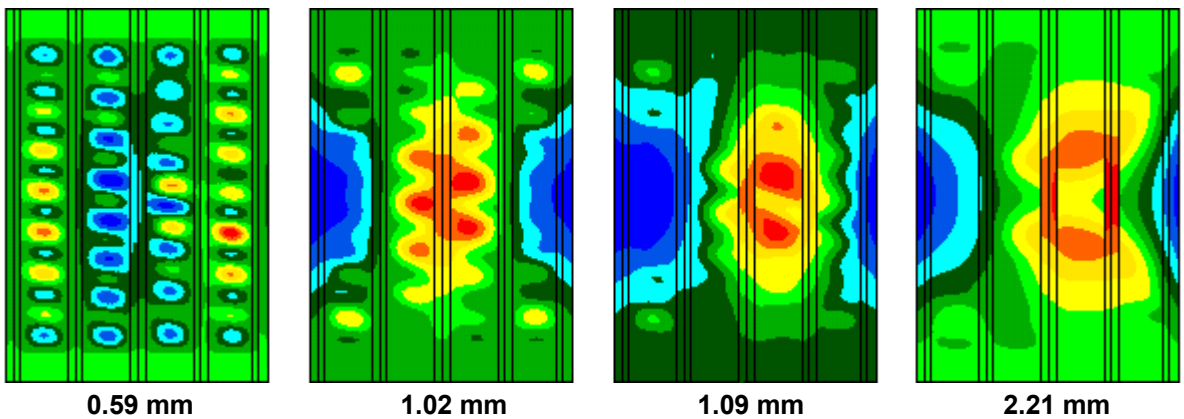

Figure 7.21: D1 panel, out-of-plane deformation (stiffener side)

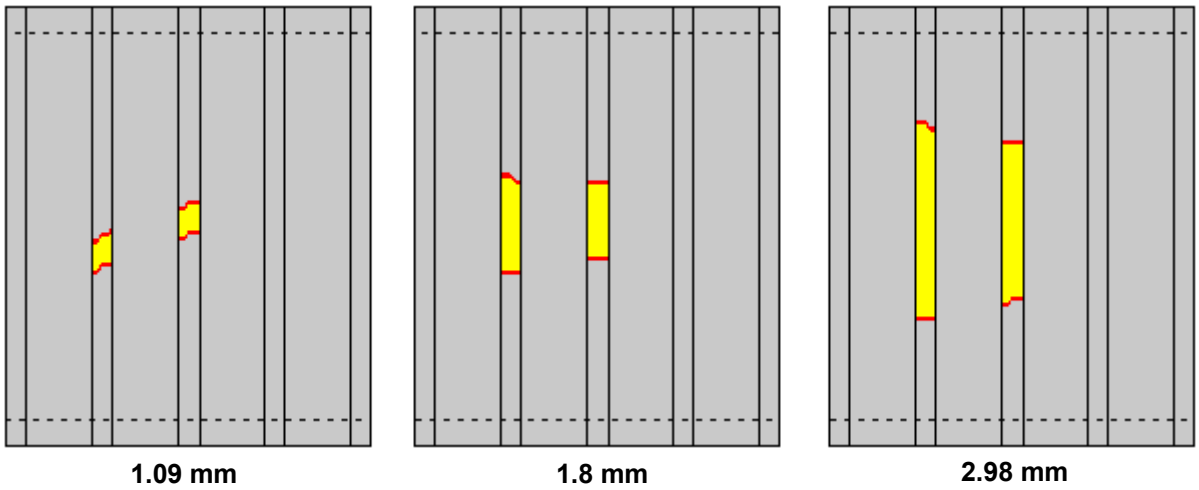

Figure 7.22: D1 panel, debonded area at applied displacement (skin side)

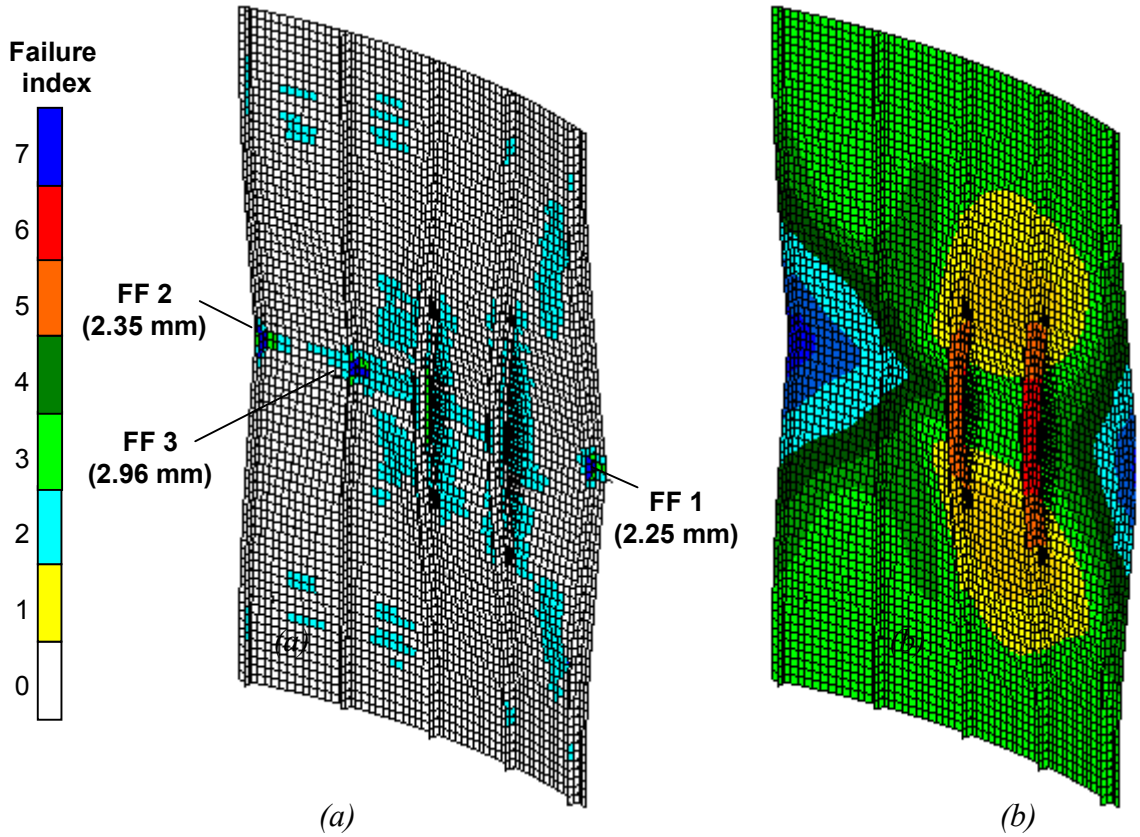

Figure 7.23: D1 panel at 2.98 mm applied displacement (collapse): (a) Ply failure index showing stiffener fibre failure (FF) sequence (b) Out-of-plane deformation

From Figure 7.21, the FE model gave a local buckling pattern of 15 half waves per bay, global buckling of a single central buckle at 1.02 mm compression that moved to be located between two inner stiffeners by 1.09 mm compression, all of which agreed very well with the experimental behaviour shown in Figure 7.18. In the numerical model, the movement of the

global buckle coincided with coalescence of the separate debonded regions under the two stiffeners, and some opening was seen across these interfaces. Growth of the debonded regions was then predicted to occur in a continuous manner, and was characterised by drops in the load response and increased skin-stiffener opening. This was accompanied by matrix cracking in mainly the outer 90° plies of the skin, which was focused on the centre and edges of the debonded regions. Though correspondence was not seen at all predicted locations, the experimental panel did show matrix cracking in the outer plies extending from the skin-stiffener debond edges.

Under further compression, the numerical model showed fibre fracture in mainly the central 0° stiffener plies at 2.25 mm, 2.35 mm and 2.96 mm axial compression, with the two outer stiffeners and an inner stiffener failing sequentially as shown in Figure 7.23(a). Fibre fracture was characterised by large drops in the load response of the panel of around 10 kN for the outer stiffener failures, and around 30 kN for the inner stiffener, where the latter was taken as the collapse of the panel. Though the experimental panel showed failure in the central stiffener causing collapse, the sequence and size of the load reductions, the onset of fibre fracture in the central 0° plies of the stiffeners, and the way in which the debond growth and matrix cracking contributed to fibre fracture and panel collapse all closely matched the experimental results.

Whilst it was difficult to extract precise crack growth data from the experimental results, crack opening was seen at several stages before and after fibre fracture, and the experimental debonded area under the inner stiffener showed the greater crack growth, both of which compared well with the numerical model. Additionally, the approximate final debonded lengths of the experimental panel were 224 mm and 403 mm under the central and inner stiffener respectively, which gave very good comparison with the numerical values of 282 mm and 316 mm, especially considering the fact that fibre fracture in the experimental panel would have caused additional crack growth and energy released in the same manner as was seen for the single-stiffener specimens in Chapter 5.

7.4 Discussion

The analyses given in this section have shown that the approach developed is suitable for the design of postbuckling composite structures including the effects of damage. As with all analyses, the failure predictions were largely dependent on the material properties, and the

results were sensitive to the variation typically seen in experimental material characterisations tests. However, from a design point of view, this sensitivity is less important, as the comparative nature of the design process means that different configurations can be assessed qualitatively against each other. Examples of this were shown in this chapter, and included determining which configuration of intact specimens would likely fail first or give the most stable postbuckling behaviour, or which configuration of pre-damage would give the most crack growth under varying crack opening displacement mixtures.

The results in this chapter also further demonstrated the capability of the developed approach to provide accurate predictions of the behaviour of postbuckling composite stiffened panels, and critically to capture the damage mechanisms for compression loading. For all analyses, there were a number of factors that considerably influenced comparison with experimental results. One aspect was the difficulty in accurately capturing the correct buckling mode shapes and deformation patterns, which was especially critical for crack growth in the region just ahead of any crack front. Separately, the influence of mesh density remains significant for any analysis, where though the effect on strength-based failure predictions was uncertain, using smaller elements would have led to reduced strain energy release rates and less conservative predictions in all crack growth analyses. For the comparison with the cyclically-loaded experimental panel, the effect of the repeated loading into deep postbuckling on the integrity of the panel and general structural behaviour remains largely uncertain. In spite of these aspects, the developed approach allowed for in-depth analysis of the critical damage mechanisms, and was able to illustrate the way in which these mechanisms combined to produce final panel collapse.

One aspect that remains important in the application of the developed approach for both design and analysis is the computation time. For the analysis in this chapter, computation time was from 40 to 60 minutes for 3D local models, one to eight hours for intact panels, three to eight hours for models with only crack growth monitored, two to five days for intact panels with ply damage, and from three to over ten days for models with crack growth and ply damage monitored including collapse. In general, this order of computation time fits in with the aims of the developed approach to form part of a necessarily “slow” analysis tool, capable of being used in the certification process of aircraft. However, for more complex models, particular those that involve both crack growth and ply damage, a more efficient analysis process would be desirable. There are a number of ways to achieve this, which include: re-writing the subroutines to use a more efficient implementation into the FE code; increasing

the ply softening knockdown factor from 0.1; and, limiting the use of the ply failure degradation model, especially through the use of the subroutine to only monitor the failure indices without softening, or application to only select ply layers and locations in the model. However, it must remembered that the accurate analysis of crack growth and ply failure is always going to be detrimental to computation time as part of an implicit FE analysis, and that experience is required in order to judiciously apply the degradation models within practical design and analysis procedures.

7.5 Conclusion

In this chapter, the developed analysis methodology was applied in a range of different cases to demonstrate its functionality and applicability for advanced structural analysis. To demonstrate the applicability of the methodology for structural design, the process performed within COCOMAT for designing intact fuselage-representative panels was first summarised, and results using the developed approach were shown to be in excellent agreement. For the design of pre-damaged specimens, the developed approach was included as part of the COCOMAT design procedure, and the results of this process were summarised. To demonstrate the application for the analysis of structures as post-test simulations, experimental results for both intact and pre-damaged panels were presented, and the success of the analysis methodology in capturing the specimen behaviour and critical damage mechanisms was shown.

CHAPTER 8

CONCLUSION

8.1 Summary of Findings

The overall goal of this research was to develop a validated analysis methodology and accompanying software tool for the collapse analysis of composite postbuckling structures taking degradation into account. Through the development, results and discussion of the previous chapters it was demonstrated that this goal was successfully achieved. This involved meeting the objectives that were defined in Chapter 1, and additional work that was completed within the COCOMAT project. As detailed conclusions have been presented at the end of every chapter, only a summary of the key achievements is given below.

- A comprehensive literature review and benchmarking exercise were conducted to assess the state of the art in postbuckling analysis and damage modelling of stiffened composite structures. These were used to formulate the framework for the development work.

- A range of approaches were developed to represent the critical damage mechanisms for composite stiffened structures in compression. This included an approach for predicting interlaminar damage initiation, and degradation models for interlaminar damage growth and in-plane ply damage. These approaches were efficiently implemented into the FE code Marc using current failure theories, and showed very good comparison with experimental data.

- As part of the interlaminar damage degradation model, a significant amount of work was performed to investigate the method of crack propagation using VCCT, which despite the extensive application of VCCT has not previously been comprehensively studied. In particular, the relationship between the method for modelling crack propagation and the assumption of self-similar growth was shown to have important effects on the accuracy of the analysis. The overestimation of strain energy release rates using VCCT with a simple fail-release approach was observed, which was shown

to be based on a violation of the assumption of self-similar crack growth. A correlation between the crack opening displacements and the shape of the local crack front was proposed, and a novel approach was developed to modify the strain energy release rate values based on the local crack front. This developed approach was shown to give more accurate and realistic predictions in both comparison with experiment results and in extensive parametric studies.

- A methodology was developed for the analysis of composite stiffened structures in compression, which incorporated all the critical damage mechanisms leading to collapse. This included the approaches for damage described above, as well as techniques to make the approach suitable for large postbuckling structures. The developed approach combined nine separate Marc subroutines, and allowed for the damage types contributing to structural collapse to be analysed.

- All aspects of the analysis methodology were extensively validated using experimental results taken from the COCOMAT project. This included validating the approaches for predicting interlaminar damage initiation, modelling interlaminar growth, and the use of the analysis methodology for the design and analysis of intact and pre-damaged structures.

- A user-friendly and industry-ready software tool was developed, which incorporated all aspects of the developed analysis methodology. The tool was implemented as a menu system in Patran, which was used to provide a range of functions for analysing postbuckling composite structures including the critical damage mechanisms.

- Significant contribution was also made to the COCOMAT project as deliverables for the CRC-ACS. This included the literature review, benchmarking analysis, and analysis methodology development, and also involved the design and analysis of postbuckling structures in support of the COCOMAT experimental test program.

- This work has resulted in significant publication, including four international journal papers, eight international conference papers, twelve COCOMAT internal technical reports and four CRC-ACS internal technical memorandums.

8.2 Further Work

Throughout this work, areas of future development have been identified, both as a consequence of the scope of this thesis and in terms of extending the state of the art for structural analysis and damage modelling.

One key aspect of the interlaminar damage propagation degradation model was the properties and behaviour of the skin-stiffener interface. Specifically, the difference between an integrally manufactured ply-ply interface and a secondary bonded ply-adhesive-ply interface was identified as a key issue in terms of both material properties and behaviour. Examples of this include questions over the transferability of data for fracture toughness, mixed-mode coefficients, and general crack growth behaviour from experimental characterisation at a ply-ply interface to an adhesive interface. Whilst the skin-stiffener interface was found in the literature to be the most suitable within the FE model for the interlaminar damage layer, the behaviour of this interface is critical to the degradation model and should be investigated further. Currently within the COCOMAT project and as part of separate CRC-ACS projects, experimental investigations are underway in order to further study this interface, and the results of these will inform future analysis using the approach developed in this work.

The modification approach developed in this research for producing more realistic estimates using VCCT of the strain energy release rates could also be further extended and refined. The approach implemented in this work involved classifying crack growth according to the local crack front, and applying reduction factors from previous parametric studies. In future, a more accurate or robust approach than using the local crack front may be necessary, and could involve knowledge of crack growth at more locations around the debond area. Separately, it was seen that the modification factors may be particular to the structure investigated, so that an automated procedure to robustly test all the required crack growth steps for each crack type can be developed. Alternatively, a more accurate approach would be to control the time step such that a previous increment could be re-visited if the crack opening displacements were seen to be overestimated, though controlling the time step in this way is currently not possible within Marc, and would result in a significant increase in computation time if implemented.

For the interlaminar damage growth degradation model, the implementation could be extended to handle multiple damage interfaces through the laminate thickness. From the literature review, a single damage layer at the skin-stiffener interface was identified as the most practical and conservative modelling approach, however the investigation of multiple

delaminations may have interesting applications, especially in comparison with experimental results. Though the degradation model as currently implemented would not be practical with the use of shells, the approach could easily be extended for solid elements.

In future it may be desirable to investigate the use of the VCCT-based interlaminar damage model in conjunction with a cohesive element formulation. Though work in this project has shown the two approaches to give similar descriptions of crack growth, the differences in the formulation of each approach may be preferably suited to particular situations. Specifically, the VCCT-based approach appears more suitable for modelling brittle fracture, whilst the cohesive element formulation would be better able to describe crack growth in the presence of energy dissipating mechanisms such as fibre bridging. Future studies could be directed at comparing the two approached across a range of different crack growth scenarios, and developing a set of guidelines for their respective application.

In this work, the initiation of interlaminar damage and growth of a pre-existing interlaminar damage area were treated separately. This was based on observations of the structures investigated, where interlaminar damage initiating in intact structures was found to lead to catastrophic failure. However, in future, it may be necessary to link the two approaches, that is, to have an interlaminar damage region detected, then to introduce a region into the FE model and analyse the growth of this region. This is expected to be relevant in the analysis of larger structures, such as complete fuselage “barrels”, or structures under different loading conditions such as shear or torsion. Though the development was not shown, such an approach was investigated in this work and found to be possible within the current Marc subroutine structure, though further development would be required, particularly in determining the appropriate size of any introduced damage region.

Using the in-plane damage degradation model, the capacity to introduce impact damage into the model prior to loading was implemented. This was achieved by setting the ply damage failure indices for any elements, which were then read in at the start of the analysis to introduce softening in the model. However, as mentioned previously, there was no correlation with experimental impact sites in order to attempt to characterise impact damage, and no recommendations for the softening were made. Further research could be performed to investigate accurate methods for introducing realistic impact damage zones into the model using this approach, which could then be incorporated into the analysis tool.

The developed analysis methodology could also be extended and improved in a number of ways in order to incorporate more accurate failure theories or apply to different design scenarios. Examples of this include the use of more advanced fracture mechanics theories such as the crack tip element approach (Davidson 1998), or the use of more complex and physically-based ply failure theories such as the Puck (Puck & Schürmann 1998) or LaRC04 (Pinho et al. 2005) criteria. For the detection of interlaminar damage, the strength-based approach should be further validated using different types of skin-stiffener failure such as debonding at the flange edge and stiffener delamination, and further study is required into the effect of mesh density and 3D effects. Additionally, the developed approach could easily be applied to a range of different structures, both skin-stiffened aerospace structures or otherwise, and with almost any loading conditions, though any additional failure modes that become important in these instances would need to be incorporated.

Future work could also investigate improved predictions of the deep postbuckling mode shapes. The development in this work focused on methods for capturing the critical damage mechanisms, and applied the nonlinear solution methods available within the FE software codes. However, capturing the correct postbuckling mode shape is fundamental to any reliable prediction of structural behaviour, so much so that predicting incorrect mode shapes can actually invalidate all other aspects of the numerical results. Further study in accurately predicting the complex deformation patterns seen in deep postbuckling would be valuable, and could concentrate on either improving nonlinear solution algorithms or comparing available technologies in implicit and explicit FE solvers. One aspect that is recommended for all future work wherever possible is the incorporation of measured geometric imperfections, in order to assist in capturing the correct postbuckling deformations. In this work, sophisticated software tools were not available to perform this operation, however they have since been developed and can be applied to the database of measured imperfection data available within the COCOMAT project.

More generally, the results in the work have repeatedly demonstrated the critical need for accurate material properties, and the influence of experimental variance in all test data. This was seen in the different material properties reported for the same material, and the different experiment results recorded for nominally identical structures. In particular, the use of the correct material properties was especially critical from a modelling point of view, and in some instances the failure predictions were very sensitive to the strength and toughness values used. In order to mitigate these issues, it may be desirable to investigate theories and approaches

that are specifically selected so as to be less dependent on uncertain material data, or alternatively it may become necessary to consider the sensitivities of a structure as part of the design process.

8.3 Final Remarks

Despite years of extensive research, countless theories of ranging complexity, and a great deal experimental and numerical results, the fields of postbuckling analysis and failure prediction in composites remain something of a "black art" within both industry and the research community. Developments in these areas are also complicated by the competing needs of each group, where industry searches for safe, trusted and robust solutions for immediate application, whilst researchers look to push the state of the art and search for deeper understanding at all levels of analysis. The work in this thesis has attempted to bridge the gap between research and industry, and provide a physically sound yet practical and experimentally validated analysis tool for postbuckling composite structures. It is hoped that the work will provide insight and direction into these "black arts", and continue to inform and inspire future analysis of composite structures for the next generation of aircraft and beyond.

REFERENCES

ABAQUS Version 6.6 Documentation 2006, ABAQUS, Inc., Rhode Island, USA.

Abramovich, H & Weller, T 2006, *Skin-stringer separation tests − Panels with drop-off plies*, COCOMAT Technical Report, Israel Institute of Technology.

Abramovich, H 2007, *Manufacture of the pre-damaged panels and non-destructive inspection*, COCOMAT Technical Report, Israel Institute of Technology.

Abramovich, H, Grunwald, A, Pevsner, P, Weller, T, David, A, Ghilai, G, Green, A & Pekker, N 2003, 'Experiments on axial compression postbuckling behavior of stiffened cylindrical composite panels', in *44th AIAA/ASME/ASCE/AHS Structures, Structural Dynamics and Materials Conference*, Norfolk, VI, USA, AIAA paper no. 2003-1893.

Allix, O & Ladevèze, P 1992, 'Interlaminar interface modelling for the prediction of delamination', *Composite Structures*, vol. 22, pp. 235-242.

Ambur, DR, Jaunky, N & Hilburger, MW 2004, 'Progressive failure studies of stiffened panels subjected to shear loading', *Composite Structures*, vol. 65, pp. 129-142.

Ambur, DR, Jaunky, N, Hilburger, MW & Dávila, CG 2004, 'Progressive failure analyses of compression-loaded composite curved panels with and without cutouts', *Composite Structures*, vol. 65, pp. 143-155.

Andersons, J & König, M 2004, 'Dependence of fracture toughness of composite laminates on interface ply orientations and delamination growth direction', *Composites Science and Technology*, vol. 64, pp. 2139-2152.

Arnold, RR & Parekh, JC 1987, 'Buckling, postbuckling and failure of stiffened panels under shear and compression', *Journal of Aircraft*, vol. 24, no. 11, pp. 803-811.

Baker, A, Dutton, S & Kelly, D 2004, *Composite Materials for Aircraft Structures*, 2nd edn, American Institute of Aeronautics and Astronautics, Virginia, USA.

Baranski, AT & Biggers Jr, SB 1999, 'Post-buckling analysis of tailored composite plates with progressive damage', *Composite Structures*, vol. 46, pp. 245-255.

Barbero, EJ 1998, *Introduction to Composite Material Design*, Taylor & Francis, Inc., Philadelphia, USA.

Bayandor, J, Thomson, RS, Scott, ML, Nguyen, MQ & Elder, DJ 2003, 'Investigation of impact and damage tolerance in advanced aerospace composite structures', *International Journal of Crashworthiness*, vol. 8, no. 3, pp. 297-306.

Benzeggagh, ML & Kenane, M 1996, 'Measurement of mixed-mode delamination fracture toughness of unidirectional glass/epoxy composites with mixed-mode bending apparatus', *Composites Science and Technology*, vol. 56, pp. 439-449.

Bisagni, C & Cordisco, P 2003, 'An experimental investigation into the buckling and post-buckling of CFRP shells under combined axial and torsion loading', *Composite Structures*, vol. 60, pp. 391-402.

Bisagni, C 2000, 'Numerical analysis and experimental correlation of composite shell buckling and post-buckling', *Composites: Part B*, vol. 31, pp. 655-667.

Bogetti, TA, Hoppel, CPR, Harik, VM, Newill, JF & Burns, BP 2004, 'Predicting the nonlinear response and progressive failure of composite laminates', *Composites Science and Technology*, vol. 64, pp. 329-342.

Borg, R, Nilsson, L & Simonsson, K 2001, 'Simulation of delamination in fiber composites with a discrete cohesive failure model', *Composites Science and Technology*, vol. 61, pp. 667-677.

Borg, R, Nilsson, L & Simonsson, K 2002, 'Modeling of delamination using a discretized cohesive zone and damage formulation', *Composites Science and Technology*, vol. 62, pp. 1299-1314.

Borg, R, Nilsson, L & Simonsson, K 2004a, 'Simulating DCB, ENF and MMB experiments using shell elements in a cohesive model', *Composites Science and Technology*, vol. 64, pp. 269-278.

Brunner, J 2000, 'Experimental aspects of Mode I and Mode II fracture toughness testing of fibre-reinforced polymer-matrix composites', *Computational Methods in Applied Mechanical Engineering*, vol. 185, pp. 161-172.

Bruno, D & Greco, F 2001, 'Mixed mode delamination in plates: a refined approach', *International Journal of Solids and Structures*, vol. 38, pp. 9149-9177.

Büsing, S & Reimerdes, H-G 2006, *Investigation of degradation by tests and development of degradation models*, COCOMAT Technical Report, RWTH Aachen University.

Camanho, PP & Dávila, CG 2002, *Mixed-mode decohesion finite elements for the simulation of delamination in composite materials*, NASA/TM-2002-211737, NASA Langley Research Center, Virginia, USA.

Caputo, F, Esposito, R, Perugini, P & Santoro, D 2002, 'Numerical-experimental investigation on post-buckled stiffened composite panels', *Composite Structures*, vol. 55, pp. 347-357.

Car, E, Zalamea, F, Oller, S, Miquel, J & Oñate, E 2002, 'Numerical simulation of fiber reinforced composite materials — two procedures', *International Journal of Solids and Structures*, vol. 39, pp. 1967-1986.

Cauvin, A & Testa, RB 1999, 'Damage mechanics: basic variables in continuum theories', *International Journal of Solids and Structures*, vol. 36, pp. 747-761.

Chang, F-K & Chang, K-Y 1987, 'A progressive damage model for laminated composites containing stress concentrations', *Journal of Composite Materials*, vol. 21, pp. 834-855.

Chang, F-K & Kutlu, Z 1990, 'Delamination effects on composite shells', *Journal of Engineering Materials*, vol. 112, pp. 336-340.

Chang, F-K & Lessard, LB 1991, 'Damage tolerance of laminated composites containing an open hole and subject to compressive loadings: part I – analysis', *Journal of Composite Materials*, vol. 25, pp. 2-43.

COCOMAT Home Page 2007, www.cocomat.de.

Crisfield, MA 1991, *Nonlinear finite element analysis of solids and structures, Volume 1: Essentials*, John Wiley & Sons, New York.

Cui, W & Wisnom, MR 1993, 'A combined stress-based and fracture mechanics-based model for predicting delamination in composites', *Composites*, vol. 24, pp. 467-474.

Cuntze, RG & Freund, A 2004, 'The predictive capability of failure mode concept-based strength criteria for multidirectional laminates', *Composites Science and Technology*, vol. 64, pp. 344-377.

D'Ottavio, M & König, M 2006, 'Numerical models for delamination', in Busse, G, Kröplin, B-H & Wittel, FK (eds) *Damage and its evolution in fiber-composite materials: Simulation and non-destructive testing*, Stuttgart University: ISD Verlag, pp. 381-424.

Davidson, BD 1990, 'An analytical investigation of delamination front curvature in double cantilever beam specimens', *Journal of Composite Materials*, vol. 24, pp. 1124-1137.

Davidson, BD 1996, 'Effect of stacking sequence on energy release rate distributions in multidirectional DCB and ENF specimens', *Engineering Fracture Mechanics*, vol. 55, no. 4, pp. 557-569.

Davidson, BD 1998, *A predictive methodology for delamination growth in laminated composites − Part I: Theoretical development and preliminary experimental results*, DOT/FAA/AR-97/87, Office of Aviation Research, Federal Aviation Administration, US Department of Transportation.

Davidson, BD, Hu, H & Hongwei, Y 1996, 'An efficient procedure for determining mixed-mode energy release rates in practical problems of delamination', *Finite Elements in Analysis and Design*, vol. 23. pp. 193-210.

Dávila, CG & Camanho, PP 2003, *Failure criteria for FRP laminates in plane stress*, NASA/TM-2003-212663, NASA Langley Research Center, Virginia, USA.

de Moura, MFSF, Gonçalves, JPM, Marques, AT & de Castro, PMST 2000, 'Prediction of compressive strength of carbon-epoxy laminates containing delamination by using a mixed-mode damage model', *Composite Structures*, vol. 50, pp. 151-157.

Degenhardt, R, Kling, A, Klein, H, Hillger, W, Goetting, HC, Zimmermann, R, Rohwer, K & Gleiter, A 2007, 'Experiments on buckling and postbuckling of thin-walled CFRP structures using advanced measurement systems', *International Journal of Structural Stability and Dynamics*, vol. 7, no. 2, pp. 337-358.

Degenhardt, R, Rolfes, R, Zimmermann, R & Rohwer, K 2006, 'COCOMAT – Improved MATerial Exploitation at Safe Design of COmposite Airframe Structures by Accurate Simulation of COllapse', *Composite Structures*, vol. 73, pp. 175-178.

Determination of Interlaminar Fracture Toughness Energy - Mode I - G_{IC} 1996, European Normative Standard DIN EN 6033, Deutsches Institut für Normung, e. V.

Determination of Interlaminar Fracture Toughness Energy - Mode II - G_{IIC} 1996, European Normative Standard DIN EN 6034, Deutsches Institut für Normung, e. V.

Eason, TG & Ochoa, OO 1996, 'Modelling progressive damage in composites: a shear deformable element for ABAQUS', *Composite Structures*, vol. 34, pp. 119-128.

Engelstad, SP, Reddy JN & Knight Jr, NF 1992, 'Postbuckling response and failure prediction of graphite-epoxy plates loaded in compression', *AIAA Journal*, vol. 30, no. 8, pp. 2106-2113.

Falzon, BG & Hitchings, D 2003, 'Capturing mode-switching in postbuckling composite panels using a modified explicit procedure', *Composite Structures*, vol. 60, pp. 447-453.

Falzon, BG, Stevens, KA & Davies, GAO 2000, 'Postbuckling behaviour of a blade-stiffened composite panel loaded in uniaxial compression', *Composites: Part A*, vol. 31, pp. 459-468.

Feih, S & Shercliff, HR 2005, 'Adhesive and composite failure prediction of single-L joint structures under tensile loading', *International Journal of Adhesion and Adhesives*, vol. 25, no. 1, pp. 47-59.

Feih, S 2002, 'Design of composite adhesive joints', PhD thesis, Cambridge University.

Frostig, Y, Siton, G, Segal, A, Sheinman, I & Weller, T 1991, 'Postbuckling behavior of laminated composite stiffeners and stiffened panels under cyclic loading', *Journal of Aircraft*, vol. 28, no. 7, pp. 471-480.

Gamble, K, Pilling, M & Wilson, A 1995, 'An automated finite element analysis of the initiation and growth of damage in carbon fibre composite materials', *Composite Structures*, vol. 32, pp. 265-274.

Gaudenzi, P, Perugini, P & Riccio, A 2001, 'Post-buckling behavior of composite panels in the presence of unstable delaminations', *Composite Structures*, vol. 51, pp. 301-309.

Goldmanis, M & Riekstinsh, A 1994, 'Post-buckling finite element analysis of composite cylindrical panels in axial compression', *Composite Structures*, vol. 29, pp. 457-462.

Gosse, JH & Christensen, S 2001, *Strain invariant failure criteria for polymers in composite materials*, AIAA paper, AIAA-2001-1184.

Goyal, VK, Jaunky, NR, Johnson, ER & Ambur, DR 2004, 'Intralaminar and interlaminar progressive failure analyses of composite panels with circular cutouts', *Composite Structures*, vol. 64, pp. 91-105.

Greenhalgh, ES, Meeks, C, Clarke, A & Thatcher, J 2003, 'The effect of defects on the performance of post-buckled CFRP stringer-stiffened panels', *Composites: Part A*, vol. 34, pp. 623-633.

Gu, H & Chattopadhyay, A 1999, 'An experimental investigation of delamination buckling and postbuckling of composite laminates', *Composites Science and Technology*, vol. 59, pp. 903-910.

Gummadi, LNB & Palazotto, AN 1998, 'Progressive failure analysis of composite cylindrical shells considering large rotation', *Composites: Part B*, vol. 29, pp. 547-563.

Hachenberg, D & Kossira, H 1993, 'Stringer peeling effects at stiffened composite panels in the postbuckling range', *Journal of Aircraft*, vol. 30, no. 5, pp. 769-776.

Hansen, P & Martin, R 1999, *DCB, 4ENF and MMB Delamination Characterisation of S2/8552 and IM7/8552,* Materials Engineering Research Laboratory Ltd (MERL), Hertford, UK, N68171-98-M-5177.

Hart-Smith, LJ 1998, 'Predictions of the original and truncated maximum-strain failure models for certain fibrous composite laminates', *Composites Science and Technology*, vol. 58, pp. 1151-1178.

Hashin, Z 1980, 'Failure criteria for unidirectional composites', *Journal of Applied Mechanics*, vol. 47, pp. 329-334.

Herszberg, I, Kotler, A, Orifici, AC, Abramovich, H & Weller, T 2007, 'Failure modes in loaded carbon/epoxy composite T-sections', in *12th Australian International Aerospace Congress*, Melbourne, Australia, 19-22 March.

Hilburger, MW & Starnes Jr, JH 2004, 'Effects of imperfections of the buckling response of composite shells', *Thin-Walled Structures*, vol. 42, pp. 369-397.

Hwang, WC & Sun, CT 1989, 'Failure analysis of laminated composites by using iterative three-dimensional finite element method', *Computers and Structures*, vol. 33, no. 1, pp. 41-47.

Hyer, MW, Loup, DC & Starnes Jr, JH 1990, 'Stiffener/skin interactions in pressure-loaded composite panels', *AIAA Journal*, vol. 28, no. 3, pp. 532-537.

Ireman, T, Thesken, JC, Greenhalgh, E, Sharp, R, Gädke, M, Maison, S, Ousset, Y, Roudolff, F & La Barbera, A 1996, 'Damage propagation in composite structural elements-coupon experiments and analysis', *Composite Structures*, vol. 36, pp. 209-220.

Irwin, GR 1958, 'Fracture I', in: *Handbook der Physik*, Flügge, ed., pp. 558-590.

Jansson, E & Larsson, R 2001, 'A damage model for simulation of mixed-mode delamination growth', *Composite Structures*, vol. 53, pp. 409-417.

Jensen, HM & Sheinman, I 2002, 'Numerical analysis of buckling-driven delamination', *International Journal of Solids and Structures*, vol. 39, pp. 3373-3386.

Johnson, WS, Butkus, LM & Valentin, RV 1998, *Applications of Fracture Mechanics to the Durability of Bonded Composite Joints*, U.S. Department of Transportation, Federal Aviation Administration DOT/FAA/AR-97/56.

Kachanov, LM 1958, 'Time of the rupture process under creep conditions', Isv. Nauk SSSR, Otd. Tehk. Nauk, vol. 8, pp. 26-31.

Kaddour, AS, Hinton, MJ & Soden, PD 2004, 'A comparison of the predictive capabilities of current failure theories for composite laminates: additional contributions', *Composites Science and Technology*, vol. 64, pp. 449-476.

Kim, HJ 1997, 'Postbuckling analysis of composite laminates with a delamination', *Computers & Structures*, vol. 62, no. 6, pp. 975-998.

Kling, A & Degenhardt, R 2006, *Characterization of material properties - Results of the EU project COCOMAT*, DLR Internal Report, IB 131-2006/18, April.

Knight Jr, NF & Starnes Jr, JH 1988, 'Postbuckling behaviour of selected curved stiffened graphite-epoxy panels loaded in axial compression', *AIAA Journal*, vol. 26, no. 3, pp. 344-352.

Knight Jr, NF, Rankin, CC & Brogan, FA 2002, 'STAGS computational procedure for progressive failure analysis of laminated composite structures', *International Journal of Nonlinear Mechanics*, vol. 37, pp. 833-849.

Krueger, R 2002, *The Virtual Crack Closure Technique: History, Approach and Applications*, NASA/CR-2002-211628, ICASE Virginia, USA.

Krueger, R, König, M & Schneider, T 1993, 'Computation of local energy release rates along straight and curved delamination fronts of unidirectionally laminated DCB- and ENF-specimens', in: *Proceedings of the 34th AIAA/ASME/ASCE/AHS/ASC SSDM Conference,* La Jolla, CA, AIAA Washington, pp. 1332-1342.

Krueger, R, Paris, IL, O'Brien, TK & Minguet, PJ 2002, 'Comparison of 2D finite element modeling assumptions with results from 3D analysis for composite skin-stiffener debonding', *Composite Structures*, vol. 57, pp. 161-168.

Lanzi, L & Giavotto, V 2006, 'Post-buckling optimization of composite stiffened panels: Computations and experiments', *Composite Structures*, vol. 73, pp. 208-220.

Lee, SM 1993, 'An edge crack torsion method for mode III delamination fracture testing', *ASTM Journal of Technology and Research*, vol. 15, no. 3, pp. 193-201.

Li, J, Lee, SM, Lee, EW & O'Brien, TK 1997, 'Evaluation of the edge crack torsion ECT Test for mode III interlaminar fracture toughness of laminated composites', *Journal of Composites Technology and Research*, vol. 19, pp. 174-183.

Li, J, O'Brien, TK & Rousseau, CQ 1997, 'Test and analysis of composite hat stringer pull-off test specimens', *Journal of the American Helicopter Society*, pp. 350-357.

Liu, K-S, & Tsai, SW 1998, 'A progressive quadratic failure criterion', *Composites Science and Technology*, vol. 58, pp. 1023-1032.

Lonetti, P & Zinno, R 2003, 'Simulation of multiple delaminations in composite laminates under mixed-mode deformations', *Simulation Modelling Practice and Theory*, vol. 11, pp. 483-500.

Luciano, R and Zinno, R 2000, 'A micromechanical approach for the analysis of damage in laminated composite structures', *Computers and Structures*, vol. 74, pp. 201-214.

Masters, JE & Reifsnider, KL 1982, 'An investigation of cumulative damage in quasi-isotropic graphite/epoxy laminates', in Reifsnider, KL, ed., *Damage in Composite Materials*, ASTM STP 775, American Society for Testing and Materials, pp. 40-62.

Matthews, FL, Davies, GAO, Hitchings, D & Soutis, C 2000, *Finite Element Modelling of Composite Materials and Structures*, Woodhead, Cambridge, UK.

Meeks, C, Greenhalgh, E & Falzon, BG 2005, 'Stiffener debonding mechanisms in post-buckled CFRP aerospace panels', *Composite Structures*, vol. 36, pp. 934-946.

Meyer-Piening, H-R & Anderegg, R 1995, 'Buckling and postbuckling investigations of imperfect curved stringer-stiffened composite shells. Part A: Experimental investigation and effective width evaluation', *Thin-Walled Structures*, vol. 23, pp. 323-338.

Mi, Y, Crisfield, MA, Davies, GAO & Hellweg, HB 1998, 'Progressive delamination using interface elements', *Journal of Composite Materials*, vol. 32, no. 14, pp. 1246-1272.

MSC.Marc and MSC.Mentat User Manuals Version 2005r3 2006, MSC.Software Corporation, Santa Ana, California.

Nilsson, KF, Asp, LE, Alpman, JE & Nystedt, L 2001, 'Delamination buckling and growth for delaminations at different depths in a slender composite panel', *International Journal of Solids and Structures*, vol. 38, no. 17, pp. 3039-3071.

O'Brien, TK 1982, 'Characterization of delamination onset and growth in a composite laminate', in Reifsnider, KL, ed., *Damage in composite materials*, ASTM STP 775, ASTM pp. 140-167.

O'Brien, TK 1985, 'Analysis of local delaminations and their influence on composite laminate behaviour', in Johnson, WS, ed., *Delamination and debonding of materials*, ASTM STP 876, American Society for Testing and Materials, pp. 282-297.

O'Brien, TK 1998, 'Interlaminar fracture toughness: The long and winding road to standardization', *Composites: Part B*, vol. 29, pp. 57-62.

Ochoa, OO & Reddy, JN 1992, *Finite Element Analysis of Composite Laminates*, Kluwer Academic Publishers, Dordrecht, The Netherlands.

Orifici, AC, Thomson, RS, Degenhardt, R, Kling, A, Rohwer, K, & Bayandor, J 2007, 'Degradation investigation in a postbuckling composite stiffened panel', *Composite Structures*, doi: 10.1016/j.compstruct.2007.01.012.

Orifici, AC, Thomson, RS, Gunnion, AJ, Degenhardt, R, Abramovich, H & Bayandor, J 2005, 'Benchmark finite element simulations of postbuckling composite stiffened panels', in *11th Australian International Aerospace Congress*, Melbourne, Australia, 13-17 March.

Park, O & Sanker, BV 2002, 'Crack-tip force method for computing energy release rate in delaminated plates', *Composite Structures*, vol. 55, pp. 429-434.

Pavier, MJ & Clarke, MP 1996, 'A specialized composite plate element for problems of delamination buckling and growth', *Composite Structures*, vol. 34, pp. 43-53.

Pendleton, RL & Tuttle, ME, eds, 1989, *Manual on Experimental Methods for Mechanical Testing of Composites*, Elsevier Applied Science Publishers, London, UK.

Petrossian, Z & Wisnom, MR 1998, 'Prediction of delamination initiation and growth from discontinuous plies using interface elements', *Composites: Part A*, vol. 29A, pp. 503-515.

Pinho, ST, Dávila, CG, Camanho, PP, Iannucci, L & Robinson, P 2005, *Failure models and criteria for FRP under in-plane or three-dimensional stress states including shear non-linearity*, NASA/TM-2005-213530, NASA Langley Research Center, Virginia, USA.

POSICOSS Home Page 2007, www.posicoss.de.

Puck, A & Schürmann, H 1998, 'Failure analysis of FRP laminates by means of physically based phenomenological models', *Composites Science and Technology*, vol. 58, pp. 1045-1067.

Qin, M & Dzenis, Y 2001, 'Nonlinear numerical and experimental analysis of single lap adhesive composite joints with delaminated adherends', in: *Proceedings of the Thirteenth International Conference on Composite Materials (ICCM13)*, Zhang, Y, ed., Beijing.

Qiu, Y, Crisfield, MA & Alfano, G 2001, 'An interface element formulation for the simulation of delamination with buckling', *Engineering Fracture Mechanics*, vol. 68, pp. 1755-1776.

Reddy, JN 1990, 'A review of refined theories of laminated plates', *Shock and Vibration Digest*, vol. 22, no. 7, pp. 3-17.

Reedy Jr, ED, Mello FJ & Guess, TR 1997, 'Modelling the initiation and growth of delaminations in composite structures', *Journal of Composite Materials*, vol. 31, no. 8, pp. 812-831.

Rotem, A 1998, 'Prediction of laminate failure with the Rotem criterion', *Composites Science and Technology*, vol. 58, pp. 1083-1094.

Rybicki, EF & Kanninen, MF 1977, 'A finite element calculation of stress intensity factors by a modified crack closure integral', *Engineering Fracture Mechanics*, vol. 9, pp. 931-938.

Schellekens, JCJ & de Borst, R 1993, 'A nonlinear finite element approach for the analysis of Mode-I free edge delamination in composites', *International Journal of Solids and Structures*, vol. 30, pp. 1239-1253.

Schön, J, Nyman, T, Blom, A and Ansell, H 2000a, 'A numerical and experimental investigation of delamination behaviour in the DCB specimen', *Composites Science and Technology*, vol. 60, pp. 173-184.

Schön, J, Nyman, T, Blom, A and Ansell, H 2000b, 'Numerical and experimental investigation of a composite ENF-specimen', *Engineering Fracture Mechanics*, vol. 65, pp. 405-433.

Sheinman, I & Frostig, Y 1988, 'Post-buckling analysis of stiffened laminated panels', *Journal of Applied Mechanics*, vol. 55, no. 3, pp. 635-640.

Sheinman, I, Kardomateas, GA & Pelegri, AA 1998, 'Delamination growth during pre- and post-buckling phases of delaminated composite laminates', *International Journal of Solids and Structures*, vol. 35, no. 1-2, pp. 19-31.

Short, GJ, Guild, FJ & Pavier, MJ 2002, 'Delaminations in flat and curved composite laminates subjected to compressive load', *Composite Structures*, vol. 58, pp. 249-258.

Singh, SB & Kumar, A 1999, 'Postbuckling response and strength of laminates under combined in-plane loads', *Composites Science and Technology*, vol. 59, pp. 727-736.

Skrna-Jakl, IC & Rammerstorfer, FG 1993, 'Numerical investigations of free edge effects in integrally stiffened layered composite panels', *Composite Structures*, vol. 25, no. 1-4, pp. 129-137.

Spagnoli, A, Elghazouli, AY & Chryssanthopoulos, MK 2001, 'Numerical simulation of glass-reinforced plastic cylinders under axial compression', *Marine Structures*, vol. 14, pp. 353-374.

Standard Test Method for Mixed Mode I-Mode II Interlaminar Fracture Toughness of Unidirectional Fiber Reinforced Polymer Matrix Composites 2001, ASTM D6671–01, American Society for Testing and Materials.

Starnes, JH, Knight, NF & Rouse, M 1985, 'Postbuckling behaviour of selected flat stiffened graphite-epoxy panels loaded in compression', *AIAA Journal*, vol. 23, no. 8, pp. 1236-1246.

Stevens, KA, Ricci, R & Davies, GAO 1995, 'Buckling and postbuckling of composite structures', *Composites*, vol. 26, pp. 189-199.

Stiftinger, MA, Skrna-Jakl, IC & Rammerstorfer, FG 1995, 'Buckling and postbuckling investigations of imperfect curved stringer-stiffened composite shells. Part B: Computational investigations', *Thin-Walled Structures*, vol. 23, pp. 339-350.

Tafreshi, A 2004, 'Efficient modelling of delamination buckling in composite cylindrical shells under axial compression', *Composite Structures*, vol. 64, pp. 511-520.

Thomson, RS & Scott, ML 2000, 'Modelling delaminations in postbuckling composite shear panels', *Computational Mechanics*, vol. 26, pp. 75-89.

Thomson, RS 2001, 'The durability of postbuckling composite stiffened shear panels', PhD thesis, Royal Melbourne Institute of Technology.

Tong, L 1997, 'An assessment of failure criteria to predict the strength of adhesively bonded composite double lap joints', *Journal of Reinforced Plastics and Composites*, vol. 16, no. 8, pp. 698-713.

Tsai, SW & Wu, EM 1971, 'A general theory of strength for anisotropic material', *Journal of Composite Materials*, vol. 5, pp. 58-80.

Tsouvalis, NG, Zafeiratou, AA, Papazoglou, VJ, Gabrielides, NC & Kaklis 2001, 'Numerical modelling of composite laminated cylinders in compression using a novel imperfection modeling method', *Composites: Part B*, vol. 32, pp. 387-399.

Vautrin, A & Sol, H, eds, 1991, *Mechanical Identification of Composites*, Elsevier Applied Science Publishers, London, UK.

VCCT for ABAQUS User's Manual, Version 1.1 2005, ABAQUS, Inc., Rhode Island, USA.

Wahab, MMA 2000, 'On the use of fracture mechanics in designing a single lap adhesive joint', *Journal of Adhesive Science and Technology*, vol. 19, pp. 851-865.

Wang, ASD 1984, 'Fracture mechanisms of sublaminate cracks in composite materials', *Composites Technology Review*, vol. 6, no. 2, pp. 45-62.

Wang, JT & Qiao, P 2004, 'On the energy release rate and mode mix of delaminated shear deformable composite plates', *International Journal of Solids and Structures*, vol. 41, pp. 2757-2779.

Wang, JT & Raju, IS 1996, 'Strain energy release rate formulae for skin-stiffener debond modeled with plate elements', *Engineering Fracture Mechanics*, vol. 54, pp. 211-228.

Whitcomb, JD 1989, 'Three-dimensional analysis of a postbuckled embedded delamination', *Journal of Composite Materials*, vol. 23, pp. 862-889.

Whitcomb, JD 1992, 'Analysis of a laminate with a post-buckled embedded delamination, including contact effects', *Journal of Composite Materials*, vol. 26, pp. 1523-1535.

Wiggenraad, JFM, Aoki, R, Gädke, M, Greenhalgh, E, Hachenberg, D, Wolf, K & Bübl, R 1996, 'Damage propagation in composite structural elements - analysis and experiments on structures', *Composite Structures*, vol. 36, pp. 173-186.

Williams, JG 1988, 'On the calculation of energy release rates for cracked laminates', *International Journal of Fracture*, vol. 36, pp. 101-119.

Wisheart, M & Richardson, MOW 1998, 'The finite element analysis of impact induced delamination in composite materials using a novel interface element', *Composites: Part A*, vol. 29A, pp. 301-313.

Wisnom, MR, Hill, GFJ & Jones, MI 2001, 'Through thickness failure prediction of composite structural elements', in *13th International Conference on Composite Materials*, Beijing, China, paper no. 1623.

Xie, D & Biggers Jr, SB 2003, 'Postbuckling analysis with progressive damage modeling in tailored laminated plates and shells with a cutout', *Composite Structures*, vol. 59, pp. 199-216.

Yang, W & Boehler, JP 1992, 'Micromechanics modelling of anisotropic damage in cross-ply laminates', *International Journal of Solids and Structures*, vol. 29, pp. 1303-1328.

Yap, JWH, Scott, ML, Thomson, RS & Hachenberg, D 2002, 'The analysis of skin-to-stiffener debonding in composite aerospace structures', *Composite Structures*, vol. 57, pp. 425-435.

Yap, JWH, Thomson, RS, Scott, ML & Hachenberg, D 2004, 'Influence of post-buckling behaviour of composite stiffened panels on the damage criticality', *Composite Structures*, vol. 66, pp. 197-206.

Zhao, D & Wang, Y 1998, 'Mode III fracture behavior of laminated composite with edge crack in torsion', *Theoretical and Applied Fracture Mechanics*, vol. 29, pp. 109-123.

Zimmermann, R, Klein, H & Kling, A 2006, 'Buckling and postbuckling of stringer stiffened fibre composite curved panels − tests and computations', *Composite Structures*, vol. 73, pp. 150-161.

Zou, Z, Reid, SR & Li, S 2003, 'A continuum damage model for delaminations in laminated composites', *Journal of the Mechanics and Physics of Solids*, vol. 51, pp. 333-356.

Zou, Z, Reid, SR, Li, S & Soden, PD 2002, 'Application of a delamination model to laminated composite structures', *Composite Structures*, vol. 56, pp. 375-389.

Appendix A – Modification Factor Investigation

In this Appendix, the parametric studies used in support of the interlaminar damage propagation model are described.

Numerical studies were used to determine the modification factors, f_m, for propagation method 4, and involved a series of two-step crack growth analyses. The two-step approach was used to investigate the difference between crack opening displacements assumed in a one-step VCCT calculation, and the actual displacements generated upon crack growth. There were a number of different specimen configurations investigated, corresponding to analysis of crack growth in mode I, II and III and mixed-mode behaviour. As explained in Chapter 4, the models consisted of two layers of shells joined with MPCs, so that crack growth consisted of the release of an MPC, and the local crack front was defined as a central MPC with up to two adjacent MPCs. For each specimen configuration, crack growth in the range of different crack types and growth types were investigated, where each crack type was a different configuration of the local crack front, and each growth type corresponded to the number of MPCs that were released in crack growth.

The models used for mode I, II and III investigations were taken from those presented previously in Chapter 4, with the only difference being the use of a unidirectional instead of the quasi-isotropic lay-up.

Double Cantilever Beam: Mode I

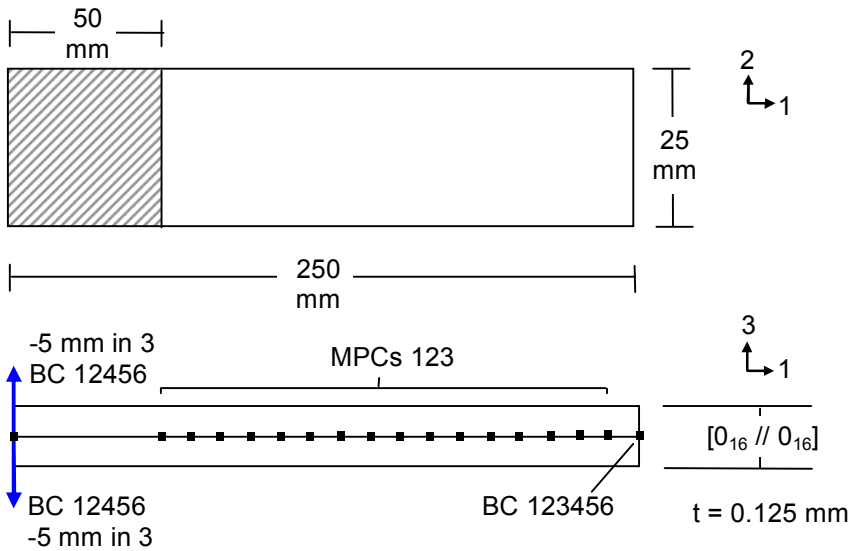

Crack type	Growth type	Growth pattern	Displacement	f_m
# 01	**# 1**	1a all else held	0.0663991	
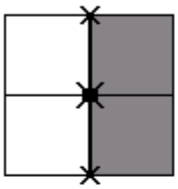	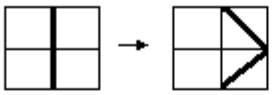	1b only above held	0.0512748	
		1c edges released	0.0651087	2.5
		1d close edge released	0.0597645	
		1e further edge released	0.0716299	
		1f further side released	0.0573296	
1 intact 1 debond	**# 2**	2a all above held	0.1154430	
	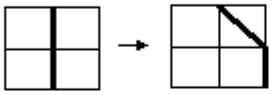	2b all else retained	0.1214790	1.5
		2c only above held	0.1042130	
Assumed displacement	**# 3**	3a full width	0.1656900	
0.1964995	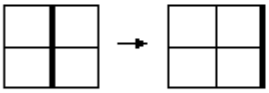	3b all else retained	0.1747970	
		3c only edges retained	0.1714380	1.0
		3d further edge held	0.1660600	
		3e closer edge held	0.1710000	

Crack type	Growth type	Growth pattern	Displacement	f_m
# 02	**# 1**	1a only above released	0.1200140	
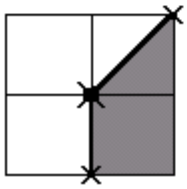	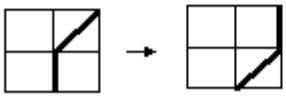	1b held below, diag above	0.1177840	2.0
		1c straight, above released	0.1236140	
1 intact 2 debond	**# 2**	2a held below, diag above	0.1832690	
	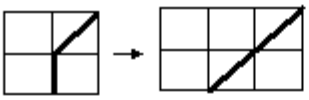	2b only above released	0.1974500	1.0
		2c from straight, all held	0.1825780	
Assumed displacement	**# 3**	3a grow entire crack front	0.2080970	
0.2874099	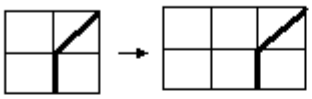	3b only above released	0.1974500	1.0
		3c close edge held	0.2134730	
		3d both edges held	0.2164510	

Crack type	Growth type	Growth pattern	Displacement	f_m
# 03	**# 1**	1a only above grown	0.1656900	
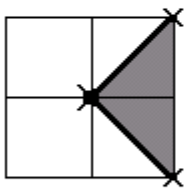	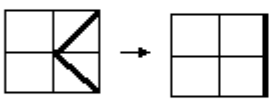	1b all else grown	0.1607050	
		1c all above grown	0.1626680	1.5
		1d concave, only above	0.1747970	
		1e concave, all else grown	0.1656900	
1 intact 3 debond	**# 2**	2a all above grown	0.2080970	
	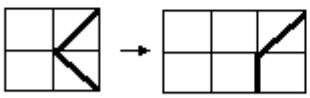	2b only above grown	0.1920140	1.33
		2c concave, only above	0.1825780	
		2d concave, all above grown	0.1920140	
Assumed displacement	**# 3**	3a all grown	0.2365610	
0.2775010	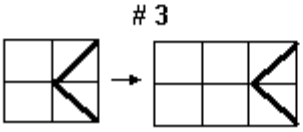	3b only above grown	0.2147460	1.0
		3c concave, only above	0.1978420	
		3d concave, all grown	0.2147160	

Crack type	Growth type	Growth pattern		Displacement	f_m
# 04 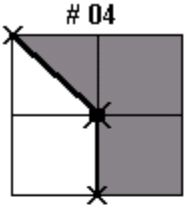 2 intact 1 debond **Assumed displacement** 0.1386980	**# 1** 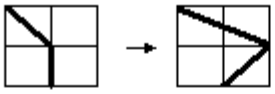	1a	only above grown	0.0186341	6.0
		1b	all above grown	0.0082781	
		1c	all grown	0.0012482	
	# 2a 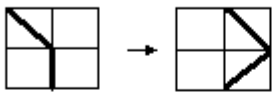	2a	only above grown	0.0707602	2.0+
		2b	all above grown	0.0663991	
		2c	all others grown	0.0597645	
	# 2b 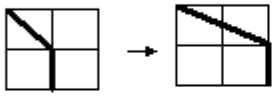	2d	only above grown	0.0581137	3.0+
		2e	all below released	0.0529623	
		2f	all grown	0.0415665	
	# 3 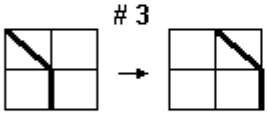	3a	all grown	0.1154430	1.0
		3b	only above grown	0.1269930	

+Choice between values made based on which crack front node is released

Crack type	Growth type	Growth pattern		Displacement	f_m
# 05 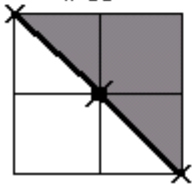 2 intact 2 debond **Assumed displacement** 0.3847969	**# 1** 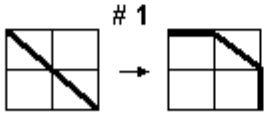	1a	only above grown	0.0592397	6.0
		1b	all others grown	0.0500034	
		1c	only close edge grown	0.0580757	
		1d	straight, only above grown	0.0529623	
		1e	straight, all others grown	0.0396853	
	# 2a 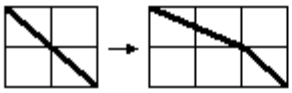	2a	only above grown	0.0970247	2.0* 1.0
		2b	all others grown	0.0943635	
		2c	straight, only above grown	0.0779517	
		2d	straight, all others grown	0.0714769	
	# 2b 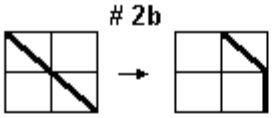	2e	only above grown	0.0994652	2.0* 1.0
		2f	all above grown	0.1219350	
		2g	straight, only above grown	0.1201680	
		2h	straight, all others grown	0.1133890	
	# 3 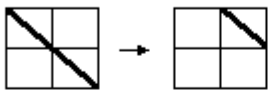	3a	all grown	0.1862580	1.0
		3b	only above grown	0.1487290	
		3c	straight, all grown	0.1627690	
		3d	straight, only above grown	0.1608100	

*Choice between values made based on whether crack growth occurs at other MPCs in model

Crack type	Growth type	Growth pattern		Displacement	f_m
# 06 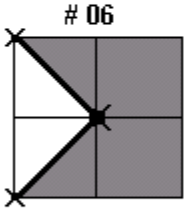 3 intact 1 debond **Assumed displacement** 0.0807145	**# 1** 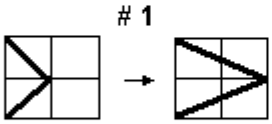	1a	only above grown	0.0219292	2.0
		1b	all others grown	0.0381126	
	# 2 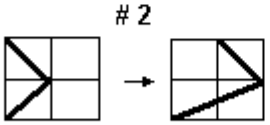	2a	only above grown	0.0260271	3.0
		2b	all others grown	0.0143159	
		2c	reversed, only above grow	0.0238195	
		2d	reversed, close edge grown	0.0186341	
	# 3 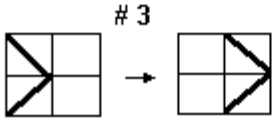	3a	only above grown	0.0774717	1.0
		3b	all grown	0.0663991	

Crack type	Growth type	Growth pattern	Displacement	f_m
# 07 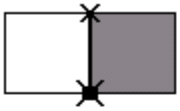 1 intact 1 debond edge **Assumed displacement** 0.0807145	**# 1** 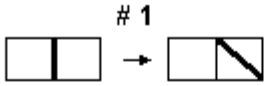	1a only above grown 1b other edge grown 1c all others grown	0.1375020 0.1389440 0.1101660	1.33
	# 2 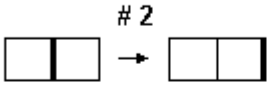	2a only above grown 2b other edge grown 2c 2 from far edge grown 2d all grown	0.1808360 0.1807210 0.1713710 0.1600010	1.0

Crack type	Growth type	Growth pattern	Displacement	f_m
# 08 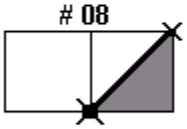 1 intact 2 debond edge **Assumed displacement** 0.3216010	**# 1** 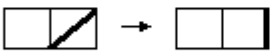	1a only above grown 1b 2 on other edge grown 1c all others grown 1d convex, only above grown 1e convex, other edge grown 1f convex, all others grown	0.1808360 0.1713710 0.1600010 0.1616520 0.1600010 0.1420580	1.33
	# 2 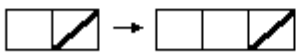	2a only above grown 2b all others grown 2c convex, only above 2d convex, all other grown	0.1981890 0.2145200 0.2173590 0.2334570	1.0

Crack type	Growth type	Growth pattern	Displacement	f_m
# 09 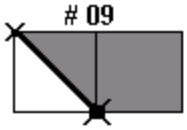 2 intact 1 debond edge **Assumed displacement** 0.1717550	**# 1** 	1a only above grown 1b other edge grown 1c 2 on other edge grown 1d all others grown	0.0314451 0.0326681 0.0248455 0.0092195	5.0
	# 2 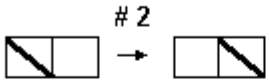	2a only above grown 2b other edge grown similar 2c all others grown	0.1549330 0.1515600 0.1389440	1.0

Crack type	Growth type	Growth pattern	Displacement	f_m
# 10 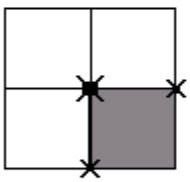 0 intact 2 debond **Assumed displacement** 0.5358360	**# 1** 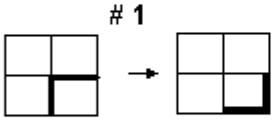	1a only above grown 1b all others grown	0.1665970 0.1802930	2.0
	# 2 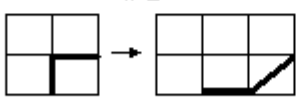	2a only above grown 2b all others grown 2c reversed, only above 2d reversed, all lower grown	0.2258340 0.2690820 0.2134730 0.2080970	2.0
	# 3 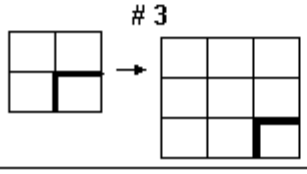	3a only above grown 3b all other grown	0.3625890 0.4747860	1.0

Crack type	Growth type	Growth pattern		Displacement	f_m
# 11 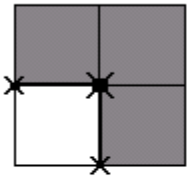 2 intact 0 debond **Assumed displacement** 0.1423060	# 1 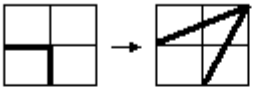	1a	only above grown	-0.0484992	3.0
		1b	all others grown	-0.0533056	
	# 2 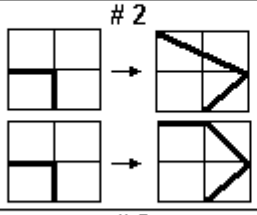	2a	only above grown	0.0186341	3.0
		2b	all others grown	0.0012482	
		2c	reversed, only above grow	-0.0483633	
	# 3 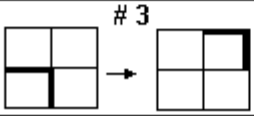	3a	only above grown	0.0581137	1.0
		3b	all others grown (2d)	0.1154430	

End-Notched Flexure: Mode II

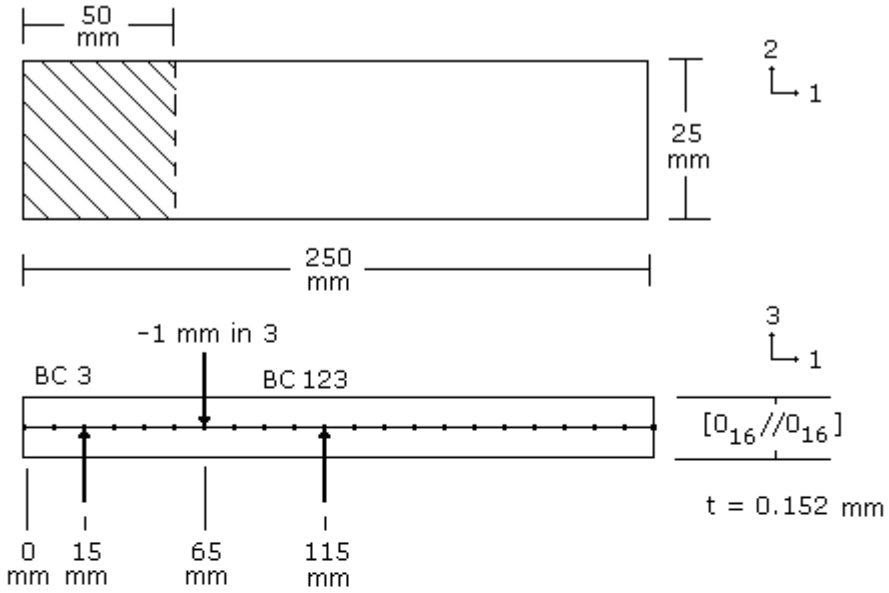

Crack type	Growth type	Growth pattern		Displacement	f_m
# 01 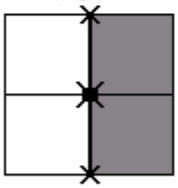 1 intact 1 debond **Assumed displacement** 0.0239499	# 1 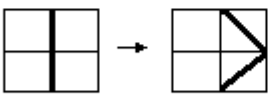	1a	all else held	0.0251719	1.0
		1b	only above held	0.0277478	
		1c	edges released	0.0264524	
		1d	close edge released	0.0264191	
		1e	further edge released	0.0252415	
		1f	further side released	0.0265585	
	# 2 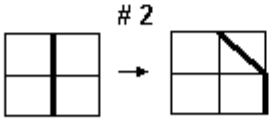	2a	all above held	0.0246570	1.0
		2b	all else retained	0.0234323	
		2c	only above held	0.0260125	
		2d	reversed, all above	0.0246878	
	# 3 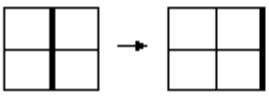	3a	full width	0.0239435	1.0
		3b	all else retained	0.0217449	
		3c	only edges retained	0.0228921	
		3d	further edge held	0.0226433	
		3e	closer edge held	0.0227724	

Crack type	Growth type	Growth pattern	Displacement	f_m
# 02 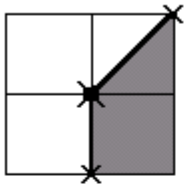 1 intact 2 debond	# 1 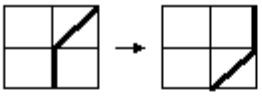	1a only above grown	0.0246838	
		1b held below, grown above	0.0253919	2.0
		1c held above, grown below	0.0258841	
	# 2a 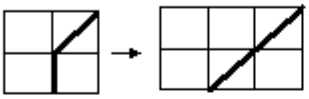	2a only above grown	0.0276192	
		2b held below, grown above	0.0282123	1.0
		2c held above, grown below	0.0288539	
	# 2b 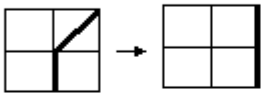	2d only above grown	0.0227724	
		2e all except far edge	0.0245239	1.0
		2f all released	0.0245950	
Assumed displacement 0.0289825	# 3 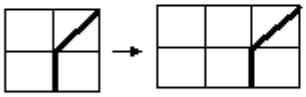	3a only above released	0.0236451	
		3b close edge held	0.0263549	1.0
		3c both edges held	0.0260912	
		3d grow entire crack front	0.0274457	

Crack type	Growth type	Growth pattern	Displacement	f_m
# 03 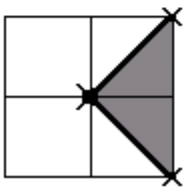 1 intact 3 debond	# 1 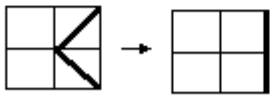	1a only above grown	0.0239435	
		1b all else grown	0.0250745	
		1c all above grown	0.0245950	1.33
		1d concave, only above	0.0214095	
		1e concave, all else grown	0.0239435	
	# 2 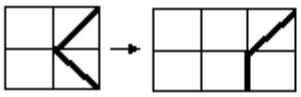	2a all above grown	0.0274497	
		2b only above grown	0.0269446	1.0
		2c concave, only above	0.0237682	
		2d concave, reversed above	0.0259941	
Assumed displacement 0.0318517	# 3 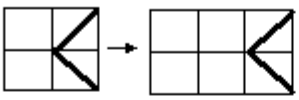	3a only above grown	0.0306417	
		3b all grown	0.0313155	1.0
		3c concave, only above	0.0266233	
		3d concave, all grown	0.0306417	

Crack type	Growth type	Growth pattern	Displacement	f_m
# 04 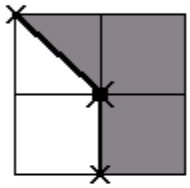 2 intact 1 debond	# 1 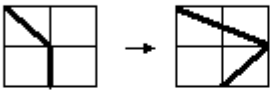	1a only above grown	0.0210044	
		1b all above grown	0.0218444	1.0
		1c all grown	0.0230462	
	# 2a 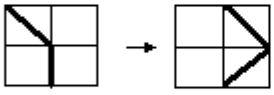	2a only above grown	0.0244566	
		2b all above grown (concave)	0.0251719	1.0
		2c all others grown	0.0264191	
	# 2b 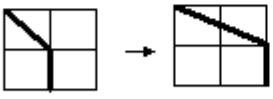	2d only above grown	0.0192261	
		2e all below released	0.0204508	1.0
		2f all grown	0.0212815	
Assumed displacement 0.0244321	# 3 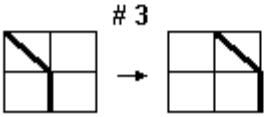	3a only above grown	0.0226905	
		3b all grown	0.0246570	1.0

Crack type	Growth type	Growth pattern	Displacement	f_m
# 05 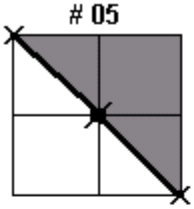 2 intact 2 debond	# 1 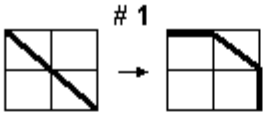	1a only above grown	0.0204508	1.33*
		1b only close edge grown	0.0209699	1.0
		1c all others grown	0.0217922	
	# 2a 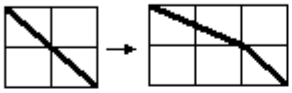	2a only above grown	0.0235954	
		2b only close edge grown	0.0326196	1.0
		2c all others grown	0.0246011	
	# 2b 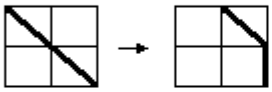	2e only above grown	0.0239696	
		2f only close edge grown	0.0245200	1.0
		2g all others grown	0.0251894	
Assumed displacement 0.0278393	# 3 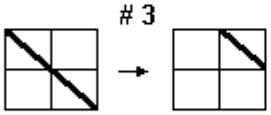	3a only above grown	0.0273125	
		3b only close edge grown	0.0275212	1.0
		3c all grown	0.0281668	

* Choice between values made based on whether crack growth occurs at other MPCs in model

Crack type	Growth type	Growth pattern	Displacement	f_m
# 06 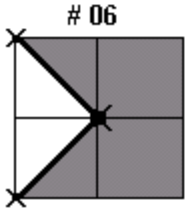 3 intact 1 debond	# 1 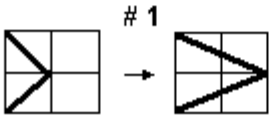	1a only above grown	0.0171358	
		1b only close edge grown	0.0180063	1.33
		1c all others grown	0.0188677	
	# 2 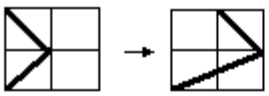	2a only above grown	0.0200954	
		2b all others grown	0.0217368	1.0
		2c reversed, only above grow	0.0204569	
		2d reversed, all grown	0.0218444	
Assumed displacement 0.0247877	# 3 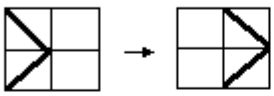	3a only above grown	0.0239185	1.0
		3b all grown	0.0251719	

Crack type	Growth type	Growth pattern	Displacement	f_m
# 07 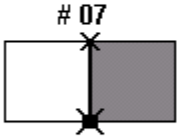 1 intact 1 debond edge	# 1 	1a only above grown	0.0263313	
		1b other edge grown	0.0256299	1.0
		1c 2 from further edge grown	0.0252345	
		1d 3 from further edge grown	0.0277560	
		1e all others grown	0.0276442	
Assumed displacement 0.0240170	# 2 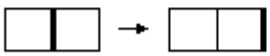	2a only above grown	0.0223732	
		2b 2 from further edge grown	0.0213152	1.0
		2c all grown	0.0236501	

Crack type	Growth type	Growth pattern		Displacement	f_m
# 08 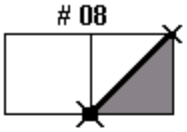 1 intact 2 debond edge **Assumed displacement** 0.0392348	# 1 	1a	only above grown	0.0223732	1.33
		1b	2 on other edge grown	0.0213152	
		1c	all others grown	0.0236501	
		1d	convex, only above grown	0.0236501	
		1e	convex, 2 on other edge	0.0225157	
		1f	convex, all others grown	0.0233839	
	# 2 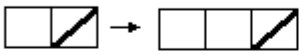	2a	only above grown	0.0277868	1.0
		2b	2 on other edge grown	0.0266607	
		2c	all others grown	0.0304322	
		2d	convex, only above	0.0304322	
		2e	2 on other edge grown	0.0272658	
		2f	convex, all other grown	0.0298941	

Crack type	Growth type	Growth pattern		Displacement	f_m
# 09 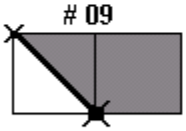 2 intact 2 debond edge **Assumed displacement** 0.0263511	# 1 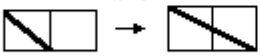	1a	only above grown	0.0190112	1.33
		1b	2 on other edge grown	0.0182241	
		1c	all others grown	0.0198974	
	# 2 	2a	only above grown	0.0255972	1.0
		2b	2 on other edge grown	0.0247740	
		2c	all others grown	0.0263273	

Crack type	Growth type	Growth pattern		Displacement	f_m
# 10 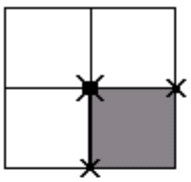 0 intact 2 debond **Assumed displacement** 0.0409875	# 1 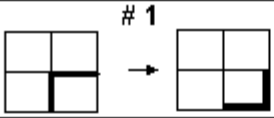	1a	only above grown	0.0246838	1.33
		1b	all others grown	0.0293802	
	# 2 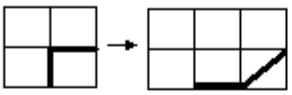	2a	only above grown	0.0359470	1.0
		2b	all others grown	0.0406268	
		2c	reversed, only above	0.0227724	
		2d	reversed, all lower grown	0.0274497	
	# 3 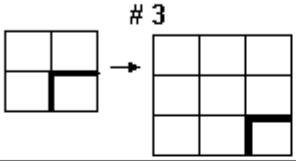	3a	only above grown	0.0357851	1.0
		3b	all others grown	0.0402610	

Crack type	Growth type	Growth pattern		Displacement	f_m
# 11 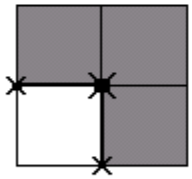 2 intact 0 debond **Assumed displacement** 0.0124909	# 1 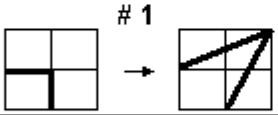	1a	only above grown	0.0060376	1.0
		1b	all others grown	0.0102259	
	# 2 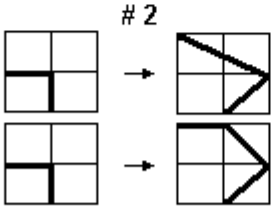	2a	only above grown	0.0219818	1.0
		2b	all others grown	0.0264191	
		2c	reversed, only above	0.0036352	
		2d	reversed, all others grown	0.0079909	
	# 3 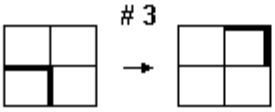	3a	only above grown	0.0192261	1.0
		3b	all others grown	0.0246570	

Edge Cracked Torsion: Mode III

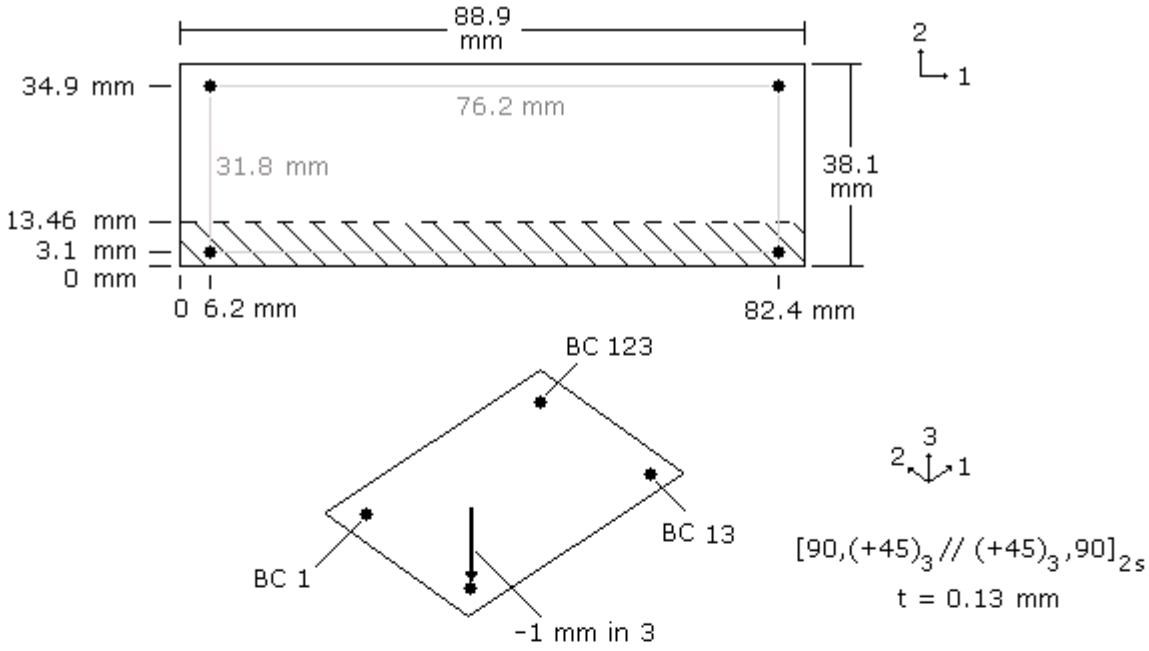

Crack type	Growth type	Growth pattern	Displacement	f_m
# 01 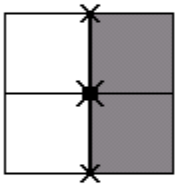 1 intact 1 debond **Assumed displacement** 0.0093657	# 1 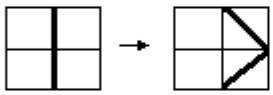	1a all else held 1b few either side released 1c all released	0.0086102 0.0055041 0.0053663	1.0* 1.5
	# 2 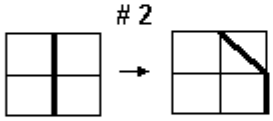	2a all else held 2b few lower side released 2c all released	0.0065512 0.0074786 0.0073376	1.33* 1.0
	# 3 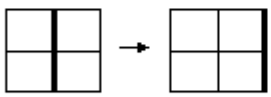	3a all else held 3b few either side released 3c all released	0.0082249 0.0101024 0.0098609	1.0

* Choice between values made based on whether crack growth occurs at other MPCs in model

Crack type	Growth type	Growth pattern	Displacement	f_m
# 02 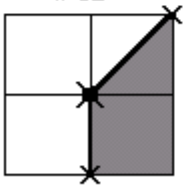 1 intact 2 debond **Assumed displacement** 0.0091917	# 1 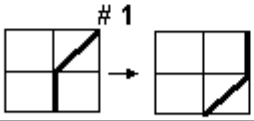	1a only above released 1b few below released 1c all released	0.0072849 0.0075216 0.0078441	1.0
	# 2 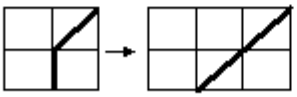	2a only above released 2b few above released 2c few either side released 2d all released	0.0080939 0.0089979 0.0092539 0.0090597	1.0
	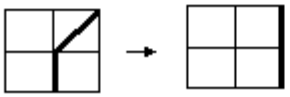	2e only above released 2f few either side released 2g all released	0.0090358 0.0105337 0.0103059	1.0
	# 3 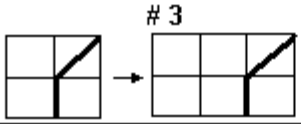	3a only above released 3b few either side released 3c all released	0.0099433 0.0119511 0.0116945	1.0

Crack type	Growth type	Growth pattern	Displacement	f_m
# 03 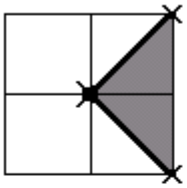 1 intact 3 debond **Assumed displacement** 0.0122678	# 1 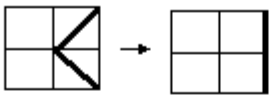	1a only above grown	0.0098609	
		1b few either side grown	0.0109789	
		1c all released	0.0107590	1.0
		1d concave, only above	0.0082249	
		1e concave, all else grown	0.0098609	
	# 2 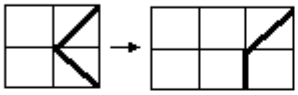	2a all above grown	0.0107929	
		2b few either side grown	0.0123918	
		2c all released	0.0121455	1.0
		2d concave, only above	0.0089364	
		2e concave, all else grown	0.0107929	
	# 3 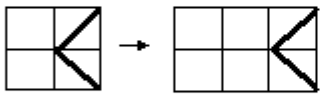	3a only above grown	0.0117790	
		3b all grown	0.0136228	1.0
		3c concave, only above	0.0096672	
		3d concave, all grown	0.0117790	

Crack type	Growth type	Growth pattern	Displacement	f_m
# 04 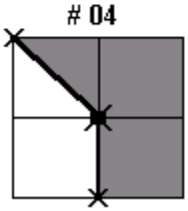 2 intact 1 debond **Assumed displacement** 0.0061813	# 1 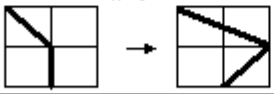	1a only above grown	0.0030516	
		1b few either side grown	0.0032418	2.0
		1c all grown	0.0031377	
	# 2a 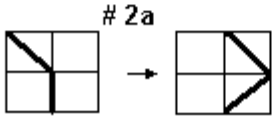	2a only above grown	0.0044467	
		2b few either side grown	0.0045004	1.33
		2c all others grown	0.0052291	
	# 2b 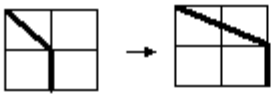	2d only above grown	0.0041614	1.33
		2e all grown	0.0047287	
	# 3 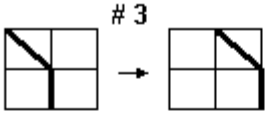	3a only above grown	0.0058171	1.0
		3b all grown	0.0072942	

Crack type	Growth type	Growth pattern	Displacement	f_m
# 05 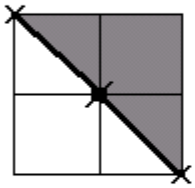 2 intact 2 debond **Assumed displacement** 0.0111544	# 1 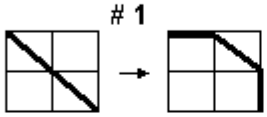	1a only above grown	0.0047536	
		1b few either side grown	0.0051902	1.5
		1c all others grown	0.0050404	
	# 2a 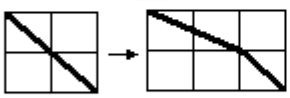	2a only above grown	0.0053141	
		2b few either side grown	0.0059627	1.33+
		2c all others grown	0.0057936	
	# 2b 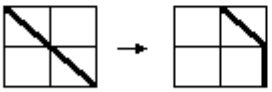	2d only above grown	0.0065437	
		2e few either side grown	0.0079563	1.0+
		2f all others grown	0.0077166	
	# 3 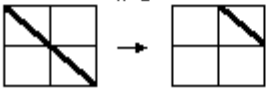	3a only above grown	0.0072642	
		3b few either side grown	0.0091590	1.0
		3c all others grown	0.0089174	

+Choice between values made based on which crack front node is released

Crack type	Growth type	Growth pattern	Displacement	f_m
# 06 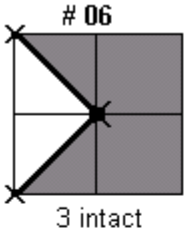 3 intact 1 debond **Assumed displacement** 0.0036610	# 1 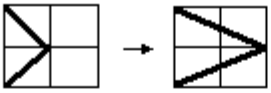	1a only above grown 1b few either side grown 1c all others grown	0.0014948 0.0015052 0.0014532	2.0
	# 2 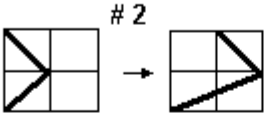	2a only above grown 2b few either side grown 2c all others grown	0.0025307 0.0031366 0.0030169	1.33* 1.0
	# 3 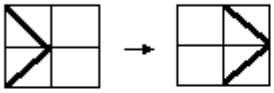	3a only above grown 3b few either side grown 3c all others grown	0.0038247 0.0052908 0.0050851	1.0

* Choice between values made based on whether crack growth occurs at other MPCs in model

Crack type	Growth type	Growth pattern	Displacement	f_m
# 07 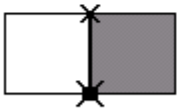 1 intact 1 debond edge **Assumed displacement** 0.0009329	# 1 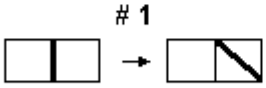	1a only above grown 1b few on side grown 1c all others grown	-0.0007722 -0.0075964 0.0000619	1.5
	# 2 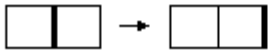	2a only above grown 2b few on side grown 2c all others grown	-0.0004499 0.0006409 0.0007219	1.0

Crack type	Growth type	Growth pattern	Displacement	f_m
# 08 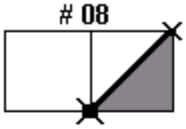 1 intact 2 debond edge **Assumed displacement** 0.0030810	# 1 	1a only above grown 1b few on side grown 1c all others grown	0.0007219 0.0016465 0.0018114	1.0
	# 2 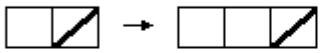	2a only above grown 2b few on side grown 2c all others grown	0.0022036 0.0037843 0.0038523	1.0

Crack type	Growth type	Growth pattern	Displacement	f_m
# 09 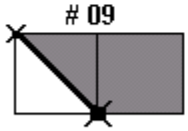 2 intact 1 debond edge **Assumed displacement** -0.0007881	# 1 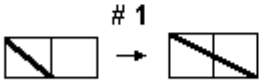	1a only above grown 1b few on side grown 1c all others grown	-0.0000795 0.0000039 0.0000219	1.0
	# 2 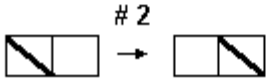	2a only above grown 2b few on side grown 2c all others grown	-0.0015509 -0.0009080 -0.0007722	1.0

Crack type	Growth type	Growth pattern	Displacement	f_m
# 10 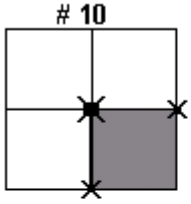 0 intact 2 debond **Assumed displacement** 0.0203471	# 1 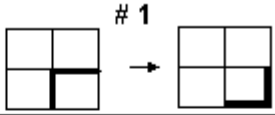	1a only above grown 1b all others grown	0.0089065 0.0102532	1.33
	# 2 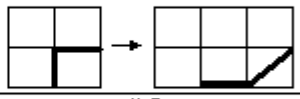	2a only above grown 2b all others grown	0.0108306 0.0126774	1.0
	# 3 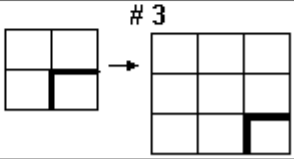	3a only above grown 3b all other	0.0131833 0.0173695	1.0

Crack type	Growth type	Growth pattern	Displacement	f_m
# 11 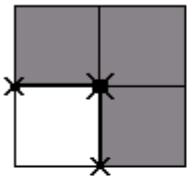 2 intact 0 debond **Assumed displacement** 0.0075551	# 1 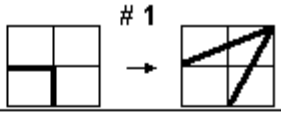	1a only above grown 1b all others grown	0.0019874 0.0029288	4.0 2.0*
	# 2 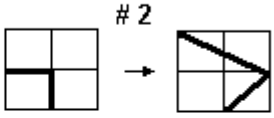	2a only above grown 2b all others grown	0.0030396 0.0031114	1.0
	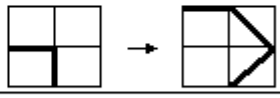	2c only above grown 2d all others grown	0.0030424 0.0032241	1.0
	# 3 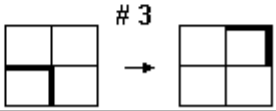	3a only above grown 3b all others grown	0.0041503 0.0072849	1.0

* Choice between values made based on whether crack growth occurs at other MPCs in model

Mixed-Mode Bending: Mixed-Mode I-II

For the mixed-mode bending investigation, the MMB 50% model defined in Chapter 4 was used, and the displacements in mode I, II and III were examined to determine whether the modification factors found from the single-mode tests were conservative. Any non-conservative factors were then modified within the subroutine.

Crack type	Growth type	Growth pattern	Displacement		
# 01 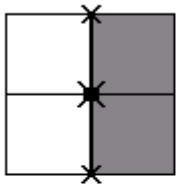 1 intact 1 debond	# 1	1a all else held	0.0108310	-0.0121164	0.0003588
		1b only above held	0.0102750	-0.0147925	0.0001752
		1c further edge released	0.0108070	-0.0123315	0.0001826
		1d further side released	0.0104580	-0.0137880	-0.0000870
	# 2	2a only above grown	0.0194060	-0.0124017	0.0002751
		2b further edge grown	0.0192370	-0.0127088	-0.0000446
		2c all else grown	0.0190460	-0.0137296	0.0003162
	# 3	3a only above held	0.0366830	-0.0126781	0.0006692
		3b further edge grown	0.0364650	-0.0130012	0.0002050
		3c all else released	0.0589990	-0.0149806	0.0012255

Assumed displacement

I: 0.0596880
II: -0.0147865
III: 0.0012016

From single-mode

	I	II	III
g 1	2.5	1	1 or 1.5*
g 2	1.5	1	1.33 or 1*
g 3	1	1	1

From mixed-mode

	I	II	III
g 1	4	1	3 or 5*
g 2	3	1	4
g 3	1.5 or 1*	1	1.5 or 1*

all conservative

Crack type	Growth type		Growth pattern	Displacement		
# 02	# 1	1a	only above released	0.0285190	-0.0139211	-0.0014117
		1b	all above released	0.0301170	-0.0150272	-0.0020964
		1c	all released	0.0300210	-0.0160514	-0.0016287
	# 2a	2a	only above released	0.0305610	-0.0158182	-0.0015108
		2b	above edge released	0.0302520	-0.0163778	-0.0020729
		2c	all released	0.0370240	-0.0182488	-0.0022520
	# 2b	2d	only above released	0.0533750	-0.0140156	-0.0017804
		2e	all above released	0.0558870	-0.0151609	-0.0029951
		2f	all released	0.0613390	-0.0160929	-0.0003437
	# 3	3a	only above released	0.0577930	-0.0160035	-0.0018679
		3b	all above released	0.0700510	-0.0172289	-0.0038090
		3c	all released	0.0757490	-0.0182212	-0.0011780

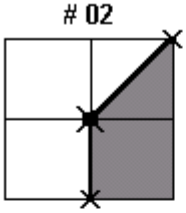

1 intact
2 debond

Assumed displacement

I:	0.0674050
II:	-0.0159815
III:	-0.0028763

From single-mode

	I	II	III
g 1	2	1	1
g 2	1	1	1
g 3	1	1	1

From mixed-mode

	I	II	III
g 1	2	1	1.33
g 2	2 or 1^+	1	1 or 1.33
g 3	1	1	1

all conservative

Crack type	Growth type		Growth pattern	Displacement		
# 03	# 1	1a	only above grown	0.0589990	-0.0149806	0.0012255
		1b	all above grown	0.0613390	-0.0160929	-0.0003437
		1c	all else grown	0.0610640	-0.0165893	0.0007221
	# 2	2a	only above grown	0.0635550	-0.0170501	0.0013106
		2b	all above grown	0.0757490	-0.0182212	-0.0011780
		2c	all else grown	0.0752950	-0.0187616	0.0000198
	# 3	3a	only above grown	0.0686040	-0.0197246	0.0012499
		3b	all above grown	0.0804240	-0.0210681	-0.0014976
		3c	all else grown	0.0829960	-0.0217249	0.0009182

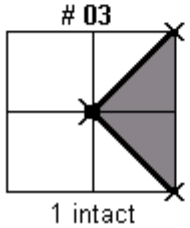

1 intact
3 debond

Assumed displacement

I:	0.0860310
II:	-0.0219354
III:	0.0008679

From single-mode

	I	II	III
g 1	1.5	1.33	1
g 2	1.33	1	1
g 3	1	1	1

From mixed-mode

	I	II	III
g 1	1.5	1.33	1
g 2	1	1	1
g 3	1	1	1

g2 f_{mI} not conservative

Crack type	Growth type		Growth pattern	Displacement		
# 04	# 1	1a	only above grown	-0.0010000	-0.0085752	0.0004578
		1b	all above grown	-0.0010000	-0.0095216	0.0005768
		1c	all grown	-0.0010000	-0.0103589	0.0006433
	# 2a	2a	only above grown	0.0061760	-0.0110612	0.0005809
		2b	all above grown	0.0108310	-0.0121164	0.0003588
		2c	all others grown	0.0106760	-0.0131075	0.0006009
	# 2b	2d	only above grown	0.0003420	-0.0089198	0.0007968
		2e	all above grown	-0.0010000	-0.0099300	-0.0019339
		2f	all grown	-0.0010000	-0.0109223	0.0022506
	# 3	3a	only above grown	0.0128290	-0.0114692	0.0009388
		3b	all above grown	0.0212710	-0.0124549	0.0007118
		3c	all grown	0.0241620	-0.0135113	0.0024904

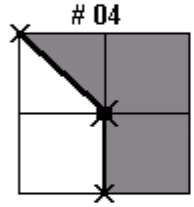

2 intact
1 debond

Assumed displacement

I:	0.0235270
II:	-0.0132119
III:	0.0023792

From single-mode

	I	II	III
g 1	6	1	2
g 2	2 or 3^+	1	1.33
g 3	1	1	1

From mixed-mode

	I	II	III
g 1	-	1 or 1.33*	3
g 2	2 or 10^+	1	3 or 1^+
g 3	1.5 or 1*	1	1

all conservative

Crack type	Growth type		Growth pattern	Displacement		
# 05	# 1	1a	only above grown	0.0010820	-0.0098202	0.0018768
		1b	all above grown	-0.0010000	-0.0109223	0.0022506
		1c	all others grown	-0.0006910	-0.0112496	0.0023642
	# 2a	2a	only above grown	-0.0010000	-0.0116105	0.0018292
		2b	all above grown	-0.0010000	-0.0127657	0.0022317
		2c	all others grown	-0.0010000	-0.0132184	0.0027538
	# 2b	2d	only above grown	0.0148250	-0.0125487	0.0023889
		2e	all above grown	0.0251620	-0.0135113	0.0024904
		2f	all others grown	0.0241880	-0.0139771	0.0028115
	# 3	3a	only above grown	0.0160970	-0.0144852	0.0023195
		3b	all above grown	0.0262900	-0.0155120	0.0024881
		3c	all others grown	0.0281180	-0.0160806	0.0032898

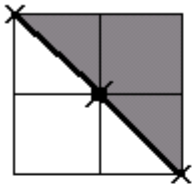

2 intact
2 debond

Assumed displacement

I:	0.0306312
II:	-0.0143577
III:	0.0040277

From single-mode

	I	II	III
g 1	6	2	2.25
g 2	2	1	1.33 or 1+
g 3	1	1	1

From mixed-mode

	I	II	III
g 1	20	1.33 or 1*	1.5
g 2	2 or 1*	1	1
g 3	1.5 or 1*	1	1.5 or 1*

g1 $f_{m\,II}$ and $f_{m\,III}$ not conservative

g2 $f_{m\,I}$ and $f_{m\,III}$ not conservative

Crack type	Growth type		Growth pattern	Displacement		
# 06	# 1	1a	only above grown	-0.0010000	-0.0058313	0.0001089
		1b	all others grown	-0.0010000	-0.0070878	0.0001284
	# 2	2a	only above grown	-0.0010000	-0.0077634	-0.0002743
		2b	all above grown	-0.0010000	-0.0088000	-0.0000677
		2c	all others grown	-0.0010000	-0.0093876	-0.0001762
	# 3	3a	only above grown	0.0054950	-0.0102675	0.0001569
		3b	all above grown	0.0098130	-0.0113980	-0.0001267
		3c	all others grown	0.0108310	-0.0121164	0.0003588

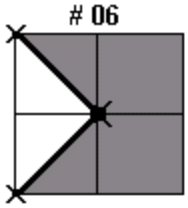

3 intact
1 debond

Assumed displacement

I:	0.0106110
II:	-0.0117921
III:	0.0003350

From single-mode

	I	II	III
g 1	2	1.33	2
g 2	3	1	1.33 or 1*
g 3	1	1	1

From mixed-mode

	I	II	III
g 1	-	1.5	2
g 2	-	1	-
g 3	1.5 or 1*	1	-

all conservative

Crack type	Growth type		Growth pattern	Displacement		
# 07	# 1	1a	only above grown	0.0049800	-0.0131159	0.0045949
		1b	other edge grown	0.0049330	-0.0128209	0.0044686
		1c	all others grown	-0.0010000	-0.0152419	0.0048615
	# 2	2a	only above grown	0.0210500	-0.0137042	0.0080251
		2b	other edge grown	0.0202720	-0.0134348	0.0078106
		2c	all others grown	0.0410040	-0.0154506	0.0091168

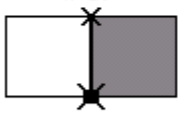

1 intact
1 debond
edge

Assumed displacement

I:	0.0427040
II:	-0.0155817
III:	0.0090590

From single-mode

	I	II	III
g 1	1.33	1	1.5
g 2	1	1	1

From mixed-mode

	I	II	III
g 1	6	1	1.5
g 2	1.5 or 1*	1	1

all conservative

Crack type	Growth type		Growth pattern	Displacement		
# 08	# 1	1a	only above grown	0.0410040	-0.0154506	0.0091168
		1b	other edge grown	0.0401200	-0.0153507	0.0077318
		1c	all others grown	0.0448820	-0.0168282	0.0074676
	# 2	2a	only above grown	0.0519540	-0.0195959	0.0090218
		2b	2 on other edge grown	0.0508720	-0.0196679	0.0075147
		2c	all others grown	0.0865570	-0.0209910	0.0063886

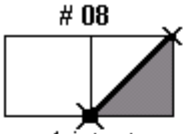

1 intact
2 debond
edge

Assumed displacement

I:	0.0923880
II:	-0.0214824
III:	-0.0028079

From single-mode

	I	II	III
g 1	1.33	1.33	1
g 2	1	1	1

From mixed-mode

	I	II	III
g 1	2	1	-
g 2	1.5 or 1*	1	-

all conservative

Crack type	Growth type		Growth pattern	Displacement		
# 09	# 1	1a	only above grown	-0.0010000	-0.0072161	0.0020143
		1b	other edge grown	-0.0010000	-0.0068464	0.0021367
		1c	all others grown	-0.0010000	-0.0078174	0.0023730
	# 2	2a	only above grown	0.0010030	-0.0114190	0.0037498
		2b	other edge grown	0.0006540	-0.0113392	0.0039374
		2c	all others grown	0.0049800	-0.0131159	0.0045949

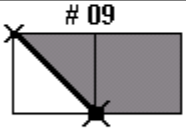

2 intact
1 debond
edge

Assumed displacement

I:	0.0059190
II:	-0.0130588
III:	0.0044231

From single-mode

	I	II	III
g 1	5	1.33	1
g 2	1	1	1

From mixed-mode

	I	II	III
g 1	-	1.5	1.5
g 2	4 or 1*	1	1

all conservative

Crack type	Growth type		Growth pattern	Displacement		
# 10	# 1	1a	only above grown	0.0285200	-0.0139210	-0.0014118
		1b	all above grown	0.0301170	-0.0150272	-0.0020965
	# 2	2a	only above grown	0.0277940	-0.0171109	-0.0015059
		2b	all above grown	0.0292910	-0.0291330	-0.0022130
		2c	all others grown	0.0391956	-0.0224347	-0.0024992
	# 3	3a	only above grown	0.0592880	-0.0181639	-0.0020746
		3b	all above grown	0.0611240	-0.0200143	-0.0034063
		3c	all others grown	0.1055370	-0.0229713	-0.0054397

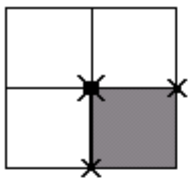

0 intact
2 debond

Assumed displacement

I:	0.0953250
II:	-0.0226012
III:	-0.0040678

From single-mode

	I	II	III
g 1	2	1.33	1.33
g 2	2	1	1
g 3	1	1	1

From mixed-mode

	I	II	III
g 1	3	1.33	1.33
g 2	2	1	1.5
g 3	1.5 or 1*	1	1.5 or 1*

all conservative

Crack type	Growth type		Growth pattern	Displacement		
# 11	# 1	1a	only above grown	-0.0010000	-0.0034780	-0.0001356
		1b	all others grown	-0.0010000	-0.0069005	-0.0001078
	# 2	2a	only above grown	-0.0030000	-0.0088000	-0.0000677
		2b	all others grown	0.0207200	-0.0142224	0.0001107
	# 3	3a	only above grown	0.0007290	-0.0090642	-0.0003008
		3b	all others grown	0.0285200	-0.0139210	-0.0014118

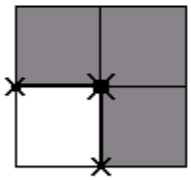

2 intact
0 debond

Assumed displacement

I:	0.0235270
II:	-0.0132119
III:	-0.0023792

From single-mode

	I	II	III
g 1	3	1	4 or 2*
g 2	3	1	2
g 3	1	1	1

From mixed-mode

	I	II	III
g 1	-	1.5	10
g 2	1	1	10
g 3	1	1	1

all conservative

Single-Stiffener Specimens D1 and D2

For the single-stiffener specimens, the crack opening displacements, δ, resulting from the first 25 instances of crack growth were investigated. From these, the ratio of the assumed displacement at increment *n* to the actual displacement at increment (*n* + 1) was calculated, in the three crack opening directions. These were grouped according to the crack type and growth type, and a new set of modification factors were determined that were applied to the analysis of all D1 and D2 configurations.

D1 single-stiffener opening displacements

Crack type	Growth type	$(\delta_n/\delta_{n+1})_I$	$(\delta_n/\delta_{n+1})_{II}$	$(\delta_n/\delta_{n+1})_{III}$
1	1	6.54	3.06	1.47
1	1	15.81	3.18	1.49
1	1	15.51	0.00	2.06
1	2	8.38	1.93	1.02
2	1	10.50	3.25	1.49
2	1	13.59	3.34	1.30
2	1	10.86	3.24	1.45
2	1	13.84	3.32	1.21
2	1	12.77	3.20	2.00
2	1	10.86	3.15	1.60
2	1	14.85	3.21	1.43
2	1	31.02	3.21	2.24
2	1	66.70	3.38	286.68
2	1	-647.31	3.36	61.41
2	2	2.39	1.98	1.51
2	2	2.69	1.63	1.24
2	2	2.31	1.56	1.04
7	1	-53.81	2.31	1.53
7	1	-46.70	2.12	1.27
7	1	-37.67	2.19	1.63
7	1	-38.67	2.12	1.28
7	2	5.92	1.56	0.91
8	1	4.15	1.70	0.81
8	1	4.41	1.71	0.81
8	1	179.21	1.90	1.24

D2 single-stiffener opening displacements

Crack type	Growth type	$(\delta_n/\delta_{n+1})_I$	$(\delta_n/\delta_{n+1})_{II}$	$(\delta_n/\delta_{n+1})_{III}$
1	1	2.14	1.35	1.11
1	1	2.14	1.36	2.23
1	1	1.08	1.43	-0.48
1	1	2.50	1.43	-1.88
2	1	1.60	1.60	7.57
2	1	9.26	3.78	3.86
2	1	8.91	3.89	7.45
2	1	4.73	4.16	-0.71
2	1	7.86	3.97	1.48
2	1	7.20	3.71	0.16
2	1	8.42	3.54	1.90
2	1	7.19	3.73	-4.83
2	1	5.16	4.06	-0.25
3	1	1.51	0.89	2.25
3	1	1.32	1.56	3.16
3	1	1.51	1.07	1.96
3	1	1.29	1.60	8.00
7	1	3.80	0.16	-4.91
7	1	4.27	0.06	11.54
7	1	1.47	1.21	-1.08
7	1	1.63	1.21	-1.07
7	1	1.72	1.14	-0.33
7	1	3.92	0.25	-1.60
7	1	1.81	1.17	-0.21
7	1	4.64	0.12	-4.83

D1 modification factors

Crack type	Growth type	f_{m_I}	$f_{m_{II}}$	$f_{m_{III}}$
1	1	6.00	3.00	1.50
1	2	8.00	2.00	1.00
2	1	10.00	3.00	1.33
2	2	2.33	1.50	1.00
7	1	100.00	2.00	1.33
7	2	5.50	1.50	1.00
8	1	4.00	1.50	1.00

D2 modification factors

Crack type	Growth type	f_{m_I}	$f_{m_{II}}$	$f_{m_{III}}$
1	1	2.00	1.33	1.00
2	1	5.00	3.50	1.00
3	1	1.33	1.00	1.00
7	1	1.50	1.00	1.00